Performance Limitations in Practical Transparent Conducting Oxide Thin Films

Alex T. Vai

Balliol College

University of Oxford

Supervisor: Professor Peter P. Edwards FRS

A thesis submitted in partial fulfillment of
the requirements for the degree of

Doctor of Philosophy in Inorganic Chemistry

2015

Performance Limitations in Practical Transparent Conducting Oxide Thin Films

Alex T. Vai (Balliol College)

A thesis submitted in partial fulfillment of the requirements for the degree of Doctor of Philosophy in Inorganic Chemistry, Michaelmas Term 2015

Abstract

Zinc oxide (ZnO) has long been advanced as a low cost, earth-abundant transparent conducting oxide (TCO) with potential as a replacement for high-performance, but costly, indium oxide (In_2O_3) based materials in a wide range of technological applications. However, despite decades of research and development efforts, ZnO-based materials have still failed to displace the incumbents in any large-scale applications.

Given the compelling materials cost advantages of ZnO, it is almost certain that its poor adoption is due to deficits in its technical performance. This thesis aims to fulfill the need for systematic, fundamental work to identify and examine the factors that limit TCO performance, and in particular, those that limit ZnO relative to In_2O_3.

Using spray pyrolysis as the primary deposition method, many different series of ZnO and In_2O_3 films have been prepared and examined using a range of chemical, structural, and optoelectronic characterization techniques.

After essential background information on the basic physics and chemistry of TCOs, as well as a detailed discussion of the chosen deposition and characterization methods, three main classes of performance limitations will be covered: 1) those related to the intrinsic properties of electronic transport in crystalline TCO domains, 2) those arising in the course of impurity doping, and 3) those occurring due to grain boundary effects and the polycrystalline nature of thin film TCO samples.

Taken together, these results will show that preparing ZnO-based TCOs with performance approaching that of the best In_2O_3-based materials, while very likely to be *technically* possible, will almost certainly involve overcoming significant engineering and process development challenges that, importantly, are not required to make high quality In_2O_3. Ultimately, whether ZnO will ever find significant, real-world use as a TCO will depend on whether the deep differences between ZnO and In_2O_3 performance limits that will be highlighted and examined in this thesis can be bridged in a practical and cost-effective manner.

Performance Limitations in Practical Transparent Conducting Oxide Thin Films

Alex T. Vai (Balliol College)

A thesis submitted in partial fulfillment of the requirements for the degree of Doctor of Philosophy in Inorganic Chemistry, Michaelmas Term 2015

Extended Abstract

For some time, ZnO has been advanced as a low cost, earth-abundant transparent conducting oxide (TCO) with potential as a replacement for the high-performance, but costly, In_2O_3-based materials that currently dominate in applications ranging from photovoltaics and electronic displays to solid-state lighting and energy-efficient glass coatings. However, despite enormous research and development efforts, ZnO-based materials have thus far failed to significantly displace the incumbents in any large-scale applications.

Especially given that ZnO has compelling cost and resource availability advantages over its competitors, it is almost certain that its poor adoption is primarily due to deficits in its technical performance. This thesis aims to fulfill the need for systematic, fundamental work to identify and examine the factors that limit TCO performance, and in particular, those that limit ZnO relative to In_2O_3. The insights thus obtained will be used to critically assess whether further research focus on ZnO is likely to lead to new methods for overcoming its performance limitations, and where such future work might most productively be directed.

To do this, we have chosen spray pyrolysis as our primary method for depositing ZnO and In_2O_3 thin films because of its speed, flexibility, and demonstrated ability to produce high-quality research samples. Many different series of doped and undoped TCO films have been prepared and examined in detail using a wide range of chemical, structural, and optoelectronic characterization techniques.

After providing essential background information on the basic physics and chemistry of TCO materials, as well as a detailed discussion and validation of the chosen deposition and characterization methods, three main classes of performance limitations will be covered:

The first relates to the intrinsic properties of electronic transport in crystalline TCO domains, which are dictated by both the structure of the oxide and the presence of defects and impurities. It will be examined how such factors interact to set limits on the maximum achievable electrical performance of these materials, and whether any of these limits might be more flexible than others. We will also assess the extent to which real, experimental samples can be adequately described using concepts from this single crystal picture.

The second class of limits arises because the impurity doping needed to achieve high levels of electrical conductivity is only effective up to a certain point. The chemical, structural, and electrical role played by extrinsic atoms in a host lattice will be examined and used to describe mechanisms that restrict effective and efficient doping. Both material- and deposition process-specific factors will be considered, along with examples of techniques for overcoming some of these.

Finally, the third class of limitations is due to the fact that virtually all scalable techniques for the deposition of TCO thin films produce polycrystalline samples, whose performance will depend on both the properties of grain interiors and grain boundaries. The mechanisms by which grain boundaries can exert their sometimes dominating influence on thin film electrical performance will be examined. Furthermore, grain boundary effects will be revealed as one of the most important factors differentiating ZnO and In_2O_3. A variety of practical approaches for modifying the extent of grain boundary influences will be discussed.

Taken together, these results will show that the preparation of ZnO-based TCOs with performance approaching that of the best In_2O_3-based materials, while very likely to be *technically* possible, will almost certainly involve overcoming significant engineering and process development challenges that, importantly, are not required to make high quality In_2O_3. Ultimately, whether ZnO will ever find significant, real-world use as a TCO will come down to whether the deep differences between ZnO and In_2O_3 performance limits that will be highlighted and examined in this thesis can be bridged in a practical and cost-effective manner.

The work described in this thesis was carried out in the Inorganic Chemistry Laboratory at the University of Oxford from October 2012 until October 2015, under the supervision of Professor Peter P. Edwards. All of the work is my own unless otherwise stated, and has not been previously submitted for a degree at this or any other university.

Alex T. Vai

October 2015

To my parents, for whom nothing I've ever needed has been too much...

...and to every teacher who has helped make me who I am.

Acknowledgments

When I first arrived at Oxford, I had in my head that I would be working on combinatorial methods for discovering new hydrogen storage materials. This is what I had told to everyone I knew, had written in all of my application materials, and had said in all of my interviews. However, my very first meeting with my supervisor, Professor Peter Edwards, put a quick end to that notion. I'm fairly certain the first thing that he said to me after hello was "I'd like for you to work on Transparent Conducting Oxides." And that was that.

Yet, other than this one exception, I am incredibly grateful to Pete for the almost complete freedom he has given me to define my project, choose my questions, and carry out my research. His full support has really given me the opportunity to grow and learn in a way that would not have otherwise been possible, and I sincerely hope that I have lived up to the trust that he has placed in me.

Far too many people have assisted me with technical aspects of my project to be listed here, and so their invaluable contributions will be detailed in separate acknowledgments in the chapters to follow. Here, I will only highlight Dr. Vladimir Kuznetsov and Prof. Jon Dilworth for all of the discussions, advice, and reality checks that they have so freely and generously offered.

I am most grateful to all of my friends and colleagues in the PPE Group, particularly Drs. Nazanin Rashidi and Andrew Seel, who have always been a welcome breath of sanity in a sometimes chaotic world. I must also mention the contribution of the chemistry department support staff, and most especially Ms. Linda Webb, for all that they do to make things actually *happen* around here.

Beyond the walls of the Inorganic Chemistry Laboratory, many thanks to all those who have added to the richness and camaraderie of my Oxford experience. I am incredibly fortunate to have been part of an incredible cohort of Balliol graduate

students (especially the chemists!) and an incomparable group of housemates at 49 Ferry Road. I also want to add a particular thank you to the Oxford University Orienteering Club (OUOC), whose unreserved welcome of even rubbish beginner orienteers has given me a chance to see far-flung corners of Britain, indulge my sense of adventure, and stay fit despite my thesis work. Hopefully, the desire to seek orange flags in the woods that they have instilled in me will last for a long time to come.

The Clarendon Fellowship and Balliol College have provided invaluable financial and logistical support for my research, without which I would not have had the chance to study abroad. I am also grateful to my employer, Ambri, Inc. (Cambridge, MA, USA), for allowing me leave to pursue my dream of earning a doctorate and being willing to take me back once this is all done.

Finally, there is not enough that can be said to thank all of my friends and family back home. I know that doing a PhD across the sea has made me more distant than I wanted to be, and than you've deserved. And most especially, to my friend D.: I am so sorry that I had to be away when you had to go.

I am profoundly grateful for everyone's continuing support, encouragement, and well-wishes. Thank you!

—Alex T. Vai
October 2015, Oxford, UK

Contents

Abstract **iii**

Acknowledgments **xi**

List of Figures **xix**

List of Tables **xxv**

1 Introduction: The Cases For and Against Zinc Oxide Transparent Conductors **1**

1.1 The Economic Case for ZnO 3

1.2 The Search for an ITO Replacement 6

1.3 Practical and Fundamental Limitations 8

1.4 Summary of Upcoming Chapters 11

2 The Basic Physics of Transparent Conducting Oxides **17**

2.1 The Drude Free-electron Model 17

2.2 Transparent *and* Conductive Oxides 20

2.2.1 Electronic Band Structure 20

2.2.2 Optical Transparency 23

2.2.3 Electrical Conductivity and the Generation of Carriers 26

2.3 Carrier Scattering Mechanisms 28

2.4 The Metal-to-Non-Metal Transition in TCOs 29

2.5 Summary 33

3 The Measurement and Characterization of TCOs **37**

3.1 Electronic Transport Measurements 38

3.1.1 Conductivity 38
3.1.2 The Hall Effect 41
3.2 Optical Properties 43
3.2.1 Transmission Spectrophotometry 43
3.2.2 Dielectric Modeling 49
3.3 Microstructural Characterization 52
3.3.1 Thin Film X-ray Diffraction 52
3.3.2 Electron Microscopy 56
3.4 Chemical Analysis 60
3.4.1 Energy-dispersive X-ray Spectroscopy 61
3.4.2 X-ray Photoelectron Spectroscopy 63
3.4.3 X-ray Absorption Spectroscopy 66
3.5 Experimental 71
3.5.1 Electrical Transport Measurements 71
3.5.2 Optical Measurements 72
3.5.3 X-ray Diffraction 72
3.5.4 Electron Microscopy 72
3.5.5 X-ray Photoelectron Spectroscopy 73
3.5.6 Acknowledgments 73

4 Preparation of TCOs by Spray Pyrolysis 79
4.1 Spray Pyrolysis in Context 80
4.1.1 Pulsed-laser Deposition 80
4.1.2 Sputtering 82
4.1.3 Spray Pyrolysis 83
4.2 Spray Pyrolysis Hardware 84
4.2.1 Solution Atomization and Gas Control 85
4.2.2 Substrate Heater Assembly 86
4.2.3 Substrate Selection 88
4.3 Precursor Solutions 90
4.3.1 Precursor Screening and Selection 90
4.3.2 Dopants 94
4.3.3 Solution Chemistry 96

4.4 Process Variables . . . 105
4.4.1 Substrate Surface Temperature . . . 105
4.4.2 Carrier Gas . . . 111
4.4.3 Solution Amount and Sample Thickness . . . 112
4.4.4 Process Timing . . . 115
4.4.5 Other Process Variables . . . 117
4.5 Characterization of Platform Reproducibility . . . 118
4.5.1 Assessment of Reproducibility . . . 118
4.5.2 Remaining Sources of Error . . . 120
4.6 Conclusion . . . 122
4.7 Experimental . . . 123
4.7.1 Base Precursor Solutions . . . 123
4.7.2 Spray Pyrolysis Procedures . . . 124
4.7.3 Thermal Analysis of Precursors . . . 125
4.7.4 Acknowledgments . . . 126

5 The Intrinsic Conductivity of Zinc and Indium Oxides 131
5.1 Single Crystal Behavior: A Literature Review . . . 132
5.1.1 Transport Limitations at Lower Defect Concentrations . . . 132
5.1.2 Transport Limitations at Higher Defect Concentrations . . . 134
5.2 The Case of Bromide-doped In_2O_3 . . . 137
5.2.1 Electrical Properties . . . 137
5.2.2 Determination of Chemical Identity . . . 139
5.2.3 Potential Workarounds to Mobility Limits . . . 141
5.2.4 Current Limitations and Future Work . . . 145
5.3 A Doping-induced Transition to the Metallic State in ZnO . . . 146
5.3.1 Electronic Transport Measurements . . . 146
5.3.2 Identifying the Location of the MNMT . . . 149
5.4 Optical Frequency Transport Measurements . . . 153
5.4.1 Motivation . . . 153
5.4.2 Approach . . . 156
5.4.3 Deposition Temperature Dependence . . . 160
5.4.4 Proposed Future Measurements . . . 162

5.5 Conclusion 163
5.6 Experimental 164
5.6.1 Deposition of Bromide-doped In_2O_3 164
5.6.2 Geometry Optimization of In_2O_3 and IBrO 164
5.6.3 10 K Resistance Measurements 165
5.6.4 Acknowledgments 165

6 Limitations on Impurity Doping 169
6.1 Finding the Limits of Indium-doped ZnO 170
6.1.1 Preliminary Characterization 171
6.1.2 Optoelectronic Properties and Doping Efficiency 176
6.2 The Nature of Compensating Defects 181
6.2.1 General Thermodynamic Limits to Doping 181
6.2.2 Dopant Disposition in IZO: An XAS Study 184
6.3 Doping Limits from Solution Chemistry: The Fluoride-enhanced Silicon doping of ZnO 197
6.3.1 Ruling out Co-Doping 198
6.3.2 The Solution Chemistry of Silicon and Fluoride 201
6.3.3 Implications for Process Design 204
6.4 Conclusion 207
6.5 Experimental 209
6.5.1 Preparation of Indium-doped ZnO (IZO) 209
6.5.2 EDX Analysis of IZO Films 209
6.5.3 EXAFS Data Collection and Modeling 210
6.5.4 Silicon-doped ZnO (SiZO) 211
6.5.5 NMR Analysis of Model Precursor Solutions 213
6.5.6 Acknowledgments 213

7 Grain Boundary Effects in Transparent Conducting Oxides 217
7.1 Basic Concepts 218
7.1.1 Polycrystallinity 218
7.1.2 Defects at Grain Boundaries 220
7.1.3 Models for Electronic Transport in Polycrystalline Materials . 223

7.2 Grain Boundaries in ZnO and In_2O_3 227
7.2.1 Room Temperature Properties 227
7.2.2 Variable Temperature Hall Effect 230
7.2.3 X-ray Photoelectron Spectroscopy of ZnO Surfaces 234
7.2.4 Photoconductive Response 236
7.2.5 Intrinsic Differences between ZnO and In_2O_3 241
7.2.6 T_{dep}-dependent Morphological Changes 244
7.3 Mitigating Grain Boundary Effects in ZnO 247
7.3.1 *in situ* UV: A New and Permanent Photoconductive Effect . . 248
7.3.2 Doping 255
7.3.3 Deposition Technique 259
7.3.4 Encapsulation 264
7.4 Conclusion: Revising the Central Question 266
7.5 Experimental 267
7.5.1 Photoconductivity Measurements 267
7.5.2 *in situ* Irradiation during Spray Pyrolysis 268
7.5.3 Vacuum-based Thin Film Deposition Techniques 268
7.5.4 Preparation of Tin-doped In_2O_3 Thin Films 269
7.5.5 Accelerated Aging Test 269
7.5.6 Acknowledgments 270

8 Conclusions: Where Next for ZnO? 275
8.1 Current Status of ZnO-based TCOs 275
8.2 Opportunities for Future Research 277
8.3 Concluding Remarks 281

Appendix A Swanepoel Calculator 285

Appendix B Derivation of Electric Susceptibilities 291

Appendix C Standard Equipment and Procedures for Spray Pyrolysis 293
C.1 Mount Compressed Gas Spray Nozzle 294
C.2 Prepare and Mount Glass Substrate 295
C.3 Chamber Set-up 297

C.4 Heat-up 298
C.5 Spraying 300
C.6 Cool-down 301
C.7 Quick Analysis 302
C.8 Clean Apparatus 302
C.9 Detailed Analysis 303

Appendix D Thermal Analysis of Precursors 309
D.1 TVA 309
D.2 Cold Trap and NMR Experiment 314

Appendix E Pawley Refinements 317

Appendix F Optical Frequency Transport Modeling 323
F.1 Fits to 5 at% Indium-doped ZnO 323
F.2 Fits to 5 at% Tin-doped In_2O_3 325

Appendix G EXAFS Fitting Logs 329
G.1 Defining Path Nomenclature 329
G.2 Fitting Logs 331
G.2.1 Models for 0.5IZO 331
G.2.2 Models for 1.5IZO 331
G.2.3 Models for 5IZO 333
G.2.4 Models for 12.5IZO 335

Appendix H Publications Resulting From This Work 339

List of Figures

1.1 A transparent conducting oxide thin film 2
1.2 Historic indium metal pricing 4
1.3 Cost advantage for ZnO-based films 5
1.4 Elements reported as dopants in ZnO 7
1.5 Characteristics of common TCO deposition techniques 7
1.6 Optoelectronic performance of TCOs in 1983 and 2012 9
1.7 Divergent conductivity of ZnO and In_2O_3 deposited by spray pyrolysis 10

2.1 Electronic band structure 21
2.2 Band structures of ZnO and In_2O_3 23
2.3 Burstein-Moss effect 24
2.4 Optical properties arising from Drude model electrons 25
2.5 Electronic structures of TCOs with defects 27
2.6 Schematic of impurity conduction at various n 31
2.7 Mott-Edwards-Sienko plot 32

3.1 Bar geometry for definition of resistance 39
3.2 The van der Pauw measurement geometry 40
3.3 A schematic illustrating the Hall effect 42
3.4 Representative UV-Vis-NIR transmission spectrum 44
3.5 Effect of haze on UV-Vis-NIR transmission spectra 45
3.6 Features of Swanepoel envelope method calculation 46
3.7 Determination of optical bandgap using the Tauc method 49
3.8 Geometric model of TCO samples used for dielectric modeling 52
3.9 The effects of preferred orientation on XRD patterns 55
3.10 Secondary electron detection in SEM 57

3.11 Cross-sectional SEM 58
3.12 Electron beam interaction volume 62
3.13 Example XPS data 66
3.14 Example XAS data 67
3.15 Reduced XAS data 69

4.1 Vacuum-based thin film deposition processes 81
4.2 Spray pyrolysis apparatus schematic 85
4.3 TGA of $[Zn(Ac)_2(H_2O)_2]$ and $InCl_3{\cdot}4H_2O$ in N_2 92
4.4 Anhydrous decomposition of zinc carboxylates 93
4.5 TGA of zinc acetate dihydrate under wet and dry N_2 95
4.6 ZnO deposited using different solvents 97
4.7 Speciation of Zn^{2+} and In^{3+} in aqueous solutions 100
4.8 Structure-directing effects in ZnO crystal growth 105
4.9 ZnO deposited using acetate and formate precursors 106
4.10 X-ray diffraction patterns of ZnO deposited at various T_{dep} 107
4.11 SEM surface morphology of ZnO deposited at various T_{dep} 107
4.12 UV-Vis-NIR spectra, thickness, and transmittance of ZnO prepared at various T_{dep} 109
4.13 Electrical transport in ZnO prepared at various T_{dep} 111
4.14 Effect of choice of carrier gas on electronic properties of undoped and indium-doped ZnO 113
4.15 Effect of carrier gas on preferred orientation of indium-doped ZnO . . 113
4.16 Influence of precursor solution amount on thickness and mobility . . . 114
4.17 Distribution of transport properties in ZnO reproducibility study . . 119
4.18 Visualization of temperature non-uniformity during deposition 121

5.1 Single crystal Hall mobilities 133
5.2 Performance limits due to ionized impurity scattering 135
5.3 Hall effect measurements of In_2O_3 prepared using $InBr_3$ 138
5.4 XRD of In_2O_3 films prepared using $InBr_3$ and $InCl_3$ precursors 139
5.5 EDX of In_2O_3 films prepared using $InBr_3$ and $InCl_3$ precursors 140
5.6 Calculated local environment around bromide in IBrO 143

5.7 Distribution of In-In distances in IBrO and In_2O_3 143
5.8 The MNMT in condensed matter systems 147
5.9 Variable-temperature Hall effect on doped ZnO 147
5.10 Variable-temperature resistivity of doped ZnO between 300 and 10 K 149
5.11 Activation energy for impurity conduction 151
5.12 Ioffe-Regel estimate of MNMT 152
5.13 Summary of electrical properties of spray pyrolyzed films 155
5.14 Example of dielectric modeling: 5 at% IZO deposited at ∼417 °C . . . 157
5.15 Example of dielectric modeling: 5 at% ITO deposited at ∼417 °C . . . 158
5.16 Correlation of thickness from dielectric modeling and other methods . 159
5.17 Optical and Hall carrier concentrations of IZO and ITO 161
5.18 Optical and Hall carrier mobilities of IZO and ITO 161

6.1 EDX elemental analysis of IZO thin film series 173
6.2 XRD of IZO films as a function of In concentration 174
6.3 Lattice parameters of IZO thin films 174
6.4 SEM of IZO films as a function of In concentration 176
6.5 Transport properties of IZO films as a function of In concentration . . 177
6.6 Doping efficiency in doped ZnO films 178
6.7 UV-Vis-NIR transmission spectra of IZO samples 180
6.8 Photograph of IZO samples 180
6.9 Thermodynamically stable values of E_F 182
6.10 Comparison of stable E_F values with electronic structure 183
6.11 Processed EXAFS data for IZO thin films 185
6.12 Substitutional and interstitial positions for In in ZnO 186
6.13 0.5 and 1.5 at% IZO fitted with substitutional indium only 188
6.14 1.5 at% IZO fitted with substitutional and interstitial indium 188
6.15 Local structure around In in In_2O_3 189
6.16 Models for EXAFS data of 12.5 at% IZO 191
6.17 Models for EXAFS data of 5 at% IZO 193
6.18 First shell coordination environment of In in IZO 195
6.19 Conductivity improvement in SiZO films with fluoride addition 198
6.20 Absence of F^- in films prepared with F^--containing solutions 199

6.21 Changes in Si incorporation with addition of F^- 200
6.22 Enhanced Si solubility due to F^- addition 203
6.23 ^{19}F NMR spectra of model Si- and F-containing precursor solutions . 203
6.24 Overall doping efficiency in SiZO prepared with various techniques . . 205
6.25 Estimated costs of potential silicon precursors 206
6.26 Summary of general doping process in TCOs 208

7.1 Evidence for the polycrystalline nature of In_2O_3 thin films 218
7.2 TEM of domain boundaries in Si-doped ZnO 219
7.3 Chemisorption and electron localization at grain boundaries 221
7.4 Intergrain electronic transport 222
7.5 Boundary barrier height relative to Fermi level 223
7.6 Simple equivalent circuit for material with resistive grain boundaries . 226
7.7 Room temperature electrical conductivity of undoped In_2O_3 and ZnO 228
7.8 X-ray diffraction patterns of undoped In_2O_3 and ZnO 229
7.9 Room temperature Hall effect of undoped In_2O_3 and ZnO 229
7.10 Surface morphology of undoped In_2O_3 and ZnO 231
7.11 Mobility vs. temperature for ZnO and In_2O_3 thin films 231
7.12 Three-component model for ZnO O(1s) XPS data 235
7.13 O(1s) XPS of ZnO vs. T_{dep} 236
7.14 Photoconductivity of ZnO under various atmospheres 237
7.15 Photoneutralization of grain boundary acceptor defects 238
7.16 Photoconductive response of ZnO and In_2O_3 samples with varying T_{dep} 239
7.17 Effect of post-deposition UV irradiation on ZnO surface speciation . . 241
7.18 Comparison of large and small area grain-grain contacts 244
7.19 Spray pyrolysis scheme incorporating *in situ* and/or *ex situ* UV treatment 249
7.20 Conductivity of ZnO samples with and without *in situ* irradiation . . 249
7.21 Persistence of *ex situ* photoconductivity 251
7.22 Hall effect of ZnO deposited with and without *in situ* irradiation . . . 251
7.23 Hall effect of ZnO deposited with *in situ* and/or *ex situ* irradiation . 253
7.24 O(1s) XPS of ZnO deposited with and without *in situ* irradiation . . 253
7.25 Changes in mobility of doped ZnO and In_2O_3 with temperature . . . 257
7.26 Surface morphology of Si-doped ZnO deposited by various techniques 260

7.27 Carrier mobility vs. T for Si-doped ZnO prepared by various techniques 262
7.28 Accelerated aging of TCO films prepared using various techniques . . 263

C.1 Overview of spray pyrolysis apparatus 293
C.2 Pneumatic spray nozzle 294
C.3 Heater stage 295
C.4 Heating elements and thermocouple 297
C.5 Heater stage installed in chamber 297

D.1 TVA pressure curves for zinc carboxylates 309
D.2 Analysis of volatile fractions in cold trap from decomposition of zinc formate 311
D.3 Analysis of volatile fractions in cold trap from decomposition of zinc acetate 311
D.4 Analysis of volatile fractions in cold trap from decomposition of zinc propionate 312
D.5 Identification of TVA fractions using MS and FTIR 313
D.6 TVA of zinc acetate without cold trap 313
D.7 ^{1}H NMR data from decomposition of $Zn(Ac)_2$ under spray pyrolysis conditions 314

E.1 Pawley fit and residual for In_2O_3 deposited from $InCl_3$ precursor . . . 317
E.2 Pawley fit and residual for IBrO deposited from $InBr_3$ precursor . . . 318
E.3 Pawley fit and residual for ZnO 319
E.4 Pawley fit and residual for 0.25 at% IZO 320
E.5 Pawley fit and residual for 1.5 at% IZO 320
E.6 Pawley fit and residual for 2.5 at% IZO 321
E.7 Pawley fit and residual for 5 at% IZO 321
E.8 Pawley fit and residual for 20 at% IZO 322

F.1 Optical fitting results for IZO 324
F.2 Optical fitting results for ITO 326

G.1 Scattering paths for In_{Zn} 330
G.2 Scattering paths for $In_{i,oct}$ in ZnO 330

G.3 Scattering paths for In at In_2O_3-like sites 330

List of Tables

1.1 Key requirements for TCO films in various applications 2

4.1 Temperature correction factors for various substrate materials 87
4.2 Qualitative observations for various halide precursors 99
4.3 Qualitative observations for acetate and acetylacetonate precursors . 99
4.4 Summary of time required for deposition of a typical sample 116

7.1 Best-fit parameter values describing temperature-dependent mobility in ZnO and In_2O_3 233
7.2 Photoconductive response of IZO and ITO films 258
7.3 Properties of Si-doped ZnO films prepared by various techniques . . . 260

F.1 IZO optical model parameters 323
F.2 ITO optical model parameters 326

Chapter 1

Introduction: The Cases For and Against Zinc Oxide Transparent Conductors

Many of the defining technologies of the modern world rely essentially on the interaction of light and electricity.

For instance, the proliferation of flat-panel displays and touchscreens of all shapes and sizes is inextricably linked to the rise of a mobile and digitally networked world over the past few decades. The pressing questions of climate change and long-term environmental sustainability have motivated, among many other things, an incredible wave of research and investment into photovoltaics, solid-state lighting, and smart window technologies. Heat-reflective and self-defrosting glasses are used for many applications and play an essential role in keeping our built environment safe, comfortable, and efficient.[1] Even more recently, transparent thin-film transistors and flexible electronics have also become new areas of significant growth.[2]

Such optoelectronic technologies inevitably require the use of thin film materials that are highly transparent to light, while *simultaneously* possessing the requisite (often high) electrical conductivity needed for the operation of a given device (Figure 1.1). This is a combination of properties possessed by only a few materials, most notably a set of wide bandgap d^{10} and d^0 metal oxides, known appropriately as Transparent Conducting Oxides (TCOs).

Given the wide range of potential applications for TCOs, each with its own specific set of requirements, no single material (or even small group of materials) will be the best for all situations.[3] Indeed, as can be seen in Table 1.1, many factors beyond

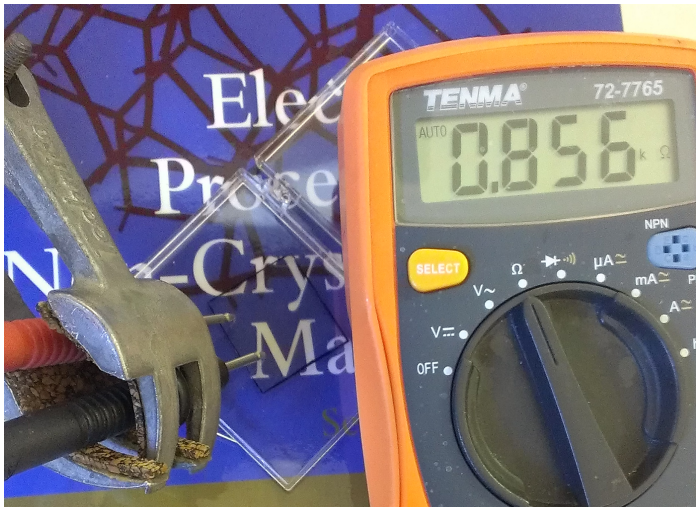

Figure 1.1: An optically transparent and electrically conductive oxide (TCO) thin film on a glass slide. The edge of this silicon-doped zinc oxide (SiZO) film is highlighted in black using a permanent marker.

Table 1.1: A selection of common transparent conductor applications and key requirements for the properties of the associated TCO layer

Application	Key requirements for TCO layer
Photovoltaics	High conductivity, high transparency (visible and IR), moderate haze, environmental stability
Flat Panel Displays	High conductivity, high transparency (visible), patternable
Touchscreens	Moderate conductivity, high transparency, patternable
Thin-Film Transistors	Extremely low conductivity, high carrier mobility, high transparency, good interfacial properties
Heat-Reflective Glasses	High transparency (visible), high reflectivity (IR), scalable deposition, low-cost
Smart Windows	High conductivity, high transparency (visible and IR), scalable deposition, low-cost
Solid-State Lighting	High conductivity, high transparency (visible), appropriate work function, high smoothness
Flexible Electronics	High transparency, flexibility, environmental stability, low deposition temperature

the namesake properties of transparency and conductivity go into determining how suitable materials are for a given use. That being said, with only a few exceptions, high optical transparency and high electrical conductivity are necessary prerequisites for a successful thin film TCO material.

In this typical case where maximizing conductivity and transparency is desirable, materials based on indium oxide (In_2O_3), and particularly tin-doped indium oxide (ITO), are the undisputed leaders. Not only is it possible to prepare ITO with class-leading conductivity ($\sim 10^4\,(\Omega\,\mathrm{cm})^{-1}$) and excellent transparency (typically $>85\,\%$), such high quality films can be easily prepared not only in the highly controlled conditions of the laboratory, but also by industry on very large scales. And while the vacuum-based sputtering techniques typically used to prepare commercial ITO are relatively complex and capital intensive, they are also technologically mature, well-understood, and once optimized for a specific process, highly reproducible and reliable.

1.1 The Economic Case for ZnO

This being said, In_2O_3-based materials are not entirely without faults, though these are primarily economic, not technical. The fundamental problem is that indium is a relatively rare element with an average crustal abundance of around 50 ppb (about one-third lower than that of silver), meaning that it can only be produced as a byproduct of the mining of other metals.[4,5] Furthermore, the top four national producers of indium (China, South Korea, Japan, and Canada) accounted for $\sim 86\,\%$ of total worldwide production in 2014. While there is substantial recycling and warehousing, it is also worth noting that global primary production in this year was estimated at just slightly over half of total consumption.[4]

When coupled with sharply growing demand, the result of this scarcity and geographical concentration is an indium market price that is both high and volatile (Figure 1.2).[6,7] Furthermore, many analyses have noted that these facts raise the possibility of future supply insecurity and have thus rated indium as a "critical" material from a resource availability perspective.[8–11]

Zinc oxide (ZnO) is one of the prototypical TCOs and is perhaps the most often cited when low-cost alternatives to indium oxide are being discussed.[12] It is

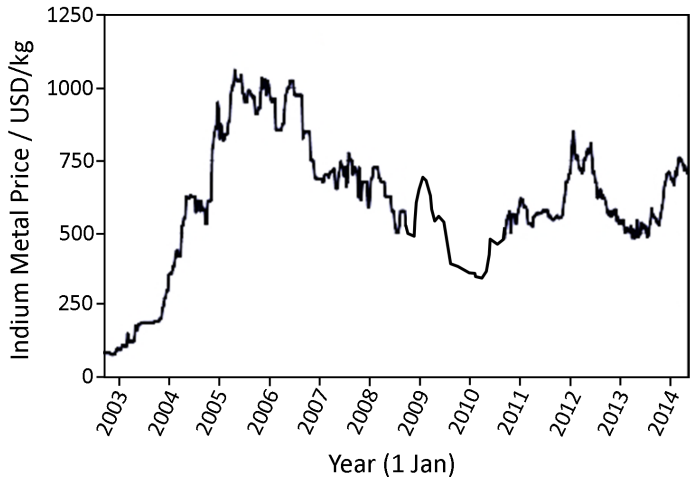

Figure 1.2: Historic commodity pricing for indium metal (min. 99.99 % purity, FOB Rotterdam) from September 2002 to July 2014 as compiled from public sources.

worth showing just how much of a cost advantage a ZnO-based TCO material could have over one based on In_2O_3. From the point of view of raw materials availability, the crustal abundance of zinc is about three orders of magnitude higher than that of indium, thus making zinc the most abundant of the traditional TCO cations.[i] Correspondingly, the bulk commodity price for zinc of a purity suitable for TCO applications (min. 99.995 %) currently averages just over 2 USD/kg.

Annual global consumption of zinc for all purposes in 2014 was just over 13.6 million metric tons, dwarfing the ∼1500 tons of indium used over the same period.[13] Unlike indium, whose only significant use is in the production of ITO, zinc and its compounds are used for a tremendous range of purposes. This scale and diversification makes zinc pricing relatively stable against even moderate disruptions, and as such, its pricing has stayed in a relatively narrow range since late 2008 (between about 1.75 and 2.5 USD/kg).[14] The stability of its market allows ZnO to be traded as a true commodity chemical, whereas the day-to-day volatility of indium pricing usually prevents the buying and selling of In_2O_3 and ITO on credit and requires transactions on a cash-up-front basis, as would be typical for other precious metals.[15]

Of course, it is not fair to compare ZnO and In_2O_3 solely on the basis of material cost, as the other costs in the manufacturing process (capital, labor, other consumables, etc.) will dilute ZnO's advantage. Nevertheless, a simple thought experiment,

[i] Indeed, virtually all indium is extracted as a byproduct of zinc, tin, and copper mining.[5]

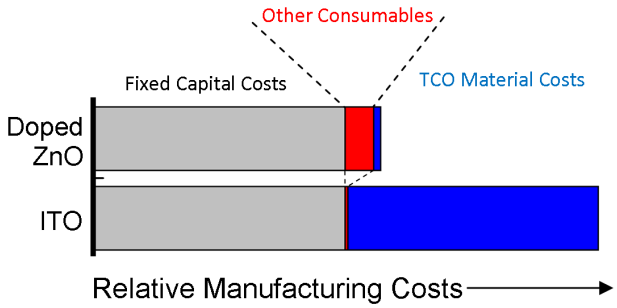

Figure 1.3: Summary of thought experiment illustrating how the difference in raw materials costs between ZnO and ITO carries through to the total cost of a prepared TCO film, assuming that the two materials can be prepared using the same technique. Despite conservatively assuming a very high fixed cost of capital (equal to the materials cost for ITO) and the need for ten times more doped ZnO than ITO to produce a thin film with the same sheet resistance, the cost advantage for ZnO is still nearly twofold.

summarized in Figure 1.3, can illustrate how powerful and persistent the materials cost advantage of ZnO could be, even in the face of these additional factors.

Let us assume that the same deposition process can be used to prepare thin films of either ITO or a less-conductive doped ZnO. Generally speaking, even in a capital-intensive manufacturing process like magnetron sputtering, overall costs are dominated by those of the consumables. However, for the sake of argument, we can take a highly conservative scenario where fixed capital costs are as much as the cost of the ITO per unit area of product.[16] Further, the superior electrical conductivity of ITO is acknowledged by requiring that 10 times the thickness of doped ZnO must be deposited to achieve the same sheet resistance. This also causes a proportional increase in non-material consumable costs like labor and electricity for the preparation of the doped ZnO.

While this thought experiment is far from quantitative, Figure 1.3 shows that the nearly insignificant material cost of ZnO compared to that of In_2O_3 is the dominant factor in differentiating their relative costs. Even in the extremely conservative scenario posed, the ITO thin film would be nearly twice as costly as one prepared from doped ZnO. For electronic component manufacturers with profit margins that are often just a few percent, such a reduction in the cost of an expensive starting material would be highly significant.

1.2 The Search for an ITO Replacement

In fact, these economic arguments would strongly suggest that ZnO-based materials should dominate on a cost basis, so long as samples with adequate technical performance can be prepared using a deposition technique similar to that used for the incumbent. In other words, as a low-cost material, the question of ZnO adoption more or less can be reduced to one of its performance. The better its practically achievable performance, however defined, the more applications will be accessible.

This potential of replacing a scarce and precious material with a cheap and abundant commodity chemical like ZnO has motivated a tremendous body of research over the past three decades, and especially over the past 10 years. Perhaps inspired by the industrially driven optimization of ITO deposition that has taken place since the early reports of its transparent conductivity in the late 1940s,[17,18] many efforts to find high-performance reduced-indium and indium-free TCOs have treated this task as a multi-parameter optimization problem, to be solved by an empirical search over the parameter space of possible TCO compositions, deposition techniques, and process conditions. Stadler has laboriously counted over ten thousand papers published on TCOs between just 2007 and 2011.[19]

Even just considering materials based on zinc oxide (ZnO), Figure 1.4 shows that chemical elements from every region of the periodic table except the noble gases and transuranics have been studied as potential extrinsic dopants.[20–32] When one further considers the possibility of double and even higher variants of co-doping, the difficulties of treating this as a combinatorial problem are quite apparent.[33–38]

On top of the number of material combinations, the preparation of these doped zinc oxides has been carried out using a full range of physical and chemical deposition techniques, each with its own set of process parameters to be optimized.[39] On one end are highly specialized laboratory techniques that can be used for preparing epitaxial, nearly defect-free thin films, such as molecular-beam epitaxy (MBE), atomic-layer deposition (ALD), and pulsed-laser deposition (PLD). Sputtering techniques are a more easily scalable class of physical deposition methods, and are by far the most commonly used by industry today for the production of TCO coatings. On the other end are the fast and relatively simple, but far less controlled solution-based techniques such as spray pyrolysis and various sol-gel coating methods, including spin coating

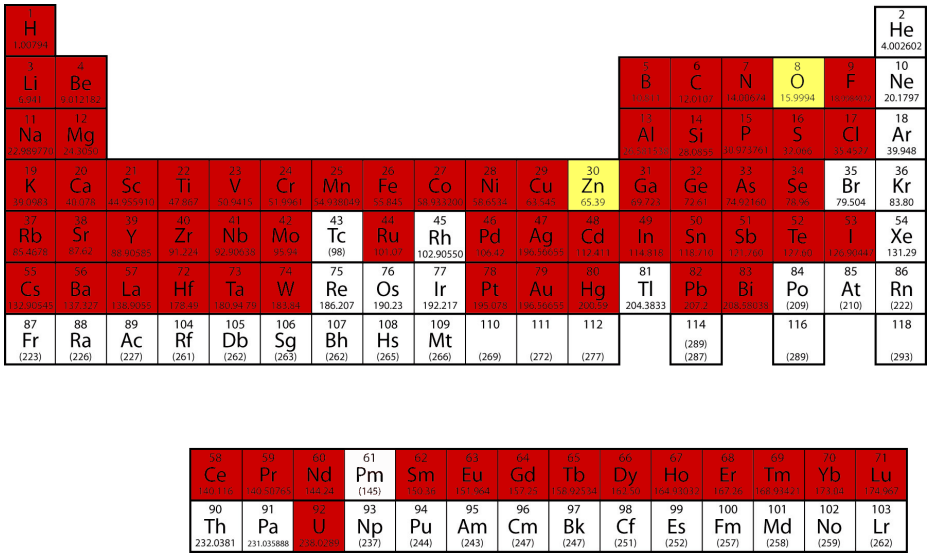

Figure 1.4: Periodic table showing chemical elements which have reportedly been used as an extrinsic dopant in zinc oxide. Elements marked in red are those where a database search for the phrase "*element*-doped zinc oxide" returns at least one citation.

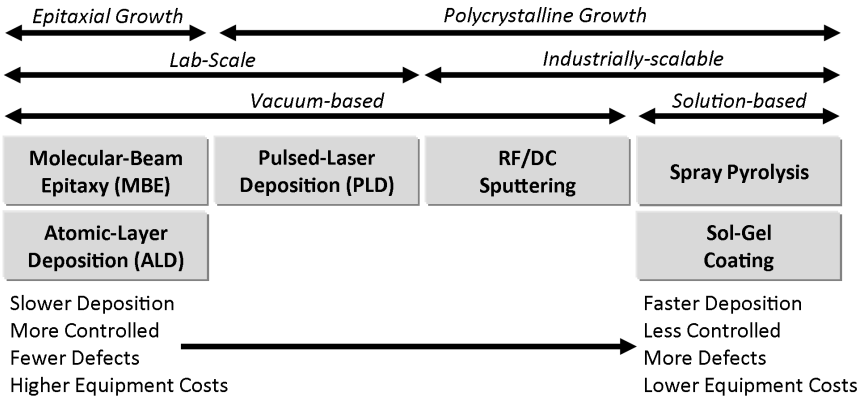

Figure 1.5: A summary of the general characteristics of the most commonly used thin film TCO deposition techniques. More binary features are placed above the technique names, while more continuous ones are below.

and doctor-blading. While many variants of these deposition techniques exist and exceptions abound, some of their general characteristics are summarized in Figure 1.5.

In addition to doping and deposition techniques, much of the composition space bounded by the traditional TCOs of indium, zinc, tin, cadmium, and gallium oxides has been searched, revealing a structurally and functionally diverse array of binary and higher multicomponent oxide phases, both crystalline and amorphous.[1,40–42] It is also worth noting that the broader field of transparent conductors now includes numerous approaches beyond the scope of traditional TCOs, including those based on metal meshes and nanowires,[43–45] low-dimensional carbon,[46,47] titanium oxide,[48,49] conductive polymers,[50] cement-based electrides,[51] and various hybrid structures.[52,53]

Yet, despite all of these extensive efforts to find low-cost alternatives, the simple fact is that very little overall progress has been made to improve the optoelectronic performance of TCOs in several decades. This is perhaps best demonstrated by comparing a 1983 review by Chopra, *et al.*, which shows leading TCO performance from ITO thin films with a sheet resistance $\sim 5\,\Omega/\square$ at a transparency of $\sim 90\,\%$, and a 2012 review by Ellmer showing that the frontiers of performance have remained virtually unchanged in the intervening 29 years (Figure 1.6).[54,55]

The practical result of this lack of progress is that ITO coatings still retain a greater than 90 % market share in the thin film transparent conductor market.[56] Looked at another way, it follows that the performance of alternatives to ITO must remain inadequate in one or more important ways. Developing a better understanding of how and why this is the case is the key purpose of this thesis.

1.3 Practical and Fundamental Limitations

The sheer number of groups, material combinations, and deposition techniques that have already been examined suggest that achieving further breakthroughs in this field by chance is rather unlikely. As such, the main approach in this thesis will not be merely to expand the already large empirical mapping of deposition conditions to TCO properties in hopes of stumbling upon a magic combination. Instead, the aim here will be to determine which physical processes most limit the performance of TCO materials, in the belief that improved understanding will naturally suggest the

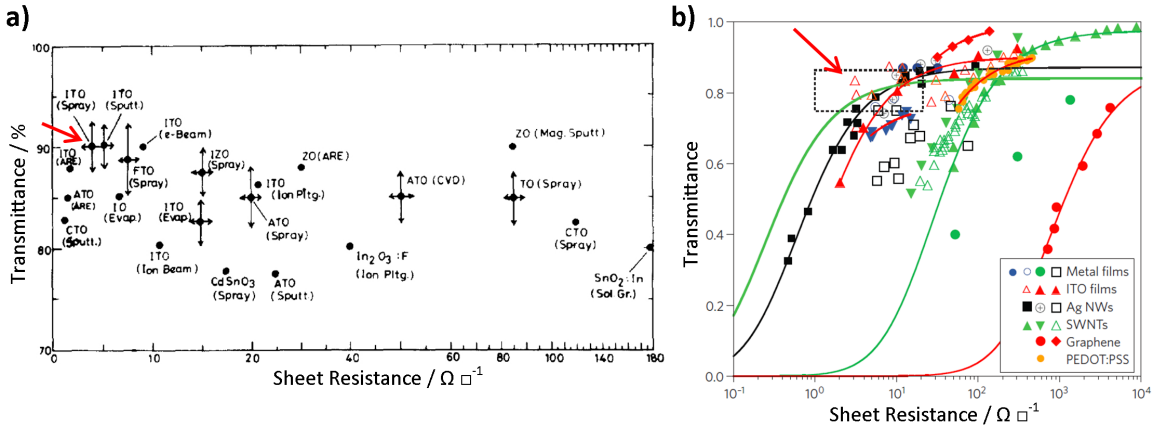

Figure 1.6: Summaries of sheet resistance and transmittance of various leading TCO materials prepared by (a) Chopra, *et al.* in 1983,[54] and (b) Ellmer in 2012.[55] The position of the materials combining the best electrical and optical performance (red arrows, top left points) is almost the same in both, showing the lack of progress in the field over the intervening 29 years. The dotted rectangle in (b) indicates the range of performance values suitable for most transparent conductor applications.

most productive areas for future research. As will be demonstrated, this approach already has allowed, and hopefully will continue to inspire, the systematic design of new approaches for increasing TCO performance.

However, the relative lack of progress in finding suitable replacements for ITO also brings up an even more basic (and perhaps somewhat uncomfortable) question: Is it even possible to improve the performance of any given TCO, especially low-cost ZnO-based TCOs, beyond what has already been achieved?

To this end, it is essential to try to make a distinction between whether the performance of a material (say, ZnO) is being limited by *fundamental* or *practical* limits. If an aspect of performance is limited by a truly *fundamental* factor, then it will not be surmounted regardless of the effort applied. However, if a limit is 'merely' *practical* — for example related to the current choice of material, deposition technique, or processing conditions — then there is at least a theoretical chance of improving performance, given a sufficiently clever approach. Admittedly, the boundaries between these categories can be hazy. What seems for a time like a fundamental limitation can sometimes become decidedly surmountable if a previously unanticipated mode of thought is found. Nevertheless, this distinction is useful for highlighting the areas in TCO research where process optimization within the current paradigm would likely be fruitful, and those where radical changes in the basic approach will be necessary

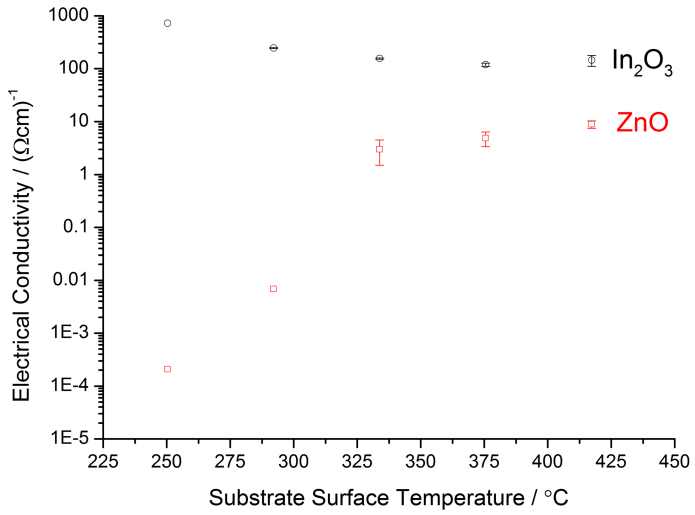

Figure 1.7: Comparison of electrical conductivity of undoped In_2O_3 (black) and ZnO (red) samples deposited by spray pyrolysis at different substrate temperatures. Both the superior absolute performance of In_2O_3 and its comparative insensitivity to deposition conditions are clearly visible.

for progress.

For instance, Figure 1.7 compares the electrical conductivity of undoped ZnO and In_2O_3 deposited by spray pyrolysis in N_2 at various substrate temperatures. It is immediately obvious that all of the In_2O_3 samples here are at least an order of magnitude more conductive than any of the ZnO samples. Furthermore, the In_2O_3 is far less sensitive to changes in deposition conditions, maintaining a stable (or even slightly increasing) conductivity with decreasing substrate temperature, while the same changes cause a five order of magnitude decrease in the conductivity of the ZnO thin films. The root causes of these differences must first be identified and understood before it can be assessed whether some means might be found to overcome them. Only then can it be seen if ZnO-based materials are ever likely to seriously threaten the dominant position held today by ITO.

With TCO research in particular, it is also important to keep in mind their intended end use as large-scale engineering materials. This has important implications and places significant constraints on the range of practicable solutions. For instance, the deposition techniques used to prepare TCO thin films on a suitably large scale for industry will inevitably introduce defects that could be lessened by the use of more highly-controlled, but impractically slow laboratory techniques. There is no question

that the study of highly idealized samples can provide many useful insights. However, the practical performance limits that arise directly from the use of larger-scale deposition techniques must also be addressed. Such can no longer simply be dismissed as "non-idealities" or "engineering problems." They must be tackled head-on by chemists, physicists, and engineers alike.

1.4 Summary of Upcoming Chapters

With the ideas and problems just presented by this introduction in mind, the following chapters are structured to examine three categories of performance limits in TCO thin films, with a particular emphasis on comparing and contrasting the behavior of incumbent In_2O_3-based systems with that of low-cost ZnO-based materials and deposition techniques. Ultimately, the goal is to assess whether continued work on ZnO-based TCOs is likely to ever produce a viable, low-cost replacement for ITO, and if so, to suggest where future research might be most efficiently directed to achieve this goal.

Chapter 2 contains an overview of the basic materials chemistry and physics of TCOs, which serve as essential background for the chapters to come. How the electronic structure of these materials leads to transparent conductivity will be discussed, as well as the fundamental mechanisms by which carrier generation, transport, and scattering occur. A free-electron framework for examining these processes will be established here and used extensively in later chapters.

The following two chapters include technical details about the techniques used for the characterization and preparation of thin film TCO samples in this thesis.

Chapter 3 discusses the key experimental methods used in this thesis to measure the optoelectronic, structural, and chemical properties of TCO thin films. While some basics of theory are covered, the reader is referred to other works for a comprehensive review of each technique. Instead, the focus is on how these techniques can specifically be applied to the study of TCOs, how they have been applied in the course of this thesis, and the types of useful information that can be obtained.

Chapter 4 is a detailed discussion of spray pyrolysis, the solution-based thin film deposition technique that forms the core experimental platform for this thesis. Spray

pyrolysis is compared with other common methods for preparing TCOs like sputtering and pulsed-laser deposition. Then, a step-by-step analysis is performed of the considerations and design choices that went into the development of the apparatus and procedures used here. Observations with significance to spray pyrolysis process design in general are made, and where possible, illustrated with real experimental examples.

The many potential limits to the performance of TCO materials are often intertwined and difficult to truly isolate from each other. Nevertheless, we will make an effort to divide them into three broad categories to be discussed in turn:

Chapter 5 covers limitations to electronic transport within the crystalline domains of transparent conducting oxides. This chapter considers several key aspects of electronic transport in single crystals, including some theoretical limits to conduction and the doping-induced metal-to-non-metal transition. It will be examined how these considerations apply to ZnO and In_2O_3 in practice. Then, the behavior of polycrystalline TCO thin films prepared by scalable deposition techniques will be considered in this context, with a particular focus on the extent that single-crystal performance limits are relevant in such samples.

Chapter 6 considers the mechanism of and limits to impurity doping, which is almost always required to achieve useful levels of electrical conductivity in TCO materials. Doping limitations based on both the fundamental thermodynamics of the material and the choice of deposition technique will be covered. This chapter includes some of the first direct experimental evidence of a structural mechanism explaining limited doping efficiency in indium-doped ZnO (IZO). It will also consider the difficulties of preparing silicon-doped ZnO (SiZO) using solution-based techniques. New mechanistic knowledge will suggest a simple technique to dramatically improve the cost and flexibility of deposition methods for this low-cost, earth-abundant TCO.

Chapter 7 examines the implications of the fact that virtually all TCO thin films deposited by practical techniques are polycrystalline, resulting in macroscopic electrical performance that results from a composite of grain interior and grain boundary properties. Several new analytical approaches will be used to show that environmental influences are a root cause of the sometimes dominating influence of grain boundaries on electrical properties, and that dramatic differences exist between the

grain boundary behaviors of ZnO and In_2O_3. These go a long way towards explaining the dissimilar technical performance of these two materials under practical conditions. The influence of various deposition parameters on grain boundary effects will be studied and used to suggest a means by which ITO-competitive performance can be achieved using ZnO-based materials.

And finally, the conclusion, *Chapter 8*, contains a review of key findings, suggestions for future work, and concluding remarks, which make a best attempt to paint a realistic picture of the prospects for future ZnO TCO research.

References

[1] Ginley, D.; Hosono, H.; Paine, D. C. *Handbook of Transparent Conductors*; Springer: New York, NY, 2011.

[2] Salleo, A.; Wong, W. S. *Flexible Electronics: Materials and Applications*; Springer: New York, NY, 2009.

[3] Gordon, R. G. *MRS Bull.* **2000**, *25*, 52–57.

[4] Tolcin, A. C.; *Mineral Commodity Summary: Indium*; Tech. Rep.; United States Geological Survey; 2015.

[5] Nassar, N. T.; Graedel, T. E.; Harper, E. M. *Sci. Adv.* **2015**, *1*, E1400180.

[6] *Indium 99.99% (FOB Warehouse Rotterdam); Accessed: 25 May 2015; www.metalprices.com.*

[7] *Fact Sheet: Indium*; Tech. Rep. 39; Polinares: EU Policy on Natural Resources; 2012.

[8] Moss, R. L.; Tzimas, E.; Kara, H.; Willis, P.; Kooroshy, J.; *Critical Metals in Strategic Energy Technologies Assessing Rare Metals as Supply-Chain Bottlenecks in Low-Carbon Energy Technologies*; Tech. Rep. M1: EUR–24884-EN-2011; 2011.

[9] Graedel, T. E.; Barr, R.; Chandler, C.; Chase, T.; Choi, J.; Christoffersen, L.; Friedlander, E.; Henly, C.; Jun, C.; Nassar, N. T.; Schechner, D.; Warren, S.; Yang, M.-Y.; Zhu, C. *Environ. Sci. Technol.* **2012**, *46*, 1063–1070.

[10] Harper, E. M.; Kavlak, G.; Burmeister, L.; Eckelman, M. J.; Erbis, S.; Espinoza, V. S.; Nuss, P.; Graedel, T. E. *J. Ind. Ecol.* **2014**, *19*, 628–644.

[11] Weiser, A.; Lang, D. J.; Schomerus, T.; Stamp, A. *J. Clean. Prod.* **2015**, *94*, 376–393.

[12] Feng, Z. C. *Handbook of Zinc Oxide and Related Materials*; CRC Press: Boca Raton, FL, 2012.

[13] Tolcin, A. C.; *Mineral Commodity Summary: Zinc*; Tech. Rep.; United States Geological Survey; 2015.

[14] *LME Zinc 99.995%; Accessed: 23 July 2015; www.metalprices.com.*

[15] Baluch, D.; *Personal Communication*; 2015.

[16] Schuler, S.; Luck, I.; Berghold, J. *Total cost of Ownership for Thin-Film PV Module Production*; 4th Thin Films Forum; Berlin, Germany, 2012.

[17] Zunick, M. J.; *Conductive coating on glass*; 1950; US Patent 2,516,663.

[18] Holland, L.; Siddall, G. *Vacuum* **1953**, *3*, 375–391.

[19] Stadler, A. *Materials* **2012**, *5*, 661–683.

[20] Kronenberger, A.; Polity, A.; Hofmann, D. M.; Meyer, B. K.; Schleife, A.; Bechstedt, F. *Phys. Rev. B* **2012**, *86*, 115334.

[21] Lee, J.; Cha, S.; Kim, J.; Nam, H.; Lee, S.; Ko, W.; Wang, K. L.; Park, J.; Hong, J. *J. Adv. Mater.* **2011**, *23*, 4183–4187.

[22] Fang, D.; Li, C.; Wang, N.; Li, P.; Yao, P. *Cryst. Res. Technol.* **2013**, *48*, 265–272.

[23] Lin, Y.; Jiang, D.; Lin, F.; Shi, W.; Ma, X. *J. Alloys Compd.* **2007**, *436*, 30–33.

[24] Bouznit, Y.; Beggah, Y.; Ynineb, F. *Appl. Surf. Sci.* **2012**, *258*, 2967–2971.

[25] Eleruja, M. A.; Adedeji, A. V.; Egharevba, G. O.; Lambi, J. N.; Akanni, M. S.; Jeynes, C.; Ajayi, E. O. B. *Opt. Mater.* **2002**, *20*, 119–123.

[26] Chavillon, B.; Cario, L.; Renaud, A.; Tessier, F.; Chevir, F.; Boujtita, M.; Pellegrin, Y.; Blart, E.; Smeigh, A.; Hammarstrm, L.; Odobel, F.; Jobic, S. *J. Am. Chem. Soc.* **2012**, *134*, 464–470.

[27] Das, A. K.; Misra, P.; Kukreja, L. M. *J. Phys. D* **2009**, *42*, 165405.

[28] Cho, J.; Lin, Q.; Yang, S.; Simmons, J. G., Jr.; Cheng, Y.; Lin, E.; Yang, J.; Foreman, J. V.; Everitt, H. O.; Yang, W.; Kim, J.; Liu, J. *Nano Res.* **2012**, *5*, 20–26.

[29] Noirfalise, X.; Godfroid, T.; Guisbiers, G.; Snyders, R. *Acta Mater.* **2011**, *59*, 7521–7529.

[30] Zhang, H.; Liu, H.; Lei, C.; Yuan, C.; Zhou, A. *Vacuum* **2010**, *85*, 184–186.

[31] Kim, K. H.; Park, K. C.; Ma, D. Y. *J. Appl. Phys.* **1997**, *81*, 7764–7772.

[32] Chauhan, R.; Kumar, A.; Chaudhary, R. *J. Sol-Gel Sci.Techn.* **2012**, *63*, 546–553.

[33] Yamamoto, T. *Phys. Status Solidi A* **2002**, *193*, 423–433.

[34] Joseph, M.; Tabata, H.; Kawai, T. *Jpn. J. Appl. Phys.* **1999**, *38*, L1205–L1207.

[35] Kim, J.-P.; Bae, J.-S.; Hong, T.-E.; Won, M.-S.; Yoon, J.-H.; Lee, B.-S.; Lee, H.-J. *Thin Solid Films* **2010**, *518*, 6179–6183.

[36] Nomoto, J.; Miyata, T.; Minami, T. *J. Vac. Sci. Technol., A* **2009**, *27*, 1001–1005.

[37] Altamirano-Juárez, D. C.; Torres-Delgado, G.; Jiménez-Sandoval, S.; Jiménez-Sandoval, O.; Castañedo-Pérez, R. *Sol. Energy Mater. Sol. Cells* **2004**, *82*, 35–43.

[38] Maldonado, A.; Rodríguez-Baez, J.; de la Luz Olvera, M. *Mater. Chem. Phys.* **2011**, *129*, 109–115.

[39] Hartnagel, H. L.; Dawar, A. L.; Jain, A. K.; Jagadish, C. *Semiconducting Transparent Thin Films*; Institute of Physics Publishing: Bristol, UK, 1995.

[40] Hoel, C. A.; Mason, T. O.; Gaillard, J.-F.; Poeppelmeier, K. R. *Chem. Mater.* **2010**, *22*, 3569–3579.

[41] Minami, T. *MRS Bull.* **2000**, *25*, 38–44.

[42] Robbins, J. J.; Fry, C.; Wolden, C. A. *J. Cryst. Growth* **2004**, *263*, 283–290.

[43] Madaria, A. R.; Kumar, A.; Zhou, C. *Nanotechnology* **2011**, *22*, 245201.

[44] Morag, A.; Ezersky, V.; Froumin, N.; Mogiliansky, D.; Jelinek, R. *Chem. Commun.* **2013**, *49*, 8552–8554.

[45] Guo, H.; Lin, N.; Chen, Y.; Wang, Z.; Xie, Q.; Zheng, T.; Gao, N.; Li, S.; Kang, J.; Cai, D.; Peng, D.-L. *Sci. Rep.* **2013**, *3*, 1–8.

[46] Wassei, J. K.; Kaner, R. B. *Mater. Today* **2010**, *13*, 52–59.

[47] Zhang, D.; Ryu, K.; Liu, X.; Polikarpov, E.; Ly, J.; Tompson, M. E.; Zhou, C. *Nano Lett.* **2006**, *6*, 1880–1886.

[48] Yamada, N.; Hitosugi, T.; Hoang, N. L. H.; Furubayashi, Y.; Hirose, Y.; Shimada, T.; Hasegawa, T. *Jpn. J. Appl. Phys.* **2007**, *46*, 5275–5277.

[49] Hitosugi, T.; Kamisaka, H.; Yamashita, K.; Nogawa, H.; Furubayashi, Y.; Nakao, S.; Yamada, N.; Chikamatsu, A.; Kumigashira, H.; Oshima, M.; Hirose, Y.; Shimada, T.; Hasegawa, T. *Appl. Phys. Express* **2008**, *1*, 111203.

[50] Kulkarni, V. G. *Transparent Conductive Coatings*; Skotheim, T. A.; Elsenbaumer, R. L.; Reynolds, J. R., Eds.; Handbook of Conducting Polymers; Marcel Dekker, Inc.: New York, NY, 1998; pp 1059–1074.

[51] Hosono, H.; Kim, S. W.; Miyakawa, M.; Matsuishi, S.; Kamiya, T. *J. Non Cryst. Solids* **2008**, *354*, 2772–2776.

[52] Guillén, C.; Herrero, J. *Thin Solid Films* **2011**, *520*, 1–17.

[53] Hwang, J. O.; Lee, D. H.; Kim, J. Y.; Han, T. H.; Kim, B. H.; Park, M.; No, K.; Kim, S. O. *J. Mater. Chem.* **2011**, *21*, 3432–3437.

[54] Chopra, K. L.; Major, S.; Pandya, D. K. *Thin Solid Films* **1983**, *102*, 1–46.

[55] Ellmer, K. *Nat. Photonics* **2012**, *6*, 809–817.

[56] Ghaffarzadeh, K.; Das, R.; *Transparent Conductive Films (TCF) 2014-2024: Forecasts, Technologies, and Players*; Tech. Rep.; IdTechEx; 2014.

Chapter 2

The Basic Physics of Transparent Conducting Oxides

If one thinks through the many materials that are regularly encountered, it quickly becomes apparent that simultaneous transparency and conductivity are a rather unusual combination of properties. Most materials that are transparent do not conduct, and most conductors are not optically transparent. As such, before proceeding any further, it is worth taking some time to consider what is required for a material to be both optically transparent and electrically conductive at the same time. We will also take this opportunity to lay out the basic, free-electron theoretical framework that is used throughout this thesis to understand and describe the optoelectronic properties of TCOs.

The focus here will be on classic n-type TCOs like those based on zinc and indium oxide, where electrons are the dominant charge carriers. p-type TCOs, where the dominant charge carriers are holes, are certainly of both theoretical and practical interest, but are outside the scope of this thesis.

2.1 The Drude Free-electron Model

Before considering how free electrons arise in a material, it is useful to first discuss how the behavior of such electrons can be described.

For this purpose, we start from a model first proposed by Paul Drude in 1900.[1,2] His model treats electrons as free, classical particles moving amidst a lattice of sta-

tionary nuclei and assumes the following equation of motion:

$$\frac{d\vec{p}}{dt} = e\vec{E} + \frac{e(\vec{p} \times \vec{B})}{m} - \frac{\vec{p}}{\tau}, \tag{2.1}$$

where $\vec{p}$ is the carrier momentum, e is the electronic charge, $\vec{E}$ is the applied electric field, $\vec{B}$ is the applied magnetic field, m is the mass of the electron, and τ is the mean time between scattering events for a given electron.[3]

The first two terms of Equation 2.1 straightforwardly describe the acceleration of a free charge by an electric field and the orthogonal acceleration of a moving charge by a magnetic field, respectively.[i] The final term describes the loss of momentum due to the scattering events that occur on average every τ. In this model, the scattering events are assumed to be instantaneous collisions (for example, with the lattice ions) that result in the electron emerging with a random momentum in a distribution dictated by thermal equilibrium with the lattice. In other words, the carrier electron has completely lost any memory of its momentum prior to the scattering event.

Importantly, the Drude model completely neglects any Coulombic interactions that occur among electrons or between the electrons and the positively charged nuclei. Furthermore, the model does not consider the fact that electrons must obey Fermi-Dirac statistics. These are clearly gross approximations and would, at first glance, seem to be very problematic for a model aiming to describe a system of highly interacting electrons. Remarkably, however, it can be shown that such a system can be described, to a very good approximation, as a collection of non-interacting quasiparticles possessing properties different from those of the real, interacting particles that make up the system.[4] Given this fact, Equation 2.1 can still be used to describe the motion of a collection of electrons, so long as an effective mass (m^*) is used in place of the electron rest mass (m_e) in order to account for the net effect of inter-particle interactions.

When further combined with generalizations and extensions proposed by Lorentz, Sommerfeld, Bethe, and others, the result is a beautifully simple, yet incredibly useful model for electronic transport in semiconductors and metals. Most relevant to the

[i] In the context of a rapidly oscillating electromagnetic field, such as that which will be encountered in the upcoming discussion on the optical properties of free electrons, the charges do not have time to build up large values of momentum and the acceleration due to the magnetic field is small compared to that of the electric field, meaning that it can be safely neglected for most purposes.

present work are the results on electronic motion under both static and time-varying fields (*i.e.*, DC and AC), which can be used to describe the optoelectronic properties of TCOs.

Starting from the Drude model, the motion of electrons in response to a static electric field (and in the absence of a magnetic field) can be straightforwardly derived using arguments from classical kinetic theory. Consider an electron that has just experienced a scattering event. Since momentum is randomized by this event, the average momentum of such electrons is zero. It is also known that an electron is accelerated by an electric field $\vec{E}$ for an average period of time τ between scattering events. Therefore, the average momentum of the electrons in the system is

$$\langle \vec{p} \rangle = e\vec{E}\tau \,. \tag{2.2}$$

Recalling that we are now considering effective masses and given the definition of momentum $\langle \vec{p} \rangle = m^* \langle \vec{v} \rangle$, it is elementary to write

$$\langle \vec{v} \rangle = \frac{e\tau}{m^*}\vec{E} \,. \tag{2.3}$$

The proportionality constant between average carrier velocity and the applied electric field is conventionally called the *carrier mobility* and denoted by $\mu = e\tau/m^*$.

The current density (due to electrons) through a plane normal to $\vec{E}$ can be written as

$$\vec{J} = ne\langle \vec{v} \rangle \,, \tag{2.4}$$

where n is the volume density of mobile electrons. By substituting Equation 2.3 into Equation 2.4, we are left with a form of the microscopic Ohm's Law:

$$\vec{J} = \frac{ne^2\tau}{m^*}\vec{E} = ne\mu\vec{E} \,, \tag{2.5}$$

where the conductivity σ is

$$\sigma = ne\mu \,. \tag{2.6}$$

Equation 2.6 is the key result of this derivation and lays the foundation for how electrical conductivity in TCOs will be examined throughout the rest of this thesis. This equation states that the electrical conductivity of a material is proportional to both the concentration of charge carriers (n) and the mobility of these carriers (μ).

This is certainly an intuitive and beguilingly simple statement! But as will be seen, the richness and complexity of optoelectronic behaviors in TCOs arises in large part from the myriad of interacting factors that go into determining the values of n and μ for a given material under a given set of conditions.

2.2 Transparent *and* Conductive Oxides

2.2.1 Electronic Band Structure

Armed with an essential tool for describing electronic transport in TCOs, we can now consider what features of these systems allow them to posses simultaneous electrical conductivity and optical transparency. Both of these properties ultimately arise from the particular electronic structure possessed by these materials.

In general, the electronic structure of a solid can be described in terms of energy bands, or ranges of energies that electrons within that solid may possess. These bands result from the mixing of individual atomic orbitals, the energies and occupancies of which will of course be determined by which atoms or ions are interacting.[5]

The overall width of such bands is a function of the spatial overlap between the component orbitals.[6] Given that the bands have finite width, one resulting from the combination of a large enough number of components (as would be the case in an extended solid) will contain states so close to each other in energy as to be effectively continuous. The finite width of the bands also means that they will not necessarily cover all energies, and that certain energy ranges will contain no electron states. The formation of energy bands in a solid is schematically illustrated in Figure 2.1.

This is of essential importance because how these bands are filled with electrons determines whether a material will be electrically conductive. For instance, there can be no *net* motion of electrons among the states of a completely filled band; the only possibility is the exchange of two filled states. Likewise, there can be no net motion of electrons in a completely empty band, simply because there are no electrons. Electrical conduction can only occur in a partially filled band.[ii] Because of this, the part of the band structure that determines the electrical properties of a

[ii]It should be noted that the converse is not necessarily true. The presence of a partially filled band does not always lead to a conductive material. Examples of this include Mott insulators, or cases where structural disorder leads to localized states in band edges, so-called Anderson localization.

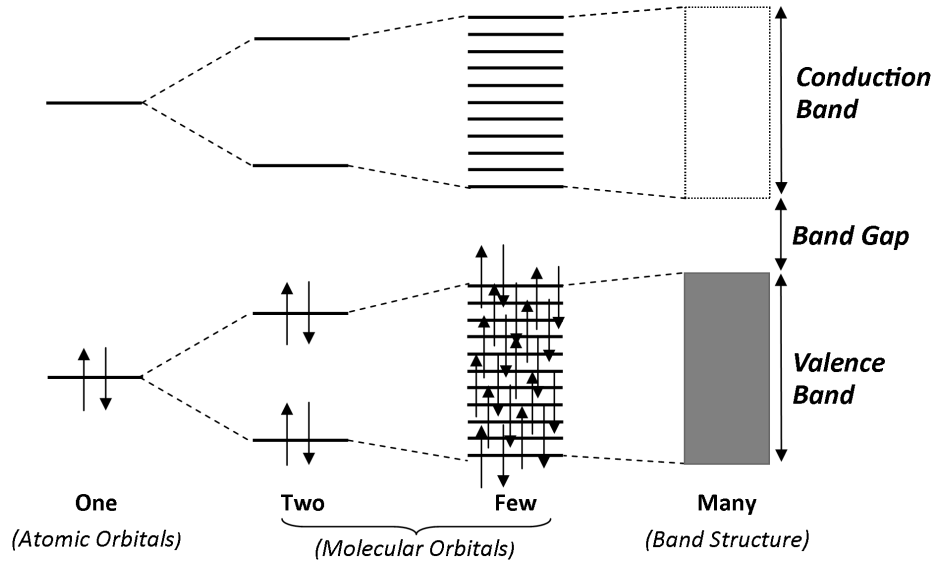

Figure 2.1: Schematic illustrating the formation of electronic bands via the interaction of atomic orbitals in a one-dimensional system. This example shows the formation of the valence band and the conduction band from the highest occupied and lowest unoccupied orbitals of the atomic unit, respectively. In this case, the finite width of the bands leads to the formation of a band gap containing no electronic states.

material is the region near where the highest filled states meet the lowest unfilled states.

The extent of filling of these band structures is conventionally described using the *Fermi energy*, E_F, which is located midway between the highest filled and lowest unfilled states of the band structure in its ground state. This is also equivalent to the chemical potential of electrons in the system. Intuitively, E_F can be thought of as a measure of how electron-rich a material is. Processes and defects that donate electrons to the system raise E_F, while those that result in the net loss of electrons lower E_F. This concept can be generalized to cases where the material is excited, say, by finite temperatures or an applied voltage. In these cases, it is common to refer to a Fermi *level*, defined as the energy that would have a one-half probability of occupancy at thermal equilibrium.

In the case of TCOs, the critical region of the electronic structure near the Fermi energy consists of two bands, the lower energy *valence band* and the higher energy *conduction band* separated by an energy range called the *band gap* (Figure 2.1). When a TCO is pure, stoichiometric, and in its ground state, the valence band is completely filled, the conduction band is completely empty, and there are no states within the

band gap. Electrical conductivity can therefore only arise when this configuration is changed by the presence of defects and/or when enough energy is supplied to excite the system.

It is possible to use computational methods to calculate the electronic band structures of materials from their three-dimensional crystal structures. Examples of such calculations for ZnO and In_2O_3 are shown in Figure 2.2. Zinc oxide typically adopts the hexagonal structure of wurtzite under ambient conditions (space group $P6_3mc$), consisting of zinc cations filling one set of tetrahedral holes in a hexagonal close-packed lattice of oxide anions.[7] Indium oxide's cubic bixbyite structure (space group $Ia\bar{3}$) has a particularly complex unit cell containing 80 atoms and can be thought of as a modified fluorite structure with one quarter of the anions missing. There are two symmetry inequivalent sites for indium having six-fold coordination, but differing in whether the missing anions are arranged across a face diagonal or a body diagonal.[8,9]

Despite resulting from substantially different crystal structures, the electronic structures of ZnO and In_2O_3 possess some striking similarities that hint at their commonalities as n-type TCOs. In one dimension, the effective mass of a carrier near an approximately parabolic band extrema is

$$m^* = \hbar^2 \left(\frac{d^2E}{dk^2} \right)^{-1} , \tag{2.7}$$

where $E(k)$ is the band energy as a function of wavevector, and $\hbar = h/2\pi$ is the reduced Planck constant.[iii]

Since both materials possess a wide conduction band with a tightly curved minimum (that is, large $\frac{d^2E}{dk^2}$) near the Brillouin zone center Γ, any conduction electrons can be expected to have relatively low effective masses. Indeed, electron effective mass values for the bottom of the conduction band in ZnO and In_2O_3 are generally reported in the range of ∼0.25–0.4 times the mass of the free electron.[12–14] These values allow for the possibility of high electron mobilities and good n-type conductivity. Effective mass values generally increase as the carrier concentration increases, demonstrating the non-parabolicity of the conduction band away from the band minimum.[12,13] Similarly, both valence band maxima are relatively flat, suggesting that hole conduction would be sluggish in these materials.

[iii] In a general 3D case, the effective mass is a tensor relating the components of force and acceleration.

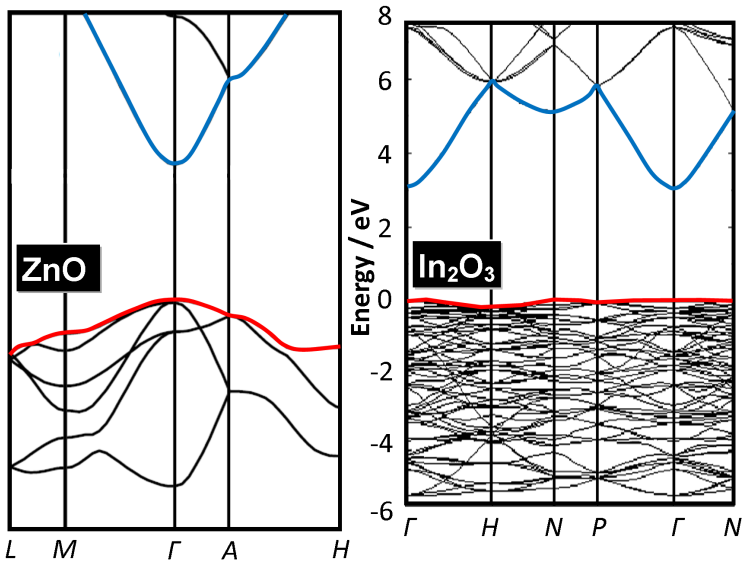

Figure 2.2: Calculated electronic band structures for wurtzite ZnO[10] and bixbyite In_2O_3.[11] The boundaries of the valence and conduction bands are highlighted in red and blue, respectively. The valence band maxima defines the zero of energy in these figures.

Such calculations can also be used to determine the relative contribution of the various atomic orbitals to each of the energy bands of the extended solid. As is common for *n*-type TCOs, the conduction bands in these cases are primarily composed of metal s orbitals, while the top of the valence bands consist largely of oxygen 2p states and some minor contributions from metal d orbitals.[15–17]

2.2.2 Optical Transparency

To possess a high intrinsic transparency, a given material must necessarily absorb and reflect very little light in the wavelengths of interest.

Any photon with high enough energy to excite an electron across the band gap from the valence band to the conduction band has a finite probability of being absorbed by the material. Thus, in order to avoid absorbing significantly in the visible spectrum (∼400–750 nm, or ∼3.1–1.7 eV) a TCO must have an optical band gap >3.1 eV. Since d-d transitions from HOMO to LUMO (that is, valence to conduction band in the context of an extended solid) are lower in energy than this threshold, generally only d^0 and d^{10} metal oxides can be suitable as TCOs.

Figure 2.2 shows that this constraint is easily met by ZnO, which has a direct

band gap of about 3.4 eV.[7] However, In_2O_3 shows an additional subtlety in this regard. Its band structure diagram shows that the smallest band gap in In_2O_3 is about 2.9 eV, which would appear to be smaller than the 3.1 eV limit. However, because the bixbyite crystal structure of In_2O_3 is centrosymmetric, Laporte selection rules apply to optical transitions and the 2.9 eV transition is dipole forbidden. In fact, the lowest energy optically-allowed transition occurs at ∼3.7 eV, which corresponds to the experimentally observed onset of strong absorption and is what allows In_2O_3 to still be a transparent conductor.[18]

For a given material, if the Fermi energy is increased above the conduction band minimum, for example, by increasing extrinsic doping, states near the conduction band edge will become filled. In this case, electrons in the valence band can only be excited if they absorb enough energy to surmount the fundamental bandgap *and* the range of filled states at the bottom of the conduction band (Figure 2.3). This resulting blueshift in observed bandgap with increasing carrier concentration is generally referred to as the Burstein-Moss effect.[19,20]

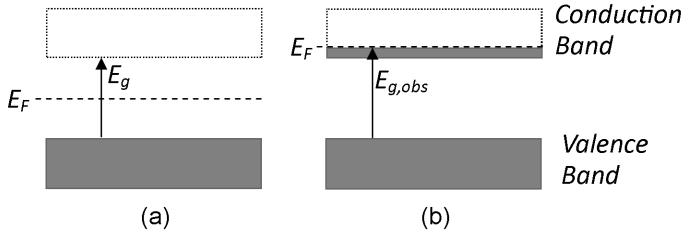

Figure 2.3: Schematic of the Burstein-Moss effect explaining the increase in observed bandgap energy ($E_{g,obs}$) from a) the stoichiometric case to b) a case where the Fermi energy (E_F) has been raised above the conduction band minimum. The filled states near the conduction band edge in (b) mean that valence band electrons require more energy to be excited across the bandgap to the lowest unfilled state.

The other limit to transparency in TCOs arises from the very fact that they are conductive. The Drude equation of motion for free electrons (Equation 2.1) can also be solved for an oscillating electromagnetic field (Appendix B). The key result here is that the electron gas possesses a characteristic *plasma frequency* (ω_p) at which the real part of the frequency-dependent dielectric function vanishes.

$$\omega_p = \sqrt{\frac{\omega_n^2}{\epsilon_\infty} - \Gamma^2}\,, \tag{2.8}$$

with

$$\omega_n = \sqrt{\frac{ne^2}{\epsilon_0 m^*}}\,, \tag{2.9}$$

and where ϵ_∞ is the high-frequency permittivity of the material, Γ $(= 1/\tau = e\mu/m^*)$ is the damping constant for the oscillation of the free electrons, n is the density of free charge carriers, e is the electronic charge, m^* is the effective mass of the electron, and ϵ_0 is the permittivity of free space.[21] Figure 2.4a shows an example calculation for a hypothetical material, showing the shift in the plasma frequency with changing values of Γ.

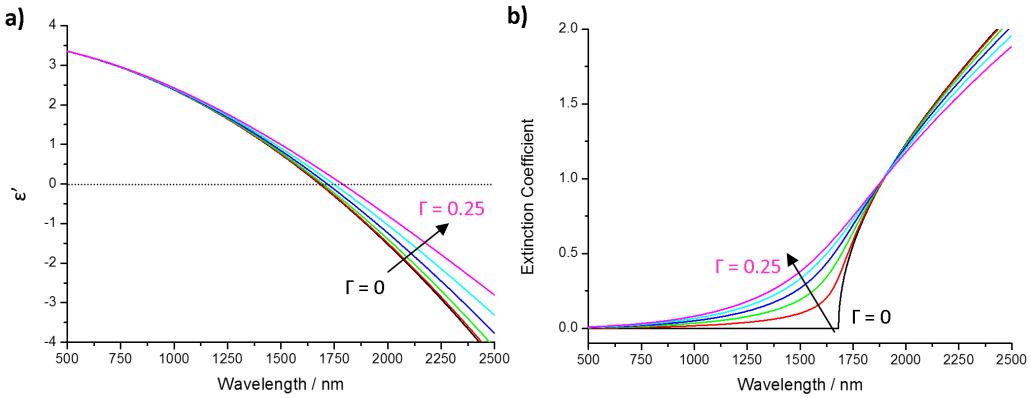

Figure 2.4: (a) Real part of permittivity and (b) extinction coefficient as a function of incident photon wavelength for a material having free electrons with $\epsilon_\infty = 3.67$, $\omega_n^2 = 2\,\mathrm{eV}^2$, and various values for Γ increasing from 0 to 0.25 eV in 0.05 eV increments in the direction indicated by the arrows. The plasma frequency is when $\epsilon' = 0$.

When the damping constant is zero (*i.e.*, in the absence of scattering), the free electrons can move in phase with incident photons having lower frequency than the plasma frequency and incoming light is reflected. As the damping constant increases, the plasma frequency shifts to slightly lower frequencies and noticeable absorption can occur above ω_p, as seen from the non-zero values of extinction coefficient for $\lambda > 2\pi c/\omega_p$ in Figure 2.4b. In this way, the plasma frequency defines a lower bound on the range of photon energies to which the TCO is transparent. The sharpness of this boundary depends on the amount of carrier scattering.

As can be seen from Equations 2.8 and 2.9, the location of the plasma frequency also depends strongly on the concentration of free electrons and is hence further coupled to the electronic transport properties of the material. The value of n must be controlled depending on the window of optical transparency required for a given

application of the TCO material. For example, while ω_p typically falls in the near- to mid-infrared for most TCO materials, when the free electron concentration is very high (typically $>10^{21}\,\mathrm{cm}^{-3}$), the plasma frequency can encroach on the visible portion of the spectrum and lead to a loss of transparency visible to the naked eye. Similarly, applications requiring transparency in the near- or mid-IR would require relatively low carrier concentrations.

Taken in sum, the intrinsic upper and lower frequency limits for the window of transparency in a TCO material are defined by the fundamental band gap absorption and the reflectivity and absorption due to free carrier electrons, respectively.

2.2.3 Electrical Conductivity and the Generation of Carriers

A partially-filled electronic band is necessary for electronic conduction. However, the requirement of optical transparency dictates that a TCO material should have a relatively wide bandgap in excess of about 3.1 eV. Near room temperature (where $k_B T \approx 25\,\mathrm{meV}$), this is far larger than can be surmounted by simple thermal excitation of electrons from the valence band to the conduction band (Figure 2.5b).

Instead, n-type conductivity in TCOs relies on the presence of structural defects which produce filled electronic states near in energy to the bottom of the conduction band (Figure 2.5a). Only a small addition of energy is then required to excite electrons from these so-called *shallow donor* states to the conduction band. Now in a partially filled band, these electrons are part of the population of free conduction electrons (n) in the material and can contribute to electronic conductivity at room temperature per Equation 2.6. In some cases, the donor defect states can themselves be delocalized through the material, meaning that conduction can occur without any further addition of energy.[22] At the same time, the closeness of these shallow defect states to the conduction band means that they are only a small perturbation on the fundamental bandgap and do not interfere with transparency.

The ground-state occupancy of a defect state can be assessed by considering the constraint that the overall material must remain electrically neutral. If whatever occupies a defect site is more positive in charge than what would be present in the defect-free parent material, extra electrons must be associated with the defect for charge compensation. Formally, the associated defect states can be considered filled

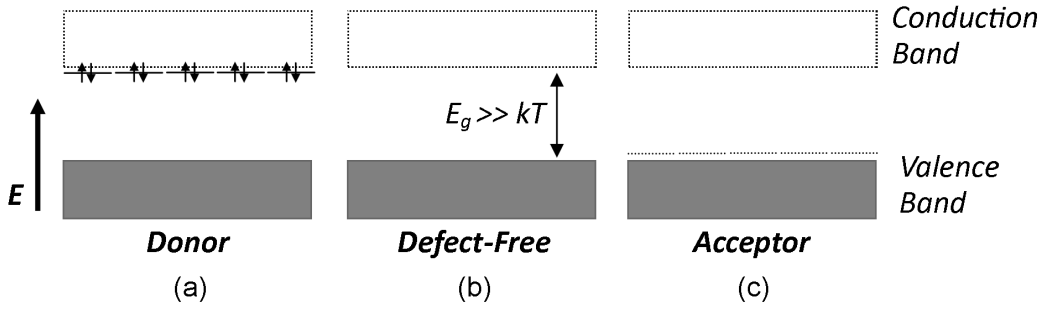

Figure 2.5: Schematic energy level diagram illustrating the formation of (a) filled shallow donor states and (c) unfilled acceptor states due to the presence of defects.

in the ground state and thus are a net *donor* of electrons (Figure 2.5a). The converse is true for defect sites whose occupant is more negative than what would be present in the parent material. Such defects must provide an empty site for the localization of electrons and are termed *acceptor* defects (Figure 2.5c).

For example, one of the canonical donor defects in n-type TCOs is the oxygen vacancy (V_O). A vacancy is neutrally charged, and is thus 2 e more positively charged than the oxide anion that would have occupied the site had no vacancy been present. This means that V_O is a donor defect whose presence leads to an electronic state filled with up to two electrons. In chemical terms, this could be written as

$$O^{2-}_{lattice} \rightarrow \frac{1}{2}O_2 + V_O^{2-} \,. \tag{2.10}$$

In principle, there is then an equilibrium between states where the electrons are free (for example, excited to the conduction band) and localized at the site of the vacancy:

$$V_O^{2-} \rightleftharpoons V_O^{-} + e^{-} \rightleftharpoons V_O + 2e^{-} \,. \tag{2.11}$$

While there has been some recent controversy (see, for example, the work of Van de Walle[23]), the conventional view is that the excitation of electrons from V_O to the conduction band is easily achieved at room temperature, thus making these donor defects shallow.

Precisely the same arguments apply when considering extrinsic defects caused by the incorporation of impurities into a host metal oxide. Whenever a position in the host lattice is substituted with something in a more positive oxidation state than what would be there in the defect-free material (for example, Si^{4+} replacing Zn^{2+}, or F^{-} substituting for O^{2-}, or a cation at any interstitial site), extra electron(s) and

the creation of an occupied donor state are required for each substitution. Cases where these extra electrons are inherently free or easily made free are equivalent to the donor state occupying a shallow position in the electronic band structure.

Finally, it is extremely important to keep in mind that this simple picture of free electron generation is only strictly true in the limit of small perturbations on the host structure. As the concentration of defects increases, they will begin to interact with each other.[24] At this point, they can no longer be treated as isolated point defects and their net effect on the host material will change. Indeed, at a sufficiently high defect concentration, the very notion of using a host material with certain properties as a baseline often breaks down. In general, the behavior of defects at high concentrations can be a complicated matter, one that we will return to in more detail in Chapter 6.

2.3 Carrier Scattering Mechanisms

Once a free electron has been generated by the presence of an appropriately shallow donor defect state, Equation 2.3 states that its mobility is a function of its effective mass (m^*) and the average time between scattering events (τ). The effective mass is a function of the curvature of the conduction band in k space (Equation 2.7) and is largely dictated by the choice of TCO material.

The Drude model takes no account of the mechanism by which a mobile carrier is scattered, and simply includes the fact that such collisions occur. In reality, there are a large number of potential scattering mechanisms that can affect τ and hence carrier mobility. The topic of carrier scattering mechanisms in TCOs has been the subject of a number of reviews,[25,26] so only some of the most important points will be touched on here.

Bloch's Theorem holds that all wavefunctions satisfying Schrödinger's equation for a periodic potential must take the form

$$\Psi(\vec{r}) = e^{i(\vec{k}\cdot\vec{r})}u(\vec{r})\,, \tag{2.12}$$

where $u(\vec{r})$ has the same periodicity as the potential. An important consequence of this theorem is that electrons will not be scattered by a perfectly periodic lattice.[3]

Of course, a truly perfect lattice is not achievable in practice, and any imperfection will allow electron scattering events to occur. In general, there are two main classes

of deviations, static and dynamic. Static defects include vacancies, point or clustered impurities, dislocations, and grain boundaries. Dynamic periodicity breaking arises primarily from thermal vibrations of the lattice, which are conveniently described as quasiparticles called phonons.

While possible, events involving an electron and more than one other scatterer are rare and only of any significance at very high defect concentrations. Thus, it is usually sufficient to assume that these various scattering processes are occurring independently. In this case, Matthiessen's rule can be used to express the total scattering rate in terms of the scattering rate of the individual processes:

$$\tau^{-1} = \sum_i \tau_i^{-1}\,, \tag{2.13}$$

where τ_i is the average time between scattering events for the ith mechanism acting individually.[27]

The reciprocal nature of the addition in Equation 2.13 means that the overall scattering will be dominated by terms with the highest scattering rate. In most practical TCOs, experimental measurements of mobility can be well accounted for by considering only a few of the most significant scattering mechanisms. Especially in heavily doped TCOs, scattering of electrons by ionized impurities is a major limit to their mobility.[28] At higher temperatures near room temperature and above, and in very pure samples, electron-phonon scattering plays a significant role.[29] Finally, in polycrystalline samples, the effects of scattering by grain boundaries must also be considered.[30–32] The chemical origins and sometimes dominating importance of this latter mechanism in determining the macroscopic properties of a TCO film will be covered in detail in Chapter 7. Other proposed mechanisms like electron-electron scattering, electron-plasmon scattering, and neutral impurity scattering represent higher order effects that are generally of small-to-negligible significance in practical TCO samples.

2.4 The Metal-to-Non-Metal Transition in TCOs

As we have seen, materials like ZnO or In_2O_3 are good electrical insulators when perfectly defect free, but can also exhibit metallic conductivity when prepared with an appropriate concentration and type of defects. This exemplifies one of the more

remarkable facts of nature, that electrical conductivities in materials span more than 30 orders of magnitude.

It is very interesting to consider how a significant part of this vast range in conductivity values might be traversed within a single material system. Similarly, it can be asked how some parameter of an insulator might be tuned to turn it into a conductor. Not only are these questions of fundamental significance, they are also very relevant to the present study of transparent conductors, where the ability to tune their electrical properties over a wide range is essential to their use as technological materials.

The difference between a metal and a non-metal (a semiconductor or an insulator) is only truly clear at absolute zero, where, as noted by Sir Nevil Mott, "...a metal conducts, and a non-metal doesn't."[33] In the band structure picture that has been developed through this chapter, this is equivalent to saying that a metal has partially filled bands in its ground state, whereas a non-metal does not.

This discontinuity between finite conductivity in metals and zero conductivity in non-metals at $T = 0\,\mathrm{K}$ is the simplest and purest form of the large change in conductivity that arises when a material undergoes a Metal-to-Non-Metal Transition (MNMT), which is also sometimes referred to as a Metal-Insulator Transition (MIT).[34]

At finite temperatures, there is still a large change in conductivity across a MNMT. However, this change now occurs continuously. This smoothness makes it challenging to precisely identify the critical point at which the MNMT occurs. Since measurements at absolute zero are not possible in practice, the typical determination of whether a particular sample is metallic relies on indirect measures, such as the extrapolation of temperature-dependent conductivity measurements down to absolute zero.[35–37]

Impurity Conduction and the Mott Criterion

In TCO materials, a MNMT can result from the significant modifications of band structure that occur with changes in the concentration of impurities. Band structure changes due to an increasing donor defect (and hence, free carrier) concentration are illustrated in Figure 2.6.

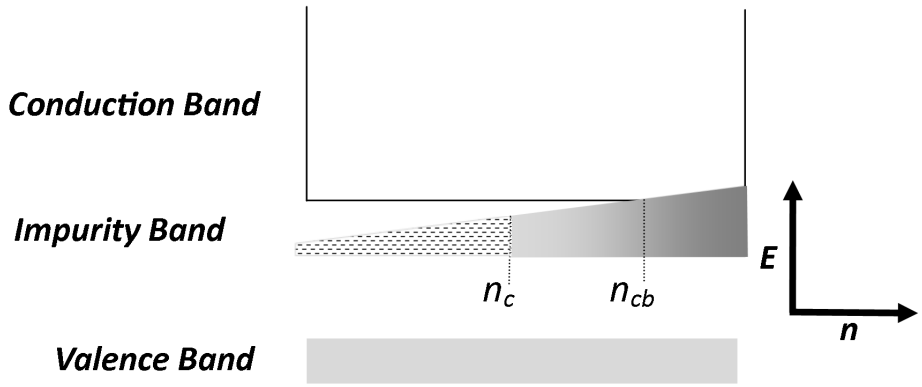

Figure 2.6: Schematic of impurity band conduction at various carrier concentrations in the absence of grain boundaries. The two critical carrier densities are n_c, representing the Mott critical concentration at which impurity wavefunctions delocalize and form a band, and n_{cb}, where the impurity band merges with the host conduction band. Adapted from Vai, *et al.*[38]

At a low concentration of donor defects, the defect sites are spatially separated and the associated wavefunctions will be localized about their defect sites. In this case, any conduction that happens within the impurity states must occur by the "hopping" of electrons from defect to defect by quantum-mechanical tunneling.

As the defect concentration increases, the average distance between defects must decrease, eventually allowing the individual wavefunctions to interact. This interaction between impurity wavefunctions begins to produce a band of impurity states in much the same way that atomic orbitals produce the electronic bands of the host material (Figure 2.1). Mott had the key insight that this increasing interaction would eventually allow the impurity wavefunctions to become delocalized throughout the material. He further proposed, on geometric grounds, that this transition should occur suddenly at a critical defect concentration, n_c, satisfying

$$n_c^{1/3} a_H^* = C\,, \tag{2.14}$$

where a_H^* is the effective Bohr radius of the isolated impurity wavefunction at low concentrations and C is a constant.[39] Data on a vast array of systems, summarized on what is now called a Mott-Edwards-Sienko plot (Figure 2.7), shows that the value of C is approximately 0.26.

At this point, it is important to note that even with a donor defect concentration above n_c such that the impurity wavefunctions are fully delocalized, the system is not

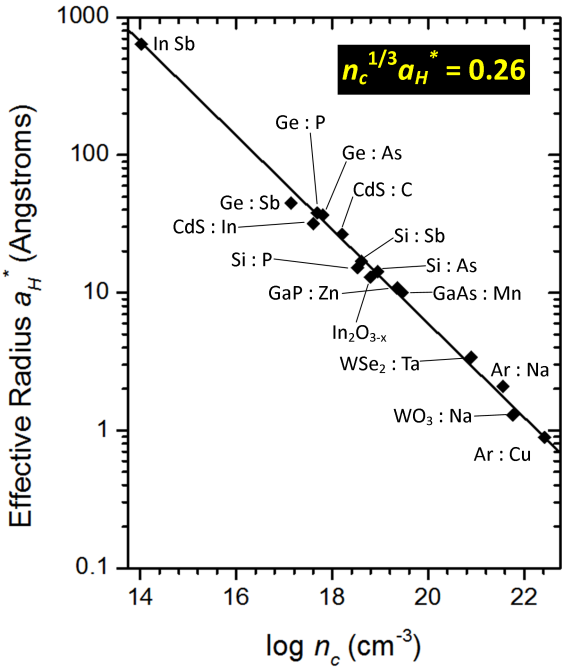

Figure 2.7: A Mott-Edwards-Sienko plot showing the linear relationship between the effective Bohr radius (a_H^*) of an impurity wavefunction and the critical carrier concentration for the MNMT. Adapted from Edwards, *et al.*[21]

necessarily metallic. If the impurity band is fully filled in the ground state and not wide enough to overlap with the host conduction band, the system will still have no partially filled bands in the absence of thermal excitation. In this case, only at an even higher defect concentration, denoted n_{cb}, will the overlap of individual impurity wavefunctions be enough to produce an impurity band with sufficient width to merge with the conduction band of the host oxide. Only when this occurs will the conduction band remain partially filled even at absolute zero, making the system truly metallic.

The situation is different for impurity states that are partially filled, for example in the case of one-electron metal-substituting donors in TCOs. Once formed, the impurity band will only be partially filled, meaning that metalization should occur at n_c, rather than at n_{cb}.

An example of the MNMT in a real experimental system will be discussed in Chapter 5, when we consider the effects of changing defect concentrations on the electrical properties of a series of ZnO-based thin films.

2.5 Summary

This chapter has introduced some of the most important aspects of the basic material physics of transparent conducting oxides that will be used repeatedly in the chapters to follow.

The behavior of free conduction electrons in TCOs can be effectively described using the Drude free electron picture, keeping in mind the need for an effective mass correction to account for electron-electron interactions. This simple and venerable model leads to $\sigma = ne\mu$, which is the core equation that is used to understand DC conductivity in TCOs.

The unusual combination of high electronic conductivity and optical transparency in TCO materials arises from unique features of their band structures, most notably a wide bandgap and a highly curved conduction band that results from excellent overlap of metal s orbitals. The presence of appropriate structural defects, both intrinsic and extrinsic, is responsible for the generation of free electrons that can then travel in the high mobility conduction band possessed by TCOs.

We have also discussed the intimate coupling of carrier concentration and optical transparency (via the plasma edge), and that of carrier concentration and mobility (via a range of scattering mechanisms). These are essential tradeoffs that must be considered in the design of TCO materials and hint at the types of performance limitations that will be covered in later chapters.

Finally, the idea of a metal-to-non-metal transition induced by changes in defect concentration was introduced and connected with the substantial tunability of electrical properties in TCOs.

References

[1] Drude, P. *Ann. Phys. (Berlin, Ger.)* **1900**, *306*, 566–613.

[2] Drude, P. *Ann. Phys. (Berlin, Ger.)* **1900**, *308*, 369–402.

[3] Ashcroft, N. W.; Mermin, N. D. *Solid State Physics*; Harcourt, Inc.: Orlando, FL, 1976.

[4] Landau, L. D. *J. Exp. Theor. Phys.* **1957**, *3*, 920–925.

[5] Slocombe, D. R.; Kuznetsov, V. L.; Grochala, W.; Williams, R. J. P.; Edwards, P. P. *Phil. Trans. R. Soc. A* **2015**, *373*, 20140476.

[6] Mohakud, S.; Datta, A.; Pati, S. K. *Theoretical Framework for Charge Carrier Mobility in Organic Molecular Solids*; Ghosh, S. K.; Chattaraj, P. K., Eds.; Concepts and Methods in Modern Theoretical Chemistry: Statistical Mechanics; CRC Press: Boca Raton, FL, 2013; pp 163–182.

[7] Jagadish, C.; Coleman, V. A. *Basic Properties and Applications of ZnO*; Jagadish, C.; Pearton, S., Eds.; Zinc Oxide Bulk, Thin Films and Nanostructures; Elsevier, Ltd.: Kidlington, UK, 2006; pp 1–20.

[8] Janowitz, C.; Scherer, V.; Mohamed, M.; Krapf, A.; Dwelk, H.; Manzke, R.; Galazka, Z.; Uecker, R.; Irmscher, K.; Fornari, R.; Michling, M.; Schmeißer, D.; Weber, J. R.; Varley, J. B.; van de Walle, C. G. *New J. Phys.* **2011**, *13*, 085014.

[9] Buchholz, D. B.; Ma, Q.; Alducin, D.; Ponce, A.; Jose-Yacaman, M.; Khanal, R.; Medvedeva, J. E.; Chang, R. P. H. *Chem. Mater.* **2014**, *26*, 5401–5411.

[10] Vogel, D.; Krüger, P.; Pollmann, J. *Phys. Rev. B* **1995**, *52*, R14316–R14319.

[11] Ginley, D.; Hosono, H.; Paine, D. C. *Handbook of Transparent Conductors*; Springer: New York, NY, 2011.

[12] Young, D. L.; Coutts, T. J.; Kaydanov, V. I.; Gilmore, A. S.; Mulligan, W. P. *J. Vac. Sci. Technol., A* **2000**, *18*, 2978–2985.

[13] Jarzebski, Z. M. *Phys. Status Solidi A* **1982**, *71*, 13–41.

[14] Ellmer, K.; Mientus, R. *Thin Solid Films* **2008**, *516*, 4620–4627.

[15] Mryasov, O. N.; Freeman, A. J. *Phys. Rev. B* **2001**, *64*, 233111.

[16] Dong, C. L.; Persson, C.; Vayssieres, L.; Augustsson, A.; Schmitt, T.; Mattesini, M.; Ahuja, R.; Chang, C. L.; Guo, J. H. *Phys. Rev. B* **2004**, *70*, 195325.

[17] Fan, J. C. C.; Goodenough, J. B. *J. Appl. Phys.* **1977**, *48*, 3524–3531.

[18] Walsh, A.; Da Silva, J. L. F.; Wei, S.-H.; Körber, C.; Klein, A.; Piper, L. F. J.; DeMasi, A.; Smith, K. E.; Panaccione, G.; Torelli, P.; Payne, D. J.; Bourlange, A.; Egdell, R. G. *Phys. Rev. Lett.* **2008**, *100*, 167402.

[19] Burstein, E. *Phys. Rev.* **1954**, *93*, 632–633.

[20] Moss, T. S. *Proc. Phys. Soc., London, Sect. B* **1954**, *67*, 775–782.

[21] Edwards, P. P.; Porch, A.; Jones, M. O.; Morgan, D. V.; Perks, R. M. *Dalton Trans.* **2004**, *19*, 2995–3002.

[22] Walsh, A. *Appl. Phys. Lett.* **2011**, *98*, 261910.

[23] Janotti, A.; Van de Walle, C. G. *Rep. Prog. Phys.* **2009**, *72*, 126501.

[24] Wang, R.; Sleight, A. W.; Platzer, R.; Gardner, J. A. *J. Solid State Chem.* **1996**, *122*, 166–175.

[25] Ellmer, K. *Electrical Properties*; Ellmer, K.; Klein, A.; Rech, B., Eds.; Transparent Conductive Zinc Oxide: Basics and Applications in Thin Film Solar Cells; Springer-Verlag: Berlin, 2008; pp 35–78.

[26] Zhang, D. H.; Ma, H. L. *Appl. Phys. A: Mater. Sci. Process.* **1996**, *62*, 487–492.

[27] Saxena, A. K.; Gurumurthy, K. S. *J. Phys. Chem. Solids* **1982**, *43*, 801–808.

[28] Bellingham, J. R.; Phillips, W. A.; Adkins, C. J. *J. Mater. Sci. Lett.* **1992**, *11*, 263–265.

[29] Kikuchi, N.; Kusano, E.; Nanto, H.; Kinbara, A.; Hosono, H. *Vacuum* **2000**, *59*, 492–499.

[30] Seto, J. Y. W. *J. Appl. Phys.* **1975**, *46*, 5247–5254.

[31] Orton, J. W.; Powell, M. J. *Rep. Prog. Phys.* **1980**, *43*, 1263–1307.

[32] Prins, M. W. J.; Grosse-Holz, K. O.; Cillessen, J. F. M.; Feiner, L. F. *J. Appl. Phys.* **1998**, *83*, 888–893.

[33] Edwards, P. P.; Lodge, M. T. J.; Hensel, F.; Redmer, R. *Phil. Trans. A* **2010**, *368*, 941–965.

[34] Mott, N. F. *Philos. Mag.* **1972**, *26*, 1015–1026.

[35] Newman, P. F.; Holcomb, D. F. *Phys. Rev. B* **1983**, *28*, 638–640.

[36] Rosenbaum, T. F.; Milligan, R. F.; Paalanen, M. A.; Thomas, G. A.; Bhatt, R. N.; Lin, W. *Phys. Rev. B* **1983**, *27*, 7509–7523.

[37] Marley, J. A.; Dockerty, R. C. *Phys. Rev.* **1965**, *140*, A304–A310.

[38] Vai, A. T.; Kuznetsov, V. L.; Jain, H.; Slocombe, D.; Rashidi, N.; Pepper, M.; Edwards, P. P. *Z. Anorg. Allg. Chem.* **2014**, *640*, 1054–1062.

[39] Mott, N. F. *Can. J. Phys.* **1956**, *34*, 1356–1368.

Chapter 3

The Measurement and Characterization of TCOs

The technical performance of a TCO thin film ultimately arises from a complex interplay of its chemical and structural properties. Thus, the task of understanding how and why TCO materials work relies on the application of a wide range of characterization techniques, not just to extract the industrially relevant outputs of conductivity and transparency, but also to relate these properties to the preparation conditions via other physical characteristics of the material. The search for these so-called *structure-property relations* lies at the heart of TCO research, and indeed, all semiconductor and oxide research as a whole.

Given that TCOs are generally used as thin films and engineered through the use of defects, the bulk or single crystal properties of the base oxide are just a part of what determines the overall behavior of the sample. This means that bulk-, surface-, and locally-sensitive characterization techniques are all needed to develop any reasonably complete picture of a real TCO thin film.

Since many of the techniques for the characterization of TCO thin films are widely used and described in detail elsewhere, this chapter does not attempt to give a comprehensive review of these topics. Instead, the focus will be on the techniques used later in this thesis, highlighting their specific uses and limitations in the study of TCOs, and introducing a few less commonly used techniques in somewhat greater depth.

3.1 Electronic Transport Measurements

3.1.1 Conductivity

Basic Definitions

Electrical conductivity σ (or, equivalently, resistivity $\rho = 1/\sigma$) is an intrinsic property of materials and one of the essential, basic descriptors of TCO performance. σ has units of $\Omega^{-1}\text{cm}^{-1}$ and is the proportionality constant that relates the current density in a material to an applied electric field:

$$\vec{J} = \sigma \vec{E}\,. \tag{3.1}$$

In general, σ is a complex-valued tensor of second rank in order to deal with the possibility of anisotropic materials. However, conduction in ZnO, In_2O_3, and most other TCOs is largely isotropic, so in these cases, it suffices to treat σ as a scalar.[1]

The extrinsic property of resistance R (which is the reciprocal of conductance G) has units of Ω and is defined as

$$\frac{dI}{dV} = R = \frac{1}{G}\,, \tag{3.2}$$

where I is the current and V is the corresponding voltage. R is clearly dependent on the geometry of the sample under test and that of the contacts used to impose and measure I and V. R can be simply related to σ and ρ for a bar-shaped sample of uniform material with ideal contacts covering opposite faces by

$$R = \frac{1}{\sigma}\frac{L}{A} = \rho\frac{L}{A}\,, \tag{3.3}$$

where L is the length of the current path and A is the cross-sectional area of the sample (Figure 3.1).

Because TCOs are generally prepared as thin films of a nominally uniform thickness where current mostly flows parallel to the plane of the sample, it is often convenient to refer to a sheet resistance R_s. This is defined as

$$R_\text{s} = \frac{\rho}{d}\,, \tag{3.4}$$

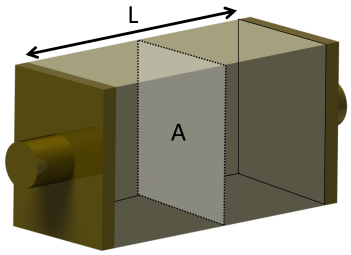

Figure 3.1: A hypothetical bar-shaped construction of uniform material with length L, cross-sectional area A, resistivity ρ, and ideal contacts on opposite faces, used to relate resistivity and resistance via $R = \rho\frac{L}{A}$.

where d is the sample thickness. Strictly speaking, R_s has units of Ω. However, it is conventional to refer to sheet resistance as having units of $\Omega/\square$ (read as "Ohms per square") in order to avoid confusion with conventional resistance.[i]

The quantity of sheet resistance has several useful characteristics. First, it can be calculated from four-point measurements without prior knowledge of the sample thickness (a substitution of Equation 3.4 into Equation 3.6 results in cancellation of the thickness terms). Second, the resistance of a rectangular (or parallelogrammatic) TCO film as measured from contacts running along two parallel edges can be expressed as $R = R_s\frac{L}{W}$, where L and W are the length and width of the film. Thus, R_s allows simple calculation of the resistance of a given TCO film prepared with different surface areas, which is directly applicable to the assessment of devices and architectures requiring TCO films of various sizes.

The van der Pauw Technique

The van der Pauw technique is particularly useful for TCO research because it allows the accurate determination of conductivity for a uniform, hole-free thin film of arbitrary shape.[2]

Four small (ideally, point) electrical contacts are placed anywhere on the periphery of the sample and labeled A, B, C, and D in clockwise order (Figure 3.2). These contacts must also be Ohmic (have linear current/voltage characteristics) in the range of the measurement. The voltage difference between two neighboring contacts (say,

[i]This somewhat odd unit is so named because a square sample with sheet resistance of a certain number of $\Omega/\square$ will have a numerically equivalent resistance in Ω if measured using electrical contacts along the full length of two opposite edges of the square.

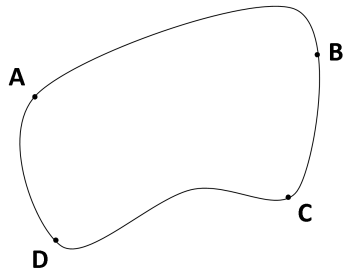

Figure 3.2: The van der Pauw measurement geometry with four small electrical contacts allowing the convenient measurement of resistivity and Hall effect on a thin, uniform, hole-free sample of arbitrary shape.

V_{AB}) is measured while a known current is imposed across the remaining two contacts (I_{CD}). A resistance can then be calculated via

$$R_{\mathrm{CD,AB}} = \frac{V_{\mathrm{AB}}}{I_{\mathrm{CD}}}\,. \tag{3.5}$$

Van der Pauw then proved that

$$\exp(-\frac{\pi d}{\rho}R_{\mathrm{AB,CD}}) + \exp(-\frac{\pi d}{\rho}R_{\mathrm{BC,DA}}) = 1\,, \tag{3.6}$$

where d is the sample thickness, holds for samples satisfying the conditions above.[3] If the sample thickness is known (see Sections 3.2.1 or 3.3.2), ρ is the only unknown and can be solved for. While Equation 3.6 is not analytically solvable in general, numerical methods can be straightforwardly employed to determine the value of resistivity.

The reciprocity theorem for Ohmic materials means that a switching of the pairs of voltage and current contacts should produce the same value of resistance (*i.e.*, $R_{\mathrm{AB,CD}} = R_{\mathrm{CD,AB}}$).[4] Likewise, reversing the direction of imposed current within a given contact configuration should also produce the same resistance value (*i.e.*, $R_{\mathrm{AB,CD}} = R_{\mathrm{BA,DC}}$). These relations generate two sets of four independent resistance measurements that can averaged and substituted into Equation 3.6 to improve the precision of the technique.

Two- and Four-Point Resistance Measurements

There are occasions where a simple resistance measurement is adequate for a rapid, qualitative assessment of a sample. Also, in cases where using the van der Pauw geometry is inconvenient, resistance measurements with an arbitrary, fixed geometry can be used to easily observe relative changes in the electrical resistivity of a

sample. These relative measurements can be made absolute by normalization to an independently measured value of resistivity.

A four-probe technique is the preferred method for accurate resistance measurements of relatively low resistance samples. Two sample contacts are used for passing current and two high impedance leads are used for measuring the voltage change that results from the flow of current. The two voltage contacts are typically placed geometrically between the two current contacts. Because virtually no current is flowing through the voltage leads, there is no voltage drop due to lead or contact resistances, and the measured voltage difference is almost entirely due to sample resistance. Where lead and contact resistances are of insignificant magnitude compared to sample resistance, a simpler two-point measurement will suffice.

It is possible to directly calculate sheet resistance from a four-point measurement if sample geometry and the relative position of the current and voltage leads are known.[5] However, this was generally not necessary as the resistivities of the thin film samples studied in this thesis could be independently measured using the van der Pauw technique, thus providing an absolute reference.

3.1.2 The Hall Effect

The most common technique for determining the free carrier concentration, the sign of the majority carriers, and the carrier mobility in semiconductors is based upon the Hall effect.[6] The force caused by electric and magnetic fields acting on a charge is given by

$$\vec{F} = e(\vec{E} + \vec{v} \times \vec{B}) \,, \tag{3.7}$$

where $\vec{v}$ is the drift velocity of the charge carrier, and $\vec{E}$ and $\vec{B}$ are the applied electric and magnetic fields, respectively. In a situation where $\vec{E}$ and $\vec{B}$ are imposed perpendicular to each other, the path of the moving charges will deviate from the $\vec{E}$ direction due to the orthogonal acceleration imposed by $\vec{B}$. Given a finite sample, the resulting asymmetry of charge in the $\vec{E} \times \vec{B}$ direction will lead to a *Hall voltage* V_{H} whose sign depends on whether the majority charge carrier in the system is negatively or positively charged (Figure 3.3).

Conveniently, the van der Pauw geometry (Figure 3.2) is also useful for the measurement of the Hall effect. When a magnetic field is applied perpendicular to the

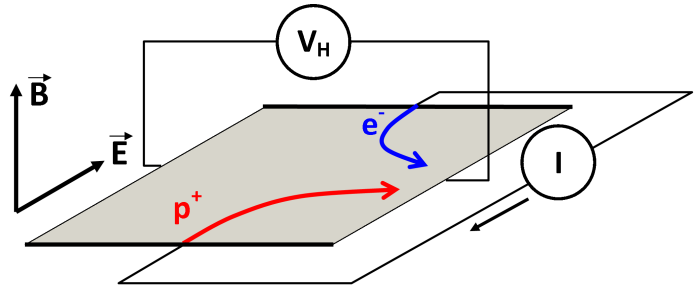

Figure 3.3: The Hall effect: with an electric field $\vec{E}$ imposed by an external current source I and an applied magnetic field $\vec{B}$ in the directions shown, positive charges (red) will be deflected to the right of the path they would have taken in the absence of a magnetic field, while negative charges (blue) will be deflected to the left of their unperturbed path. Since charges of both signs are deflected toward the same side of the sample, the sign of the measured Hall voltage V_{H} depends on the sign of the majority charge carrier.

film and a current is passed through a pair of non-neighboring contacts, a voltage measured between the remaining two contacts is the sum of the Hall voltage and an Ohmic voltage drop due to the current being passed through the sample. Because the Ohmic voltage is not magnetic field dependent, it can be canceled out by finding the difference of the voltage measurements with the magnetic field in opposite directions.

Generally, the voltage measurement is repeated for each of four such pairs of contacts (AC, CA, BD, DB) and each orientation of the magnetic field (+,−) for a total of eight measurements. The Hall voltage can then be written as

$$V_{\mathrm{H}} = \frac{(V_{\mathrm{AC},+} - V_{\mathrm{AC},-}) + (V_{\mathrm{CA},+} - V_{\mathrm{CA},-}) + (V_{\mathrm{BD},+} - V_{\mathrm{BD},-}) + (V_{\mathrm{DB},+} - V_{\mathrm{DB},-})}{8}\,. \tag{3.8}$$

The bulk carrier concentration (n) can then be written in terms of V_{H} as

$$n = \frac{IB}{edV_{\mathrm{H}}}\,, \tag{3.9}$$

where I and B are the magnitudes of the applied current and magnetic fields, respectively, e is the electronic charge, n is the bulk carrier concentration, and d is the sample thickness.[7] The sign of n will indicate the sign of the majority carrier in the case where one carrier type dominates, as is typically true for TCO materials. If the resistivity is known from another measurement, it is then a straightforward matter to calculate carrier mobility using $1/\rho = ne\mu$.

If the sample thickness is not known, then it is still possible to calculate a sheet carrier concentration (with units of length^{-2}), which can then be used along with the sheet resistance R_s to calculate the carrier mobility.

From a practical perspective, the magnitude of V_H will be significantly smaller than the voltage drop resulting from the passage of current through the sample. For an experimental setup with a given magnetic field, power supply, and measurement electronics, there will be sample resistance above which sufficient current cannot be passed to generate a measurable V_H, even if sometimes resistivity can still be measured.

3.2 Optical Properties

For the purposes of this thesis, optical properties can be taken to refer to how materials interact with light in the ultraviolet, visible, and infrared ranges of the electromagnetic spectrum. The applications of other parts of the spectrum, such as X-rays, in the characterization of TCOs will be treated separately.

The optical property that most readily comes to mind in the study of TCOs is probably transparency, one of the two namesake properties of this class of materials. However, since the interaction of a thin film sample with light is intimately related to both its electronic structure and its microstructure, there is also a great deal more useful information that can be extracted from such measurements.

3.2.1 Transmission Spectrophotometry

Figure 3.4 is a UV-Vis-NIR transmission spectrum collected from a $\sim$1 μm thick indium-doped ZnO sample that illustrates many of the features that can be interpreted to provide useful information about a TCO sample.

Visible Transmittance

The window of highest transparency, including the visible range (400–750 nm), is clearly observed in the middle, unshaded portion of Figure 3.4. Somewhat problematically, there is no consistent standard for the quantification of transparency in the TCO literature, which makes the direct comparison of results difficult. Most sources

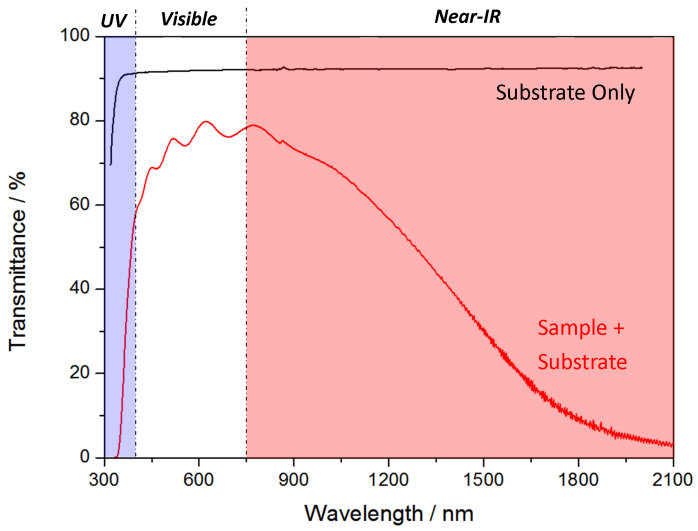

Figure 3.4: UV-Vis-NIR transmission spectrum of an indium-doped ZnO thin film (red curve) illustrating common features of these data (see main text). A transmittance curve for a bare ∼0.17 mm thick Schott D263T glass substrate is also shown for reference. The glitch near 860 nm is a spectrometer artifact related to a detector switch.

simply quote single numbers for transparency without indicating whether this is the value at a single wavelength, or an average over some range.

As can also be seen from Figure 3.4, a bare glass substrate is approximately 92 % transparent (mostly due to reflection at its two surfaces) in the visible range. It is not always clear whether TCO transparency values quoted in the literature have been corrected for the presence of the substrate. If desired, this can be done by dividing the sample plus substrate transmittance signal by the substrate signal at each frequency.

Finally, there is an oscillation in the transmittance signal which arises from self-interference of internally reflected light within the TCO layer. The presence of these so-called *interference fringes* can lead to changes in apparent transparency at a given wavelength that do not reflect changes in the intrinsic properties of the material, but instead factors like the sample thickness. It can be shown that the sample transmittance in the absence of interference fringes is the geometric mean of the upper and lower envelopes that encompass the experimental signal (Figure 3.6).[8] Using this fact, this thesis reports transmittance values in the *absence* of interference fringes, averaged over the full range of visible wavelengths to prevent any frequency-specific bias. Unless otherwise noted, reported values here are also corrected for the presence

of the substrate.

Calculating transparency in this way produces a value that better reflects the intrinsic properties of the thin film, which are of most interest here. A different choice may well make more sense if the emphasis were, for example, to be on engineering the position and spacing of fringes to maximize transparency at certain frequencies.

Haze

A sample that scatters incident light will appear visually hazy. Scattering occurs mostly from surface roughness, but can also arise from inhomogeneities within the volume of a film.[9] A sample surface morphology with many well-defined flat facets oriented at a many different angles can also enhance light scattering.

Depending on whether the length scale of the scatterers is large or small compared to the incident wavelength, the scattering probability varies inversely with either the second or fourth power of wavelength, meaning that blue light is scattered more strongly than red.[10] Thus, a hazy sample will show a gradual decrease in transmission as the UV wavelengths are approached from the visible, whereas a non-hazy sample will have relatively flat transmittance in the visible followed by a sharp onset of the fundamental bandgap absorption in the UV (Figure 3.5).

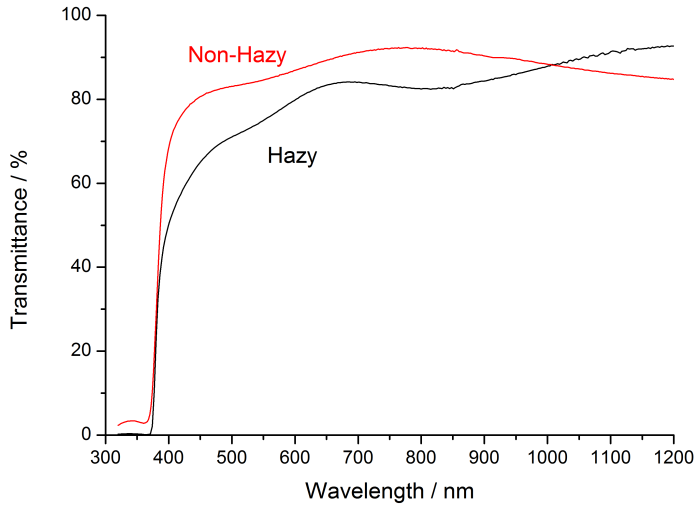

Figure 3.5: UV-Vis-NIR transmission spectra of a non-hazy ZnO sample deposited at $T_{\mathrm{dep}} = 292\,^{\circ}\mathrm{C}$ (red) and a hazy undoped ZnO sample deposited at $T_{\mathrm{dep}} = 376\,^{\circ}\mathrm{C}$ (black) showing a preferential decrease in blue light transmission due to scattering.

Haze is a useful feature of films intended for some applications. For instance, the light scattering by TCO layers reportedly enhances the light trapping efficiency in some photovoltaic cell designs.[11–13] In situations where the amount of haze in a sample needs to be quantified more precisely, this can be achieved using a spectrophotometer with an integrating sphere following the procedure specified in ASTM Method D1003.[14] However, such quantification was not necessary for the purposes of the present work.

Film Thickness via Swanepoel's Envelope Method

In samples where several interference fringes are clearly visible, they can be used to conveniently estimate the thickness of samples using a method described by Manifacier, *et al.*, and subsequently refined by Swanepoel.[8,15] The basic equation that must be satisfied by the fringes is

$$2nd = m\lambda\,, \tag{3.10}$$

where n is the index of refraction, d is the thickness of the film, and m is the "order" of the fringe reflecting that constructive or destructive interference will only occur at positive integer or half-integer multiples of the wavelength, respectively.

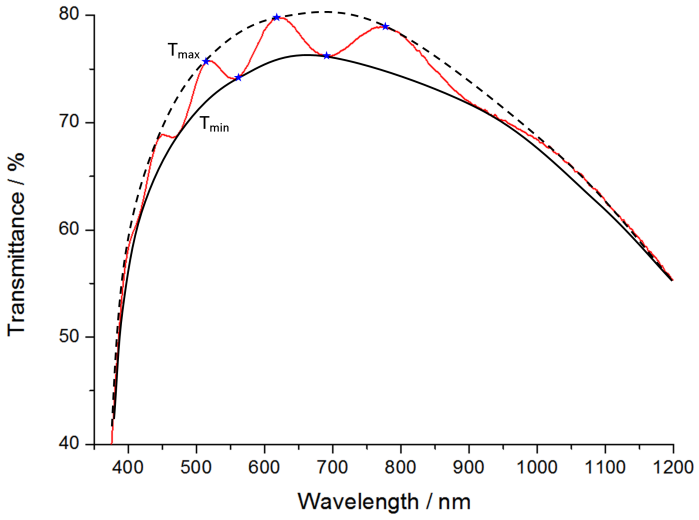

Figure 3.6: Example UV-Vis-NIR transmission spectrum (red curve) with features used in the Swanepoel method thickness calculation highlighted. $T_{\max}$ and $T_{\min}$ envelope functions are shown by dashed and solid black curves, respectively. The extrema that would be used in a calculation are marked with blue stars.

For the case of a thin film on a thick, but finite, transparent substrate, the transmittance as a function of the incident wavelength, the complex indexes of refraction of the sample and substrate, and the sample thickness can be rather tediously written down starting from the basic equations of optics.

Under the approximation of low film absorbance, the equations simplify somewhat and allow the index of refraction of the sample, $n(\lambda)$, to be expressed in terms of the $T_{\max}$ and $T_{\min}$ envelope functions as

$$n(\lambda) = [N(\lambda) + (N(\lambda)^2 - s^2)^{1/2}]^{1/2}\,, \tag{3.11}$$

where

$$N(\lambda) = 2s\frac{T_{\max}(\lambda) - T_{\min}(\lambda)}{T_{\max}(\lambda)T_{\min}(\lambda)} + \frac{s^2+1}{2} \tag{3.12}$$

and s is the index of refraction of the substrate, which is known either from tabulated values[ii] or can be calculated from the transmittance of the substrate alone using $T_{\text{subs}}(\lambda) = (2s)/(s^2+1)$. For the D263T borosilicate substrates typically used, s is taken to be 1.51 and constant in relevant wavelength range.

Once $n(\lambda)$ is known, the sample thickness d can then be determined using

$$d = \frac{\lambda_1\lambda_2}{4(\lambda_1 n(\lambda_2) - \lambda_2 n(\lambda_1))}\,, \tag{3.13}$$

where λ_1 and λ_2 are the wavelengths of successive extrema in the transmission curve. An improvement in accuracy can be obtained by using the initial estimates of thickness from Equation 3.13 to determine the integer or half-integer order of each extrema. Then, a plot of m as a function of n/λ should yield a line with a slope of $2d$. A graphical illustration of the spectral features used in this fitting procedure is shown in Figure 3.6.

In our implementation of the Swanepoel method, the relevant envelope functions are defined using cubic splines over a series of points manually placed based on the transmission data. A custom Python program was used to provide a graphical interface for the definition of the envelope functions and extrema, which were then used to automatically calculate sample thickness and transparency (Appendix A).

Clearly, at least two, and preferably several more well-resolved fringes are needed to use this method for thickness determination. For very thin samples (for which the

[ii] www.refractiveindex.info is a useful free resource for many common materials.

fringes are very widely spaced) or for hazy or uneven samples (which suppresses the amplitude of the fringes) two consecutive extrema are not always clearly visible and an alternative method must be used for thickness determination, such as scanning electron microscopy of a cleaved sample cross-section (Section 3.3.2) or alternative optical means such as the full modeling and fitting of optical data. If a reasonably sharp step can etched into a TCO film, various forms of profilometry can also be used for the determination of sample thickness.

Such alternative methods have also been used several times to verify the results obtained from the Swanepoel calculation. Though this has not been determined rigorously, based on comparison with other thickness results, $\pm 50\,\text{nm}$ would in general be a reasonable, conservative error estimate for Swanepoel thickness values. It also appears that the thicknesses obtained from the envelope method include that of the surface roughness layer present in most TCO thin films (Figure 3.8).

A favorable evaluation of the speed and accuracy of the Swanepoel method compared to other methods for the determination of optical constants of thin films is given by Poelman and Smet.[16] Additionally, several extensions and generalizations of this method have been reported, for example, to include the effect of substrate absorption or to account for spatial variations in film thickness or optical properties. However, these extensions have not been used in this thesis.[17,18]

UV: Optical Band Gap

A sharp decrease in transmission is observed in the short wavelength region of the example transmission spectrum in Figure 3.4. This comes from increased absorption due to the excitation of electrons across the band gap of the TCO (Section 2.2.2).

This feature of the transmission spectrum can be used to calculate the energy of the bandgap transition E_g using the Tauc relation, which states that

$$\alpha(\hbar\omega) \propto (\hbar\omega - E_\text{g})^\gamma \,, \tag{3.14}$$

where α is the absorption coefficient, $\hbar\omega$ is the energy of a photon with angular frequency $\omega = 2\pi\nu$, and γ is a constant whose value varies with the nature of the transition.[19] γ is 1/2 for the intrinsic interband transitions in ZnO and In_2O_3, which are direct and allowed.[20]

If it is assumed that most of the decrease in transmission in the UV is due to bandgap absorption, E_g can be determined by extrapolating the linear portion of a plot of $(\alpha\hbar\omega)^2$ *vs.* $\hbar\omega$ to where $\alpha = 0$. An example of this fitting procedure is shown in Figure 3.7 for a series of ZnO thin films doped to various carrier concentrations.

The measured bandgap energy increases sharply above a carrier concentration of about $7 \times 10^{19}\,\mathrm{cm}^{-3}$, which is consistent with the Burstein-Moss effect (Section 2.2.2). Incidentally, this type of analysis provides one method for estimating the carrier concentration at which the Fermi energy in ZnO crosses into the conduction band, and the resulting value is consistent with those found independently using other methods in Chapter 5.

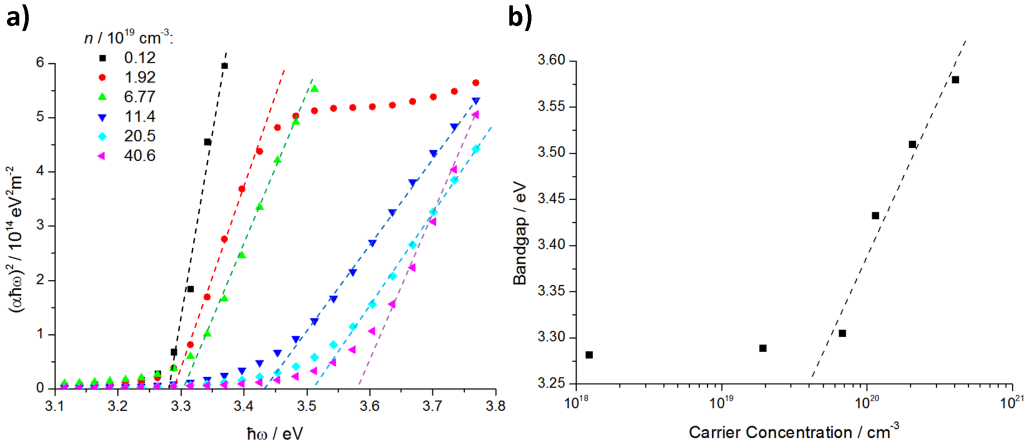

Figure 3.7: a) Tauc plots for various ZnO films with the indicated carrier concentrations. The dashed lines are an extrapolation of the linear portion of each dataset to the x-axis, which indicates the bandgap energy E_g. b) Bandgap as a function of carrier concentration for this series, showing the approximately exponential dependence of E_g on carrier concentration once the Fermi level has entered the conduction band.

3.2.2 Dielectric Modeling

Purpose

Since light is an oscillating electromagnetic field, the optical response of a material is a function of the charges present within it. Thus, optical frequency measurements are a different way to study the electronic structure of TCOs than the direct current methods discussed in Section 3.1.

A DC measurement implies that charge carriers are traversing the macroscopic distances between electrical contacts, which means that they will necessarily be in-

fluenced by macroscopic inhomogeneities. The most obvious example of these are the grain boundaries in polycrystalline TCO films. In contrast, charges respond to optical frequency measurements ($\sim 10^{12}$–10^{14} Hz) by oscillating rapidly within a confined space and only sample their local environments.

Combining DC and optical frequency measurements thus provides a means of distinguishing different types of carrier scattering mechanisms based on their characteristic frequencies and spatial scales.

The extraction of basic electronic transport properties like carrier concentration and mobility from optical data is somewhat more involved than from direct current measurements. Therefore, a brief introduction on theory and techniques will be provided here. A more complete derivation of the results in this section is provided in Appendix B.

Theory

Within the UV-Vis-NIR frequency range, the optical properties of the material are dominated by the behavior of free conduction electrons and those electrons involved in the fundamental bandgap transition.

The relative permittivity[iii] for a material containing multiple types of electron oscillations can be written as

$$\tilde{\epsilon}(\omega) = \epsilon_\infty + \sum_{i=1}^{n} \chi_i(\omega)\,, \tag{3.15}$$

where ϵ_∞ is the dielectric constant of the material in the high frequency limit, and χ_i refers to the contribution to electric susceptibility of the i^{th} induced charge oscillation relevant in the frequency range under study.

The conduction electrons can be modeled by assuming that their motion in response to an oscillating electric field can be described by the Drude free electron model. Starting from Equation 2.2, it is possible to show that the Drude model implies a frequency-dependent susceptibility of the form

$$\chi_{\mathrm{Dr}}(\omega) = \frac{\omega_{\mathrm{n,Dr}}^2}{-\omega^2 + i\Gamma_{\mathrm{Dr}}\omega}\,, \tag{3.16}$$

[iii]Here we adopt the convention $\tilde{\epsilon} = \epsilon' - i\epsilon''$. Also, because the TCOs being studied here are non-magnetic, the complex index of refraction, often used in the discussion of optical properties of materials, can simply be expressed as $\tilde{n}(\omega) = \sqrt{\tilde{\epsilon}(\omega)}$.

where $\Gamma_{\mathrm{Dr}} = 1/\tau$ is the damping constant of the oscillator and also the inverse of the mean time between carrier scattering events.

The bandgap absorption can be modeled as a Lorentz oscillator, which is a generalization of the Drude oscillator including the effect of a restoring force that leads to a characteristic resonant frequency ω_0. The Lorentz oscillator leads to a susceptibility of the form

$$\chi_{\mathrm{Lor}}(\omega) = \frac{\omega_{\mathrm{n,Lor}}^2}{\omega_{\mathrm{0,Lor}}^2 - \omega^2 + i\Gamma_{\mathrm{Lor}}\omega}\,. \tag{3.17}$$

Substitution of Equations 3.16 and 3.17 into Equation 3.15 leads to a dispersion relation incorporating the effect of both the free conduction electrons and the bandgap excitation

$$\tilde{\epsilon}(\omega) = \epsilon_\infty + \frac{\omega_{\mathrm{n,Dr}}^2}{-\omega^2 + i\Gamma_{\mathrm{Dr}}\omega} + \frac{\omega_{\mathrm{n,Lor}}^2}{\omega_{\mathrm{0,Lor}}^2 - \omega^2 + i\Gamma_{\mathrm{Lor}}\omega}\,, \tag{3.18}$$

where the Dr and Lor subscripts represent the parameters of their respective oscillator models.

Several authors have noted that modification of the Drude model by inclusion of a frequency-dependent Γ_{Dr} is required to adequately describe $\tilde{\epsilon}(\omega)$ near the energy of the plasma edge.[21–23] We have also found this to be the case for some samples, and have adopted a model for frequency-dependent scattering proposed by Mergel and Qiao:[24]

$$\Gamma_{\mathrm{Dr}}(\omega) = \Gamma_{\mathrm{L}} - \frac{(\Gamma_{\mathrm{L}} - \Gamma_{\mathrm{H}})}{\pi}\left[\arctan\left(\frac{\omega - \Omega_{\Gamma\mathrm{Dr}}}{\Gamma_{\Gamma\mathrm{w}}}\right) + \frac{\pi}{2}\right] \tag{3.19}$$

where $\Gamma(\omega \to 0) = \Gamma_{\mathrm{L}}$ and $\Gamma(\omega \to \infty) = \Gamma_{\mathrm{H}}$ and $\Omega_{\Gamma\mathrm{Dr}}$ and $\Gamma_{\Gamma\mathrm{w}}$ are fit parameters that describe the midpoint and steepness, respectively, of the transition between Γ_{L} and Γ_{H}.

Experimental Measurements

Given that the optical properties of a material at each frequency are determined by the permittivity $\tilde{\epsilon}(\omega)$, a complex quantity, at least two independent sets of measurements are needed in principle to uniquely determine the real and imaginary parts of $\tilde{\epsilon}$.[iv] Examples of commonly used combinations of measurements include spectroscopic

[iv] Theoretically, as linear optical systems, the real and imaginary parts of $\tilde{\epsilon}$ in TCOs are related by the Kramers-Kronig relations,[25,26] however to calculate ϵ' from ϵ'', or vice versa, requires measurements over *all* frequencies, which is generally impractical.

ellipsometry (which includes independent information from both the amplitude and phase of the signal), a combination of transmission and reflectance spectrophotometry, or reflection data from varying angles of incidence.[27–29]

The WVase32 software[30] was used to simulate various optical measurements given a geometrical model and dispersion relation for the materials under study. Figure 3.8 shows the geometric model used throughout this thesis compared with an experimentally observed thin film cross-section. Parameters such as those in Equation 3.18 and 3.19, as well as those related to the sample geometry (thickness, surface roughness, degree of uniformity, etc.) are varied in order to find a set that best reproduces the experimental optical data. Once this has been achieved, physical quantities of interest such as n_{opt} and μ_{opt} can be calculated from the best fit values for $\omega_{\text{n,Dr}}$ and Γ_{Dr}. This modeling approach is applied to doped ZnO and In_2O_3 samples in Chapter 5.

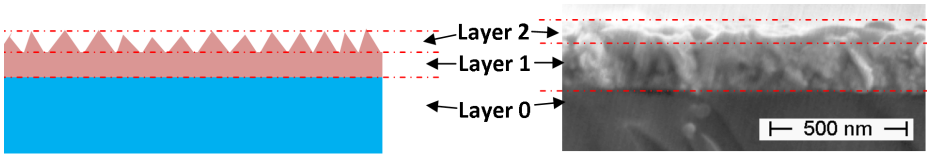

Figure 3.8: a) Geometric model of TCO thin films used for dielectric modeling compared with b) a real TCO film cross-section. Both show Layer 0) substrate, Layer 1) the TCO film, and Layer 2) a roughness layer consisting of a mixture of the TCO and air.

3.3 Microstructural Characterization

3.3.1 Thin Film X-ray Diffraction

Basics

X-ray diffraction is one of the classic methods for characterizing crystalline materials and as such is commonly used as part of the standard characterization suite for TCOs. It relies on the fact that an incoming X-ray photon can be elastically scattered as a spherical wave by the electron density associated with atoms in a material. When the electron density is nearly periodic, as in a crystalline domain, the scattered waves will constructively interfere only in certain special directions, which are given by the

well known Bragg's Law

$$2d\sin(\theta) = n\lambda\,, \tag{3.20}$$

where d is the distance between diffraction planes (*i.e.*, repetitions in the periodic electron density along a given direction), θ is the angle between the incident X-ray and the diffraction plane, λ is the wavelength of the incident radiation, and n is the positive integer "order" of the reflection.[31] The crystalline lattice thus defines the angles at which a strong scattered signal can be detected. The intensity at each Bragg angle depends on the amount of electron density in the corresponding diffraction plane.

Since, in general, physical crystals are three-dimensional constructs, the pattern of diffraction peaks also varies in three dimensions. However, when an X-ray diffraction experiment is carried out on a polycrystalline sample, the beam simultaneously irradiates multiple crystalline domains with potentially differing orientations. The simplest case is when the number of domains measured is large and all orientations are equally represented within the sample. In this case, because of the averaging over two angular coordinates, the resulting diffraction pattern is simply a projection onto one dimension of the three-dimensional pattern that would have been obtained if a single crystal of the same material was measured. Given this, most diffractometers for powdered or polycrystalline samples only vary the incident angle of the X-ray beam along one axis.

In principle, a great deal of useful information can be extracted from diffraction data.[32] There are several databases of the characteristic polycrystalline diffraction patterns of known materials, allowing fingerprint identification and quantification of the crystalline phase(s) present in a sample. A systematic shift in the position of diffraction peaks (for example, upon insertion of a dopant) could indicate that the base crystal structure is maintained, but with systematic changes in the lattice parameters that define the spatial repetition of the electron density.

The shape and broadness of the peaks can provide information about particle size distribution and the degree and type of strain in the material. Such perturbations of the periodicity of the electron density lead to broadening or asymmetry of the diffraction signal which can be modeled.[33] One of the simplest examples of this relates to peak broadening which occurs when the diffracting domains are too small to be

approximated as semi-infinite in size. In this case, the interference which generates the Bragg peaks will not be perfectly constructive or destructive at a given angle. This is typically described using the Scherrer formula:

$$\ell = \frac{K\lambda}{\beta \cos(\theta)}\,, \tag{3.21}$$

where ℓ is the volume average of the thickness of crystallites in the direction perpendicular to the diffracting plane, K is a *shape factor* whose value depends on the shape of the ordered domains,[34] λ is the X-ray wavelength, β is the integral breadth of the diffraction peak, and θ is the Bragg angle. Unfortunately, this equation is much abused in the TCO literature. Many authors use $K \approx 0.9$, the value for spherical particles, without regard for the actual shape of the crystallites or the fact that K can vary depending on the precise definition chosen for "average crystallite size".[35] Furthermore, instrumental effects that lead to peak broadening are often neglected; in practice, instrumental broadening on most laboratory instruments is enough to obscure broadening due to sample if the ordered domains are much larger than $\sim$100 nm.[36]

An alternative to using relations like Equation 3.21 to extract information from X-ray diffraction is to generate a theoretical diffraction pattern from a structural model and knowledge of the instrument used. The goal is then to carry out a non-linear optimization of the parameters to find a physically sensible set that minimizes the difference between the simulated and experimental data. Examples of such methods include the Pawley, Le Bail, and Reitveld methods, which are commonly used for the study of powdered samples.

Limitations of XRD in Thin Film Characterization

The thinness of thin film samples can make it difficult to place an optimum quantity of sample into the beam. In some situations, this can lead to low signal-to-noise ratios which reduce the precision with which quantitative information can be extracted from the patterns. It is also common for the X-ray beam to penetrate through the thin film into the substrate, leading to an observable signal not due to the sample. The glass substrates commonly used here lead to a broad, low background between about $2\theta = 10$–$40\,^\circ$ that does not substantially interfere with observation of the TCO signal (for example, as seen in the red curve in Figure 3.9). If a crystalline substrate like

sapphire is used, more care needs to be taken to account for the diffraction peaks that may arise from those materials.

Furthermore, unlike most powders, the crystallites in a TCO film typically adopt a preferred orientation with respect to the substrate. Since the X-ray beam no longer samples all orientations equally, the relative intensities of the diffraction peaks in a preferentially oriented sample will differ from when the crystallites are truly randomly oriented. In cases where one preferred orientation dominates, only a few of the peaks that would have been seen in the diffraction pattern of a randomly oriented sample might be detectable (Figure 3.9).

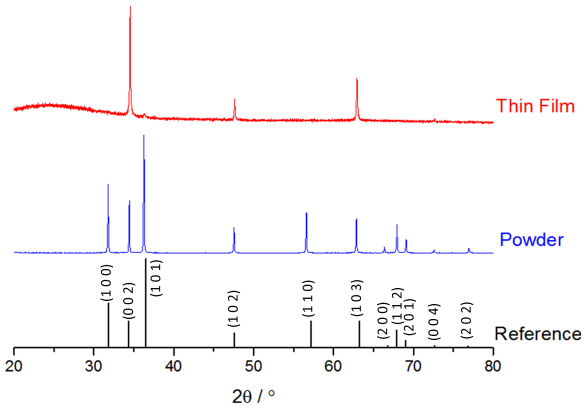

Figure 3.9: Normalized XRD pattern for a highly-oriented ZnO film (red) compared with the pattern for randomly oriented ZnO powder (blue). The ZnO thin film shows strong preferred orientation of its crystallites with respect to the substrate, leading to substantial changes in relative peak intensities and the disappearance of some peaks altogether. A literature reference pattern for ZnO is shown as a stick chart and annotated with the crystalline plane in wurtzite ZnO that leads to each reflection.[37]

Preferred orientation does not by itself change the positions of diffraction peaks. Since a known TCO is being deposited, there is generally no difficulty in confirming that the peaks present are a subset of those in the randomly oriented diffraction pattern for the expected oxide. However, it can be challenging to conclusively identify unexpected secondary phases if only a few peaks inconsistent with the expected material are observed.

Furthermore, Rietveld refinement, which calculates peak intensities based on the structure factors of an assumed model structure, is substantially complicated because the effects of preferred orientation on peak intensities must be included in the model as additional parameters. Even if this can be done satisfactorily, having only a few

peaks visible decreases the amount of information in the diffraction data and increases the possibility of non-unique parameter sets if the number of model parameters cannot be reduced.

Since significant preferred orientation was observed for virtually every thin film sample prepared in this work, the Pawley method was used instead.[38] Instead of constraining peak intensities based on crystal structure, the Pawley method allows the intensity of all reflections defined by the given space group to vary independently, which accounts for the intensity changes caused by preferred orientation without need to model the underlying distribution. Since the identity of the diffracting phase is generally known in TCO samples, not obtaining structure factors is not a great loss. At the same time, this fitting is enough to permit estimation of lattice parameters, strain, and crystallite size distribution.

3.3.2 Electron Microscopy

Most microstructural features in TCO thin films are at most hundreds of nanometers in extent and often much smaller, making electron microscopy one of the few techniques capable of direct, real space imaging of such samples.

Electron microscopy can be broadly divided into two classes, Scanning Electron Microscopy (SEM) and Transmission Electron Microscopy (TEM). Both techniques exploit the short wavelength of the electron in order to provide far higher resolving power than can be achieved with a light microscope. Sub-Ångstrom resolutions are possible using some modern, high-resolution TEM instruments.

In both cases, electrons from a source[v] are accelerated toward the sample through a vacuum chamber while being focused and directed using a variety of electromagnetic lenses. The interaction of the beam with the sample produces various signals which can then be measured and used to produce images.

However, beyond these basics, sample preparation for and usage of SEM and TEM in TCO research differ quite significantly, and so from here, these techniques will be discussed separately.

[v]Examples include thermionic sources like heated tungsten or LaB_6, or alternatively, cold field-emission sources relying on quantum-mechanical tunneling from the source into the vacuum. Cold field-emission sources produce superior results because the electrons they produce have a narrower momentum distribution and experience less dispersion upon passing through an electromagnetic lens.

Scanning Electron Microscopy

In scanning electron microscopy, the electron beam is focused onto the sample and then rastered across its surface to produce an image. The study of TCOs in this thesis primarily used a detector sensitive to the low-energy secondary electrons produced by inelastic collisions of the primary electron beam. Because the secondary electrons are low energy, they can only be emitted from near the surface of the sample. It is also easier for secondary electrons from topographically high parts of the sample to reach the detector. Thus, the highest parts will produce a stronger signal than the lower, more shielded parts (Figures 3.10 and 3.12), and the images generated using such a detector provide a representation of sample surface morphology.

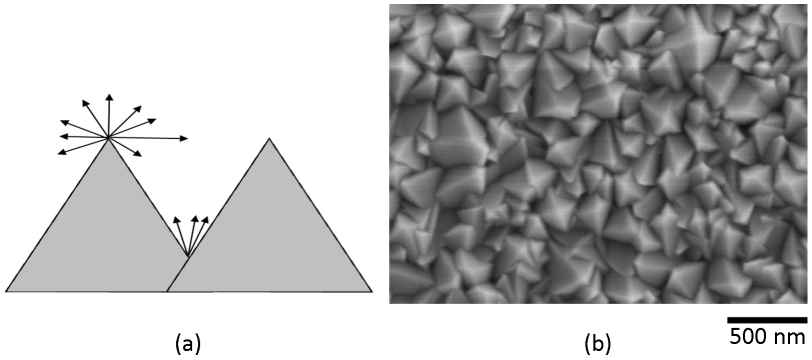

Figure 3.10: (a) Cartoon illustrating the greater ease with which secondary electrons are emitted from topologically exposed portions of a sample than from more shielded valleys. Detection of secondary electrons in a SEM yields micrographs showing sample morphology like the example in (b).

One of the key advantages of SEM is the relative ease of sample preparation. An as deposited TCO sample can simply be affixed with the side to be observed up on an appropriately sized sample holder. Beyond this only a few additional considerations should be kept in mind. Because the samples will go into a high vacuum chamber, care should be taken to use only low vapor pressure adhesives (such as specialty carbon-based cements) and to avoid touching the samples with ungloved hands, lest the transfer of volatile skin oils eventually contaminate the microscope.

Additionally, since the sample will be irradiated with electrons, a low-resistance path must generally be provided from where the electron beam meets the sample to ground, or else the sample will accumulate negative charge. Buildup of charge on the sample can deflect the electron beam as it rasters, producing image artifacts. A

charged sample will also tend to attract residual impurities (particularly hydrocarbons) present in the vacuum chamber and lead to sample contamination.

The carbon-based cement used for affixing samples also serves as an electrical bridge between the TCO film and the grounded metal SEM sample holder. If the TCO film is highly conductive, this is often sufficient for the dissipation of charge and good imaging results. However, when the TCO layer is less conductive, a 2–3 nm layer of platinum metal can be sputter-coated onto the sample surface prior to observation in the SEM. This amount of metal does not substantially affect the observed morphology of the TCO sample, while at the same time providing an adequate current path for imaging even the least conductive samples studied here. Use of a relatively low accelerating voltage (∼5 kV) for the primary electron beam can also reduce problems related to sample charging.

While too involved to be used routinely in this way for every sample, SEM also provides a means of directly measuring the thickness and roughness of thin film samples. This is particularly useful as an independent verification of results obtained using the Swanepoel envelope method (Section 3.2.1) and for samples that are too thin or hazy to be reliably measured using optical means. For this purpose, a custom sample holder has been designed and fabricated, allowing a freshly cleaved sample to be mounted perpendicularly and observed in cross-section (Figure 3.11).

In addition, this different perspective on film microstructure can be a useful complement to conventional SEM images of the sample surface.

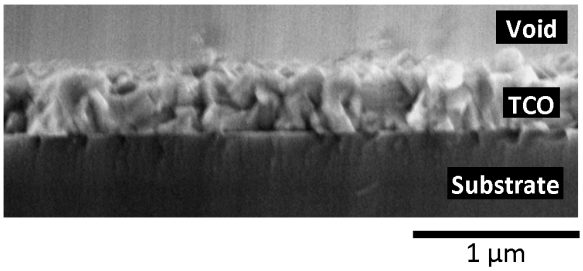

Figure 3.11: Example of a SEM image of the cross-section of a TCO sample with layers labeled. In addition to providing a different perspective on sample microstructure, these images allow a direct determination of sample thickness and roughness.

Transmission Electron Microscopy

Instead of relying on a signal emitted from the top of the sample surface, transmission electron microscopy (TEM) relies on analyzing how the primary electron beam is changed by passage through a sample. With modern aberration-corrected instruments and very good samples, features as small as a few tenths of Ångstroms can be resolved, small enough to see individual atoms and defects in a crystal and a few orders of magnitude better than the best SEMs.

A number of different detectors can be used to generate an image from the transmitted electron beam. The most straightforward is "bright field" imaging, which is simply a measure of electron transmission through various parts of the sample. Thinner, or otherwise less absorbing parts of the sample thus appear brighter. Variations in crystallite orientation can also be observed because different amounts of beam intensity will be diffracted away from the detector by different crystalline orientations.

An "annular dark field" (ADF) detector measures electrons that exit from the sample at an angle, either due to scattering or diffraction. Portions of a sample rich in higher Z atoms will scatter more and appear brighter in such images. The same is true for crystals oriented such that one or more diffraction peak(s) (see Equation 3.20) occur at an angle sampled by the detector. An image generated using an ADF detector can thus show both chemical contrasts and the presence of different crystalline orientations within a sample. Changing the angle being sampled will change the relative proportion of these two signals, with higher angles increasing the relative effect of chemical differences.

In addition to imaging in real space, a TEM can also be used to carry out electron diffraction experiments on specific parts of a sample.

The requirement that an electron beam pass through the sample introduces several significant complications when it comes to using TEM for the study of TCO films. Samples must be extremely thin, on the order of hundreds of nanometers for bright field measurements and tens or even single-digits of nanometers for some more sophisticated techniques, such Electron Energy Loss Spectroscopy. Given that TCO films are generally several hundred nanometers thick and deposited on an even thicker substrate, TEM can only be performed on cross-sections of such films.

Preparing a TEM cross-section of an oxide thin film on a substrate can be very challenging. This can be done in principle by a laborious, 1-to-2 week long manual process of rough sectioning, hand polishing to a thickness of less than 100 μm, followed by final thinning using an argon ion mill. Unfortunately, the yield of this process is low and does not produce samples with large areas of uniform thickness, as ion milling results in a wedge-shaped sample profile.

An alternative is to use a Focused Ion-Beam (FIB) instrument, which uses an electromagnetically focused beam of ions (usually gallium) to cut thin cross-sectional samples out of a larger thin film. A micromanipulator can then be used to position the cross-section on a support grid for observation in a TEM. Large, uniform samples can be reliably prepared in about a day or less by a skilled operator. Unfortunately, FIB has some severe drawbacks. The ion beam appears to cause significant erosion of zinc oxide samples (probably *during* deposition of a "protective" platinum capping layer meant to protect the sample during the rest of the FIB processing). There is also the risk of gallium ion implantation into the sample, which could potentially lead to spurious changes in sample chemistry and microstructure. Nevertheless, such problems must be tolerated because FIB has proven to be the only reliable means of producing cross-sectional samples of TCOs for TEM.

Finally, to maximize penetrating power, a TEM also uses significantly higher accelerating voltages for its electron beam than a SEM. Common instruments operate between 80 to 300 kV, though 1 MV instruments are not unheard of. At these voltages, sample radiation damage due to high energy electrons must be considered. While zinc oxide appears to be quite resistant to 200 kV electrons, the borosilicate glass slides typically employed as substrates were severely damaged by this electron beam. This led to glass components being sputtered over the rest of the sample, interfering with any attempts at chemical analysis. Fortunately, this problem can be mitigated by the use of more radiation-resistant substrate materials like sapphire to prepare thin films destined for observation by TEM.

3.4 Chemical Analysis

Finally, in this section we turn to a number of techniques that have been used in this thesis to elucidate the chemical makeup of TCO thin films.

3.4.1 Energy-dispersive X-ray Spectroscopy

Energy-dispersive X-ray Spectroscopy (typically abbreviated EDS or EDX) uses excitation of a sample caused by energetic electrons to determine its elemental composition. These instruments are usually integrated into an electron microscope to take advantage of the ready source of energetic electrons.

When electrons in an incident beam have enough energy to do so, core electrons can be ejected from the atoms in the sample.[vi] These core holes are quickly refilled by the relaxation of higher energy electrons, which is sometimes accompanied by the emission of an X-ray photon with appropriate energy to compensate for the energy of the transition. Because atoms of each element have a characteristic core electronic structure with energy levels that are little perturbed by chemical environment, each element will generate X-rays with a characteristic set of energies and probabilities that can be indexed against its possible electronic transitions.

With a detector able to count emitted X-rays as a function of energy, it then becomes possible to identify the presence and concentration of an element by looking for its characteristic pattern of X-ray emissions. Modern EDX spectrometers are generally capable of detecting all elements heavier than carbon, with signal strength and quantitative accuracy improving as the elements become heavier. Detection limits can vary widely depending on experimental conditions, but 0.1 at% is often a reasonable estimate in the absence of more specific information.[39,40]

When this capability is coupled with an electron microscope, which allows precise aiming of the incident electron beam, a spatially resolved map of a sample's chemical composition can be obtained. However, in a SEM which uses thick samples, it is extremely important to keep in mind that even a tightly focused electron beam will interact with a relatively large teardrop-shaped volume of material within the bulk of the sample (Figure 3.12). The exact volume of interaction depends on the microscope accelerating voltage and properties of the material under study, but characteristic X-rays can be detected from a depth of greater than $\sim 10\,\mu$m in some cases.

This has obvious implications for the study of thin films which may only be a few hundred nanometers thick. Care must be taken to select a low enough accelerating

[vi] When the electron energy is insufficient, only a continuous spectrum of *Bremsstrahlung* or braking radiation will be observed, which results from the deceleration of the incident electrons.

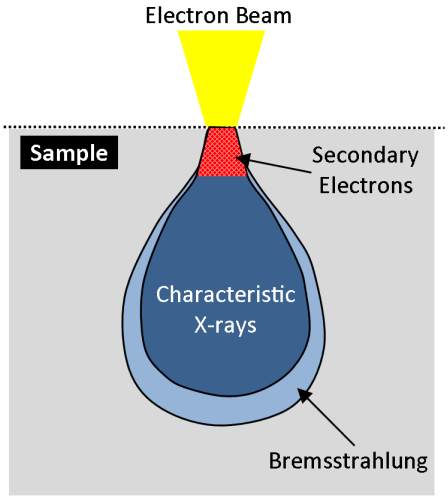

Figure 3.12: Schematic showing teardrop-shaped interaction volume of an electron beam with a thick sample (like in a SEM). Characteristic X-rays and continuum Bremsstrahlung radiation are generated from a significant volume of the bulk, perhaps as deep as $\sim 10\,\mu$m in some circumstances. The secondary electrons used for SEM imaging only escape from the top few tens of nanometers. Other products of electron-sample interaction such as backscattered or Auger electrons are not shown.

voltage to minimize signal from the substrate, all while keeping the voltage high enough to generate a sufficient intensity of characteristic X-rays from the elements of interest in the sample. In cases where these constraints cannot both be satisfied, the only option is to use a substrate containing neither the elements of interest nor those producing any interfering signals.

Because TEM uses very thin samples and very high energy electrons, there is limited opportunity for electron scattering as the beam passes through. Thus, such a significant interaction volume does not develop. In this way, EDX coupled with TEM is indeed able to achieve spatial resolution similar to the electron spot size.

It is possible to use EDX to quantify the relative concentration of various elements in a sample by deconvoluting their contributions in the full experimental spectrum. However, the signal intensity for different elements can vary with the physical characteristics of the sample, such as surface roughness. As such, the most precise quantification is generally only possible if a calibration curve can be developed based on similar samples of known composition. Since it was not possible to prepare such reference TCO samples, the EDX analyses presented in this thesis should be assessed with this caveat in mind. In the absence of well-defined references, accuracy of around

a percent of value is generally considered reasonable for heavier elements, whereas the values for lighter elements like oxygen are probably less reliable.

3.4.2 X-ray Photoelectron Spectroscopy

X-ray Photoelectron Spectroscopy (XPS) is in some sense the inverse measurement of EDX. XPS uses an incident photon with known energy and measures the energy of photoelectrons ejected from the sample after an inelastic scattering event. XPS results are typically expressed in terms of binding energy using

$$E_{\text{binding}} = h\nu - (E_{\text{kinetic}} + \phi)\,, \tag{3.22}$$

where E_{binding} is the binding energy between the electron and the material, $h\nu$ is the energy of the incident X-ray photon, E_{kinetic} is the measured kinetic energy of the photoelectron, and ϕ is a correction term combining the work function of the sample and the transmission characteristics of the spectrometer.

In XPS, the binding energies are not only a function of the element's identity and the orbital from which the photoelectron is ejected, but also the chemical environment of the atom. For instance, the more electron-rich an atom, the more shielded and loosely bound will be its electrons. In this way, XPS not only allows the identification and quantification of which elements are present, but also provides information on their chemical state. This is often done by comparing experimental binding energies to those observed for appropriately chosen reference materials, and by consultation of the extensive tables of binding energies for common species that have been compiled in various references.[41]

XPS can also be used to measure electrons which are not directly associated with specific nuclei, a notable example being electrons in the loosely bound valence states near the bandgap. This serves as a direct experimental measure of the density of these occupied states. While XPS generally does not have the energy resolution to resolve specific defect states, these data can still be used to infer broader changes in valence band structure.[42,43]

Because XPS relies on the emission of electrons rather than X-rays from the sample, the technique is surface sensitive. In typical configurations, almost all photoelectrons are emitted from the top ∼5–10 nm of the sample. Further surface specificity

can be achieved by using grazing angles of incidence.[44] Thus, when combined with a method for gradually etching the surface to be analyzed (such as an argon ion gun), XPS is also very useful for determining sample composition as a function of depth within the sample.[45]

Quantification and Data Fitting

While data tables for approximate binding energies are readily available, the values obtained from different instruments are not directly comparable and energy corrections on the order of a few eV must be made for each spectrometer configuration. The presence of adventitious surface carbon is more or less a certainty on any TCO sample exposed to air, and the resulting main carbon 1s peak at a binding energy of 284.7 ± 0.2 eV often serves as a convenient internal reference.[46] Alternatively, external references such as a high purity metal foil (freshly etched in high vacuum to remove oxidation) or a metal oxide are often also suitable.

Having aligned spectra in energy, an appropriate background function must be selected prior to analysis of peaks. The three most common choices are 1) a simple linear background, 2) the Shirley algorithm which infers a background based on changes in the data,[47] or 3) the Tougaard universal cross-section which assumes that the experimental data is a convolution of a background function defined over all energies and the contributions from the signal.[48] In practice, none of these (or any other) backgrounding approaches has a theoretical basis, and selection of a background function is more or less a matter of avoiding "obviously wrong" choices rather than trying to find a single "correct" one.

A general XPS signal resulting from electrons in a given orbital of a given element will be a combination of multiple signals. For orbitals with non-zero angular momentum ℓ (*i.e.*, p, d, and f orbitals), coupling of ℓ with the net electron spin s created by loss of an electron from a filled orbital (spin-orbit coupling) leads to spin-orbit splitting of the XPS signal for that orbital into a doublet. These two signals are typically labeled by the total angular momentum j of the final state. For instance, a 3d signal will split into $3d_{3/2}$ and $3d_{5/2}$ because the spin-orbit coupling of $\ell = 2$ and $s = 1/2$ gives rise to $j = 3/2$ and $j = 5/2$ states, with the latter case leading to the lower binding energy peak.

Each spin-orbit split peak will itself contain multiple signals, each reflecting a different chemical state of that element in the sample. While the chemical shifts can sometimes be large enough to fully resolve separate signals, in many practical cases the shifts are much more subtle and a deconvolution procedure must be carried out in order to determine the relative contribution of the individual, overlapping components.

The theoretical shape and width of the individual signal components is a rather complicated subject. While there is a theoretical basis for asymmetric lineshapes in some materials, the use of such models is fraught with difficulties and pitfalls, principally because the area beneath common asymmetric functional forms is ill-defined.[49,50] This makes the quantification of signal intensity by simple integration impossible without use of known reference standards. For the types of chemical analysis undertaken in this thesis and indeed most routine work, it is adequate to assume that XPS signal components have a symmetric Voigt lineshape. The Voigt lineshape is a convolution of Gaussian components, mostly related to the measurement process, and Lorentzian components, due to time-energy broadening in the samples.

In deconvoluting the experimental signal into components, the full widths at half maximum (FWHM) of the components are generally constrained to be equal. This follows from the reasonable assumption that chemical environment will not significantly alter the broadening processes that contribute to signal width for a given element in a given spectrometer. An example of the results of such a deconvolution process is shown in Figure 3.13 for the adventitious carbon on the surface of a ZnO thin film. The largest component centered at 284.7 eV can be assigned as aliphatic carbons, while the higher binding energy signals at 286.3 eV and 288.6 eV are likely due to the more electron-deficient carbons singly and doubly bonded to oxygen, respectively.

Finally, once a satisfactory fit is obtained consistent with the constraints discussed above, the relative concentration of various components in samples can be determined by comparison of the integrated areas of their respective signals. When comparing signals originating from different orbitals or different elements, the raw peak areas must be scaled for differences in their X-ray inelastic scattering cross-sections. The most commonly used set of relative sensitivity factors necessary for quantification were calculated and tabulated by Scofield.[51]

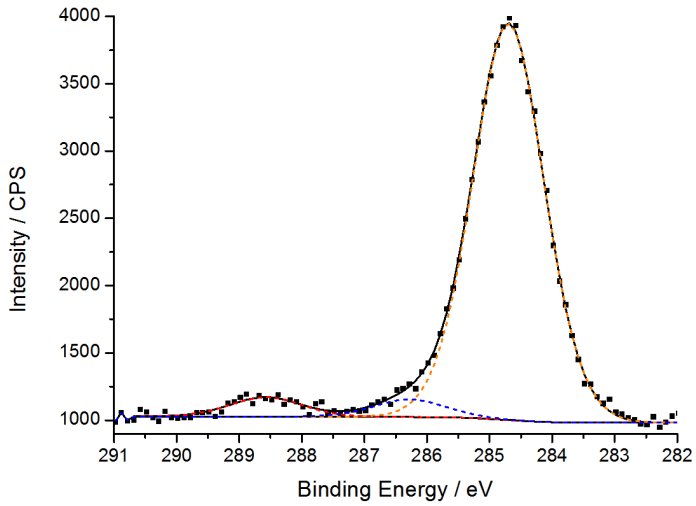

Figure 3.13: Example experimental C(1s) X-ray photoelectron spectrum of adventitious carbon on the surface of a ZnO film (square symbols). The fit to the experimental data (solid line) consists of 3 Voigt components (colored dashed lines). A Shirley background was used for this fit.

3.4.3 X-ray Absorption Spectroscopy

Basic Theory

In an X-ray absorption spectroscopy (XAS) experiment, the absorption of X-rays by a sample is measured as a function of the X-ray energy. An example of data from such a measurement is shown in Figure 3.14. As the energy of the incident X-rays increases, a sharp increase in absorption called an *edge* will be observed when the energy of the incident photon becomes enough to excite a particular electronic transition in the material. In the X-ray region of the spectrum, this is usually the ionization of a core electron; here specifically, it is the ionization of an electron from the K-shell of indium.

In addition to the absorption edge, a gradually decaying oscillation can be seen in the signal at energies above the edge. These oscillations are termed the X-ray Absorption Fine Structure (XAFS), and can be roughly divided into a X-ray Near-Edge Structure (XANES) region close to the edge and an Extended X-ray Absorption Fine Structure (EXAFS) region at still higher energies. While the physics that leads to these oscillations is the same for both regions, they are conventionally distinguished because the techniques needed to model and analyze the two are quite distinct.

When the X-ray photon ejects an electron from an atom, the photoelectron can be

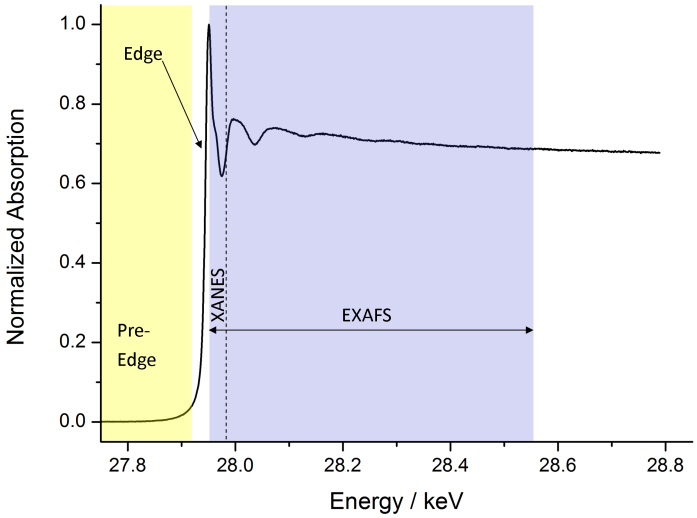

Figure 3.14: Normalized X-ray absorption spectrum near the In K-edge for a 12.5 at% indium-doped zinc oxide thin film. The pre-edge, edge, and XANES/EXAFS regions are indicated.

thought of as exiting as a spherical wave that can reflect off nearby atoms. XAFS oscillations arise because the reflected waves can interfere constructively or destructively with the outgoing wave at the site of the absorbing atom. Constructive interference increases the effective electron density at the absorbing atom, which is equivalent to less net absorption and photo-ionization. The opposite is true for destructive interference.

The nature of the interference at the absorbing atom therefore depends on its own chemical state and on its local environment, including factors like the identity, number, and distance of nearby atoms. The equation describing the signal $\chi(k)$ that results from this interference is

$$\chi(k) = S_0^2 \sum_i N_i \frac{f_i(k)}{kD_i^2} e^{\frac{-2D_i}{\lambda(k)}} e^{-2k^2\sigma_i^2} \sin(2kD_i + \delta_i(k)) \,, \tag{3.23}$$

where S_0^2 is the amplitude reduction factor. The sum is over scattering paths originating and ending at the absorbing atom. For the i^{th} of these paths being considered, N_i is the degeneracy, $f_i(k)$ is the scattering probability, D_i is the effective length, σ_i is the variance in path length, and $\delta_i(k)$ is the phase shift associated with the path. $\lambda(k)$ is the mean free path of the photoelectron. Where an absorber atom is present in multiple environments, the total signal will be a weighted sum of the contributions of

the scattering paths associated with each environment. Calvin provides an excellent pedagogical derivation of this formula.[52]

The $\exp(\frac{-2D_i}{\lambda(k)})$ term in Equation 3.23 is the reason that XAS is a method for characterizing *local* structure. Since the mean free path of a photoelectron is quite short, the exponential decay of signal intensity with increasing D_i means that nearby scatterers contribute far more to the observed signal than distant ones. Scatterers more distant than about 1 nm from the absorber are almost always negligible. Another implication is that long-range structure is not required for the development of a signal. Therefore, XAS can be equally applied to crystalline, nano-crystalline, amorphous, liquid, or even gaseous samples.

The distinction between EXAFS and XANES lies in the types of scattering paths that must be considered. Because EXAFS involves higher energy photoelectrons, the probability of each individual scattering event is relatively low, and $\chi(k)$ is dominated by paths involving only one (or perhaps two) scattering events. The number of significant scattering paths is thus small enough to make considering them individually practical. These discrete scattering paths can then be intuitively connected to the details of local structure around an absorbing atom. On the other hand, in XANES, the lower energy of the photoelectron makes the scattering probability higher. In this case, it is generally necessary to perform computationally expensive *full multiple scattering* calculations to adequately model this region of the XAFS data.

Reduction and Presentation of Data

For data analysis, raw absorption data are typically normalized to the height of the edge jump as shown in Figure 3.14. A background subtraction is then applied to extract the oscillating signal, with the point of maximum slope in the edge jump typically used as the zero of energy. The convention is then to present this extracted or "reduced" XAFS data as a function of k and then multiplied by some power of k. For example, $\chi(k)\cdot k^2$ extracted from Figure 3.14 is shown in Figure 3.15a. The power of k of course does not change the underlying data; it is generally used to compensate for the decay of the oscillation amplitude with increasing energy for the purposes of both presentation and data fitting.

It is also common to see XAFS data presented as the magnitude of the Fourier transform of a chosen range of $\chi(k)$, resulting in a quantity $|\chi(r)|$ having units of

distance (Figure 3.15b). Despite any potential resemblance, it is very important to note that $|\chi(r)|$ is *not* a radial distribution function. To produce a true radial distribution function, the contribution of multiple scattering paths must be removed and any phase shifts in the photoelectron wavefunction upon scattering accounted for. However, keeping these cautions in mind, $|\chi(r)|$ can sometimes be useful as a qualitative visualization because the peaks in the signal can be roughly correlated to coordination shells about the absorbing atom. Additionally, it should be remembered that the phase of $\chi(r)$ must also be considered along with $|\chi(r)|$ to retain all of the information that was originally present in $\chi(k)$.

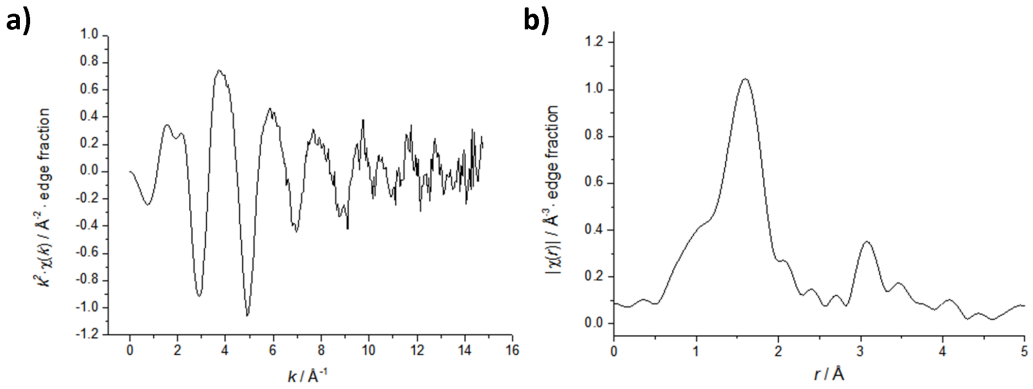

Figure 3.15: a) The XAFS signal extracted from Figure 3.14 after background subtraction and data reduction, plotted as a function of wave vector and with a k^2-weighting. b) Magnitude of the Fourier transform of the EXAFS signal from $k = 3$ to $13\,\text{Å}^{-1}$ using a Hanning window. The window is chosen to exclude the XANES region at low k and the excessively noisy data at high k.

Applying EXAFS to TCO Thin Film Characterization

In this work, we used the EXAFS region of XAS data to study the local structure around indium in indium-doped ZnO samples. Because the incident X-ray photon energy can be tuned to selectively excite a given absorbing element, XAS is an *element-specific* probe of local structure. This makes it almost uniquely suited for the study of a dilute element in a chemically distinct matrix, as is the case with the dopants added to modify the properties of transparent conductors. Substitutional impurities or nano-precipitates that would not be easily detected using techniques like XRD can be observed using XAS.

The signal intensity resulting from a dilute dopant will be low, particularly if the samples are in the form of a thin film that has a small total volume. A number of experimental refinements can assist with this problem, including the use of samples of a maximum reasonable thickness, the use of fluorescence detection instead of direct absorption measurements[vii], and the use of a grazing incident beam angle to maximize the volume of sample illuminated by the X-ray beam. Nevertheless, even with such methods, it is still necessary to use very intense synchrotron radiation in order to acquire a useful signal in a reasonable time period. Unfortunately, the limited availability of synchrotron time restricts the number of samples that can be studied using this technique.

Perhaps intuitively, there is not enough information in an EXAFS dataset to completely define a structure in the absence of any other information. Thus, a common approach for making use of EXAFS data relies on the fact that the inverse problem of simulating an EXAFS signal using a given structure and set of scattering paths requires only a straightforward application of Equation 3.23. This approach allows wrong models to be ruled out, and for surviving candidate structures to be further refined to better match experimental data.

When developing theoretical models for comparison with measured EXAFS data, one must keep in mind the information content of the experimental data. Clearly, if an infinite number of well-chosen parameters is used to define a model, any experimental dataset can be fitted with arbitrary accuracy but no physical significance. In EXAFS, an application of the Nyquist-Shannon theorem estimates the information content of a dataset as

$$N_{\mathrm{idp}} \approx \frac{2\Delta k \Delta r}{\pi} + 2\,, \tag{3.24}$$

where N_{idp} is the maximum number of independent parameters that can be defined by the data, and Δk and Δr are the range of k and r values used in the fit.[53] A chosen model is only likely to be unique and physically significant if the number of independent parameters used to define the model is less than N_{idp}.

[vii] Fluorescence is directly proportional to absorption.

3.5 Experimental

In this section, details are given of the specific implementations used in this thesis of the characterization techniques that have been discussed in general above.

3.5.1 Electrical Transport Measurements

Hall effect and resistivity measurements were typically performed with samples in the van der Pauw geometry using an Ecopia HMS-3000 Hall effect measurement system equipped with a 0.55 T permanent magnet. Indium solder was used to create four Ohmic electrical contacts of minimum size on the corners of an approximately 7 mm × 7 mm piece of a thin film TCO sample. Some samples were not of sufficient conductivity to allow reliable Hall effect measurements, and only resistivity could be determined. Where shown, error bars indicate the standard deviation of a measured property across a population of samples prepared using the same nominal conditions and procedures.

Hall effect measurements at temperatures below (to ∼80 K) and above (to ∼360 K) ambient temperature were achieved using the Ecopia instrument in concert with a custom-designed heating and cooling system. Sample temperatures were measured with a Type T thermocouple embedded in the sample mount and in contact with the back side of the film substrate.

Light-sensitive samples were allowed to equilibrate in the dark under open air prior to measurement.

Where the van der Pauw geometry was not used, for example in photoconductivity measurements, an approximately 10 mm × 2 mm rectangular piece of sample was used. Indium solder was used to create four electrical contacts along the long axis of the sample in an I+, V+, V−, I− configuration. The electrical resistance of the samples and changes therein due to various treatments were then measured and recorded by using an Agilent 34401A 6.5 digit multimeter in four-lead resistance mode. These resistance values could be converted to resistivity values if the starting resistivity of the sample was known from an independent van der Pauw measurement.

In cases where a rapid, qualitative assessment of a sample was useful, two handheld probes were pressed firmly onto the surface of a TCO sample allowing a two-lead resistance measurement to be made.

3.5.2 Optical Measurements

UV-Vis-NIR transmission spectra were collected from the samples using either Perkin-Elmer Lambda 19 or Lambda 950s spectrophotometers. A Varian Cary 5000 UV-Vis-NIR spectrophotometer with a V-W optical configuration was used for the collection of absolute specular reflectance spectra. A Mylar-protected aluminum mirror was used as a reflectance standard.

The envelope method of Swanepoel, as implemented using a custom Python 2 program (Appendix A), was used to estimate average visible transmittance and sample thickness from the interference fringes in the high transmission portion of transmission spectra. Other modeling of optical data and extraction of the optical transport properties of samples was carried out using the WVase32 software package.[30]

3.5.3 X-ray Diffraction

X-ray diffraction measurement of samples was performed using PANalytical X'Pert PRO diffractometers with Bragg-Brentano geometries. Fixed X-ray sources with an emission current of 40 mA and an anode voltage of 45 kV were used. The spectra were recorded using either monochromated Cu-$K_{\alpha 1}$ ($\lambda = 1.5406\,\text{Å}$) or Cu-$K_\alpha$ radiation, depending on the spectrometer used. Samples were placed on a 60 rpm spinner to improve averaging of crystallite orientation.

Pawley refinements were carried out either using the TOPAS software or GSAS with EXPGUI.[54]

3.5.4 Electron Microscopy

Scanning Electron Microscopy

The surface morphology of the thin films was characterized using a JEOL JSM-840F field emission scanning electron microscope at an accelerating voltage of 5 kV and using a secondary electron detector. Samples were affixed to an aluminum sample holder using conductive carbon cement (Leit-C) and then sputter coated with a ∼2.5 nm layer of platinum before observation in the SEM to reduce the effect of surface charging and attendant artifacts.

For cross-sectional SEM, samples were carefully cleaved after being scored from the back using a diamond scribe. The cleaved surface was affixed perpendicular to the electron beam using a specially designed and machined sample holder.

A JEOL JSM-5510LV microscope with a tungsten filament and equipped with an X-Act EDX (Oxford Instruments) spectrometer was used in high vacuum mode for elemental analysis of samples. The EDX instrument uses a silicon-drift detector for energy discrimination and uses the AZtec software package for data acquisition and processing.

Transmission Electron Microscopy

Cross-sectional TEM samples of TCOs were cut from thin films using a Zeiss NVision 40 FIB-SEM and mounted to a copper support grid *in situ* using a micro-manipulator. TEM/STEM images were collected using a JEOL ARM-200F aberration-corrected microscope with a 200 kV cold field-emission electron source.

3.5.5 X-ray Photoelectron Spectroscopy

XPS was carried out at the National EPSRC XPS Users Service (NEXUS) located at Newcastle University (Newcastle-upon-Tyne, UK). Thin film samples were studied both as received and after being etched to various depths using an argon ion gun. Low energy electrons from a flood gun were directed at the surface throughout analysis for charge neutralization.

Energy calibration was performed using either the main peak in the C(1s) spectra due to adventitious carbon or an appropriate elemental sample as a reference. Data analysis, including backgrounding, signal deconvolution, and quantification were carried out using the CasaXPS software suite.[55]

3.5.6 Acknowledgments

Several members of the David Cockayne Centre for Electron Microscopy at the Oxford University Department of Materials provided training and technical assistance, and operated the FIB and TEM equipment. Drs. Tayebeh Mousavi and Gareth Hughes operated the FIB equipment, while Drs. Neil Young and Rebecca Nichols operated

the TEM on my behalf. I am also grateful to Ms. Gabriella Chapman for training and guidance on the use of SEM and EDX equipment.

Dr. Josh Makepeace operated the TOPAS software that was used to perform some of the Pawley refinements on collected datasets.

Dr. Jose Portoles was responsible for directly running the XPS experiments described in this thesis as part of the National EPSRC XPS Users Service (NEXUS).

References

[1] Wolf, M. W.; Martin, J. J. *Phys. Status Solidi A* **1973**, *17*, 215–220.

[2] van der Pauw, L. J. *Philips Tech. Rev.* **1958**, *20*, 220–224.

[3] van der Pauw, L. J. *Philips Res. Repts.* **1958**, *13*, 1–9.

[4] Chew, W. C. *IEEE Trans. Antennas Propag.* **2008**, *56*, 970–975.

[5] Smits, F. M. *Bell Syst. Tech. J.* **1958**, *37*, 711–718.

[6] Hall, E. H. *Amer. J. Math* **1879**, *2*, 287–292.

[7] Ginley, D.; Hosono, H.; Paine, D. C. *Handbook of Transparent Conductors*; Springer: New York, NY, 2011.

[8] Swanepoel, R. *J. Phys. E: Sci. Instrum.* **1983**, *16*, 1214–1222.

[9] Duparré, A.; Kassam, S. *Appl. Opt.* **1993**, *32*, 5475–5480.

[10] Elson, J. M.; Rahn, J. P.; Bennett, J. M. *Appl. Opt.* **1983**, *22*, 3207–3219.

[11] Müller, J.; Rech, B.; Springer, J.; Vanecek, M. *Sol. Energy* **2004**, *77*, 917–930.

[12] Ruske, F.; Jacobs, C.; Sittinger, V.; Szyszka, B.; Werner, W. *Thin Solid Films* **2007**, *515*, 8695–8698.

[13] Shinagawa, T.; Shibata, K.; Shimomura, O.; Chigane, M.; Nomura, R.; Izaki, M. *J. Mater. Chem. C* **2014**, *2*, 2908–2917.

[14] Billmeyer, F. W.; Chen, Y. *Color Res. Appl.* **1985**, *10*, 219–224.

[15] Manifacier, J. C.; Gasiot, J.; Fillard, J. P. *J. Phys. E: Sci. Instrum.* **1976**, *9*, 1002–1004.

[16] Poelman, D.; Smet, P. F. *J. Phys. D: Appl. Phys.* **2003**, *36*, 1850–1857.

[17] González-Leal, J.-M.; Prieto-Alcón, R.; Angel, J.-A.; Minkov, D. A.; Márquez, E. *Appl. Opt.* **2002**, *41*, 7300–7308.

[18] Swanepoel, R. *J. Phys. E: Sci. Instrum.* **1984**, *17*, 896–903.

[19] Tauc, J.; Grigorovici, R.; Vancu, A. *Phys. Status Solidi B* **1966**, *15*, 627–637.

[20] Nakajima, A.; Sugita, Y.; Kawamura, K.; Tomita, H.; Yokoyama, N. *J. Appl. Phys.* **1996**, *80*, 4006–4011.

[21] Hamberg, I.; Granqvist, C. G. *J. Appl. Phys.* **1986**, *60*, R123–R160.

[22] Ehrmann, N.; Reineke-Koch, R. *Thin Solid Films* **2010**, *519*, 1475–1485.

[23] Pflug, A.; Sittinger, V.; Ruske, F.; Szyszka, B.; Dittmar, G. *Thin Solid Films* **2004**, *455456*, 201–206.

[24] Mergel, D.; Qiao, Z. *J. Phys. D* **2002**, *35*, 794–801.

[25] Hassing, S.; Mortensen, O. S. *J. Chem. Phys.* **1980**, *73*, 1078–1083.

[26] Sharnoff, M. *Am. J. Phys.* **1964**, *32*, 40–44.

[27] Synowicki, R. A. *Thin Solid Films* **1998**, *313314*, 394–397.

[28] Ruske, F.; Pflug, A.; Sittinger, V.; Szyszka, B.; Greiner, D.; Rech, B. *Thin Solid Films* **2009**, *518*, 1289–1293.

[29] Brewer, S. H.; Franzen, S. *J. Alloys Compd.* **2002**, *338*, 73–79.

[30] Johs, B.; Herzinger, C.; Guenther, B.; *WVase32: Ellipsometry Analysis Software*; 2004.

[31] Bragg, W. L. *Proc. Cambridge Philos. Soc.* **1913**, *17*, 43–57.

[32] Pecharsky, V.; Zavalij, P. *Fundamentals of Powder Diffraction and Structural Characterization of Materials*; Springer: New York, NY, 2009.

[33] Langford, J. I.; Lour, D.; Scardi, P. *J. Appl. Crystallogr.* **2000**, *33*, 964–974.

[34] Patterson, A. L. *Phys. Rev.* **1939**, *56*, 978–982.

[35] Langford, J. I.; Wilson, A. J. C. *J. Appl. Crystallogr.* **1978**, *11*, 102–113.

[36] Holzwarth, U.; Gibson, N. *Nat. Nanotechnol.* **2011**, *6*, 534–534.

[37] Hanawalt, J. D.; Rinn, H. W.; Frevel, L. K. *Ind. Eng. Chem., Anal. Ed.* **1938**, *10*, 457–512.

[38] Pawley, G. S. *J. Appl. Crystallogr.* **1981**, *14*, 357–361.

[39] Eggert, F. *Microchim. Acta* **2006**, *155*, 129–136.

[40] Tsuji, K.; Spolnik, Z.; Wagatsuma, K.; Nullens, R.; Grieken, R. V. *Microchim. Acta* **2000**, *132*, 357–360.

[41] Crist, B. V. *Handbook of monochromatic XPS spectra: The elements and native Oxides*; XPS International, Inc., 1999; Vol. 1.

[42] Yu, H. Y.; Feng, X. D.; Grozea, D.; Lu, Z. H.; Sodhi, R. N. S.; Hor, A.-M.; Aziz, H. *Appl. Phys. Lett.* **2001**, *78*, 2595–2597.

[43] Scanlon, D. O.; Dunnill, C. W.; Buckeridge, J.; Shevlin, S. A.; Logsdail, A. J.; Woodley, S. M.; Catlow, C. R.; Powell, M. J.; Palgrave, R. G.; Parkin, I. P.; Watson, G. W.; Keal, T. W.; Sherwood, P.; Walsh, A.; Sokol, A. A. *Nat. Mater.* **2013**, *12*, 798–801.

[44] Gelius, U.; Wannberg, B.; Baltzer, P.; Fellner-Feldegg, H.; Carlsson, G.; Johansson, C. G.; Larsson, J.; Münger, P.; Vegerfors, G. *J. Electron Spectrosc. Relat. Phenom.* **1990**, *52*, 747–785.

[45] Oswald, S.; Reiche, R. *Appl. Surf. Sci.* **2001**, *179*, 307–315.

[46] Barr, T. L.; Seal, S. *J. Vac. Sci. Technol., A* **1995**, *13*, 1239–1246.

[47] Shirley, D. A. *Phys. Rev. B* **1972**, *5*, 4709–4714.

[48] Tougaard, S. *Surf. Interface Anal.* **1997**, *25*, 137–154.

[49] Doniach, S.; Sunjic, M. *J. Phys. C: Solid State Phys.* **1970**, *3*, 285–291.

[50] Hughes, H. P.; Scarfe, J. A. *J. Phys.: Condens. Matter* **1996**, *8*, 1421–1438.

[51] Scofield, J. H.; *Theoretical photoionization cross sections from 1 to 1500 keV*; Tech. Rep. UCRL-51326; University of California, Lawerence Livermore National Laboratory; 1973.

[52] Calvin, S. *XAFS for Everyone*; CRC Press: Boca Raton, FL, 2013.

[53] Farrow, C. L.; Shaw, M.; Kim, H.; Juhás, P.; Billinge, S. J. L. *Phys. Rev. B* **2011**, *84*, 134105.

[54] Larson, A. C.; Von Dreele, R. B.; *General Structure Analysis System (GSAS)*; Tech. Rep. LAUR 86-748; Los Alamos National Laboratory; 2000.

[55] Fairley, N.; *Computer Aided Surface Analysis for X-ray Photoelectron Spectroscopy (CasaXPS)*; 2009.

Chapter 4

Preparation of TCOs by Spray Pyrolysis

A stable and well-characterized platform for the preparation of samples is surely an essential component of any experimental campaign. However, there are few cases where this maxim is as acutely true as in the study of the transparent conducting oxides.

Because the uses for TCOs require that they be prepared as thin films, samples are strongly affected by surface and morphological effects. Similarly, since the properties of a TCO are heavily influenced by the concentration and type of defects present, the properties of a thin film can change markedly with varying degrees of non-stoichiometry and the presence of impurities, whether intentionally introduced or not. All of these are potentially sensitive functions of the choice of technique and the exact conditions used for sample deposition.

As was the case for the characterization techniques discussed in Chapter 3, a comprehensive discussion of all TCO deposition methods is well beyond the scope of this thesis. The emphasis here will instead be on the many varied considerations that go into the design, implementation, and use of a spray pyrolysis process, which was the primary thin film deposition technique chosen for this work. Where observations about spray pyrolysis parameters provide useful insights on performance limitations in TCO thin films, the main topic of this thesis, only a brief comment will be made in this chapter. A more detailed discussion will follow in Chapters 5–7, which are directly aimed at tackling these questions.

4.1 Spray Pyrolysis in Context

Since the report by Badeker in 1907 of the preparation of a CdO transparent conductor by the thermal oxidation of a thin cadmium layer,[1] a wide range of preparative techniques have been developed for the deposition of TCO thin films. The vast majority of samples studied in this thesis were prepared using spray pyrolysis. However, before undertaking a detailed discussion of this technique, it may be useful to place it in context amongst several other key thin film deposition techniques.

For this purpose, the three techniques that have been used to prepare samples for the present work will be briefly introduced: pulsed-laser deposition (PLD), sputtering, and finally, spray pyrolysis itself.

4.1.1 Pulsed-laser Deposition

Pulsed-laser deposition (PLD) is a physical deposition process where a target material is vaporized and ionized by high energy laser pulses (typically from an excimer laser) inside a vacuum chamber. Energetic particles thus ejected from the target can then fly through the chamber to a substrate, where they deposit to form a thin film of material.[i] A schematic of a PLD apparatus is shown in Figure 4.1a.

The target is typically a solid piece of the desired material, prepared using any of a variety of ceramics processing techniques such as slip-casting or the pressing and sintering of powders. However, it is also possible to introduce reactive gases into the vacuum chamber so that the target particles are chemically modified in flight, or after they impact the substrate. In this way, for example, TCO films can be prepared from metallic targets by the controlled introduction of oxygen into the apparatus, or doped films by introduction of the dopant element in a gaseous form.

The physics of laser-target and particle-substrate interactions are in general very complex, and the properties of deposited films depend sensitively on process parameters like the laser power and energy, the pressure and composition of atmosphere within the chamber, the substrate surface temperature, and the choice of substrate material.[4] When chosen correctly, such parameters give the PLD process substantial flexibility, making it possible to deposit TCO samples over a wide stoichiometric

[i] Good general overviews of PLD have been published by Lorenz[2] and Ashfold, *et al.*[3]

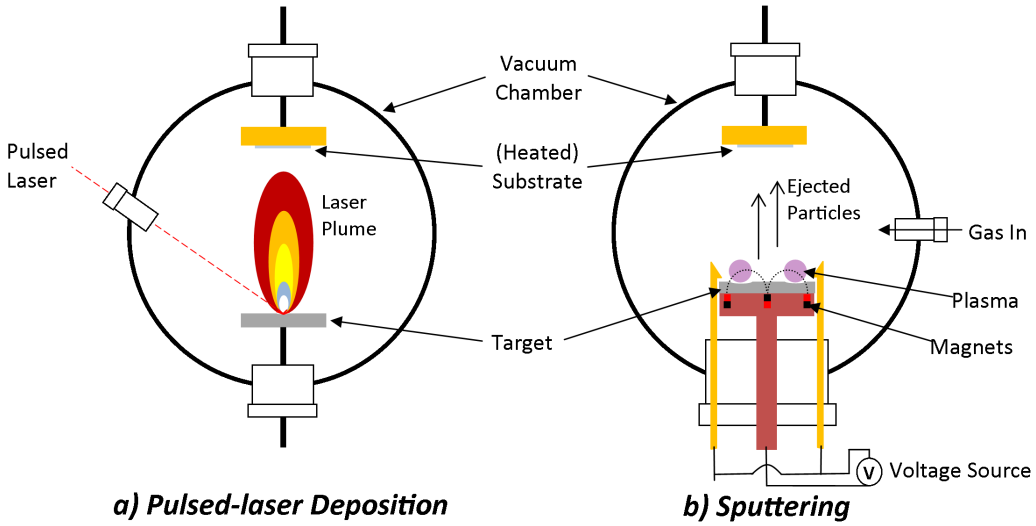

Figure 4.1: Schematic of generic a) pulsed-laser deposition (PLD) and b) sputtering setups.

range, and across a full spectrum of micro-structures from amorphous to polycrystalline to epitaxial.

Because deposition occurs inside a vacuum chamber with a carefully controlled atmosphere, the process is very clean and excellent compositional control can be achieved. Furthermore, the lasers typically used have power densities high enough to effectively vaporize the surface of a target, potentially making the process relatively insensitive to target inhomogeneities resulting from ceramics processing. For these reasons, PLD has a reputation for being able to produce extremely smooth, dense, and high-quality TCO films, sometimes possessing optoelectronic properties close to what would be expected from a single crystal of the bulk material. The ability to prepare epitaxial and amorphous films is also of substantial interest to fundamental studies of electronic transport in TCOs.

However, the localized nature of a focused laser pulse fundamentally limits the size of the uniform deposition area that can be achieved by PLD. Furthermore, the overall energy efficiency of high-powered lasers is quite low.[2] For such reasons, the cost and complexity of scaling a PLD process for large-area deposition is prohibitive. PLD remains principally a valuable tool for laboratory-scale research in solid-state physics and materials science, but has not yet found significant use in large-scale industrial applications.

4.1.2 Sputtering

Sputtering is similar to PLD in that it relies on the transfer of material from a solid target to a substrate inside a vacuum chamber.[ii] However, in sputtering processes, charged particles from a plasma bombard the target surface and result in the ejection of particles. The plasma is created when gas (often a noble gas, like argon) introduced into the chamber at low pressure is subjected to strong electric fields from either a RF or DC voltage source. The plasma is then confined near the surface of the target using a magnetic field to enhance the sputtering rate. The ejected target particles can then form a film after reaching a substrate by either ballistic or diffusive transport, depending on the gas pressure in the chamber. This is shown schematically in Figure 4.1b.

The target ablation in a typical sputtering process is less energetic than in PLD, and complete vaporization of the target material does not usually occur. This means that sputtering deposition processes tend to be more sensitive to the quality and homogeneity of the ceramic target. However, compared to PLD, sputtering can be readily scaled up by appropriate design of the electric and magnetic fields to allow uniform plasma bombardment of large area targets. Sputter deposition also retains the advantage of occurring in a closed vacuum system, which allows for a clean, controllable process.

Despite the high cost of large vacuum systems and power supplies, the fact that sputtering techniques can be used reliably on a very large scale makes them the current industry standard for the preparation of TCO films, particularly those made of ITO. For materials of interest, both the preparation of targets and the deposition processes themselves have been heavily optimized for cost and performance. Thus, from the point of view of TCO research, this makes sputtering and the films it produces the standard against which all other scalable deposition processes are compared.

As might be imagined, a large number of refinements and optimizations of this basic technique are possible. Some examples include field modifications that allow the plasma to bombard and modify growing films,[9] enhanced control of target utilization by the use of remote plasmas,[10] and the use of very high power densities at low duty

[ii] Numerous reviews and texts providing further detail on various aspects of sputtering techniques are available. A small selection of sources is listed here.[5–8]

cycles to modify the microstructure of deposited films and to decrease the influence of target condition.[11]

4.1.3 Spray Pyrolysis

Spray pyrolysis is quite different from the two vacuum-based deposition techniques previously mentioned. It operates at atmospheric pressure and formation of an oxide film results from the thermal decomposition of a precursor solution upon interaction with a heated substrate.[iii] In contrast to sputtering and PLD, spray pyrolysis can be carried out using very simple and inexpensive equipment. On top of this, fast deposition rates are readily achievable over very large areas. Given these features, it is not surprising that spray pyrolysis has long been lauded as a low-cost and highly scalable alternative to sputtering.

The fact that spray pyrolysis is solution-based means that TCOs with a wide range of chemical compositions can be easily and flexibly prepared simply by using different precursor solutions. Indeed, the ability to deposit a continuous range of compositions on demand by appropriate mixing of precursor solutions makes spray pyrolysis almost uniquely suited as a tool for materials discovery and combinatorial studies. All of these features stand in stark contrast to most laboratory setups for sputtering or pulsed-laser deposition, where the time-consuming process of ceramic target preparation must be repeated for each different composition to be studied.

Spray pyrolysis does have several potential limitations. The use of solvents and atmospheric pressure makes it a fundamentally less well-controlled process, especially when compared with the hermetically sealed chambers and carefully regulated atmospheres used in sputtering. Similarly, starting from salts which must decompose instead of pure oxides or metals can possibly introduce undesired contaminants to a TCO film if the deposition conditions are not chosen carefully.

Another key limitation is that spray pyrolysis depends on the thermal decomposition of precursors using a heated substrate. The high temperatures that are generally required for complete decomposition of common precursors restrict the range of possible substrate materials, for instance, precluding the use of the flexible polymer substrates that would be desirable in a number of emerging TCO applications.[17]

[iii] Spray pyrolysis has been reviewed in general by a number of authors.[12–16]

Nevertheless, the simplicity, speed, and flexibility of spray pyrolysis makes it extremely well-suited for high-throughput laboratory research focused on multiple materials. These are some of the major reasons that have led us to choose spray pyrolysis as the main TCO deposition technique for this work.

While spray pyrolysis is indeed fast, flexible, and conceptually straightforward, it must be recognized that the properties of prepared samples depend heavily on choices made regarding the hardware and deposition conditions. We have found that carelessness, even regarding variables that might initially seem insignificant, can sometimes lead to such large experimental errors and variance in optoelectronic properties as to render results useless. Of course, this is true to a large extent for all thin film deposition techniques, and it is probably safe to suggest that the wide scatter in results that makes the existing body of TCO literature difficult to interpret is either due to failure to control important experimental variables, or at the very least, a lack of process standardization across different research groups.

Over the course of efforts to develop a reproducible and reliable spray pyrolysis process, we have gained a fair bit of insight into which parameters contribute most significantly to a successful film deposition and also where engineering improvements and further research would be of benefit to such work in the future. The following sections will step through the spray pyrolysis process as we have used it with the goal of documenting this accumulated knowledge. Included among the observations here are several on non-obvious prerequisites to a successful deposition that, to the best of our knowledge, seem to have been thus far overlooked by the broader research community.

4.2 Spray Pyrolysis Hardware

A simplified drawing illustrating key features of the apparatus is shown in Figure 4.2. More detailed descriptions of this equipment and other associated hardware used are available in Appendix C.

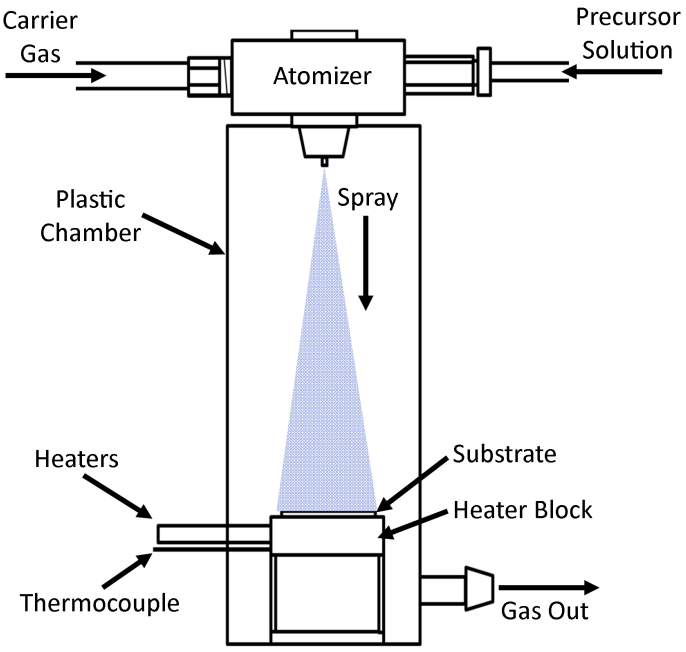

Figure 4.2: Simplified schematic of spray pyrolysis apparatus used in this work. More detailed descriptions of this equipment are available in Appendix C.

4.2.1 Solution Atomization and Gas Control

Any spray pyrolysis system must be able to deliver a precursor solution as a spray of fine droplets. In this design, a pneumatic spray nozzle is used wherein liquid supplied to the nozzle by a pump at a controlled rate is sheared into small droplets by a jet of pressurized gas.

The flowing gas also serves other key functions. It actively carries droplets downwards into the chamber and toward the substrate, improving deposition efficiency. The gas also acts a coolant, allowing the use of a plastic chamber despite the high temperature of the substrate and heater block. Importantly, the gas flowing through the nozzle also actively purges the spray chamber and is used to maintain a slight positive pressure of the desired atmosphere (whether inert, reducing, or oxidizing), removing the need for the chamber to be hermetically sealed. This does require, however, that the deposition chamber be used inside a fume hood.

Water-sensitive paper has been used to characterize the spray pattern of the chosen nozzle. At the chosen nozzle-substrate distance of $\sim$30 cm, the area of uniform spray is substantially larger than the 24 mm $\times$ 32 mm substrates typically used. Changes in the rate of solution delivery and carrier gas flow do subtly change the spray pattern

from the nozzle. However, while the solution supply rate influences deposition rate in an approximately linear fashion, testing has shown that variation of these parameters (within fairly loose bounds) does not substantially affect the intrinsic properties of a prepared film.

Other nozzle designs exist which can be used to distribute spray solution over a wider area. Ultimately, though, scaled-up spray pyrolysis systems will either incorporate multiple spray nozzles or relative motion between nozzle and substrate to achieve uniform, large-area deposition.

It is also possible to use an ultrasonic atomizing nozzle, in which a vibrating piezoelectric is used to produce small droplets from a stream of precursor solution. However, such an atomizer was not used in the apparatus here for several reasons. First, efficient atomization without the formation of any large droplets requires precise tuning of ultrasonic power and frequency for each chosen solvent mixture; finding suitable parameters was time-consuming and not always possible given the limits of the ultrasonic generator available. Second, the other essential functions of gas flow are not an intrinsic part of an ultrasonic nozzle's design and would need to be separately designed into the system, thus adding unnecessary complexity.

4.2.2 Substrate Heater Assembly

To heat the substrates, a stainless steel block is equipped with two removable cartridge heaters. Temperature control is achieved using a feedback loop consisting of a type K thermocouple inserted into the geometric center of the block and a PID controller. A substrate is held against the top surface of the block by the weight of a steel frame. The frame also acts as a mask for defining the area upon which the film is deposited.

The temperature in the system most relevant to the TCO deposition process is that of the substrate surface (or the top of a growing film). Clearly, the substrate surface will be substantially cooler than the center of the heated block, especially given the cooling flow of carrier gas from the spray nozzle. Direct measurements of substrate surface temperature during deposition were not possible because of the difficulty of forming small, but reliable thermal contacts on a disposable glass substrate. Furthermore, the IR absorption of the aqueous spray prevented the use of contactless temperature measurements during actual deposition procedures.

Table 4.1: Approximate factors for conversion of heater setpoint temperature T_{heater} to substrate surface temperature T_{sub} for various substrate materials, as determined using optical pyrometer measurements.

Material	Thickness / mm	Assumed Emissivity (8–14 μm)	$T_{\text{sub}}/T_{\text{heater}}$
D263T Borosilicate	0.17	0.91	0.834
D263T Borosilicate	2.0	0.91	0.751
Sapphire	0.5	0.84	0.809
SiO_2 on Si	0.5	0.90	0.773
Kapton^{TM} HN	0.025	0.74	0.944

Instead, an optical pyrometer was used in a series of calibration experiments to determine the surface temperature at the center of the substrate (T_{sub}) as a function of the heater setpoint temperature (T_{heater}) in the absence of liquid spraying but with the carrier gas on. This procedure was carried out with substrates of various thicknesses and materials to cover the full range of substrate types used in this thesis. For these measurements, no attempt was made to correct for the possibility of temperature-dependent emissivity in substrate materials. The relationship between T_{sub} and T_{heater} was found to be almost exactly linear in all cases measured and the approximate conversion factors are listed in Table 4.1. It should be noted that the equilibrium surface temperature across the entire substrate was found to vary by as much as $\pm 7\,^{\circ}\text{C}$; this variation should be kept in mind whenever sample deposition temperatures are considered.

Throughout this thesis, the reported deposition temperature will be that of the center of the substrate surface as derived from T_{heater} using the appropriate conversion factor. In literature reports on TCO deposition by spray pyrolysis, it is rarely made clear from where and how reported deposition temperatures are being measured. Given that the differences between T_{sub} and T_{heater} in this system are more than enough to lead to substantial changes in the properties of deposited TCO samples (Section 4.4.1), ambiguity in the reporting of deposition temperatures is one of the major standardization problems in this field that makes direct comparison of results

from various groups challenging.

From the standpoint of film-to-film reproducibility, the substrate heater assembly is one of the most problematic aspects of this spray pyrolysis system. Because the heater cartridges were designed to be removable for easy cleaning between deposition runs, it was impossible to maintain perfectly consistent thermal contact between the cartridges and the heater block. Perhaps even more significantly, at higher deposition temperatures, it was found that differential thermal expansion and/or strain release would sometimes lead to warping (and breakage) of glass substrates, which also reduced the consistency of thermal contact between the substrate and the heater block. Since the temperature is regulated from the center of the heater block and not from the substrate surface, the PID controller cannot compensate for such variations in thermal contact.

Because of the fact that variations introduced by these inconsistencies were usually manageable, no attempt was made to redesign the substrate heater assembly to address these problems. However, it is likely that such problems with thermal uniformity will be magnified by any attempt to scale up spray pyrolysis. Thus, the consistent and uniform heating of substrates will be a key engineering challenge for any future attempts to develop this technique into a commercially relevant process.

4.2.3 Substrate Selection

The chosen substrate material clearly must be physically and chemically compatible with the rest of the deposition process. The first and most commonly considered factor is temperature stability. For example, most common plastics melt or decompose at temperatures well below those required to cleanly decompose standard TCO precursors, and thus cannot be used as spray pyrolysis substrates.[18] The polyimides are an exception among commonly available plastics in that they remain stable up to ~350 °C and can be used for the deposition of some TCOs. Unfortunately, most polyimides are strongly yellow- or orange-colored, and as such are not practically useful as substrates in most applications. Recently, several types of ultra-thin glass (including Schott's eco^{TM} and Dow Corning's Willow^{TM}) have been marketed as temperature-resistant and (moderately) flexible alternatives to plastics. However, the challenges

of handling large sheets or rolls of ultra thin glass have so far limited their market penetration as TCO substrates.[19]

Silicate glasses are a common substrate material for many optoelectronic applications, combining high transparency, good temperature stability, and low cost. Nevertheless, there are still reasons to be cautious when using glass as a spray pyrolysis substrate. In addition to the possibility of warping and breakage at higher process temperatures, attention must also be paid to the *chemical* stability of the glass. We have observed that ZnO films deposited on glass coverslips produced by two different manufacturers had entirely different properties, even though both substrates were nominally composed of "optical-grade borosilicate". Films deposited on our typical Schott D263T slides were highly conducting, while films deposited on"YaoHua" glass using identical conditions were several orders of magnitude less so. A dependence of film performance on glass type has also been previously reported by others.[20,21]

It has been observed that D263T substrates have a measurable electrical conductivity when heated above approximately 300 °C and it seems likely that substantial ion diffusion is occurring in these glasses at typical spray pyrolysis substrate temperatures. Common mobile ions in glass like Na^+ or K^+ would be expected to act as acceptors and suppress *n*-type conductivity if substituted at Zn sites in ZnO. Differing alkali metal ion mobilities and concentrations in various glass compositions may well explain this substrate-sensitive thin film behavior.[22]

In the course of this work, a number of different substrate materials in addition to the standard D263T, ∼0.17 mm thick cover slips have been used as substrates for spray pyrolysis deposition of TCOs, including *c*-axis oriented sapphire, thermally oxidized silicon, polyimide (DuPont Kapton^{TM} HN), and D263T eco^{TM} ultrathin glasses between 25 μm and 100 μm thick. The films deposited on all of these substrates had properties that were the same to within experimental error. In particular, the lattice mismatch of ∼16.7 % between *c*-axis sapphire and *c*-axis ZnO appears enough to prevent the substrate from significantly influencing preferred crystallite orientation or imposing epitaxial growth during spray pyrolysis, which have been reported by other authors when using better matched substrates, such as GaN (with a lattice mismatch of <2 %) and $ScAlMgO_4$ (0.09 %).[23–25]

Given this similarity in performance, we have elected to perform most of our depositions on D263T glass, except in specific cases where the use of an alternative substrate material would be beneficial. To give one example, sapphire substrates were useful for the chemical analysis of ZnO-based thin films because of interference caused by the zinc content of D263T.

Regardless of the choice of substrate, a cleaning procedure to remove dust and other surface contaminants is useful for improving process reliability and film quality. However, highly rigorous procedures sometimes reported in the literature, such as those involving plasma etching or complex multi-step washing procedures, have not been found to offer benefits over the simpler procedure that has been employed here. For routine spray pyrolysis, a short period of ultrasonic agitation in clean acetone, drying with non-abrasive lens tissue, and then dust removal with a blast of dry nitrogen is adequate to achieve reliable results.

4.3 Precursor Solutions

4.3.1 Precursor Screening and Selection

For the deposition of ZnO, the most commonly used precursors have been zinc carboxylates (mainly acetate, but also formate and propionate), followed by zinc acetylacetonate. Recent research in our group has demonstrated several additional classes of zinc salts that can be used for the spray pyrolysis deposition of ZnO, including zinc hydroxy ammines in basic solutions and zinc with ligands based on various acetylacetonate or β-keto ester derivatives. The use of zinc nitrate and zinc halides as precursors have also been reported by other groups.[26,27]

For the spray pyrolysis preparation of In_2O_3-based films, indium(III) chloride has been used with great success to produce ITO samples with electrical conductivities meeting or exceeding those seen in commercial sputtered samples.[20] In contrast, depositions using indium acetylacetonate and indium acetate as the primary indium source have generally not been successful. A hypothesis to explain this apparently contradictory behavior of zinc and indium precursors will be presented in Section 4.3.3.

Clearly, at a minimum, a precursor must decompose to form the desired oxide. It should further have an appreciable solubility in a "practical" solvent with reason-

able cost, low toxicity, and low corrosiveness. While this may seem self-evident, lack of solubility in common solvents has halted work on more than one new precursor possessing otherwise promising properties. While it is possible in principle to perform spray pyrolysis using a colloidal solution or fine suspension of precursor, we have avoided this approach whenever possible due to the additional complications in solution handling that this entails.

It is generally desirable that thermal decomposition of the precursor to oxide occurs at as low a temperature as possible. This allows the possibility of using lower process temperatures which might be compatible with flexible polymer substrates and which would lower the overall energetic costs of the deposition. However, as will be seen later, a low decomposition temperature to oxide does not by itself guarantee the formation of a *conductive* oxide thin film at that temperature.

Furthermore, it is usually desirable for the precursor to decompose to oxide by a mechanism where the ligand is lost as one or more volatile species, in order to prevent these ligand fragments from being inadvertently incorporated into the growing film. Although there are some scenarios where residual carbon from the incomplete volatilization of ligand might act as a beneficial dopant,[28,29] incomplete precursor decomposition is usually harmful to the optoelectronic properties of a film.

Wet and Dry Decomposition Mechanisms

The conventional practice has been to assess potential precursors as isolated solids using thermal analysis techniques like thermogravimetric analysis (TGA), TGA-MS, and variable-temperature X-ray diffraction (VT-XRD). There are such studies published on most common TCO precursors.[30,31] However, when using literature results to select spray pyrolysis precursors, it is essential to remember that the precursors will ultimately be decomposed from solution. As we shall demonstrate, "dry" and "wet" mechanisms for decomposition can be markedly different, with significant implications for the spray pyrolysis process.

Figure 4.3 shows the TGA of the decomposition of zinc acetate and indium(III) chloride under dry nitrogen, as in a conventional precursor screening measurement. When heated under these conditions, both precursors have appreciable volatility, leading to a final mass that is much less than the theoretical value expected for complete decomposition of each precursor to oxide.

After loss of crystalline waters, the extrapolated onset of mass loss for zinc acetate is just under 250 °C, and completed quickly thereafter. It can be seen that there is a "kink" in the zinc acetate mass loss, suggesting that two processes — decomposition and volatilization as the tetrameric "basic zinc acetate" — are occurring, each with slightly different onset temperatures.[32,33]

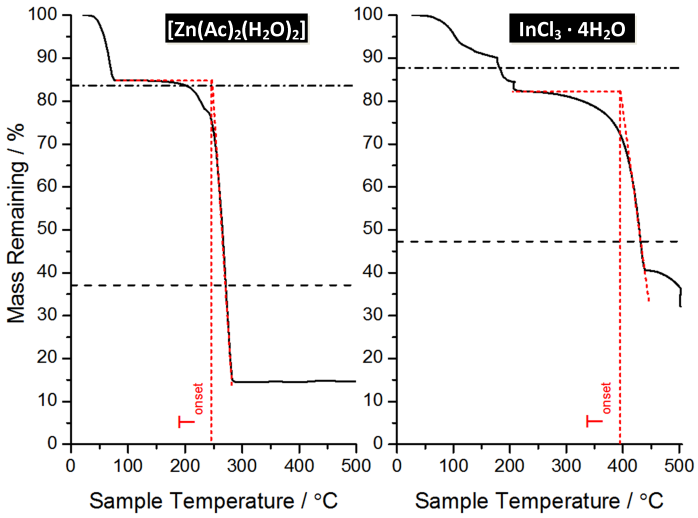

Figure 4.3: Thermogravimetric analysis of zinc acetate hydrate ($[Zn(Ac)_2(H_2O)_2]$) and indium(III) chloride hydrate ($InCl_3{\cdot}4H_2O$) under flowing N_2 at a heating rate of 0.75 K min^{-1}. The extrapolated onset temperature of each main mass loss signal (T_{onset}) is shown in red. The higher dash-dot line indicates the theoretical mass remaining after loss of water while the lower dashed line in each figure indicates the theoretical mass left after complete and exclusive decomposition of the precursor to the corresponding oxide.

For indium chloride, the extrapolated onset is not until nearly 400 °C and mass loss is not complete even after two hours at 500 °C, which is above the highest reasonable temperature for a spray pyrolysis process. It must be remembered that indium chloride is the well-characterized standard precursor for the deposition of In_2O_3 in this study, and that there is no doubt that it can be used to efficiently deposit In_2O_3 at much lower temperatures than these. The fact that the result in Figure 4.3 seems to give the wrong impression about the prospects of $InCl_3$ as a precursor is due to the inappropriate analysis conditions used. It seems sensible to assume that In_2O_3 (or perhaps InOCl) is forming slowly here because of the low oxygen levels in a nitrogen-purged instrument, whereas In_2O_3 can form rapidly at far lower temperatures in spray pyrolysis thanks to the ample supply of oxygen atoms in aqueous solutions.

As a further example of the risk in assessing spray pyrolysis precursors using classical "dry" analysis methods, a range of zinc carboxylates were thermally decomposed under vacuum using a Thermal Volatilization Analysis (TVA) apparatus at the University of Strathclyde.[34] The products of the decomposition over various temperature ranges were collected in liquid nitrogen cold traps. The cold traps were subsequently warmed back to ambient, allowing the products of the decomposition to be released in order of volatility. The identities of the components in these fractions were identified using gas phase IR and mass spectrometry, thus allowing a likely decomposition pathway to be inferred (Appendix D).

Under these dry, air-free conditions, substantial decomposition of zinc acetate began upon heating to 255 °C, and the primary volatile products were found to be carbon dioxide and acetone. These are entirely consistent with decomposition proceeding via a zinc-catalyzed ketonic decarboxylation mechanism, as shown in Figure 4.4.[35] The analogous decompositions of zinc formate and zinc propionate produce appreciable quantities of formaldehyde and diethyl ketone, respectively, which is also consistent with the same mechanism. However, the situation for these latter two precursors appears to be more complex, as the detection of products such as methyl formate from zinc formate suggests that additional decomposition pathways are also active (Appendix D).

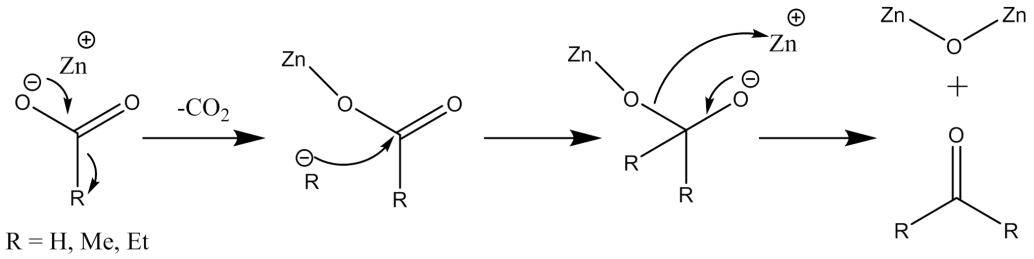

Figure 4.4: Proposed ketonic decarboxylation mechanism for thermal decomposition of zinc carboxylates under anoxic, anhydrous conditions. A carbanionic intermediate is shown, but there are also proposals that this process can occur via a radical mechanism.

However, once again, it is categorically wrong to assume that these TVA results are reflective of how zinc carboxylates behave when they are decomposed during spray pyrolysis, when ample moisture is available. To see the difference, an experiment was also performed where the exhaust from a real spray pyrolysis deposition run using a

solution of zinc acetate in deuterium oxide was first cooled to room temperature and filtered to stop any non-volatile, solid particles. The filtered exhaust was then passed through a cold trap cooled using a dry-ice/isopropanol bath (−78 °C). No trace of acetone was found in the proton NMR of the condensate, which is not what would have been expected if the dry decomposition mechanism identified using TVA had been active. Instead, a signal consistent with acetate was observed and verified by independent addition of both acetic acid and zinc acetate to the condensate. This strongly suggests that in the "wet," water-rich conditions of spray pyrolysis, zinc acetate decomposes by hydrolysis to form acetic acid and zinc hydroxide, which subsequently goes to oxide with loss of water upon further heating. Such a route occurs during the well-known hydrothermal syntheses of ZnO nanoparticles from zinc salt solutions.[36] The lack of acetone and carbon dioxide formation during wet decomposition of zinc acetate has also been reported by Paraguay, *et al.*[37]

The key point that precursor screening for spray pyrolysis should ideally be carried out under as close to spray pyrolysis conditions as possible can be emphasized once more by Figure 4.5, which shows the differences in the thermal decomposition of zinc acetate dihydrate under dry and wet nitrogen, as measured by TGA. The extrapolated onset of the main mass loss signal is at a much lower temperature under wet N_2 (∼200 °C), consistent with activity along the lower-energy hydrolysis pathway. Furthermore, the mass loss curve is smooth, suggesting that moisture availability makes decomposition via hydrolysis dominant over volatilization. The fact that the mass curve plateaus almost exactly at the theoretical value for mass remaining expected after complete decomposition to ZnO is further corroboration of this.

Finally, it can be noted that the efficient deposition of apparently phase-pure ZnO from spray pyrolysis of zinc acetate solutions can occur at substrate temperatures as low as 208 °C (Figure 4.10). This again shows that the TGA study under wet N_2 is more representative of spray pyrolysis than "dry" thermal analysis techniques.

4.3.2 Dopants

On top of the main precursor meant to decompose and form the host oxide, additional precursors are often used in order to introduce impurities that modify the properties of the resulting material. In the field of TCO research (and with semiconductors

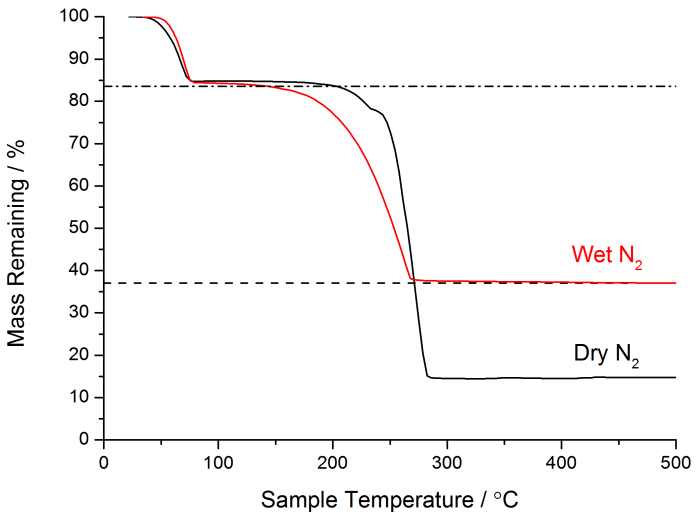

Figure 4.5: Thermogravimetric analysis of zinc acetate dihydrate under dry N_2 (black curve) and N_2 that had been passed through a water bubbler before use (red curve) at a heating rate of $0.75\,\mathrm{K\,min^{-1}}$. The dash-dot line indicates the theoretical mass remaining after loss of water while the lower dashed line indicates the theoretical mass left after complete and exclusive decomposition of the precursor to the corresponding oxide.

in general), such intentionally introduced impurities are generally termed *dopants*. Along with the deposition temperature, the choice and amount of dopant introduced is the process parameter that most dramatically affects the electrical behavior and morphology of TCO films prepared using spray pyrolysis.

While many of the considerations that apply to the selection of the main precursor apply also to the dopant precursor, the constraints on the latter appear to be less strict. Certain precursors (for instance, indium(III) acetate) that do not lead to effective deposition of an oxide film when used alone can still lead to effective doping when used in low concentrations as an additive in combination with another precursor.

In choosing precursors for cationic dopants, a good starting point is to use a salt with the same anion as the main precursor to minimize perturbation of the known good deposition conditions for the undoped TCO. For anionic dopants, the challenge is to select a counter cation that will not itself be significantly incorporated into the finished film (unless, of course, such is desired). This usually rules out alkali metal salts or complex organic cations that will not decompose or volatilize quickly and cleanly. Instead, ammonium or proton can be better choices. However as we shall see in Section 4.3.3, the presence of these cations will change the chemical equilibria

occurring in the precursor solution and can lead to unwanted effects. Furthermore, the volatility of some ammonium salts and acids can also hinder efforts to control the amount of dopant that is incorporated into a deposited film. Another sometimes elegant option is to use the same cation as that in the host TCO. One example of this is the use of zinc hexafluorosilicate ($ZnSiF_6$) as a silicon source for the preparation of silicon-doped ZnO.

We have found it very challenging to predict from first principles whether a given TCO/dopant precursor combination will work effectively. However, with inspiration from the literature and persistence in the application of trial and error, a number of effective and reproducible precursor systems for depositing doped TCOs such as indium-doped zinc oxide (IZO), silicon-doped zinc oxide (SiZO), tin-doped indium oxide (ITO), and bromide-doped indium oxide (IBrO) have been identified and studied in this thesis. The question of how these dopants are incorporated into the host material, the structural and chemical roles they play once there, and their effectiveness at inducing desirable changes to the properties of TCOs will be discussed in both Chapters 5 and 6.

4.3.3 Solution Chemistry

Having shown how the presence of water can change the mechanism by which a precursor decomposes to oxide, it should be no surprise that the choice of solvent(s) into which the precursor salt is dissolved is an important process parameter.

Engineering Considerations

There are clearly some basic engineering considerations in solvent selection. The solvent must be chemically compatible with other materials used in the system. For example, the use of a polycarbonate spraying chamber rules out many organic solvents that would attack it. Likewise, since the solvent is sprayed as a mist onto a heated substrate, excessive flammability is undesirable. Cost and environmental impact of the chosen solvents should also be considered, even though these problems could be mitigated by the use of solvent recycling in industrial implementations.

Ergo, it is typical to use water or water-alcohol mixtures as the spray pyrolysis solvent. Often it is desirable to include additives to the aqueous component of the

mixture, which can usefully modify the behavior of the precursor(s) in solution. One common example is the addition of acids to lower solution pH and reduce the extent of precursor hydrolysis and precipitation before spraying. The type and amount of alcohol can be used to tune the viscosity and the volatility of the solvent mixture.

While the use of very different solvent systems can lead to noticeable differences in film morphology (for instance, Figure 4.6), film properties do not appear to be highly sensitive to minor deviations from the nearly optimized alcohol-to-water ratios (2:1 and 1:3 ethanol:aqueous for ZnO- and In_2O_3-based samples, respectively) used for most experiments in this thesis.

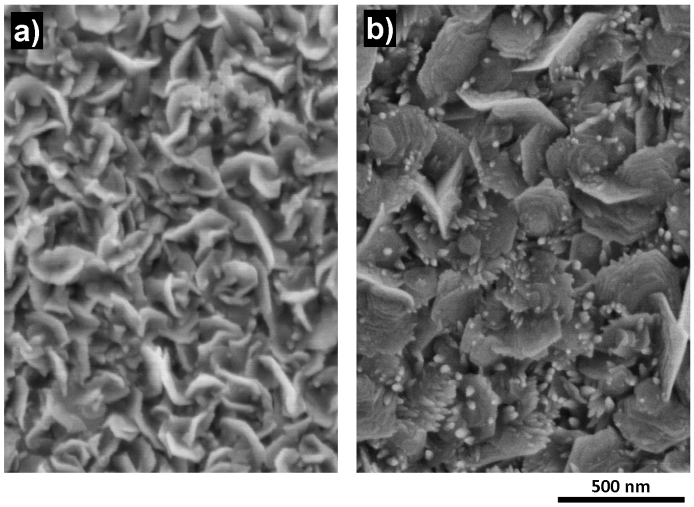

Figure 4.6: Scanning electron micrographs showing the surface morphology of ZnO thin films deposited using 0.075 M zinc acetate dissolved in a) pure water and b) 2:1 ethanol:water as the precursor solution.

A Hydroxide Model: Identifying the "Active" Species in Precursor Solutions

Predicting whether a given precursor solution will successfully deposit a TCO film goes well beyond checking that it will thermally decompose to form the oxide. For instance, we have confirmed literature reports that solution pH is an important factor governing whether a TCO film will successfully deposit. Both In_2O_3 and ZnO can deposit efficiently at pH values of 4–5, but have deposition rates that fall off rapidly to nothing as the pH decreases beyond a critical point. Caillaud, *et al.* have attempted to explain this observation in the zinc acetate system by invoking pH-dependent

changes in metal speciation, arguing that a substantial concentration of $[Zn(Ac)_2]$ must be present in the solution for deposition of ZnO to take place.[38]

Their model cannot be fully correct. For one thing, it is known that ZnO films can be deposited using zinc chloride or zinc nitrate as the precursor (though still not at excessively low pH) and from zinc hydroxy ammines at pH >10, demonstrating that the presence of acetate is not essential.[26,27,39] Furthermore, we have shown that indium acetate does *not* produce In_2O_3 films when the solution pH is between 4 and 5, where a substantial concentration of $[In(Ac)_3]$ would be expected. In contrast, excellent In_2O_3 films can be produced from an $InCl_3$ solution with pH of approximately 1.5, although the deposition rate is substantially increased if the pH of the solution is raised to 4 or 5. These and some additional qualitative observations of this type that we have made are summarized in Tables 4.2 and 4.3.

A "hydroxide model" can be hypothesized to rationalize the behavior of these disparate cases. We suggest that the critical question is whether substantial hydrolysis of the cation to hydroxide will occur as droplets of the precursor solution are rapidly heated and concentrated as interaction with the substrate boils off solvent. From that point, the formation of an oxide from a hydroxide is chemically straightforward. Indeed, this type of mechanism is supported both by our precursor decomposition studies in Section 4.3.1, and by calculations showing that the supersaturation of zinc hydroxides is necessary to produce ZnO powders from alkaline solutions.[40]

The behavior of metal ions in solution as a function of pH and the presence of one or more ligands is an extremely (and perhaps, terrifyingly) complicated topic. It is made even more so by the fact that a complete description of spray pyrolysis would involve rapid, non-equilibrium changes in solution concentration and temperature. Many speciation calculations and measurements have been reported and the methods for analyzing such systems in principle are well known, but unsurprisingly, the exact combinations of pH, metals, and ligands relevant to spray pyrolysis do not appear to have been well-characterized.[41] To make these measurements in anything approaching comprehensive detail would probably be the work of another full thesis, and we do not claim to have done so here. Nevertheless, an attempt will be made to set down a preliminary sketch of how the set of observations in Tables 4.2 and 4.3 might be explained in terms of precursor solution chemistry.

Table 4.2: Listing of qualitative observations on the results achieved using various halide precursors (X = Cl, Br, I). The conditions listed are of the aqueous portion of the spray solution but the listed approximate pH is of the spray solution after addition of alcohol (See Section 4.7.1). The concentration of zinc in these aqueous phases was 0.225 M, while that of the indium was 0.033 M.

Conditions	Approx. pH	Film Deposits?
ZnX_2 in 1.2 M $(NH_4X)_{aq}$	4.1	No
ZnX_2 in water	5.3	Yes
ZnX_2 in 0.0375 M $(HX)_{aq}$	1.5	No
InX_3 in 1.2 M $(NH_4X)_{aq}$	4.2	No
InX_3 in 0.0375 M $(NH_4X)_{aq}$	5	Yes
InX_3 in water	3	Yes
InX_3 in 0.0375 M $(HX)_{aq}$	1.5	Yes (Slowly)
InX_3 in 0.075 M $(HX)_{aq}$	1	No

Table 4.3: Listing of qualitative observations on the results achieved using acetate (Ac) and acetylacetonate (acac) precursors. The conditions listed are of the aqueous portion of the spray solution but the listed approximate pH is of the spray solution after addition of alcohol (See Section 4.7.1). The concentration of zinc in these aqueous phases was 0.225 M, while that of the indium was 0.033 M.

Conditions	Approx. pH	Film Deposits?
$ZnAc_2$ in $(HNO_3)_{aq}$	<2	No
$ZnAc_2$ in water	6.4	Yes (Solution Precipitates)
$ZnAc_2$ in 1.2 M $(HAc)_{aq}$	4.8	Yes
$Zn(acac)_2$ in 1.2 M $(HAc)_{aq}$	4.8	Yes
$Zn(Ac)_2$ in $(NH_4OH)_{aq}$	10-12	Yes
$In(acac)_3$ in 1.2 M $(HAc)_{aq}$	4.5	No
$In(Ac)_3$ in 1.2 M $(HAc)_{aq}$	4.5	No

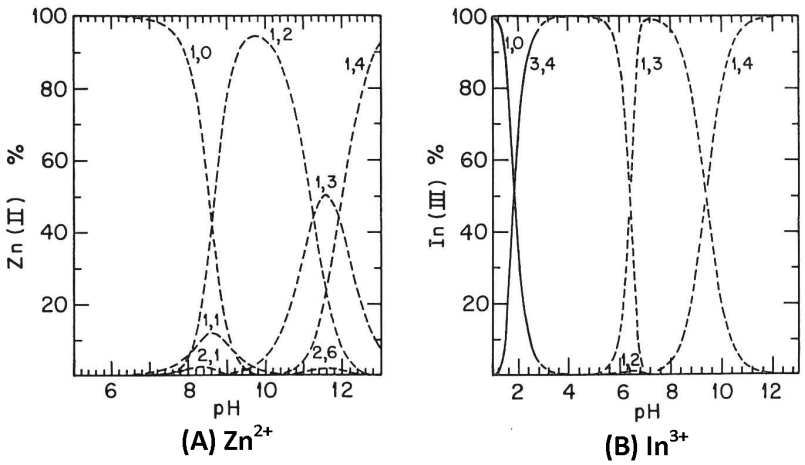

Figure 4.7: Distribution of different (A) zinc and (B) indium species in aqueous solution as a function of pH and in the absence of ligands besides water, hydroxide, and oxide. The a,b labels on the curves denote hydrolysis products of the form $[M_a^{x+}(OH)_b^-]^{(x-b)+}$. Figure reproduced from Baes Jr., *et al.*[41]

The hydroxide ion OH^- is always present in aqueous solutions due to the self-dissociation of water. However, its concentration and activity will vary over a wide range depending on the pH. Several zones across the range of achievable pH can be roughly defined, though of course the position of the boundaries and whether a given zone is reachable can vary dramatically depending on the identity of the metal in question. Figure 4.7 shows the predicted speciation of Zn^{2+} and In^{3+} in aqueous solutions as a function of pH and in the absence of ligands beside oxide, hydroxide, and water. These calculations are based on experimentally determined equilibrium constants for various hydrolysis reactions involving these metals.[41] Since these results do not account for the presence of other ligands like acetate, chloride, or ammonium, they do not fully reflect the situation in spray pyrolysis precursor solutions; nevertheless, they may be useful as qualitative guides as the various pH ranges are discussed below.

Very low pH: The activity of hydroxide is very low and there is very little driving force for the formation of a metal hydroxide via a hydrolysis reaction like

$$M^{x+}(H_2O)_w + (OH)^- \rightleftharpoons M^{(x-1)+}(H_2O)_{w-1}(OH) + H_2O \rightleftharpoons \dots . \tag{4.1}$$

Thus, at equilibrium, many metals will occur as free cations solvated by water. These species range from effectively stable aquo complexes to those where the waters are labile and in constant exchange with the bulk solvent. In the case of the latter,

the speciation of the metal is often expressed as M^{x+} to emphasize the absence of hydrolysis. In this acidic limit, the key pathway that eventually leads to oxide (via hydroxide) would not be active and no film is expected to deposit, in agreement with experimental observations.

Moderately low pH: In this regime, the activity of hydroxide is somewhat higher such that appreciable hydrolysis can occur. However, as long as the solution remains dilute, the equilibrium concentrations of the often sparingly soluble metal hydroxides remain low and the solution is stable against precipitation. As a droplet interacts with a heated substrate, the hydroxide that is present can be thermally dehydrated (*e.g.*, $Zn(OH)_2 \rightarrow ZnO + H_2O\uparrow$) and lead to formation of the desired oxide film.

Notably, the transition from the "very low" to "moderately low" pH regimes can be seen clearly in the deposition behavior of indium halides (Table 4.2). When the solution pH is ∼1, no film deposits. Then, in the standard deposition using dilute HCl as the solvent (pH ≈ 1.5), the deposition rate of In_2O_3 is finite but quite slow. However, with the progressive increase in pH that comes by replacing hydrochloric acid with ammonium chloride, a nearly ten-fold increase in the specific deposition rate[iv] of In_2O_3 is observed. Assuming the current "hydroxide model," this change is directly related to the increase in activity of hydroxide in solution, which then leads to a higher concentration of metal hydroxides being available for conversion to oxide.

Near-neutral pH: As the pH rises further, the equilibrium concentration of metal hydroxides will continue to increase in concert with the hydroxide ion activity in solution. A diverse array of mono- and poly-nuclear metal hydroxide complexes can form in solution, but in general, the solubility of transition metal and post-transition metal hydroxides is low. There will come a point where the solubility limit is reached and solids will precipitate from the precursor solution.

The challenges of nozzle clogging, etc. that come with the spraying of heterogeneous mixtures has generally made the use of solutions in this pH range undesirable for spray pyrolysis. Indeed, the addition of acetic acid to precursor solutions of zinc acetate and zinc acetylacetonate, for example, is mostly motivated by the desire to prevent excessive hydrolysis and premature precipitation of solids in precursor solutions before use.

[iv] That is, the thickness of film deposited per amount of precursor sprayed

Several groups have reported producing transparent semiconducting oxide films by spin-coating such near-neutral precursor solutions followed by thermal treatment to produce the corresponding oxide.[42–44] Interestingly, the very moderate heating temperatures (<200 °C) required in these cases speak once again to the ease of producing oxide if the hydroxide is already present in significant quantities. However, the nanoparticulate oxide film morphologies resulting from such processes generally do not result in highly conducting films and have typically been applied to the production of semiconducting channel layers in thin-film transistors.

High pH: Both ZnO and In_2O_3 are amphoteric oxides, which means that the precipitates that form near neutral pH can redissolve upon further increase of the solution pH and the activity of hydroxide. This is facilitated by the formation of soluble zincate $[Zn(OH)_6]^{4-}$ and, to a lesser extent, indate $[In(OH)_4]^-$ anions upon further hydrolysis of the neutral hydroxides or oxides.[41,45,46] If ammonia is used as the base, then various hydroxy ammines with the general formula $[M^{x+}(OH)_a(NH_3)_b]^{x-a}$ are the dominant species in solution.[47,48]

As with the near-neutral pH solutions, substantial concentrations of metal hydroxides are available, except that here they exist in a soluble form and homogeneous precursor solutions are possible. As seen in Table 4.3, it is possible to deposit ZnO thin films from zinc hydroxy ammine precursors using spray pyrolysis. This is once again consistent with the hypothesis that the presence of metal hydroxides is essential for the formation of oxide under spray pyrolysis conditions.

Ligand Effects on Speciation: Finally, there are two sets of observations in Tables 4.2 and 4.3 that would seem to be anomalous given the discussion above. The first is that indium acetate and indium acetylacetonate do not seem to lead to In_2O_3 films despite being dissolved in precursor solutions of "moderately low" pH. The second is the observation that adding ammonium chloride to a solution of indium chloride eventually causes the deposition rate to drop to zero even without substantially changing the pH. Fortunately, all of these cases can be explained by considering the effect of the ligands present.

To explain the first situation, consider that both acetate and acetylacetonate can act as bidentate ligands. Thus, it is not unreasonable to speculate that $[In(Ac)_3]$ and $[In(acac)_3]$ in solution are six-coordinate and coordinatively-saturated, and that

this shell of organic ligands hinders the access of water or hydroxide to the metal center. Hydrolysis is then disfavored to the extent where an oxide film does not form under spray pyrolysis conditions. This contrasts with the situation in solutions with monodentate and weakly coordinating chloride anions, or that of zinc acetate where the two acetate ligands would at most occupy four coordination sites (leaving two open for water). The kinetic hindrance of the ligands is much less and there is no problem with hydrolysis and eventual formation of oxide in these latter cases.

The inhibiting effect of ammonium on spray pyrolysis in the second situation can be explained by the competition between the binding of water and ammonia ligands to a metal center. The greater basicity of ammonia tends to stabilize metal-ammonia bonds relative to metal-water or metal-hydroxide bonds. Thus, given a high concentration of ammonium, hydrolysis is out-competed by ammination, the equilibrium concentration of metal hydroxides is reduced, and once again an oxide film does not form during spray pyrolysis.

Gratifyingly, we have already been successful at applying this "hydroxide model" in one small instance. Originally, a candidate precursor solution consisting of indium(III) iodide dissolved in dilute hydroiodic acid (at concentrations corresponding to those used in the standard chloride solutions) did not result in an oxide film. However, upon finding that the solution pH was slightly lower than that of the corresponding chloride-based precursor solutions, a small reduction in the HI concentration was made. The resulting slight increase in pH was found sufficient to allow successful film deposition, in accordance with the hypothesis.[v]

While admittedly preliminary and (so far) mostly phenomenological, the idea that the formation of metal hydroxides is the key chemical step in spray pyrolysis is a straightforward and testable model for explaining why certain precursor solutions lead to the deposition of oxide, while other seemingly similar ones do not. It apparently explains all of the cases listed here, and no counterexamples have yet been observed by us. Perhaps even more significantly, it suggests that systematic design of spray

[v]Unfortunately, the properties of the resulting In_2O_3 samples did not justify the expense and complication of working with iodides as compared to chlorides and this line of inquiry was eventually discontinued.

pyrolysis solutions from new starting materials or combinations might be possible, in lieu of the largely trial-and-error based approach that must be used today.

Obviously, direct characterization of the speciation in various precursor solutions and quantitatively correlating these results to film deposition rates would be of great significance in confirming or disproving this model. Another useful experiment would be spray pyrolysis depositions using water with isotopically labeled oxygens to determine the source of oxygen atoms in the deposited oxide films. However, given the constraints of time and other projects, these will have to be left to future work.

Structure-directing Effects

The crystallites in TCO films deposited by spray pyrolysis almost inevitably exhibit some degree of preferred orientation with respect to the plane of the substrate. This arises because growth of the crystals at various crystal faces will have kinetic parameters that vary differently depending on the details of the deposition process. Among the factors influencing crystal growth are the structure-directing effects of anions present in solution. These types of effects have been used with great success to produce a diverse range of morphologies in ZnO particles, from rods to platelets.[36]

Anions bind differently to the faces of a growing oxide crystallite based on factors like the polarity of the face, or the metal-ligand binding constant. For example, an anion like acetate would have a stronger interaction with a polar (001) face of ZnO than with a non-polar face. The binding of acetate can thus stabilize the polar surface and then the minimization of total surface energy will favor plate-like crystals with a larger surface area of (001) (Figure 4.8a).

All else being equal, if acetate in the spray solution is replaced by an anion with a lower stability constant for binding to zinc, such as formate, the relative energetic favorability of the (001) face should be reduced.[49] This can be illustrated by comparing the surface morphology of films deposited at a substrate surface temperature of 376 °C using zinc acetate and zinc formate precursor solutions.[vi] The acetate-containing solution clearly favors the growth of ZnO crystallites as hexagonal platelets (Figure 4.9a), whereas this tendency is notably absent in the sample deposited from solutions containing formate instead (Figure 4.9b).

[vi]Note that the zinc formate precursor solution also uses formic rather than acetic acid during the preparation of the aqueous part.

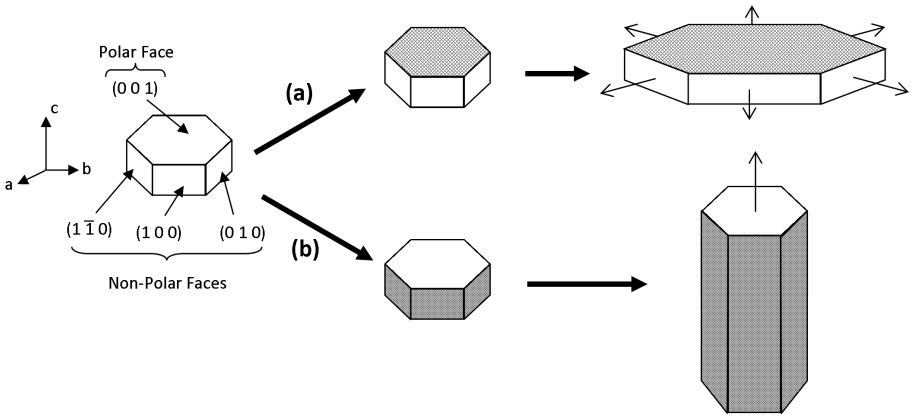

Figure 4.8: A hexagonal crystal of ZnO is shown at left, with the polar and non-polar faces indicated. The stabilized faces are shaded. Under conditions that stabilize polar faces (a) such as the presence of a strongly complexing anionic ligand, growth parallel to the stabilized face is favored leading to plate shaped crystals. In a situation favoring stabilization of non-polar faces (b), the opposite pattern of growth will be observed and longer, needle-like crystals will result.

It should be noted that the type of anion(s) present is by no means the only factor that influences the morphology of spray pyrolyzed TCO films. The deposition temperature will change the relative energetic favorability of various crystal faces, as will the impurity (dopant) concentration in the precursor solution. Such factors are often dominant. Nevertheless, given the potential correlations between crystallite morphology and the optoelectronic performance of TCOs, structure-directing effects could be a useful tool for influencing this behavior. It may be possible to exercise further control over the morphology of ZnO films by using stronger ligands (such as lactate or citrate) or weaker ligands (such as chloride) in precursor solutions; this would be an interesting topic for additional study in the future.

4.4 Process Variables

4.4.1 Substrate Surface Temperature

Unlike a sputtering or PLD process where a significant amount of the energy required for film nucleation and growth is supplied by the kinetic energy of the incoming particles, spray pyrolysis relies almost entirely on thermal energy from a heated substrate. For this reason, the temperature of the substrate surface during deposition (T_{dep}) is one of the most influential process variables in spray pyrolysis.

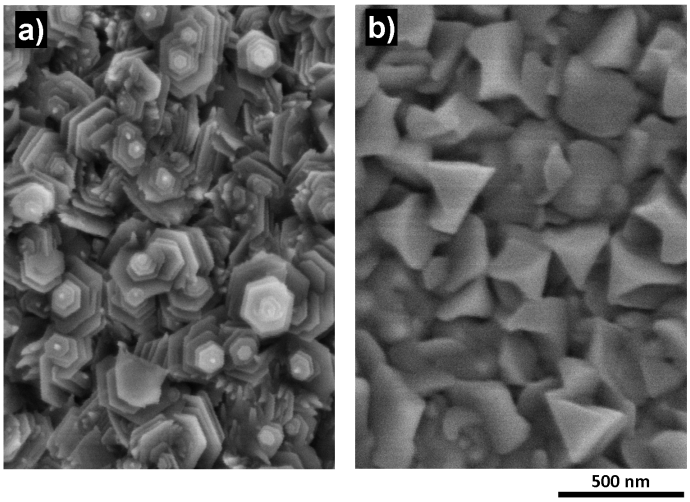

Figure 4.9: Scanning electron micrographs showing the surface morphology of ZnO thin films deposited at ∼376 °C using a) zinc acetate and b) zinc formate as the precursor.

The types of changes that can occur in TCO films as a function of T_{dep} can be usefully illustrated by considering the example of undoped ZnO deposited from a zinc acetate precursor using the baseline preparation (Section 4.7.1 and Appendix C). Clearly, other systems will show temperature-dependent behavior that varies in the details; however, these observations form the basis for later chapters and so, to limit repetition, the scope here will be restricted to ZnO.

Limits to Deposition Temperature Range

The range of usable deposition temperatures is bounded on the low end by the decomposition temperature of the precursor under spray pyrolysis conditions. Below a certain T_{dep}, the precursor will no longer cleanly decompose to oxide and a high-quality TCO film will not be possible. As far as can be seen from XRD (Figure 4.10), ZnO is the only phase observed down to a T_{dep} as low as 208 °C, and incomplete decomposition can only be observed at still lower deposition temperatures. However, it should be noted that such low T_{dep} ZnO films tend to have little practical use as TCOs because of their very low electrical conductivities, which arise because of T_{dep}-dependent grain boundary effects (Chapter 7).

It appears that the high temperature limit for spray pyrolysis is defined by the physical properties of the solvent. Above a certain threshold temperature, the hot

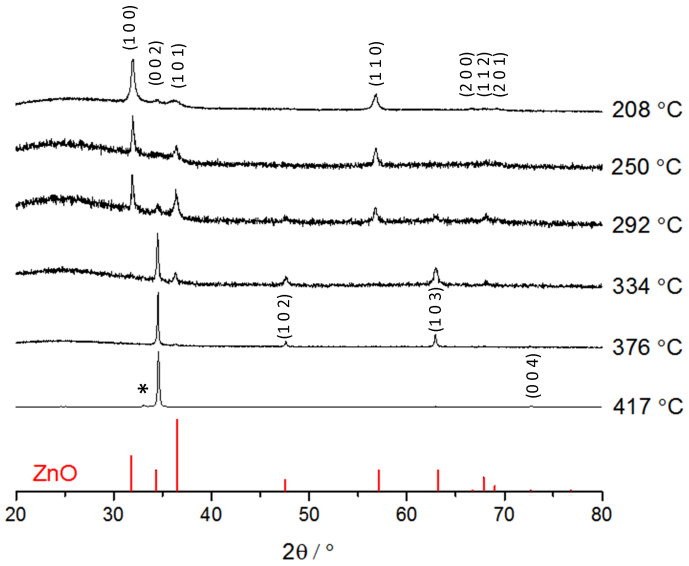

Figure 4.10: Normalized X-ray diffraction patterns of undoped ZnO films deposited from zinc acetate precursor at a range of T_{dep}. The peaks are annotated with the corresponding plane of the wurtzite ZnO structure. A reference stick chart for ZnO powder is shown in red. The minor peak labeled $*$ is due to tungsten contamination in the copper anode of the instrument used. Note that an amount of solution greater than the standard 10 mL was used for the sample deposited at ∼208 °C.

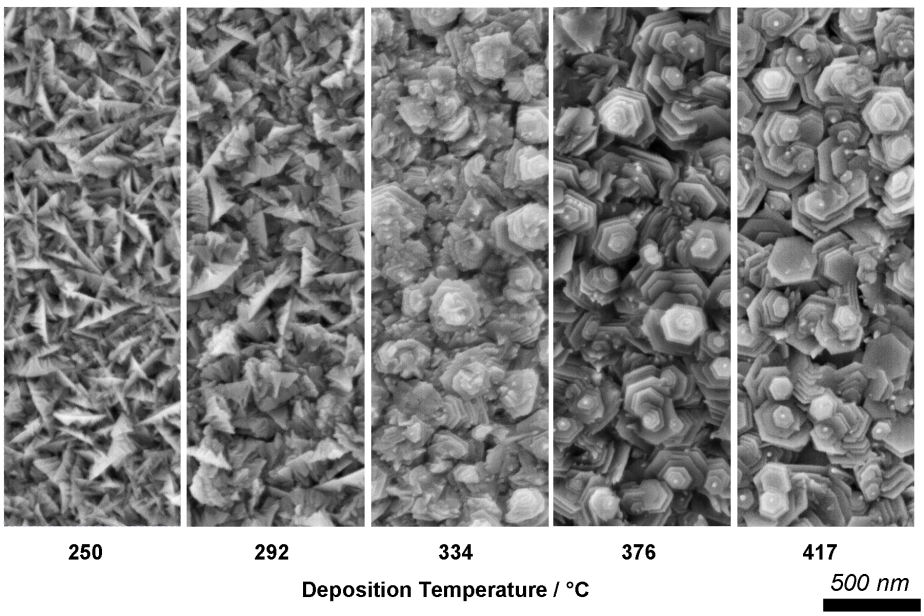

Figure 4.11: Scanning electron micrographs showing the surface morphology of undoped ZnO films deposited from zinc acetate precursor at a range of T_{dep}.

substrates can cause strong thermal convection opposing the downward flow of the carrier gas and perhaps also a Leidenfrost-type effect near the substrate surface. Both of these would act to prevent precursor solution from reaching the substrate surface. For the 2:1 ethanol:aqueous solvent system used to deposit ZnO samples, the high temperature limit is around 460 °C, near which the rate of film growth drops sharply to zero. It may well be possible to overcome these limitations through appropriate engineering of flow and further solvent optimization. However, because high quality films can be deposited at lower temperatures where these effects are not significant, no such modifications were attempted.

Structural and Morphological Changes

All of the X-ray diffraction patterns shown in Figure 4.10 are consistent with ZnO in the hexagonal wurtzite structure being the only crystalline phase present. All of the films are polycrystalline and contain crystallites exhibiting a preferred orientation relative to the substrate. The degree and direction of preferred orientation changes markedly as a function of deposition temperature. The crystallites in the sample deposited at 417 °C are almost entirely oriented with their (0 0 2) planes parallel to the substrate, whereas very little of this orientation is seen in the lower temperature samples. The transition in orientation appears to be roughly continuous, but appears to occur most rapidly between 292 °C and 334 °C and could reflect a change from kinetically to thermodynamically favored modes of crystal growth as T_{dep} increases.

No statistically significant changes in lattice parameter were observed in the ZnO samples as a function of deposition temperature. The full width at half maximum of the peaks does increase as the T_{dep} decreases, which is consistent with the changes in grain size seen by SEM (Figure 4.11).

The scanning electron micrographs also plainly show that other changes in film morphology also occur as a function of deposition temperature. The films deposited at higher deposition temperatures (∼376 °C and higher) consist of hexagonal plates stacked mostly parallel to the substrate surface, which is consistent with the strong (0 0 2) orientation observed using XRD. The sample deposited at 334 °C is transitional. The platelets are still visible but significantly less well defined, and a granular material with a different morphology is beginning to appear between the stacks.

In agreement with the orientation change seen in XRD, the SEM data show that the most significant structural transition occurs between the samples deposited at 334 °C and 292 °C. This temperature range is marked by the total disappearance of the hexagonal platelets and the appearance of the more porous feathery flakes that characterize lower T_{dep} samples.

Optical Properties

Representative UV-Vis-NIR transmission spectra from this series of undoped ZnO samples are shown in Figure 4.12a. Applying the Swanepoel envelope method to these spectra shows that the samples range in thickness from about 300–400 nm, with a distinct drop in thickness as the deposition temperature is lowered from 376 °C to 334 °C (Figure 4.12b). A change in sample growth rate has been previously been seen as diagnostic of a change in the film growth mechanism and here can also be correlated with the gradual decline of the hexagonal morphology seen in SEM and XRD.[37]

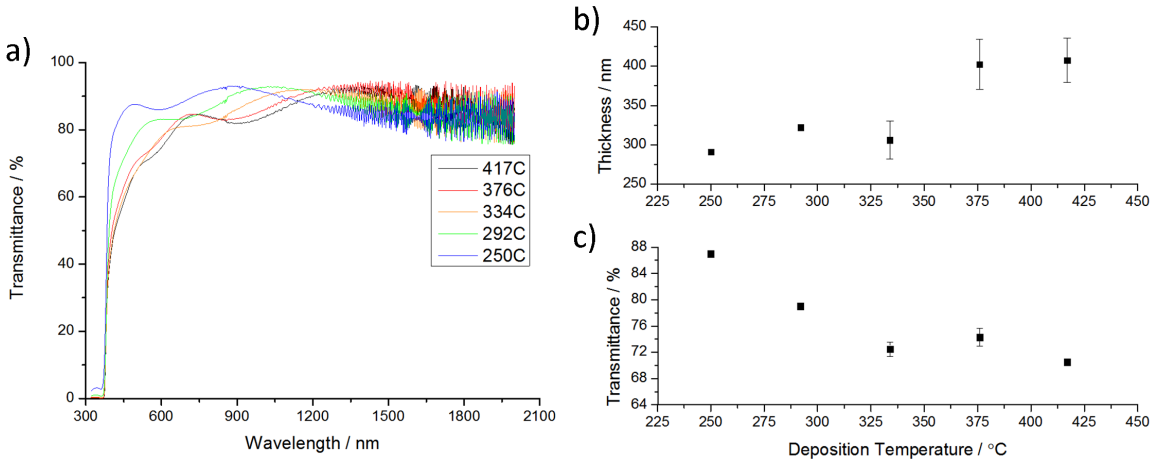

Figure 4.12: a) UV-Vis-NIR transmittance spectra for undoped ZnO samples prepared at deposition temperatures ranging from 250 °C to 417 °C. b) Sample thickness and c) average visible transmittance are also shown as a function of T_{dep}.

While a decrease in sample thickness would tend to increase sample transparency, the increase in average visible transmittance for the two lower deposition temperature samples is too large to be explained by this factor alone (Figure 4.12c). Instead, undoped ZnO samples deposited at 334 °C and above are somewhat hazy, as can be seen from the gradual decrease in transmittance as the band gap is approached from

longer wavelengths (Section 3.2.1). The lower T_{dep} samples are not hazy to the naked eye, and correspondingly show a sharper transition between the transparent region and the fundamental bandgap absorption. This reduction in scattering due to haze is reflected by the increase in average visible transmittance.

It was noted in Section 3.2.1 that surface roughness can lead to light scattering and hence haze. As such, the different optical properties of samples prepared at high and low T_{dep} can be explained by differences in their surface morphologies. Figure 4.11 clearly shows that the higher T_{dep} samples consist of clearly defined stacks of large platelets, separated by relatively deep gaps. These features of approximately the same size as the wavelength of visible light provide many surfaces and facets from which incoming light can be reflected and scattered in different directions. The reduction of deposition temperature leads to a morphology where the mean feature size is much smaller and less prone to causing scattering. Furthermore, the apparently higher porosity and lower density of packing in the lower T_{dep} samples may also mean that there is simply less material in the path of incoming light.

Electrical Properties

The deposition temperature also has a substantial effect on the electronic transport properties of ZnO thin films. Figure 4.13a shows the electrical conductivity of undoped ZnO thin films as a function of deposition temperature. The conductivity varies only modestly for the samples deposited at 334 °C and above, with values ranging from a maximum of $8.9 \pm 1.3\,\Omega^{-1}\,\text{cm}^{-1}$ at a deposition temperature of 417 °C to about $3.0 \pm 1.5\,\Omega^{-1}\,\text{cm}^{-1}$ at 334 °C. Below that, a very substantial dropoff occurs, with electrical conductivity decreasing by roughly two orders of magnitude for every 50 °C decrease in substrate temperature.

For a more detailed assessment, room temperature Hall effect measurements were also made on the three higher T_{dep} films that were of sufficiently high conductance for reliable measurements using the equipment available. The results for carrier concentration and mobility as a function of deposition temperature are shown in Figure 4.13b. In this temperature range, it is clear that most of the changes in conductivity are due to a reduction in mobility, rather than significant changes in the carrier concentration. Indeed, carrier concentration is flat to within experimental error, while

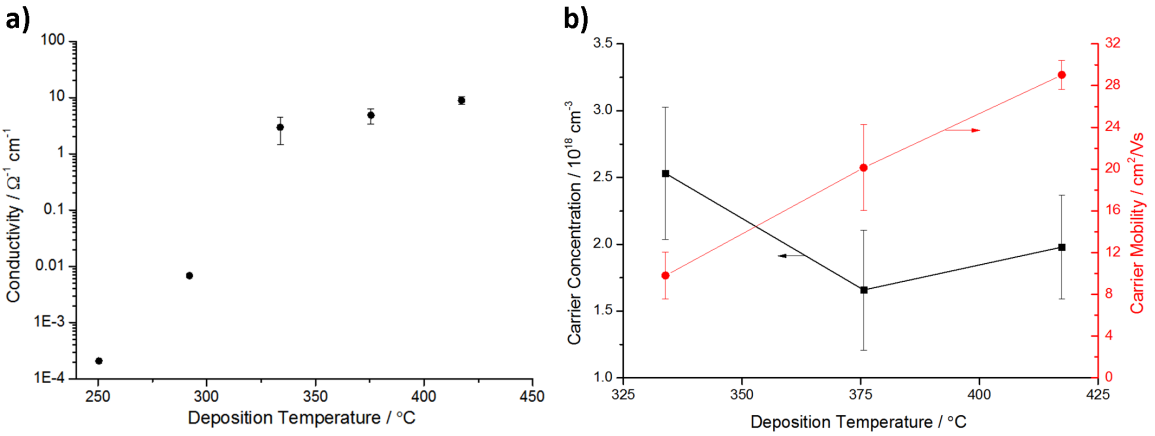

Figure 4.13: a) Electrical conductivity and b) Hall effect carrier concentration (black) and carrier mobility (red) of undoped ZnO thin film samples deposited by spray pyrolysis at various deposition temperatures. Hall effect data for lower T_{dep} samples too resistive for reliable measurements are not shown.

there is a statistically significant drop in carrier mobility from 29.0 ± 1.4 cm^2/Vs for samples deposited at $T_{\mathrm{dep}} = 417\,^{\circ}\mathrm{C}$ to $9.8 \pm 2.2\,\mathrm{cm}^2/\mathrm{Vs}$ at $T_{\mathrm{dep}} = 334\,^{\circ}\mathrm{C}$.

As has been seen, deposition temperature is one of the most influential process parameters when it comes to determining the optoelectronic performance of TCO thin films. This is to some extent true for any thin film deposition process,[50,51] but is especially true for spray pyrolysis where substrate heating provides almost all of the energy needed for the essential processes of film growth. This requirement of high deposition temperatures for high performance in ZnO is one of the most significant practical limits to its use as a low-cost TCO material. A much more detailed discussion of the reasons for and implications of temperature-dependent performance will be made in the following chapters, especially Chapter 7.

4.4.2 Carrier Gas

A TCO with an oxygen-deficient stoichiometry contains defects like oxygen vacancies or zinc interstitials which can act as net donors of carrier electrons. Therefore, the oxidizing strength of the atmosphere under which deposition occurs can have a significant effect on the electrical conductivity of the resulting thin film.

This is particularly true in the case of undoped films where oxygen deficiency is the primary source of free carriers. For example, the conductivity of an undoped ZnO film

deposited at 376 °C using high purity nitrogen as the carrier gas was approximately $4.9\,\Omega^{-1}\,\mathrm{cm}^{-1}$, whereas repeating the same process using compressed air resulted in two samples with an average conductivity of $4.2 \times 10^{-3}\,\Omega^{-1}\,\mathrm{cm}^{-1}$, or more than three orders of magnitude lower. For the samples deposited under air, the decrease in conductivity results from a decrease in carrier concentration, as might be expected, but also from a substantial reduction in carrier mobility (Figure 4.14). This is not consistent with the changes simply being due to a lower defect concentration and suggests that grain boundary effects are also involved. This is a topic that will be examined further in Chapter 7.

On this basis, it might be expected that a reducing atmosphere would improve the conductivity of undoped films. We have found that deposition of undoped ZnO using a 4 % H_2 (balance N_2) mixture as the carrier gas does increase the carrier concentration to $\sim 4 \times 10^{18}\,\mathrm{cm}^{-3}$ from $1.7 \pm 0.4 \times 10^{18}\,\mathrm{cm}^{-3}$ for ZnO deposited under pure nitrogen. However, the increase in carrier concentration is more or less canceled out by a corresponding decrease in mobility, meaning that conductivity is about the same in the two cases.

The effect of deposition atmosphere is quite different for indium-doped ZnO (IZO) samples. While the carrier concentration drops by about the same proportion upon switching from N_2 to air as for the undoped samples, there is virtually no change in carrier mobility (Figure 4.14b). For the doped samples, the different carrier gas also leads to a significant change in the preferred crystallite orientation, as seen in Figure 4.15, which is not observed at all with the undoped samples. This implies that the choice of carrier gas is influencing not only the oxygen stoichiometry of these samples, but also the way in which the indium dopant incorporates into the ZnO.

4.4.3 Solution Amount and Sample Thickness

In general, for a given set of precursors and a given deposition temperature, sample thickness is more or less directly proportional to the amount of precursor used. This can be most easily changed by altering the total volume of solution sprayed and an example of this for 1.5 at% indium-doped ZnO is shown in Figure 4.16. Within certain bounds, it is also possible to change the concentration of the precursor solution without significantly affecting solution homogeneity or the properties of the deposited

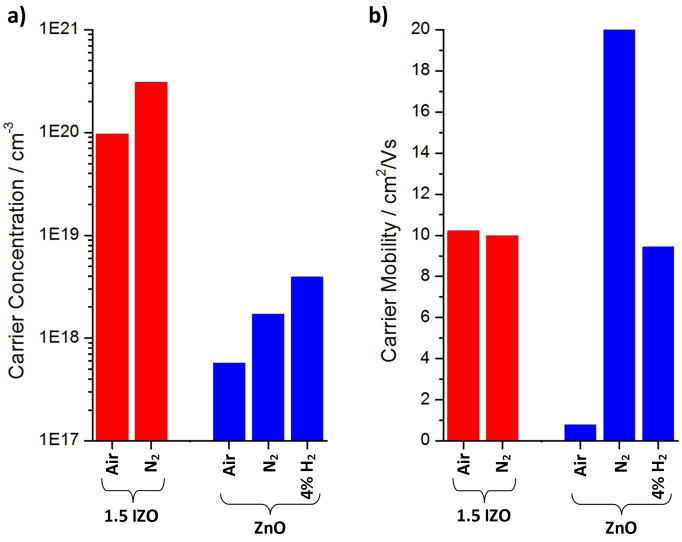

Figure 4.14: Hall effect a) carrier concentration and b) carrier mobility for undoped and 1.5 at% indium-doped ZnO deposited at ∼376 °C as a function of the carrier gas used.

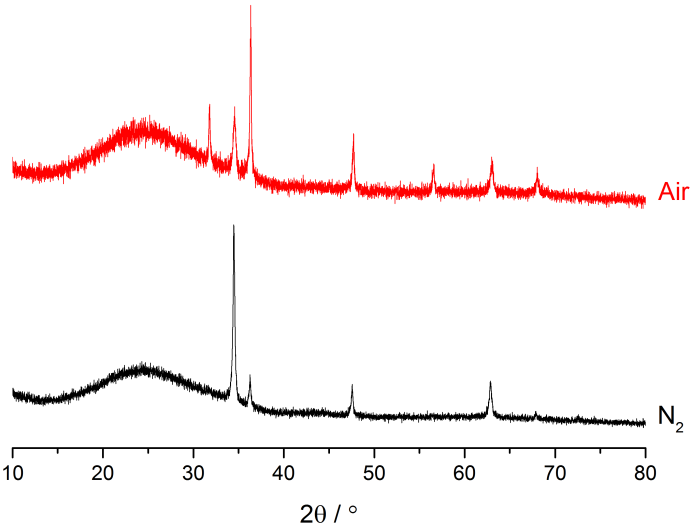

Figure 4.15: A marked difference in preferred orientation is observed in the X-ray diffraction data for 1.5 at% indium-doped ZnO thin films deposited at ∼376 °C using N_2 (black) versus compressed air (red) as the carrier gas.

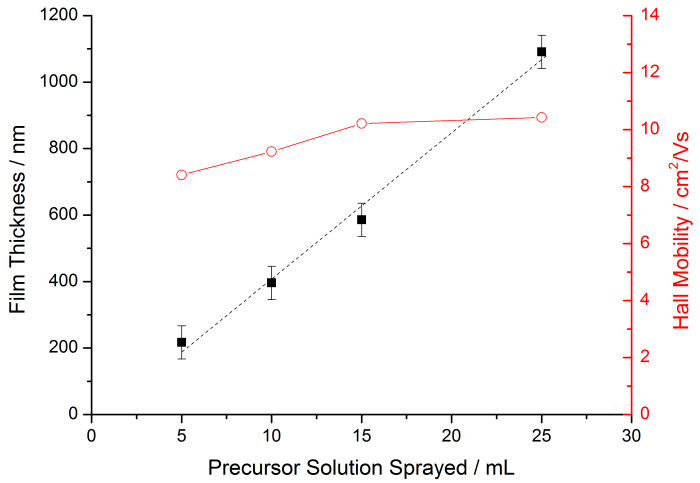

Figure 4.16: Sample thickness (black squares) and carrier mobility (red circles) for a series of 1.5 at% indium-doped ZnO thin films prepared by spray pyrolysis using different volumes of the same precursor solution. The dashed black line is a best-fit linear trendline for the thickness data, and the error bars reflect estimated uncertainty in the thickness measurement.

film. The constant of proportionality relating sample thickness and total precursor sprayed can vary quite dramatically with factors like deposition temperature, the choice of precursor, the presence of dopant, and the pH of the precursor solution; this means that the required solution volume needs to be determined empirically for each given set of process conditions.

The electrical properties of samples can vary somewhat with their thickness. In particular, carrier mobility for samples of a given composition tends to increase slightly with increasing sample thickness before plateauing at a limiting value (Figure 4.16). The reason for this thickness-dependent mobility has not been conclusively determined. However the general trend is consistent with an interface effect, whether film-substrate or film-air, that negatively affects transport within the films. For example, the amorphous glass may introduce disorder or chemical impurities into a layer at the bottom of a growing TCO film, lowering the mobility. This interface layer will then become less significant as the film becomes thicker and the mobility will then tend to the unperturbed intrinsic value for the given material. Similar arguments could be made for carrier scattering that arises due to chemical species adsorbed at exposed surfaces of the film.

For the purposes of this study, there are some sensible guidelines for choosing

film thicknesses. Given the thickness variation of film properties, the best data comparisons are within series consisting of samples with similar thicknesses. There are also some practical limits to the thicknesses of films that can be easily studied. Because Swanepoel's envelope method (Section 3.2.1) has been adopted as the standard method for thickness estimation here, it is not easy to determine the thicknesses of samples that are too thin (less than ∼200 nm). At the same time, excessively thick samples (much in excess of 1000 nm) tend to exhibit problems with film quality, such as the loss of uniform film cohesion and excessive haziness. The amount of each type of precursor solution sprayed must thus be tuned to reflect these constraints.

4.4.4 Process Timing

Given a particular volume of solution to be sprayed, a change in the rate of solution delivery to the atomizer nozzle will clearly change the time required to spray the solution. For the TCOs and deposition conditions used here, the optoelectronic properties of the deposited films were found to be relatively insensitive to the precursor solution delivery rate. For ZnO samples, little change was observed upon increasing the solution delivery rate from a value of 0.7 mL/min (the maximum value of an older peristaltic pump used in the early part of this thesis) up to 2.1 mL/min which was achievable using a syringe pump. Some test samples prepared after a further doubling of the solution spray rate to 4.2 mL/min did show evidence of slightly lower mobilities and conductivities. Therefore, unless otherwise noted, the maximum solution spray rate was fixed at 2.1 mL/min for the remainder of this work.

Another significant contributor to process time is the heating and cooling of the substrate to and from deposition temperature. It was found that a few minutes were required for stabilization of the substrate surface temperature after a heater setpoint temperature was reached. Therefore, a five minute hold was added between the reaching of the setpoint temperature and the start of spraying.

Additionally, it was found that deposition continues from residual spray within the chamber for a few minutes after the supply of precursor solution to the nozzle stops at the end of a run. Thus, if the heater is not held at temperature for several minutes after the delivery of fresh solution ceases, the top layer of TCO film is deposited at a lower temperature. Especially for ZnO, whose properties are extremely sensitive to

Table 4.4: Approximate times required for various stages of a typical spray pyrolysis film deposition run using a heater temperature of 450 °C and spraying 10.5 mL of solution.

Process Step	Time / min
Heating to 450 °C	14.5
Hold before Spray	5
Spraying (10.5 mL @ 2.1 mL/min)	5
Hold after Spray	5
Cooling to 50 °C	15
Changeover to Next Run	3
Total:	47.5

surface chemistry, even a thin layer with different properties can substantially change the overall measurement results for a sample (See Chapter 7).

Finally, for some samples, again, especially those of undoped ZnO, it was found that opening the deposition chamber to air at elevated temperatures would adversely affect the electrical conductivity of the resulting films. This is likely due to partial oxidation of exposed ZnO surfaces by air, which is accelerated at higher temperatures. Therefore, in our standard process, the chamber is not opened until the heater temperature is less than 50 °C. Since cooling down to this temperature is time consuming, even with the assistance of the flowing carrier gas, this part of the process could be optimized for samples proven to be less sensitive to a brief exposure to air at higher temperatures.

Taking all these considerations into account, the process time required to deposit one film from 10.5 mL of precursor solution using a heater temperature of 450 °C and our standard operating procedure (Appendix C) is summarized in Table 4.4. Many tasks like substrate and solution preparation can occur during a previous run, so only a few minutes are needed between runs to flush the solution delivery system with solvent and set up a new substrate. This means that one sample can be deposited in every 50 minutes or so of optimal work, which again highlights the speed and simplicity of the spray pyrolysis technique.

This speed is even more impressive since the majority of time is spent on the

repeated heating and cooling cycles of this batch process; this is time which would be saved if spray pyrolysis were ever implemented as part of a continuous assembly line. In this frame of mind, it can be argued that each film deposition only takes about five minutes.

4.4.5 Other Process Variables

Finally, there are a few additional minor process variables that are worth a brief mention because they are influential in some cases.

Room Lighting

Undoped ZnO in particular exhibits significant photoconductivity.[52–54] Therefore, its properties can be affected by the lighting conditions in the laboratory during deposition (Section 7.3.1).[55] The most consistent results for such samples are thus achieved by excluding ambient light from the deposition chamber while spray pyrolysis is taking place. In general, this is probably a sensible precaution until it can be verified that a given TCO under study is not sensitive to such environmental influences.

Post-deposition Annealing

Much as the choice of carrier gas during deposition can affect the properties of a TCO sample, re-heating an already prepared sample under various atmospheres can also affect its properties.[56,57] In general, the use of vacuum or reducing conditions tends to improve the conductivity of *n*-type TCOs, while the opposite is true of oxidizing conditions. This is not an area which has been studied extensively in this thesis, except in the sense that the result of annealing can often be considered a special case of the grain boundary effects discussed in Chapter 7. However, various processes of this type have been reported that successfully modify the properties of TCO thin films and are thus worth considering as potential additional steps in spray pyrolysis processes.[58–62]

4.5 Characterization of Platform Reproducibility

4.5.1 Assessment of Reproducibility

In acknowledgment of all of the complexities in the design of a spray pyrolysis process, both in terms of engineering and chemistry, a thorough characterization and demonstration of the reliability and reproducibility of the process used here is necessary to validate the significance of any results obtained.

Equipment and procedures were developed based on the considerations discussed previously in this chapter (also see Appendix C) and used to prepare a number of undoped ZnO samples. ZnO was chosen for these tests because experience has shown that its performance is the most sensitive to small changes in preparation conditions. In this way, the observed scatter represents an approximate upper bound on the magnitude of random experimental error for any other film of TCO material prepared using this system.

A total of 15 ZnO samples were prepared using a deposition temperature of $\sim$376 °C over several different days using nominally the same procedure. The distributions of carrier concentration (n), carrier mobility (μ), and electrical conductivity (σ) in this population of samples are shown in Figure 4.17. Both carrier mobility and concentration values are generally consistent with a normal distribution, although the distribution of n values shows a modest positive skewness.

This behavior for n is reasonable, as any slight trace of an n-type dopant present in the system would lead to an increase in carrier concentration. Assuming perfect doping efficiency, about 25 ppm of a single electron donor would be adequate to increase the electron concentration by $\sim 10^{18}\,\mathrm{cm}^{-3}$. Given the natural tendency of oxygen vacancies to form in ZnO and compensate for acceptor impurities, it is unsurprising that the net effect from any unintentional impurities would be slightly biased towards producing higher carrier concentrations.

Being the product of n and μ, the distribution of conductivity values is likewise approximately normal, with some positive skew. Taking the approximation that these values are normally distributed, the relative standard deviations in n, μ, and σ are 26.5 %, 20.4 %, and 30.6 %, respectively. Given that the range of electronic transport values as a function of doping or deposition temperature is several orders of magnitude, these values of random experimental error are certainly manageable. Of

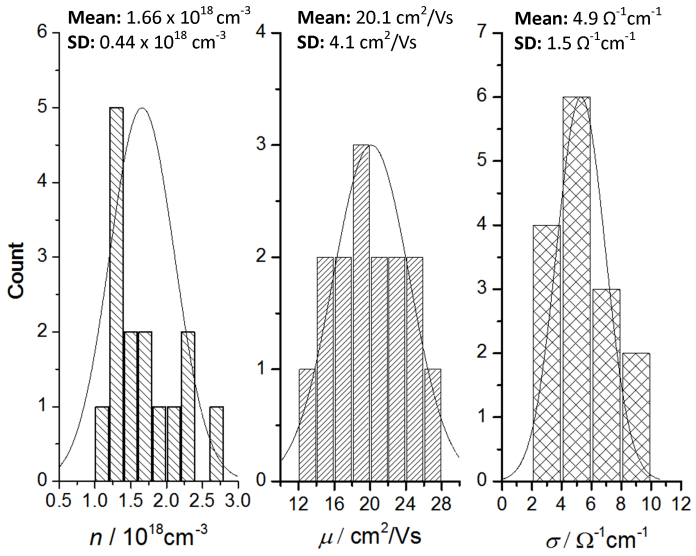

Figure 4.17: Distribution of carrier concentration (n), carrier mobility (μ), and conductivity (σ) exhibited by a set of 15 undoped ZnO samples deposited by spray pyrolysis at a deposition temperature of 376 °C using the same procedure. The best fit normal distribution to each dataset is shown, along with the associated mean and standard deviation.

course, an honest assessment of the magnitude of these errors must be kept in mind if subtler effects are being examined.

A similar calculation was performed on the thickness and transparency of these samples. We found that the average visible transmittance of the set was $74.3 \pm 1.4\,\%$, while the average sample thickness was 402 ± 32 nm. These correspond to relative errors of 1.9 % and 8.0 %, which are quite small compared to the relative errors in the electrical transport properties.

It should be emphasized that these values are the result of extensive efforts to reduce process variability in the spray pyrolysis deposition of TCO films. We have attempted to do this both through the use of detailed standard operating procedures and iterative improvements to the design of our spray pyrolysis apparatus. Although these data are not shown here, similar results for undoped ZnO have been replicated by other workers in our laboratory after training and with enforcement of careful adherence to the standard procedures. Through experience, it is safe to say that a more "casual" approach to sample preparation can lead to significantly larger experimental errors.

4.5.2 Remaining Sources of Error

Thermal Management

The largest remaining sources of error in the present spray pyrolysis apparatus are probably those related to uneven heating of the substrate. Many of the previous sections have shown the significant changes in ZnO properties that can occur with deposition temperatures in certain ranges, particularly below the sharp microstructural transition that occurs somewhere around 334 °C.

Since the current design of heater block is approximately the size of the substrate, boundary cooling effects are important and the top surface of the block is cooler at the edges. Furthermore, the thin glass cover slides used for most samples tend to warp slightly or even fracture as strain is released upon heating, leading to spatial variations in thermal contact with the heater block and thus additional temperature non-uniformity. These variations can be clearly visualized from the concentric coloration patterns seen in some deposited films (Figure 4.18), which show a spatial variation in temperature-dependent optical properties.

We have attempted to mitigate this problem by performing optical, electrical, and structural measurements on the same part of each sample whenever possible. However, the thermal non-uniformity is not the same from run-to-run and associated measurement scatter cannot be completely eliminated in this way. In particular experiments where good uniformity is extremely important, more dimensionally stable substrate materials like sapphire can be used. However, if further improvements in reproducibility are desired, redesign of the spray pyrolysis hardware is likely necessary.

Light- and Atmosphere-sensitive Film Properties

As has been noted above, both the choice of atmosphere and exposure to UV light can alter the properties of films. These effects are especially pronounced for undoped ZnO films deposited at low temperatures.

The most sensitive samples were allowed time to equilibrate under ambient atmosphere in the dark before electrical property measurements were made. However, the kinetics of conductivity changes can be quite slow (sometimes requiring multiple days to stabilize) and in some cases, electrical properties were exceedingly sensitive to minor changes in factors like room temperature and humidity. Thus, it was not

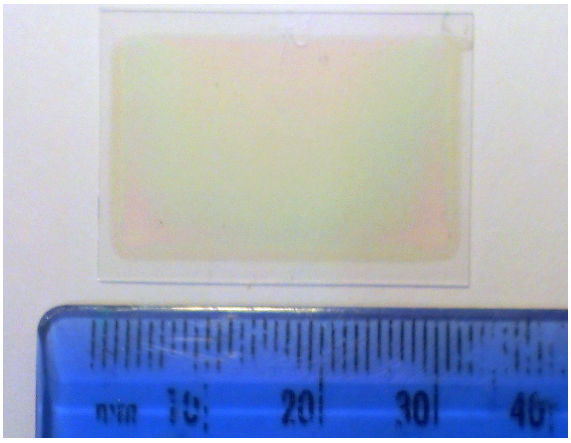

Figure 4.18: TCO film showing characteristic concentric color pattern resulting from temperature non-uniformity of the substrate surface during spray pyrolysis deposition. The contrast and levels in this photograph have been adjusted to enhance the visibility of these features.

always possible to obtain fully stable values. Additionally, the laboratory used did not posses means for the rigorous exclusion of light or regulation of humidity during sample storage, transfer, and measurement. This instability of sample properties likely contributes to some of the experimental scatter observed for certain samples.

Batch Variability in Precursor Salts

The best readily available commercial zinc and indium salts are generally specified as having purities on a trace metals basis of greater than 99.99 % or 99.995 %. This implies that up to 50–100 ppm of cationic impurities are potentially present in these starting materials, which is enough to theoretically cause changes in carrier concentration of up to 2–4×10^{18} carriers per cubic centimeter in ZnO. The reproducibility study reported on in Section 4.5.1 was performed using a single batch of zinc acetate. Results using other batches of zinc acetate or other zinc precursors show similar variance, but with differences of up to one or two standard deviations in the mean value for carrier concentration. As would be expected for impurity scattering, a higher carrier concentration tends to lead to lower mobility values.

The difference in starting material is only really significant in the absence of extrinsic doping; the up to several hundred-fold increase in free carriers upon the intentional addition of donors is more than enough to overwhelm the modest effect of starting material batch variability. For studies on undoped samples, while the

exact values for certain film properties may vary slightly as a function of the batch of starting material used, there is no reason to believe that any of the broader conclusions or trends drawn from this work are compromised by this source of error.

For the sake of comparison, a number of spray pyrolysis depositions were also carried out using conventional reagent grade zinc acetate with a specified overall purity of >98 % (Arcos Organics) and no specification on trace metals purity. For doped films, results similar to those obtained using higher purity zinc acetate were achieved. When these precursors were used to prepare undoped ZnO, the difference in carrier concentration observed was not more than would be expected from the variability observed among different batches of nominally higher purity material. In effect, this batch of far cheaper reagent grade zinc acetate was not found to be appreciably different from the high-purity materials typically used; this fact may be of interest for both future research and commercialization efforts.

Besides these factors mentioned, we believe that other potential sources of experimental error such as instrument measurement errors, variability in solution preparation or spray parameters, etc. are relatively small, either intrinsically or have been made so through process controls.

4.6 Conclusion

The strong sensitivity of spray pyrolysis to process conditions — some might say fascinating richness of the technique — is likely a major source of its reputation for being "less rigorous" than the other common thin film deposition techniques. Indeed, several critical aspects of the process, especially the fundamentals of precursor solution chemistry are not yet systematically understood, meaning that trial and error remains an important part of process design. Research to improve understanding of this aspect of the spray pyrolysis process would certainly be a worthwhile endeavor for future workers in this field.

Nevertheless, with a well-chosen starting chemistry and careful consideration of the influential factors, an informed process design is possible. By doing this, we have developed and demonstrated an implementation of spray pyrolysis with good enough reproducibility to allow detailed examination of a variety of phenomena in

TCOs, ranging from the deeply fundamental to those with immediate practical applications.[55,63,64]

With the basics of TCO thin film characterization and sample preparation by spray pyrolysis now firmly in hand, we are well positioned to return to the central questions posed at the beginning of this thesis. What are the mechanisms that most significantly limit the performance of transparent conducting oxide thin films? And are these limitations *practical* or *fundamental*?

4.7 Experimental

Unless otherwise noted, reagents were used as received without further purification. All chemical manipulations were carried out on the benchtop or in a fume hood, as appropriate.

4.7.1 Base Precursor Solutions

For Preparation of ZnO

A 0.225 M solution of anhydrous zinc acetate (99.99 % metals basis, Aldrich) is dissolved in a 7:93 (by volume) mixture of glacial acetic acid (Analytical Reagent Grade, Fisher Scientific) and deionized water (Ondeo Purite Select Analyst). For each standard deposition run, 4 mL of this aqueous solution is vigorously stirred with ethanol (8 mL, 99.8 %, puriss., absolute, Sigma-Aldrich). 10 mL of the alcohol and aqueous mixture, which has a pH of ∼4.85 and a nominal zinc concentration of 0.075 M, is used in a standard deposition. Since sample thickness is approximately proportional to the amount of precursor solution sprayed, adjustments can easily be made to the thickness of deposited samples if desired.

For Preparation of In_2O_3

A precursor solution based on one previously described in the literature is used.[20] A 0.025 M solution of indium(III) chloride (99.99 % metals basis, Alfa Aesar) is prepared in a 3:1 (by volume) mixture of 0.0375 M hydrochloric acid (Analytical Regent Grade, Fisher Scientific) and ethanol. For a standard deposition, 50 mL of this solution, which has a pH of ∼1.5, is used in the subsequent spraying step.

Conventions for Doping Level

Throughout this thesis, the term "undoped" is used to refer to samples to which no impurities have been intentionally added. (Some other workers would use the phrase "unintentionally doped" to refer to such samples.)

For some samples, various dopants or additives were added to achieve impurity doping or other modifications of the TCO samples. The total concentration of metal and metalloid ions in the final spray solution is kept constant (0.075 M for standard ZnO precursor solutions, and 0.025 M for In_2O_3 precursor solutions).

In all cases, dopant or additive amounts are quoted as a molar fraction of the total concentration of metals in the sample or solution.

Where the hydration state of a precursor is unclear or poorly characterized, the anhydrous value for molecular weight is used in all calculations for consistency. Further, if the mixture is not clear and homogeneous after extended stirring (often due to partial hydrolysis of the dopant precursor), it is gravity filtered with qualitative filter paper before further use. Clearly, both of these may lead to actual doping levels being lower than the nominal values. Further details are provided in Section 6.1.1 demonstrating how nominal doping values translate to actual impurity concentrations for indium-doped ZnO prepared using zinc and indium acetate precursors. In this case, actual doping values in the films are approximately 0.5 of the nominal value in the precursor solutions.

4.7.2 Spray Pyrolysis Procedures

The general apparatus and process used for the spray pyrolysis deposition of thin film TCO samples is as described in this chapter and in Appendix C. However, a few details will be presented here for clarity.

Atomization of Precursor Solutions

Precursor solutions are delivered to the atomizer nozzle (BETE XA PR-050 fog nozzle) at a specified rate of either 0.7 or 2.1 mL/min.

Carrier gas was supplied at a regulated rate of 14.5 L/min (at ∼1.5 atm pressure). Nitrogen carrier gas from the house supply was used, which is supplied by boil-off of high-purity liquid nitrogen. Compressed air from an in-house air compressor was used

without additional purification or filtration beyond that attached to the compressor. Other gases and gas mixtures were ultra-high purity and used as received from BOC gases.

Substrate Selection and Cleaning

24 mm × 32 mm, No 1.5 (0.16–0.19 mm thick) D263T borosilicate glass cover slips (Menzel-Gläser) were typically used as substrates. These were ultrasonically cleaned in an acetone bath, rinsed with fresh acetone, and then dried between two low-lint, low-abrasion lens tissues (Whatman). Any dust was then removed by blowing with house nitrogen prior to use.

4.7.3 Thermal Analysis of Precursors

Thermogravimetric Analysis

TGA measurements were performed either using a Perkin Elmer TGA-7 or a Mettler Toledo TGA/DSC 1 instrument. A known sample mass of between 15–50 mg was placed into an alumina crucible and loaded into the instrument. Sample analyses at the indicated heating rate were run under a constant 30 mL/min flow of the chosen atmosphere. Wet gases were obtained by passing gases through a water bubbler prior to use.

Decomposition of Zinc Acetate Under Spray Pyrolysis Conditions: Cold Trap and NMR Experiment

A spray pyrolysis deposition was carried out using a 0.075 M solution of zinc acetate in deuterium oxide (Apollo Scientific, 99.92 %D) as the precursor solution. 11 mL of this solution was sprayed using a nitrogen carrier gas onto a glass substrate heated to 376 °C. The exhaust from the chamber was routed through several centimeters of Tygon tubing packed with quartz wool and then passed through a dry ice/isopropanol cold trap before being exhausted into the fume hood.

^{1}H NMR of the neat condensate was collected on a Bruker AVIIIHD 400 Nanobay spectrometer and referenced against the **H**DO signal ($\delta = 4.79$ ppm). The only signal observed was $\delta = 1.98$ ppm which is consistent with aqueous acetate and verified by the independent addition of both zinc acetate and acetic acid. Independent addition of acetone resulted in the appearance of an additional signal (Appendix D).

Thermal Volatilization Analysis

The Thermal Volatilization Analysis (TVA) apparatus used has been previously described.[34] Between 20 and 35 mg of each sample, zinc formate dihydrate (Alfa Aesar, 98 %); anhydrous zinc acetate (Aldrich, 99.99 %); and zinc propionate hydrate (Alfa Aesar, 97 %), was loaded into a quartz tube for each analysis. The sample tube is evacuated to a base pressure of $<6 \times 10^{-5}$ Torr prior to analysis.

The samples were heated up to 550 °C at a rate of 10 °C/min, then held at the maximum temperature for 30 minutes. A linear-response Pirani pressure gauge was used to determine the instantaneous pressure of gaseous products being evolved from the samples. One set of experiments was run with a liquid nitrogen cold trap in order to capture condensible products generated above 150 °C (to avoid the collection of large amounts of water). The liquid nitrogen trap was gradually warmed back to room temperature to return the condensible products to the vapor phase in order of volatility. A 1–300 amu Hiden single quadrupole RGA mass spectrometer was used to continuously sample the product streams both during initial decomposition and during distillation of the condensible products. Additionally, several fractions were trapped separately in cells and analyzed by transmission gas-phase FTIR using a Mattson 5000 instrument. The major products of the decomposition reaction were identified by analysis of these data using literature mass and IR spectra, particularly those tabulated in the NIST WebBook.[65]

An additional experiment was run on zinc acetate without the cold trap to determine at which temperatures the now known decomposition products were forming.

Additional details regarding these precursor decomposition experiments are provided in Appendix D.

4.7.4 Acknowledgments

I am most grateful to Prof. John Liggat and Dr. Kimberley Miller of the Polymer Degradation Group at the University of Strathclyde (Glasgow) for their hospitality, as well as for access to and use of their Thermal Volatilization Analysis apparatus.

Ms. Isabel Thomlinson deposited the samples using zinc formate precursors. Ms. Charlotte Meakin provided the data on the deposition rate of In_2O_3 as a function of

precursor solution pH.

References

[1] Badeker, K. *Ann. Phys. (Leipzig)* **1907**, *22*, 749–766.

[2] Lorenz, M. *Pulsed Laser Deposition of ZnO-Based Thin Films*; Ellmer, K.; Klein, A.; Rech, B., Eds.; Transparent Conductive Zinc Oxide: Basics and Applications in Thin Film Solar Cells; Springer: Berlin, Germany, 2008; pp 303–357.

[3] Ashfold, M. N. R.; Claeyssens, F.; Fuge, G. M.; Henley, S. J. *Chem. Soc. Rev.* **2004**, *33*, 23–31.

[4] Singh, R. K.; Narayan, J. *Phys. Rev. B* **1990**, *41*, 8843–8859.

[5] Szyska, B. *Magnetron Sputtering of ZnO Films*; Ellmer, K.; Kein, A.; Rech, B., Eds.; Transparent Conductive Zinc Oxide: Basics and Applications in Thin Film Solar Cells; Springer: Berlin, 2008; pp 187–233.

[6] Ellmer, K. *J. Phys. D: Appl. Phys.* **2000**, *33*, R17–R32.

[7] Bradley, J. W.; Welzel, T. *J. Phys. D: Appl. Phys.* **2009**, *42*, 093001.

[8] Schiller, S.; Goedicke, K.; Reschke, J.; Kirchhoff, V.; Schneider, S.; Milde, F. *Surf. Coat. Technol.* **1993**, *61*, 331–337.

[9] Kelly, P. J.; Arnell, R. D.; Ahmed, W.; Afzal, A. *Mater. Des.* **1996**, *17*, 215–219.

[10] Wakeham, S. J.; Thwaites, M. J.; Holton, B. W.; Tsakonas, C.; Cranton, W. M.; Koutsogeorgis, D. C.; Ranson, R. *Thin Solid Films* **2009**, *518*, 1355–1358.

[11] Helmersson, U.; Lattemann, M.; Bohlmark, J.; Ehiasarian, A. P.; Gudmundsson, J. T. *Thin Solid Films* **2006**, *513*, 1–24.

[12] Perednis, D.; Gauckler, L. *J. Electroceram.* **2005**, *14*, 103–111.

[13] Patil, P. S. *Mater. Chem. Phys.* **1999**, *59*, 185–198.

[14] Mooney, J. B.; Radding, S. B. *Ann. Rev. Mater. Sci.* **1982**, *12*, 81–101.

[15] Tomar, M. S.; Garcia, F. J. *Prog. Cryst. Growth Ch.* **1981**, *4*, 221–248.

[16] Pamplin, B. R. *Prog. Cryst. Growth Ch.* **1979**, *1*, 395–403.

[17] Nathan, A.; et al. *Proc. IEEE* **2012**, *100*, 1486–1517.

[18] MacDonald, W. A. *J. Mater. Chem.* **2004**, *14*, 4–10.

[19] Auch, M. D. J.; Soo, O. K.; Ewald, G.; Soo-Jin, C. *Thin Solid Films* **2002**, *417*, 47–50.

[20] Benamar, E.; Rami, M.; Messaoudi, C.; Sayah, D.; Ennaoui, A. *Sol. Energy Mater. Sol. Cells* **1999**, *56*, 125–139.

[21] Lee, J.-M.; Choi, B.-H.; Ji, M.-J.; An, Y.-T.; Park, J.-H.; Kwon, J.-H.; Ju, B.-K. *Thin Solid Films* **2009**, *517*, 4074–4077.

[22] Jansen, K. W.; Delahoy, A. E. *Thin Solid Films* **2003**, *423*, 153–160.

[23] Ghosh, R.; Basak, D.; Fujihara, S. *J. Appl. Phys.* **2004**, *96*, 2689–2692.

[24] Vispute, R. D.; Talyansky, V.; Choopun, S.; Sharma, R. P.; Venkatesan, T.; He, M.; Tang, X.; Halpern, J. B.; Spencer, M. G.; Li, Y. X.; Salamanca-Riba, L. G.; Iliadis, A. A.; Jones, K. A. *Appl. Phys. Lett.* **1998**, *73*, 348–350.

[25] Ohtomo, A.; Tamura, K.; Saikusa, K.; Takahashi, K.; Makino, T.; Segawa, Y.; Koinuma, H.; Kawasaki, M. *Appl. Phys. Lett.* **1999**, *75*, 2635–2637.

[26] Studenikin, S. A.; Golego, N.; Cocivera, M. *J. Appl. Phys.* **1998**, *83*, 2104–2111.

[27] Bacaksiz, E.; Parlak, M.; Tomakin, M.; Özçelik, A.; Karakız, M.; Altunbaş, M. *J. Alloys Compd.* **2008**, *466*, 447–450.

[28] Lyons, J. L.; Steiauf, D.; Janotti, A.; Van de Walle, C. G. *Phys. Rev. Appl.* **2014**, *2*, 064005.

[29] Wagata, H.; Ohashi, N.; Katsumata, K. I.; Segawa, H.; Wada, Y.; Yoshikawa, H.; Ueda, S.; Okada, K.; Matsushita, N. *J. Mater. Chem.* **2012**, *22*, 20706–20712.

[30] Rudolph, G.; Henry, M. C. *Inorg. Chem.* **1964**, *3*, 1317–1318.

[31] Ghule, A. V.; Lo, B.; Tzing, S. H.; Ghule, K.; Chang, H.; Ling, Y. C. *Chem. Phys. Lett.* **2003**, *381*, 262–270.

[32] Koyama, H.; Saito, Y. *Bull. Chem. Soc. Jpn.* **1954**, *27*, 112–114.

[33] Betard, A.; Wannapaiboon, S.; Fischer, R. A. *Chem. Commun.* **2012**, *48*, 10493–10495.

[34] McNeill, I. C.; Ackerman, L.; Gupta, S. N.; Zulfiqar, M.; Zulfiqar, S. *J. Polym. Sci., Polym. Chem. Ed.* **1977**, *15*, 2381–2392.

[35] Renz, M. *Eur. J. Org. Chem.* **2005**, *2005*, 979–988.

[36] Baruah, S.; Dutta, J. *Sci. Technol. Adv. Mater.* **2009**, *10*, 013001.

[37] Paraguay, D. F.; Estrada, L. W.; Acosta, N. D. R.; Andrade, E.; Miki-Yoshida, M. *Thin Solid Films* **1999**, *350*, 192–202.

[38] Caillaud, F.; Smith, A.; Baumard, J.-F. *J. Am. Ceram. Soc.* **1993**, *76*, 998–1002.

[39] Jun, T.; Song, K.; Jeong, Y.; Woo, K.; Kim, D.; Bae, C.; Moon, J. *J. Mater. Chem.* **2011**, *21*, 1102–1108.

[40] O'Brien, P.; Saeed, T.; Knowles, J. *J. Mater. Chem.* **1996**, *6*, 1135–1139.

[41] Baes, Jr., C. F.; Mesmer, R. E. *The Hydrolysis of Cations*; Wiley: New York, NY, 1976.

[42] Lee, S.; Jeong, S.; Kim, D.; Park, B. K.; Moon, J. *Superlattices Microstruct.* **2007**, *42*, 361–368.

[43] Ong, B. S.; Li, C.; Li, Y.; Wu, Y.; Loutfy, R. *J. Am. Chem. Soc.* **2007**, *129*, 2750–2751.

[44] Choi, C. G.; Seo, S.-J.; Bae, B.-S. *Electrochem. Solid-State Lett.* **2008**, *11*, H7–H9.

[45] Degen, A.; Kosec, M. *J. Eur. Ceram. Soc.* **2000**, *20*, 667–673.

[46] Thompson, L. C. A.; Pacer, R. *J. Inorg. Nucl. Chem.* **1963**, *25*, 1041–1044.

[47] Meyers, S. T.; Anderson, J. T.; Hung, C. M.; Thompson, J.; Wager, J. F.; Keszler, D. A. *J. Am. Chem. Soc.* **2008**, *130*, 17603–17609.

[48] Mitra, P.; Khan, J. *Mater. Chem. Phys.* **2006**, *98*, 279–284.

[49] Martell, A. E.; Smith, R. M. *Critical Stability Constants: First Supplement*; Springer: New York, NY, 1982; pp 284–332.

[50] Minami, T.; Sato, H.; Inamoto, H.; Takata, S. *Jpn. J. Appl. Phys.* **1992**, *31*, L257–L260.

[51] Buchholz, D. B.; Ma, Q.; Alducin, D.; Ponce, A.; Jose-Yacaman, M.; Khanal, R.; Medvedeva, J. E.; Chang, R. P. H. *Chem. Mater.* **2014**, *26*, 5401–5411.

[52] Mollwo, E.; Breckendridge, R. G.; Russell, B. R.; Hahn, E. E., Eds.; Photoconductivity Conference (Atlantic City); John Wiley and Sons: New York, NY, 1954; p 509.

[53] Heiland, G. *J. Phys. Chem. Solids* **1961**, *22*, 227–234.

[54] Shapira, Y.; McQuistan, R. B.; Lichtman, D. *Phys. Rev. B* **1977**, *15*, 2163–2169.

[55] Vai, A. T.; Kuznetsov, V. L.; Dilworth, J. R.; Edwards, P. P. *J. Mater. Chem. C* **2014**, *2*, 9643–9652.

[56] Sreenivas, K.; Rao, T. S.; Mansingh, A.; Chandra, S. *J. Appl. Phys.* **1985**, *57*, 384–392.

[57] Lin, T.-C.; Chang, S.-C.; Chiu, C.-F. *Mater. Sci. Eng., B* **2006**, *129*, 39–42.

[58] Oh, B.-Y.; Jeong, M.-C.; Kim, D.-S.; Lee, W.; Myoung, J.-M. *J. Cryst. Growth* **2005**, *281*, 475–480.

[59] Chang, J. F.; Lin, W. C.; Hon, M. H. *Appl. Surf. Sci.* **2001**, *183*, 18–25.

[60] Natsume, Y.; Sakata, H. *J. Mater. Sci.: Mater. Electron.* **2001**, *12*, 87–92.

[61] Kang, H. S.; Kang, J. S.; Kim, J. W.; Lee, S. Y. *J. Appl. Phys.* **2004**, *95*, 1246–1250.

[62] Gupta, V.; Mansingh, A. *J. Appl. Phys.* **1996**, *80*, 1063–1073.

[63] Vai, A. T.; Kuznetsov, V. L.; Jain, H.; Slocombe, D.; Rashidi, N.; Pepper, M.; Edwards, P. P. *Z. Anorg. Allg. Chem.* **2014**, *640*, 1054–1062.

[64] Rashidi, N.; Vai, A. T.; Kuznetsov, V. L.; Dilworth, J. R.; Edwards, P. P. *Chem. Commun.* **2015**, *51*, 9280–9283.

[65] Stein, S. E. *Mass Spectra and Infrared Spectra*; Linstrom, P. J.; Mallard, W. G., Eds.; NIST Chemistry WebBook, NIST Standard Reference Database Number 69; National Institute of Standards and Technology: Gaithersburg, MD, 2011.

Chapter 5

The Intrinsic Conductivity of Zinc and Indium Oxides

Having covered essential background on the physics of transparent conducting oxides and laid out the means by which samples will be prepared and studied, it is now time to turn our focus specifically onto the factors which limit the performance of these materials.

With the intent of starting from the most intrinsic and fundamental behaviors of TCO materials before adding additional layers of complexity, the properties of ordered TCO domains will be the main topic of discussion in this chapter. Admittedly, with any real samples and especially the spray pyrolyzed ones that lie at the core of this thesis, it is impossible to completely separate "intrinsic" behavior from that due to "extrinsic" factors like impurity doping and grain boundaries. Nevertheless, at the risk of perpetuating a slightly contrived distinction, these latter topics will mostly be left to their own dedicated chapters which follow.

Interestingly, the performance of ZnO and In_2O_3 do not differ dramatically when they are examined as carefully prepared single crystals. The key scattering mechanisms that define maximum conductivity in this case will be discussed and illustrated using data on these materials collected from the literature. The example of bromide-doped indium oxide will then be used to highlight some of the assumptions that typically go into the modeling of these mechanisms, and thus situations where performance limits may be higher than they seem at first glance.

Then, the experimental observation of the doping-induced metal-to-non-metal transition in ZnO thin films will be examined as another example of an important

physical phenomenon that can occur within an ordered TCO domain. The transformation of a semiconductor to a metal with degenerate conduction is one of the most dramatic electronic transitions, and how it may be controlled is of central importance to applying TCOs as engineering materials.

Finally, it will be shown how and where this single crystal picture of performance limits begins to break down, especially in the case of ZnO. As a prelude to upcoming chapters, optical frequency electronic transport measurements will allow a look inside the grains of polycrystalline IZO and ITO thin films, showing that going beyond the single crystal is essential to fully understanding the performance differences between these two materials.

5.1 Single Crystal Behavior: A Literature Review

5.1.1 Transport Limitations at Lower Defect Concentrations

Carefully prepared single crystals with low defect concentrations are perhaps the clearest experimental manifestation of the intrinsic transport properties of TCO materials. In this way, such systems represent a sensible starting point for the discussion at hand. In the limit of low defect concentrations, carrier transport is most limited by scattering mechanisms related to various classes of thermally driven collective distortions in the structure of the material that can be described using quasi-particles called *phonons*.

Phonons can be classed as optical or acoustic depending on whether the oscillation of neighboring atoms is out-of-phase or in-phase at the long wavelength limit, respectively. Because the wurtzite crystal structure lacks inversion symmetry, additional piezoelectric modes must be considered in the case of ZnO (but not in In_2O_3, which has the centrosymmetric bixbyite structure). Because expressions for the temperature-dependence of carrier mobility when limited by these various phonon modes are listed in a review on this topic, they will not all be reproduced here.[1]

Ellmer has compiled data on low carrier concentration ZnO samples to demonstrate that experimental mobility data at temperatures above about 100 K can be very successfully reproduced by assuming just these carrier-phonon scattering mechanisms.[2] Thus, the room-temperature mobility of a low-defect solid is mostly determined by the details of its phonon spectrum, which arise from the connectivity

and identity of its constituent atoms. As such, this type of scattering due to atomic vibrations probably represents the most fundamental and inescapable limit on the conductivity of a TCO with a given structure.

For the comparison of ZnO and In_2O_3, the Hall effect measurements on carefully prepared single crystals with low defect concentrations previously carried out by Hutson[3] and Weiher[4] are particularly useful. In both cases, single crystals were grown by a gas phase reaction of oxygen and the appropriate metal vapor, and then characterized as a function of temperature. A selection of their data for crystals with similar room temperature carrier concentrations is presented in Figure 5.1.

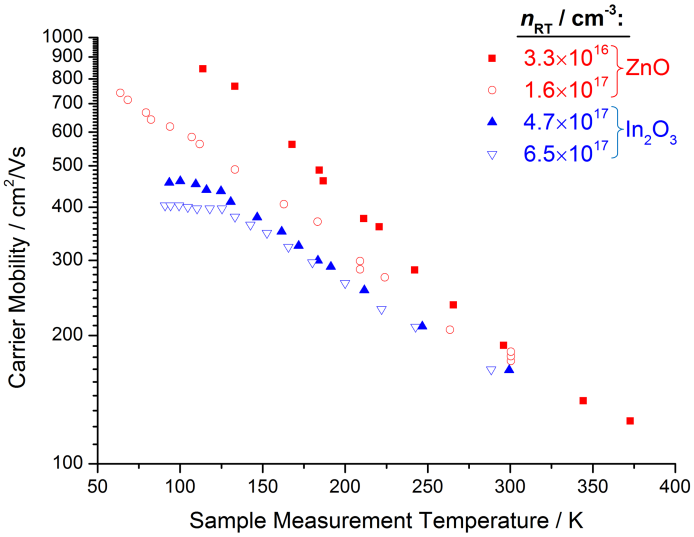

Figure 5.1: Hall mobility of low defect concentration ZnO (red) and In_2O_3 (blue) single crystals as a function of room temperature carrier concentration (n_{RT}) and sample temperature. ZnO data are from Hutson[3] and In_2O_3 data are from Weiher.[4]

The first thing that should stand out about the four datasets in this figure is their similarity. Regardless of whether the data are from ZnO or In_2O_3, the room temperature mobility for these samples lies in a fairly narrow range between 165–190 $cm^2\,V^{-1}\,s^{-1}$. This would imply that the phonon-limited mobility is very similar for both materials, a rather remarkable fact given how different the crystal structures of ZnO and In_2O_3 are. In fact, it may even be fairly argued that these two TCOs have almost the same conductivity limits in this simple, single-crystal case.

The key conclusion to be drawn is that differences in structure-dependent phonon spectrum are not nearly sufficient to explain the vastly different behavior of ZnO- and In_2O_3-based *thin films* that is observed in practice. Put another way, the majority of

the practical performance difference between these two materials must therefore arise from how they respond to impurity doping, and to the disorder, polycrystallinity, and other non-idealities that inevitably arise from the use of large area thin film deposition techniques.

5.1.2 Transport Limitations at Higher Defect Concentrations

Of course, even such carefully prepared single crystal samples are far from being truly defect free. Figure 5.1 shows that there are differences in how the carrier mobility of these samples changes with temperature. Especially as the temperature is lowered, the effects of scattering by impurities begin to substantially affect the carrier mobility in samples, even at low defect concentrations.[5,6] This arises because the drift velocity of carriers is reduced at lower temperatures, which results in longer carrier-scatterer interaction times and thus stronger scattering. The observed trend is consistent with higher defect concentrations leading to more impurity scattering at low temperatures, as is expected for such non-degenerately conducting samples.

Impurity scattering effects must be carefully considered because most of the samples discussed in this thesis (and indeed, most technologically-relevant TCO samples in general) can be considered to have "higher" defect concentrations. Regardless of whether the defects are due to intentionally introduced impurities, or result from the natural tendency of n-type TCOs to form with an oxygen-deficient stoichiometry, their role as scatterers becomes increasingly significant as their concentration increases.

Several different approaches have been adopted to model the effects of ionized impurity scattering, including that of Conwell and Weisskopf,[5] that of Brooks, Herring, and Dingle,[7] and that of Ridley.[8] Additionally, a wide range of corrections and refinements have been proposed to account for factors like the non-parabolicity of the conduction band. As with phonon scattering, a detailed review of the physics of impurity scattering is beyond the scope of this thesis and the interested reader is referred to a detailed review by Chattopadhyay and Queisser.[9]

However, several key qualitative features common to these results should be highlighted. The first is the rather intuitive point that a higher concentration of defects will naturally lead to a higher scattering rate, and hence, a lower carrier mobility. The

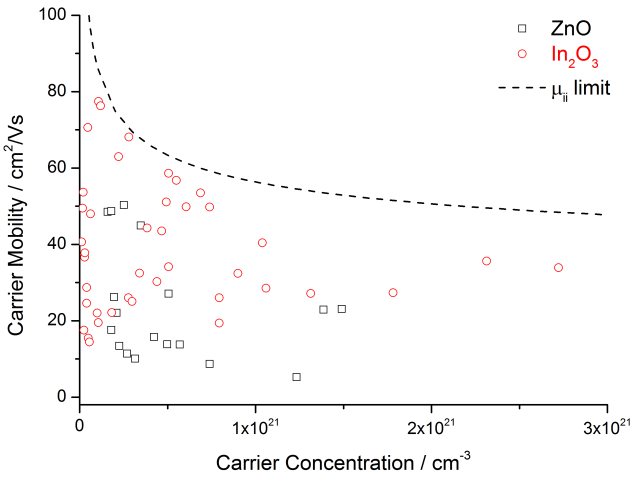

Figure 5.2: Literature carrier concentration and mobility data for ZnO (black squares) and In_2O_3 (red circles) samples compiled by Bellingham, *et al.*[10] The performance limit implied by ionized impurity scattering as described by Equation 5.1 and using the parameters listed in the main text is shown as a dashed curve.

second is that as the defect concentration continues to rise and conduction in the TCO becomes degenerate, the effect of ionized impurity scattering becomes temperature-independent, meaning that it must also be considered at and above room temperature.

Given the additive nature of scattering mechanisms (Equation 2.13), impurity scattering will only ever lower the mobility limit initially set for a material by phonon scattering in the low defect case. In fact, several authors have pointed to ionized impurity scattering as the dominant mechanism that defines the maximum achievable carrier mobility in materials with high defect concentrations.[10,11]

Figure 5.2 plots literature data on ZnO and In_2O_3 that have been compiled by Bellingham, *et al.*[10] Also included in this figure is a curve representing the limit on mobility as a function of n as calculated using a theoretical model for ionized impurity scattering in a degenerate conductor, assuming a screened impurity potential (the Brooks-Herring-Dingle approach) and a parabolic conduction band:

$$\mu_{\mathrm{ii}}(n) = \frac{3(\epsilon_s\epsilon_0)^2 h^3}{Z^2 e^3 m^{*2}} \frac{n}{N_i} \left(\ln(1+\xi) - \frac{\xi}{1+\xi} \right)^{-1}, \tag{5.1}$$

where

$$\xi = (3\pi^2)^{1/3} \frac{(\epsilon_s\epsilon_0) h^2 n^{1/3}}{m^* e^2} \tag{5.2}$$

and $(\epsilon_s\epsilon_0)$ is the low-frequency dielectric constant, n is the carrier concentration, N_i is the concentration of impurities each with charge Z, and m^* is the effective

mass of the carrier.[2] For the calculation of $\mu_{ii}(n)$ shown, it is assumed $m^* = 0.3m_e$, $\epsilon_s = 8.5$[i], and $n = N_i$. Additionally, the enhancement in impurity scattering rate by electron-electron collisions is also accounted for.[14]

The limit in electrical performance implied by even this relatively simple model of ionized impurity scattering reflects the upper limits of performance in this set of samples fairly well. The fact that the theoretical and experimentally achieved boundaries deviate more at the highest carrier concentrations could be because of a reduction in n relative to N_i due to increasingly inefficient doping at higher doping levels (Chapter 6).

As an aside, it is very interesting to note that silicon doped to similar carrier concentrations as these TCOs exhibit almost the same maximum values of carrier mobility, despite having undoped electron mobilities that are nearly an order of magnitude higher ($\sim$1400 $\mathrm{cm^2\,V^{-1}\,s^{-1}}$) than those observed in the low-defect ZnO and In_2O_3 single crystals ($\sim$180 $\mathrm{cm^2\,V^{-1}\,s^{-1}}$).[15] This clearly illustrates how, in samples with high defect concentrations, the tighter mobility limit imposed by impurity scattering effectively replaces the looser and more general one imposed by phonon scattering. Furthermore, it suggests that there is some generality to this description of ionized impurity scattering in semiconductors beyond just the TCOs.

It also should be emphasized that the performance line drawn based on impurity scattering represents a *limit* and not a guarantee. The data in Figure 5.2, clearly shows that it is possible (and indeed, likely) to produce samples that lie quite a bit below the $\mu_{ii}(n)$ limit curve. This simply reflects that one of the many other possible factors that can introduce scattering and reduce mobility — from further structural disorder to grain boundary effects (Chapter 7) — is of significance in that particular sample.

Besides phonon and ionized impurity scattering, there are also other possible scattering mechanisms intrinsic to a single crystalline domain. For example, at lower temperatures where there is not enough thermal energy for many defects to be ionized, neutral impurity scattering is likely to become more important.[6,16] Similarly, the ability of electron-electron scattering to directly change net carrier momentum

[i]This value is to approximately split the difference between reported literature values of $\sim$8 for ZnO[12] and 9 for In_2O_3.[13]

through Umklapp processes in very pure crystals at low temperature may also need to be considered in some circumstances.[17,18]

Nevertheless, near room temperature and at defect concentrations relevant to most TCO applications, these higher-order effects are comparatively insignificant and can usually be safely neglected. Thus, in the typical situation here, the upper bound of carrier mobility in a crystalline domain is first determined by the actual crystal structure of the material via lattice phonon scattering, and then increasingly by scattering due to ionized impurities as the defect concentration rises.

5.2 The Case of Bromide-doped In_2O_3

The scattering mechanisms discussed in the preceding section are indeed fairly general and will always be valid in a broad sense. However, it is inevitable that various simplifications and assumptions underlie the specific theoretical models used to quantify these phenomena. By identifying and exploiting cases where the model assumptions do not strictly hold, there arises a possibility that such apparent "theoretical limits" could be exceeded to some extent.

To illustrate this possibility, this section considers the example of bromide-doped indium oxide (IBrO) thin films that we have prepared by spray pyrolysis. Some of these samples exhibit surprisingly high carrier mobilities for a given carrier concentration, with values approaching or even slightly exceeding the limit implied by the ionized impurity scattering model of Equation 5.1. After laying out the properties of this material, we will discuss which assumptions about mobility limits might be suspect in the case of IBrO. Not only will this help to explain the behavior of this particular material, it may also be useful for suggesting a few more general workarounds to projected performance limits in TCO single crystals.

5.2.1 Electrical Properties

In the standard preparation of indium oxide by spray pyrolysis, indium(III) chloride is used as the precursor and dissolved in a solvent of dilute hydrochloric acid and ethanol. It has been found that instead substituting indium(III) bromide and dilute

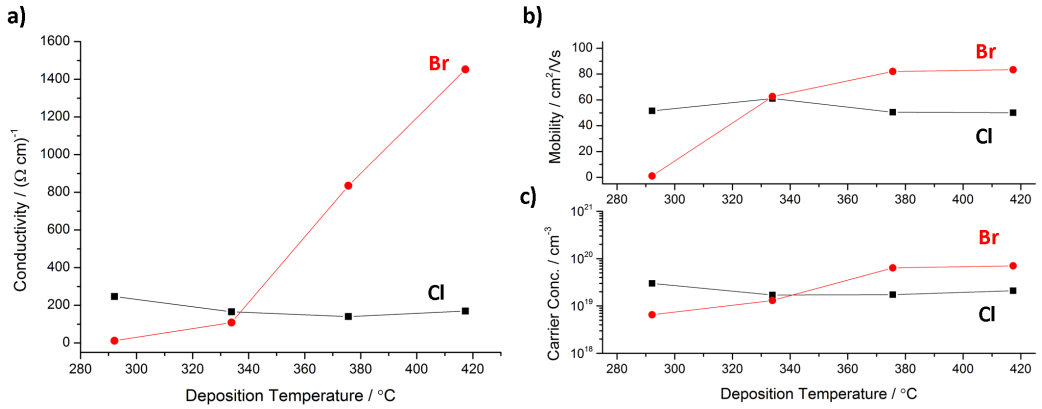

Figure 5.3: a) Electrical conductivity, and Hall effect b) mobility and c) carrier concentration of In_2O_3 films deposited using spray pyrolysis from indium(III) chloride (black) and indium(III) bromide (red) precursors.

hydrobromic acid for the analogous chloride components leads to samples with substantially different electrical properties as a function of deposition temperature. This is shown using the conductivity and Hall effect measurements in Figure 5.3.

At higher deposition temperatures, the samples prepared from bromide precursors have much higher electrical conductivity than those prepared using chlorides. For the samples with $T_{dep} = 417\,°C$, the difference is almost a factor of ten. The Hall effect data show that this conductivity improvement happens because of significant increases in both carrier concentration and mobility to average values of $n = 7 \times 10^{19}\,cm^{-3}$ and $\mu = 83.3\,cm^2\,V^{-1}\,s^{-1}$, respectively. The maximum mobility observed in samples prepared under these conditions was $89.6\,cm^2\,V^{-1}\,s^{-1}$. These results are quite surprising because an increase in carrier concentration is usually accompanied by a drop in mobility because of the effects of ionized impurity scattering.

It is also possible to achieve similar carrier concentrations around $10^{20}\,cm^{-3}$ by light tin doping of In_2O_3 prepared using the baseline $InCl_3$ precursor. While we do not have extensive results from such samples, the best carrier mobilities we have obtained for this type of spray pyrolyzed ITO are typically around 30–35 $cm^2\,V^{-1}\,s^{-1}$. This is less than half of the mobility values seen when $InBr_3$ is used. More generally, literature ITO samples prepared using any technique with approximately this carrier concentration tend to have mobilities that peak around 40–50 $cm^2\,V^{-1}\,s^{-1}$, with only a few scattered reports of higher values.[19]

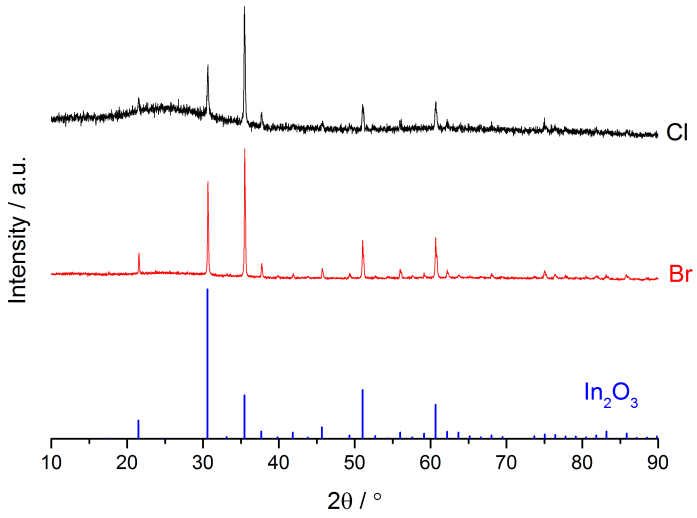

Figure 5.4: Normalized X-ray diffraction patterns of In_2O_3 thin films prepared by spray pyrolysis at $T_{dep} \approx 417\,°C$ using indium(III) chloride (black) and indium(III) bromide (red) precursors. A reference stick chart for bixbyite In_2O_3 powder is shown in blue.

5.2.2 Determination of Chemical Identity

Especially given the remarkable change in properties resulting from the replacement of chloride with bromide in the spray pyrolysis process, it was important to verify the chemical identity of these thin films and the fact that bromide doping was actually occurring. Figure 5.4 compares the XRD patterns collected from thin films deposited using each precursor at a deposition temperature of 417 °C. Bixbyite In_2O_3 is the only crystalline phase observed in each of the patterns. The signal-to-noise ratio is better for the sample deposited from $InBr_3$, which may be due to a higher specific deposition rate and a slightly thicker film.

A Pawley refinement[ii] of the two patterns revealed that the cubic lattice parameter of the sample deposited using $InBr_3$ was 10.1263 ± 0.0004 Å, significantly larger than the value of 10.1172 ± 0.0006 Å found for the films deposited using $InCl_3$ or the literature value of 10.117 ± 0.001 Å reported for undoped In_2O_3 powders.[20] Given that Br^- has an ionic radius of around 196 pm, larger than the ~140 pm for O^{2-}, this increase of lattice parameter is highly suggestive of the incorporation of bromide into the In_2O_3 lattice.[21]

[ii] Graphical fitting results and residuals are shown in Appendix E.

Several EDX spectra were also collected from the films prepared using $InBr_3$ precursors and an example is shown in Figure 5.5b. In addition to obvious signals for indium and oxygen in an atom ratio consistent with slightly oxygen deficient In_2O_3, there is a small, but very likely real signal for bromine at around 1.48 eV.[iii] The bromide doping level calculated from the spectrum shown was 0.94 ± 0.29 at% (of total metal in the sample). If this amount of bromide was assumed to be substituting for oxide in In_2O_3, it would be more than enough to account for the observed increase in carrier concentration relative to the samples prepared using $InCl_3$. Incidentally, chloride was below detection limits by EDX for thin film samples prepared using chloride precursors (Figure 5.5a).

On the basis of the observed lattice distortion suggestive of impurity doping and the EDX analysis showing appreciable bromine incorporation, these samples have been identified as bromide-doped indium oxide.

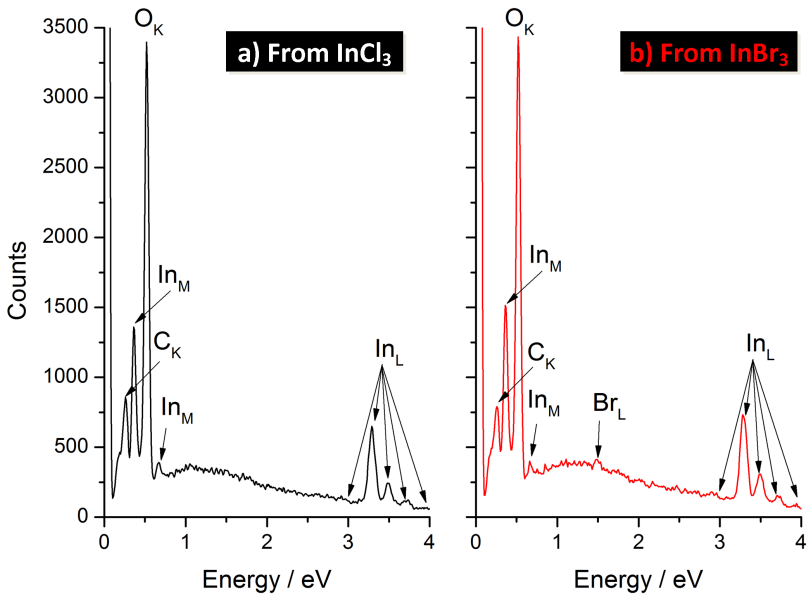

Figure 5.5: 5 kV excitation energy dispersive X-ray (EDX) spectra of In_2O_3 films prepared using a) indium(III) chloride and b) indium(III) bromide precursors. Peaks are labeled with their corresponding assignments. Bromine and chlorine (Cl_K peaks expected at 2.62 and 2.82 eV) are below detection limits in the samples deposited from a chloride precursor (a).

[iii] Based on automatic calculation of noise statistics by the AZtec software, the level of statistical significance for the signal shown is $3.2\,\sigma$ or 99.93 %

5.2.3 Potential Workarounds to Mobility Limits

The electrical properties of the most conductive of these IBrO films remain impressive even when placed in the context of all In_2O_3-based films that have ever been reported. Looking back to the literature data on TCOs from all techniques summarized in Figure 5.2, it can be seen that the best mobility values for samples prepared using $InBr_3$ are higher that those of any others shown in this carrier concentration range. This is particularly notable because Bellingham, *et al.*, who originally compiled these data, admit to having chosen literature results "showing low resistivity at any particular carrier concentration."[10]

It should be noted, however, that the results in Figure 5.2 are almost all from tin-doped indium oxide samples prepared using "conventional" vacuum-based techniques. More recently, there have been a series of reports on other In_2O_3-based materials showing anomalously high mobilities compared to more traditional ITO samples. Examples of these include molybdenum-doped indium oxide,[22–24] titanium-doped indium oxide,[25] as well as ITO itself subjected to a high temperature zone-refining process.[26] The clear implication is that the impurity scattering models that have been traditionally used to describe ITO are actually of limited scope, and that IBrO may well be a new example of this class of In_2O_3-based materials with higher than expected mobility. Two possibilities for why this could be the case will be discussed.

Structural Limits on Mobility

In calling carrier-phonon scattering a "limit" to mobility, it is implicitly being assumed that the structure of a given TCO is essentially fixed. This is not necessarily true in general. In many cases, a deviation from the base crystalline structure can be thought of as introducing defects that would act as additional scattering centers and decrease mobility. However, in principle, it is also possible to imagine structural changes that might allow for an *increase* in carrier mobility. For instance, an isotropic compression of the unit cell could improve the spatial overlap of atomic orbitals. All else being equal, this would increase the electronic band width, reducing carrier effective mass and leading to higher carrier mobilities.

Specifically in the case of n-type TCOs like In_2O_3 and ZnO, an even more remarkable case of non-harmful structural distortion can occur, namely the fact that high

electrical mobilities and conductivities can be achieved even in entirely amorphous forms of these materials. Some of the most notable examples of these are amorphous indium-zinc, and indium-gallium-zinc oxides.[27–29]

The relative insensitivity of electronic conduction in TCOs to structural disorder has been attributed to the fact that the conduction band edge is mostly composed of spherically symmetric metal s states, whose overlap depends only on the distance and not the relative angle between neighboring metal centers.[30,31] This is further helped by the tendency for local oxide coordination around metals to be maintained even in the absence of long-range order, meaning these s states are only slightly perturbed by a loss of crystallinity.[32] Contrast this to the case of silicon where the valence and conduction band edges are more directional p states whose overlap is profoundly affected by changes in local coordination. This accounts for the fact that amorphous silicon has much lower mobilities than crystalline Si.[33]

It has been reported that amorphous indium oxide thin films can exhibit nearly the same mobilities as crystalline In_2O_3.[34] Further, structural studies have been used to correlate increased mobility in amorphous In_2O_3 to structural distortions that cause reductions in the average In-In bond distance.[35]

To consider how these ideas apply to the IBrO samples here, a DFT geometry optimization was carried out on a $2\times2\times2$ supercell (640 atoms) of In_2O_3 in the bixbyite structure, and then again with one of the oxide ions near the center substituted with a bromide. Assuming perfect doping efficiency, this doping level corresponds to an impurity concentration of about $1.2\times10^{20}\,cm^{-3}$ or a doping level of $\sim$0.4 at%, which is comparable to the experimental carrier concentrations and elemental analysis results.

First, this calculation shows that the larger bromide anion can be reasonably accommodated at an oxide position in In_2O_3 even without any changes to the overall size of the supercell. Figure 5.6 shows the computationally optimized local environment within 4.2 Å of the bromide dopant atom. Second, the distortions that make this possible lead both to a broadening of the distribution of the In-In distances, as well as a marked skew towards shorter values of the same (Figure 5.7). Since electrical charge tends to travel along paths of least resistance, the creation of shorter metal-metal contacts due to bromide doping would be consistent with the higher mobilities observed in experimental IBrO samples.

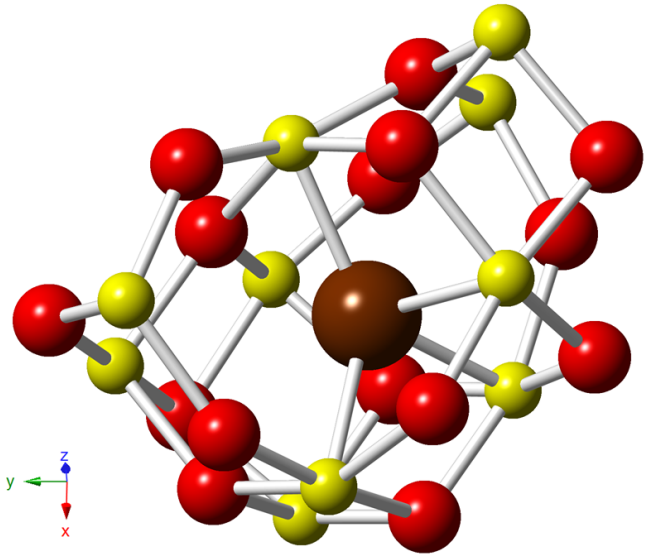

Figure 5.6: Local environment around bromide dopant (brown) at an oxide site in IBrO as calculated using DFT. Indium and oxygen atoms are shown as yellow and red, respectively.

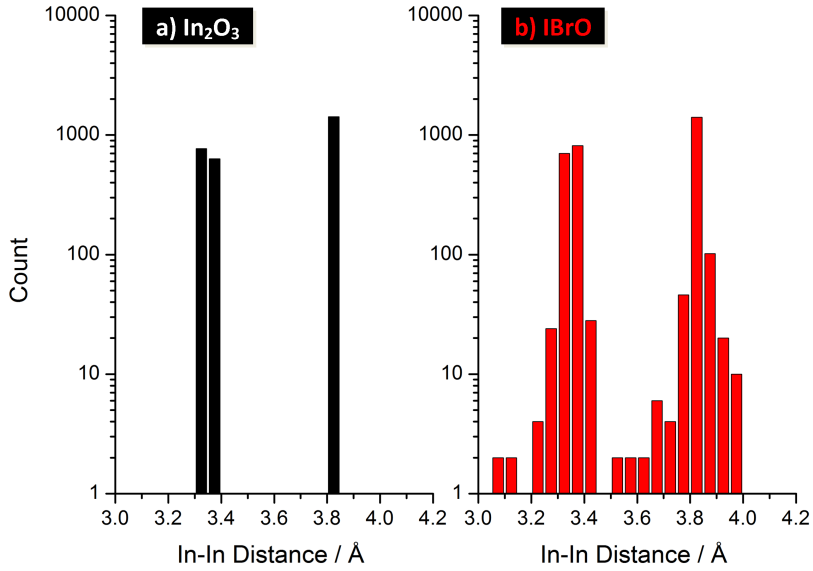

Figure 5.7: Calculated distribution of In-In bond distances (<4.2 Å) in $2 \times 2 \times 2$ supercells of a) undoped In_2O_3 and b) bromide-doped In_2O_3.

While all the classic n-type TCOs possess conduction band minima composed mostly of metal s states, this should not be taken to imply that such materials will all respond equally to the effects of structural disorder. There are numerous reports indicating that somewhat conductive amorphous ZnO is possible. However, much lower mobilities are generally reported for α-ZnO than for wurtzite ZnO.[36–38] It may be that the overlap of Zn 4s states has greater sensitivity to increases in metal-metal distance than the larger and more diffuse In 5s states that make up the conduction band in In_2O_3. This could be one of the intrinsic factors distinguishing these two TCO materials.

Ionized Impurity Scattering

As for impurity scattering, a key assumption made in almost all theoretical models is that both charge carriers and impurities are uniformly distributed through the material. Clearly, if mobile charge carriers can somehow be spatially separated from the charged defects that generate them, the net effect of ionized impurity scattering will be reduced below the levels implied by a uniform distribution.

The most direct method that has been proposed for achieving such a separation is to prepare TCO films with a layered structure. This can be done using modulation doping, where various techniques are used to introduce a spatial variation in impurity concentration,[39–41] by the use of layered superlattices of different TCO materials,[42,43] or simply by considering materials with a naturally layered structure.[44,45]

However, more subtle approaches are also possible. It has already been discussed that conduction in degenerately-doped n-type TCOs occurs within a conduction band composed mostly of metal s orbitals. If for symmetry or energetic reasons, the orbitals of a donor impurity atom do not substantially mix with those forming the conduction band, then the average distance between carriers in conduction band states and the impurity will be larger than if the carriers were truly uniformly distributed through the oxide. In this case, the total magnitude of carrier-impurity scattering is reduced. This explanation has been proposed to explain the surprisingly high electron mobilities observed in molybdenum-doped indium oxide, where computation has been used to show that molybdenum's orbitals contribute very little to the conduction band when it is substituted for indium in In_2O_3.[46]

More directly relevant to the present case, similar arguments have been advanced to suggest that anion doping should lead to less electron scattering, because the filled oxide 2p orbitals contribute mostly to the valence band in TCOs.[47] Speculatively, this could mean that the substitution of bromide for oxide in IBrO primarily perturbs the valence band, whereas substitution of tin for indium in ITO primarily perturbs the conduction band, which in turn leads to greater conduction electron scattering in the latter case.

5.2.4 Current Limitations and Future Work

While these intriguing results on IBrO suggest the promise in this doping approach, it must be admitted that the present implementation of bromide doping has significant limitations and is not yet a practical process. It can easily be seen that the concentration of bromide in the precursor solution far exceeds what is retained within the film. The vast majority of this bromide is lost during the thermal decomposition of the precursor solution, probably as volatile HBr. Thus far, we have been unable to systematically increase the amount of bromide in the film by increasing its concentration in the precursor solution.

Unfortunately, this has prevented the study of this potentially interesting material as a function of doping level, which would be essential for further elucidating the doping mechanism. The inability to control doping level in spray pyrolysis has also severely limited efforts at further optimizing electrical performance. In the future, it would be very interesting to try to prepare bromide-doped In_2O_3 using a deposition technique that offers better compositional control. One potential option would be a reactive sputtering process where bromide is introduced to the system as either gaseous Br_2 or HBr.

An improved theoretical understanding of the influence of bromide on the electronic structure of In_2O_3, perhaps obtained through a computational study, will also be useful for assessing the mechanisms proposed here and for determining how IBrO fits in with the other examples of "high-mobility" In_2O_3 that have been mentioned. Furthermore, experimental local structure measurements of the type applied to indium-doped ZnO in Chapter 6 would be useful for determining whether the

structural changes due to bromide-doping suggested by DFT are occurring in real samples.

5.3 A Doping-induced Transition to the Metallic State in ZnO

In the Drude picture, conductivity is governed not only by the mobility of free carriers, but also by their number density. In this section, it will be seen how changes in the impurity and carrier concentrations of ZnO thin films can lead to one of the most fundamental electronic transitions possible in a material, that from a semiconductor to a metal.

At very low defect concentrations, zinc oxide is a semiconductor with low electrical conductivity, in which any electronic conduction is due to electrons thermally excited into the conduction band or the hopping of carriers among spatially isolated impurity states. However, as the density of donor defects is increased beyond a certain critical point, metalization will occur. The defect states will become delocalized and conduction within the domains of the ZnO sample, even at very low temperatures, becomes metal-like.

This transformation is a canonical example of a metal-to-non-metal transition (MNMT), where relatively small changes in electron density, driven by some control variable, lead to much larger changes in electrical conductivity (Figure 5.8). This investigation into the nature of the MNMT that can be induced in ZnO through chemical control is not only of practical importance to its potential uses as a technological material, but is also another excellent example of the fascinating physics taking place within the crystalline domains of a transparent conducting oxide.

5.3.1 Electronic Transport Measurements

A series of polycrystalline ZnO thin films was prepared by spray pyrolysis with different concentrations of donor dopants, producing a range of room temperature carrier concentrations ($n_{\mathrm{RT}} = n(T = 293\,\mathrm{K})$) between 1.3×10^{18} and $3.6 \times 10^{20}\,\mathrm{cm}^{-3}$ (Figure 5.9a).[iv] These samples were first measured using the Hall effect at temperatures between ∼80 and 350 K.

[iv] For convenience, samples in this section will be identified using their n_{RT} values.

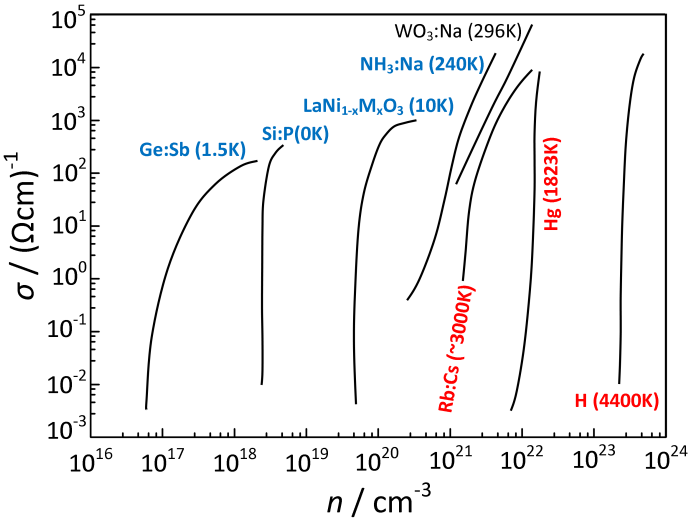

Figure 5.8: The Metal-to-Non-Metal Transition (MNMT) in a range of condensed matter systems, showing the large changes in electrical conductivity (σ) with relatively small changes in carrier concentration (n). The temperature at which each set of observations was made is shown. Figure adapted from Ganguly, *et al.*[48]

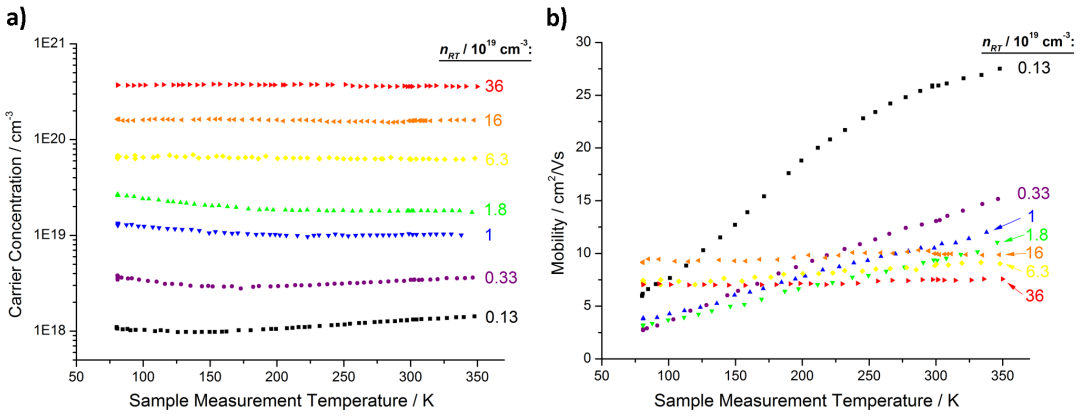

Figure 5.9: Hall effect a) carrier concentration and b) mobility as a function of temperature for ZnO thin films with the indicated room temperature carrier concentration n_{RT}.

All of the samples with $n_{RT} = 1.8 \times 10^{19}\,cm^{-3}$ or lower have a carrier concentration that increases with increasing temperature, at least in the higher temperature part of this measurement range. This behavior is consistent with carriers being thermally excited from localized bandgap states into delocalized states, such as those in the conduction band. At lower measurement temperatures, there is a somewhat puzzling decrease in the carrier concentration with increasing temperature for some of these samples; it is currently unclear what mechanism might cause such behavior. In contrast, the higher n_{RT} samples have carrier concentrations that are essentially independent of temperature, as would be expected for samples where conduction is occurring primarily in delocalized electronic bands.[49]

Two features of the Hall carrier mobility data shown in Figure 5.9b are especially worth noting. The first is that room-temperature mobility shows an initially sharp decrease with increasing carrier concentration from its value of $25.5\,cm^2\,V^{-1}\,s^{-1}$ for the lowest n_{RT} sample. Once n_{RT} has exceed $\sim 10^{19}\,cm^{-3}$, all of the room temperature mobility values are roughly in a range from 7–10 $cm^2\,V^{-1}\,s^{-1}$. This is as expected from the contribution of impurity scattering discussed in Section 5.1.2.

The second relates to the temperature dependence of these values. Carrier mobility increases monotonically with increasing temperature for all samples. However, the size of this change decreases markedly as n_{RT} increases. Especially for the three most conductive samples with $n_{RT} = 6.3$, 16, and $36 \times 10^{19}\,cm^{-3}$, the mobility is almost flat in this range with the change from lowest to highest temperatures being on the order of a few tenths of $cm^2\,V^{-1}\,s^{-1}$. In the temperature range of these measurements, the changing temperature dependence of Hall mobility is not directly related to the MNMT, but instead to changes in grain boundary behavior in these polycrystalline samples as a function of doping. Since this topic goes beyond single crystal behavior, it will be covered later in Chapter 7.

In addition to Hall effect measurements down to 80 K, we have also employed a helium cryostat to measure the electrical resistivity of these samples at temperatures from 300 K down to about 11 K. These data are shown in Figure 5.10.

The resistivity of all samples decreases as the temperature increases, with the magnitude of this change decreasing monotonically as n_{RT} increases. The lower temperature effectively magnifies the conductivity difference between the most and least

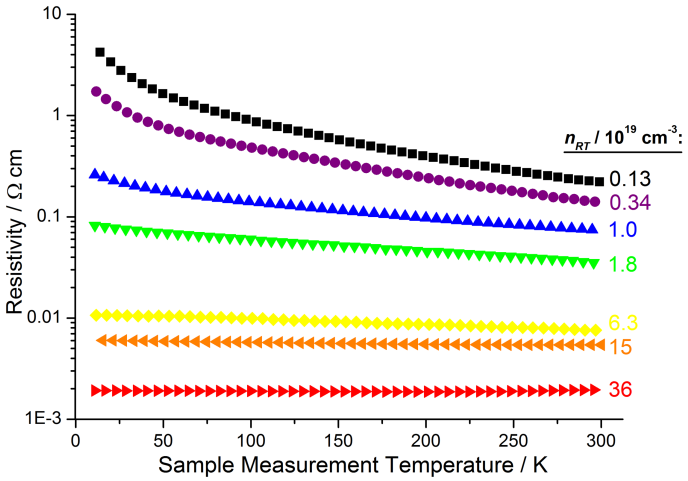

Figure 5.10: Electrical resistivity as a function of temperature for ZnO thin film samples with the indicated room temperature carrier concentration n_{RT}.

conductive samples and makes the fact that an MNMT is occurring across this series much easier to see by eye. At 11 K, a just over two order of magnitude difference in electron density manifests itself as an approximately four order of magnitude difference in conductivity. The trend in resistivity as a function of temperature would clearly suggest that this difference would continue to increase if measurements could have been made at even lower temperatures.

5.3.2 Identifying the Location of the MNMT

The temperature-dependent electrical property data presented in the previous section clearly suggest that an MNMT occurs in these samples as the dopant concentration changes. However, a truly absolute differentiation of metallic and non-metallic states can only occur at the absolute zero of temperature, where the conductivity of metals is expected to be finite and that of non-metals zero.[50] For this reason, experimental data collected at finite temperatures cannot be used directly to determine the carrier concentration that divides metallic and non-metallic samples. Furthermore, the resistivity data in Figure 5.10 come from direct current electrical measurements on polycrystalline samples. This can be problematic because there is a possibility that a sample with metallic grain interiors might still be non-conducting at low temperatures due to poor electrical contacts among the grains.

Thus, instead of directly attempting to extrapolate these data to $T = 0\,\mathrm{K}$, two

different analysis approaches will be used to estimate the location of the MNMT in this system.

Activation Energy for Thermally-Assisted Tunneling

At low temperatures, there is insufficient thermal energy to excite carriers from defect states in the bandgap to the conduction band. Any conduction that occurs must occur among these impurity states. Furthermore, if the concentration of defects is low, then their associated wavefunctions will be spatially separated, and charges must travel by "hopping" from one isolated defect to another via quantum-mechanical tunneling.

As a first approximation, it can be assumed that defects are randomly distributed within the host material, which implies that their states will occupy a range of energy levels. Since tunneling is most facile when the final and initial states are of similar energy, changes to electron energy that arise from interactions with lattice phonons can facilitate the hopping of electrons among energetically dissimilar impurity centers. This general process is often termed *thermally assisted tunneling* and conduction by this mechanism will be characterized by an activation energy.[51]

As the spatial density of defects increases, so too will the density of their associated states in energy. This will reduce the average energy difference between pairs of initial and final states, which in turn reduces the activation energy needed to promote conduction by tunneling.

When the Mott critical concentration of impurities (n_c) is reached (Equation 2.14), the overlap of defect wavefunctions becomes so great that the formerly discrete impurity states merge entirely to become an impurity *band*. At the same time, impurity wavefunctions become delocalized through the solid, allowing electrons to propagate classically and coherently without the need for tunneling. As a result, the activation energy associated with thermally assisted tunneling should thus vanish at the point of band formation.

As discussed previously in Section 2.4, the formation of an impurity band alone is not *sufficient* to imply metallic conduction. However, these one-electron cation-doped ZnO samples satisfy the additional criterion that the impurity states are partially filled, such that delocalization of the impurity wavefunctions implies the creation of a metallic state. In this case, the disappearance of hopping conduction at n_c due to the formation of an impurity band is evidence for the onset of the MNMT.

When the resistivity data for these ZnO films are plotted against reciprocal temperature, it emerges that conduction at low temperatures, less than about 30 K, can be described as an Arrhenius process with a characteristic activation energy (Figure 5.11a). We hypothesize that these activation energies can be directly correlated to those required for thermally-assisted tunneling.

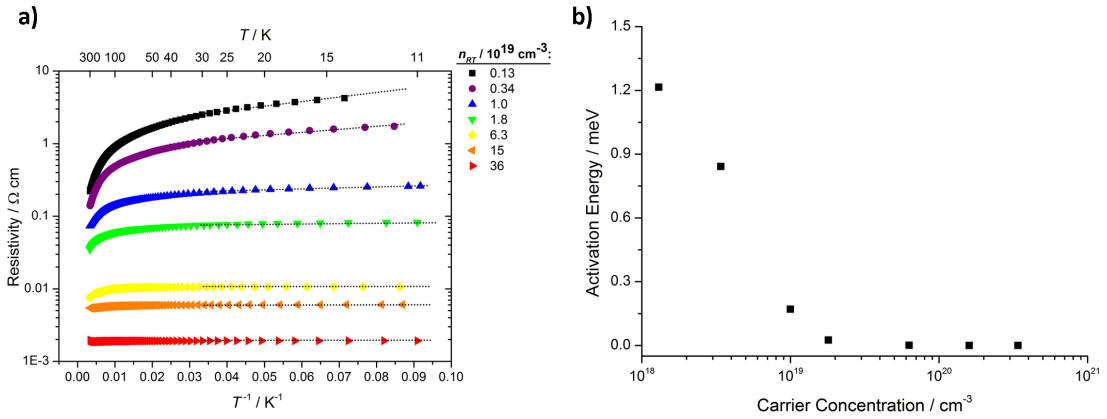

Figure 5.11: a) Resistivity of ZnO thin films with varying room temperature carrier concentrations plotted against reciprocal temperature. The linear low temperature range (<30 K) is fitted (dotted line) and used to calculate an activation energy that can be associated with conductivity via thermally-assisted tunneling among impurity states. b) Fitted activation energies as a function of room temperature carrier concentration.

Figure 5.11b shows the values of activation energy extracted from the fits shown. These clearly decrease as the carrier concentration increases and more or less vanish around $n_{\mathrm{RT}} = 2 \times 10^{19}\,\mathrm{cm}^{-3}$.[v] The x-intercept of a linear fit to the four lowest n_{RT} points implies that the room temperature carrier concentration at which metalization occurs is $\sim 1.7 \times 10^{19}\,\mathrm{cm}^{-3}$.

The Ioffe-Regel Criterion

Ioffe and Regel noted that coherent electron transport through a solid requires that the electron wavefunction maintain phase coherence over at least a full wavelength ($\lambda_{\mathrm{F}} = k_{\mathrm{F}}^{-1}$). Recognizing further that an electron's elastic mean free path (l_{e}) is the distance over which its wavefunction loses phase coherence, they argued that electrons

[v] The activation energy values for the three highest n_{RT} samples are not rigorously zero based on these fits, but are all less than 4×10^{-4} meV, which is a less than 0.04 % of $k_B T$ even at 15 K where $k_B T \approx 1.2$ meV.

must become localized if $k_\mathrm{F}l_\mathrm{e}$ becomes less than ∼1, something which has come to be called the *Ioffe-Regel Criterion*.[52] The Ioffe-Regel parameter $k_\mathrm{F}l_\mathrm{e}$ can be expressed in terms of the carrier concentration and resistivity as

$$k_\mathrm{F}l_\mathrm{e} = \frac{\hbar(3\pi^2)^{2/3}}{e^2\rho n^{1/3}}\,, \tag{5.3}$$

where e is the electronic charge, $\hbar$ is the reduced Planck constant, and ρ and n are the resistivity and carrier concentration of the sample at a given temperature. The value of n that leads to $k_\mathrm{F}l_\mathrm{e} = 1$ thus yields an estimate of the critical carrier concentration required for electrons to be delocalized within that sample under the chosen conditions.[53]

Strictly speaking, Equation 5.3 is only valid in the absence of electron correlation and where extrinsic limits to conductivity (like grain boundaries) are not present. The values of $k_\mathrm{F}l_\mathrm{e}$ are thus calculated using room temperature data, for which these two effects are minimized (Figure 5.12). Clearly, the condition of $k_\mathrm{F}l_\mathrm{e} = 1$ is satisfied at a carrier concentration just slightly higher than that of the sample with $n_\mathrm{RT} = 6.3 \times 10^{19}\,\mathrm{cm}^{-3}$. Crudely assuming a linear interpolation between the samples with $n_\mathrm{RT} = 6.3$ and $16 \times 10^{19}\,\mathrm{cm}^{-3}$, the Ioffe-Regel parameter is unity at $n_\mathrm{RT} = 7.5 \times 10^{19}\,\mathrm{cm}^{-3}$.

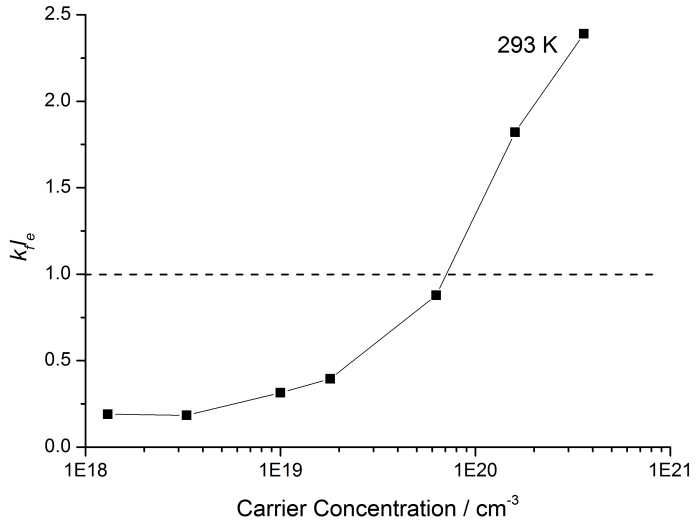

Figure 5.12: The Ioffe-Regel parameter as a function of carrier concentration in ZnO samples calculated using data collected at 293 K. The dashed line denotes $k_\mathrm{F}l_\mathrm{e} = 1$, where the MNMT is expected to occur.

It is not entirely surprising that the estimate of the critical carrier concentration from the Ioffe-Regel parameter is somewhat higher than that obtained from analysis of the thermally-assisted tunneling. Since the data for the Ioffe-Regel calculation were collected at room temperature and not low T, additional phonon modes are active that would increase the resistivity for any given carrier concentration. The influence of grain boundary scattering on these DC electrical measurements would have a similar effect. Together, these factors depress the $k_{\mathrm{F}}l_{\mathrm{e}}$ values for each sample, meaning that the point where the curve intersects $k_{\mathrm{F}}l_{\mathrm{e}} = 1$ has been pushed towards higher n. Thus, in terms of estimating the critical carrier concentration for the MNMT in an ideal single crystal domain, the value found here is likely to be an over-estimate.

These two analyses show that the Mott critical concentration for delocalization of impurity electronic states in doped ZnO occurs in the range of $n_{\mathrm{RT}} = 2$ to $7 \times 10^{19}\,\mathrm{cm}^{-3}$.

This range can likely be refined if resistivity and Hall effect data could be collected at even lower temperatures. Such low temperature data would also allow an even more vivid demonstration of the sharp transition in behavior between metals and non-metals. It would also be helpful to employ characterization techniques (such as the optical frequency spectroscopy described in the next section) that could limit the effect of grain boundaries on the measurement and allow direct use of lower-temperature transport properties in a Ioffe-Regel calculation.

Nevertheless, even these present data demonstrate that the basic theoretical picture of the electronic phase transition from metal-to-non-metal is essentially correct, and that this transition can be realized through chemical control in a real, experimental system.

5.4 Optical Frequency Transport Measurements

5.4.1 Motivation

In the previous sections of this chapter, a number of interesting physical phenomena that can occur in an ordered crystalline domain have been discussed. All of these are related to the complex interplay of n and μ as carriers move through a TCO material. These certainly are fascinating topics, and their illumination has and will

continue to provide rich fodder for both theoreticians and experimentalists. However, as has been hinted at several times already, especially in Section 5.3, it cannot be emphasized enough that this is *not* where the study of TCOs should end. Especially if the ultimate goals relate to the practical uses of these materials, single-crystal behavior only represents the foundations.

Most of the samples prepared for this thesis have been thin films of ZnO- and In_2O_3-based materials, prepared by spray pyrolysis. These unequivocally do *not* conform to the ideal of single-domain samples that has been mostly maintained so far in this chapter. For instance, instead of being single crystals, the samples here are polycrystalline thin films, deposited in the presence of solvent and organic ligands, and prepared under environmental conditions that are not rigorously controlled. While the use of spray pyrolysis does indeed magnify some of these non-ideal features, on the whole, they are present to some degree and must be accounted for in TCO samples prepared using any scalable deposition technique. In this sense especially, the magnification effect of spray pyrolysis, which makes these practical factors easier to observe and study, might be considered as much of a benefit as a potential detriment.

Over the course of this work, well over 700 ZnO- and In_2O_3-based thin film samples have been prepared by spray pyrolysis. To begin the examination of how single crystal physics and other practical factors interact, consider Figure 5.13, which provides an unfiltered representation of all spray pyrolysis samples prepared during the course of this thesis for which reasonably reliable Hall effect data are available.

There are two main clusters of data corresponding to our ZnO-based samples prepared by spray pyrolysis. The one at lower carrier concentrations, with n from roughly 10^{18}–$10^{19}\,\mathrm{cm}^{-3}$ mostly contains nominally undoped samples prepared using various baseline conditions. The other cluster is of heavily doped samples centered on $n \approx 3 \times 10^{20}\,\mathrm{cm}^{-3}$. What is obvious about the electrical performance of both groups is that they do not even come close to approaching the performance limits defined by ionized impurity scattering.

Maximum mobilities in these ZnO samples are defined by a sharp upper edge to $\mu(n)$, suggesting very strongly that additional performance limits are at play with this material deposited using spray pyrolysis. Whatever the nature of these limits are, they cannot apply equally to all ZnO samples, since some of the literature results

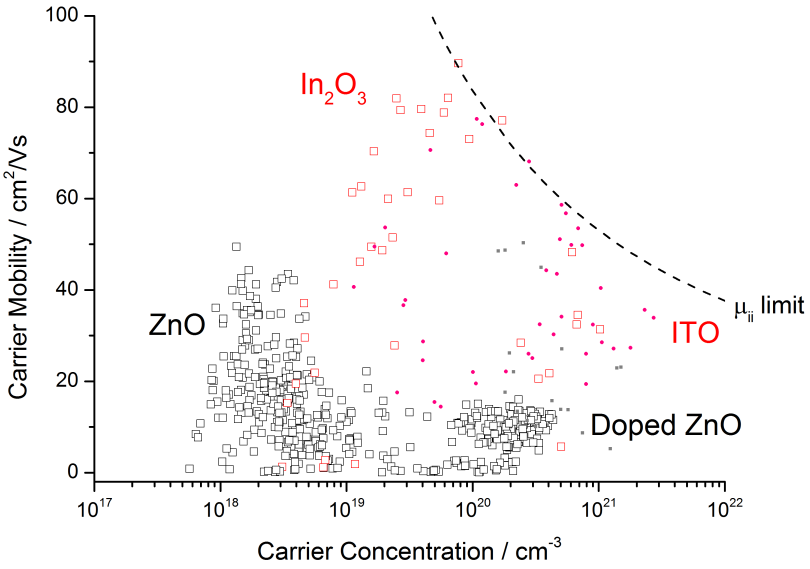

Figure 5.13: Summary of electrical properties of all ZnO-based (black) and In_2O_3-based (red) films prepared by spray pyrolysis over the course of this thesis. The μ_{ii} limit curve is calculated using Equation 5.1 as described in Section 5.1. The four labels denote the broad groupings of results. The literature data (mostly from vacuum-deposited samples) already presented in Figure 5.2 are shown here as small points for reference.

for ZnO prepared using vacuum-based techniques can clearly exceed the maximum performance of the sprayed samples. Furthermore, there also appears to be a fairly clear maximum in the carrier concentration that can be obtained in spray pyrolyzed ZnO, which will be discussed further in Chapter 6.

In stark contrast, the In_2O_3 and ITO samples, also prepared by spray pyrolysis, clearly scatter through the entire μ-n space allowed by ionized impurity scattering. In fact, as discussed in Section 5.2, a few of our highest performing samples even extend slightly beyond the impurity scattering limit curve. Even discounting these IBrO samples as a special case, it seems fairly clear that the electrical performance of these solution-processed In_2O_3 films is certainly competitive with that of samples prepared using vacuum-based techniques. In other words, unlike with ZnO, there do not seem to be any hard process- or environment-dependent limits in In_2O_3 preventing samples from approaching the single crystal performance maxima defined by intrinsic scattering processes.

This exemplifies one the main problems in trying to replace ITO with ZnO-based materials that has already been mentioned in earlier chapters. It may not be impossi-

ble to get competitive performance from a ZnO-based material under ideal conditions, but doing so in a practical context is far harder than it would be with In_2O_3.[vi]

It is easy to show that virtually all TCO films prepared using techniques suitable for large-area deposition will be polycrystalline, consisting of grains of relatively ordered crystalline material separated by disordered grain boundaries. This is one of the key features that distinguishes practical thin film samples from the single crystal case, and as such, must be a prime suspect for why these ZnO thin films behave so differently from their corresponding single crystals.

There is little doubt that the presence of grain boundaries can be of enormous significance to the performance of TCO thin films. The presence of defects at grain boundaries can lead to the development of electrostatic potential barriers that inhibit the transport of carriers from one grain to another, limiting macroscopic electronic conduction even if the carriers are free inside each of the ordered grains. Chapter 7 will cover such effects in detail.

However, this does not rule out the possibility that some of the difference between ZnO and In_2O_3 could be due to changes occurring *within* the grains. In the TCO literature, it has often been assumed that the interior of each grain is simply a small crystalline domain, and thus governed by the same physics and performance limits. It is sensible to assess the validity of this assumption before moving on.

5.4.2 Approach

In order to do this, dielectric modeling of UV-Vis-NIR transmission and specular reflectance spectra of 5 at% indium-doped ZnO (IZO) and 5 at% tin-doped In_2O_3 (ITO) samples prepared at a range of deposition temperatures was carried out using the basic approach first described in Section 3.2.2. Unlike in a direct current electrical measurement where carriers must traverse the macroscopic distance between contacts, grain boundaries and all, the relatively high frequency excitation in optical measurements limits the distance traveled by any given carrier. This means that each will primarily sample its local environment. Since grain interiors are a large fraction of the total volume of the samples, such measurements thus suppress the effects of grain

[vi] Even this overlooks the fact that it is usually more difficult to *maintain* good electrical performance in ZnO samples over time, even if it can be achieved initially by some means.

boundaries and are a useful means of probing electrical transport within the grains of a polycrystalline material.

Figure 5.14 shows an example of the results from fitting one of the IZO samples. A Lorentz oscillator is used to represent the band gap absorption while a Drude oscillator is used to represent the effect of free electrons in the sample. For these IZO samples, a frequency-dependent mobility (Equation 3.19) was used. Since the goal here is to model the transport properties of the free conduction electrons, the main priority in fitting was to achieve a good match between experiment and model in the spectral region where the optical effects of such electrons dominate. For doped samples like these with carrier concentrations in the range of 10^{20} to $10^{21}\,\mathrm{cm}^{-3}$, the region of most interest is in the near-infrared (Section 2.2.2).

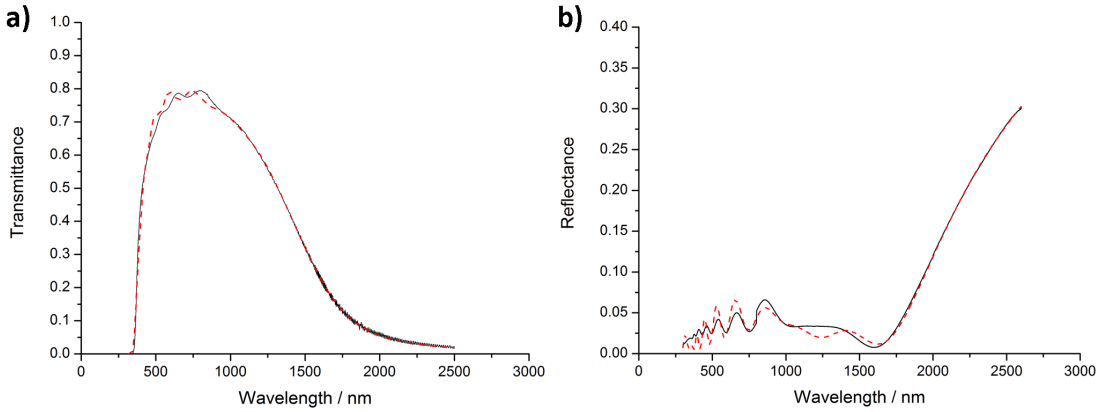

Figure 5.14: UV-Vis-NIR a) transmittance and b) reflectance spectra of a 5 at% IZO thin film deposited at ∼417 °C by spray pyrolysis (solid black). The results of simultaneous fitting to both datasets using the model described in the main text are shown as dashed red curves.

There is clearly some mismatch in the details of the interference fringes in the window of high transparency. However, this is likely due to practical limitations in the experiment rather than any fundamental flaw in the chosen model. The position and amplitude of the fringes are very sensitive to parameters like sample thickness and uniformity. Due to two different instruments being used, it was impossible to guarantee that exactly the same part of a sample was analyzed for both transmittance and reflectance. This inconsistency accounts for the inability to fit these features simultaneously in both spectra. In general, a much better match can be made if the two spectra are fit separately. Furthermore, there were unforeseen difficulties in

obtaining reliable reflectance data for the IZO sample deposited at ∼292 °C and the fit results shown are to the transmittance data only. In this case, the constraint of known sample thickness and additional uniqueness tests were used to confirm the validity of the final fit.

For the ITO samples, a different fitting approach had to be adopted. In some of these datasets, significant correlations arose between the parameters of the Lorentz oscillator used for the band gap and those of Drude oscillator used for the conduction electrons. This made finding unique fitting results to the entire dataset impossible. To address this, only a Drude oscillator was used to fit the NIR data from 1000 nm to 2500 nm. This approach removed the most problematic parameter correlations and allowed the fitting process to converge. Including an energy-dependent mobility model as for IZO did not improve fit quality, so this was not done here. Figure 5.15 shows an example of an ITO dataset analyzed in this way.

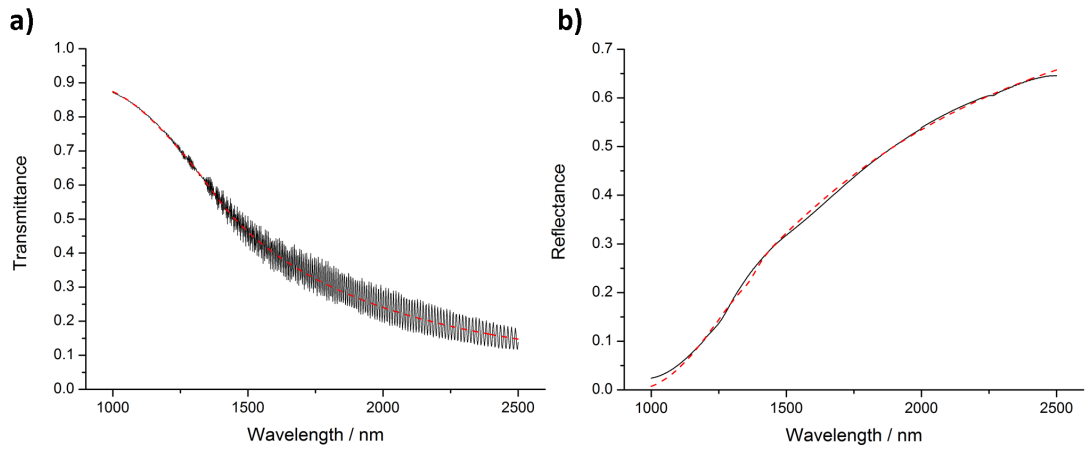

Figure 5.15: NIR a) transmittance and b) reflectance spectra of a 5 at% ITO thin film deposited at ∼417 °C by spray pyrolysis (solid black). The results of simultaneous fitting to both datasets using the model described in the main text are shown as dashed red curves.

As a further check that that the fits shown had converged on the correct minima in the parameter space, the fitted sample thicknesses (including the roughness layer) based on this modeling were compared to sample thicknesses estimated using other methods, such as the Swanepoel method. Figure 5.16 shows a very clear correlation between thicknesses determined by the two methods for all samples. Although not conclusive proof of uniqueness, this does show that the set of fitting solutions chosen are internally self-consistent.

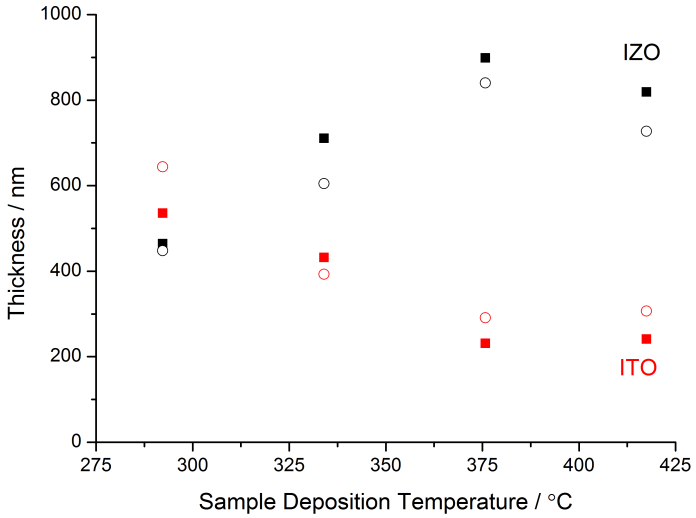

Figure 5.16: Thickness estimates for IZO (black) and ITO (red) thin film samples prepared using spray pyrolysis at various temperatures. Solid symbols are thicknesses obtained from the dielectric modeling in this section, while the open symbols are from using the Swanepoel envelope method.

The optical carrier concentrations (n_{opt}) of these samples were calculated from the best-fit value of the Drude frequency of the free electrons ω_{n} using

$$n_{\mathrm{opt}} = \frac{\omega_{\mathrm{n}}^2 \epsilon_0 m^*}{e^2}\,, \tag{5.4}$$

where ϵ_0 is the permittivity of free space, m^* is the effective mass of the carrier, and e is the electronic charge.

The optical mobilities (μ_{opt}) of these samples were obtained using the damping constant of the Drude oscillator (Γ_{Dr}) via

$$\mu_{\mathrm{opt}} = \frac{e}{m^* \Gamma_{\mathrm{Dr}}}\,. \tag{5.5}$$

Where a frequency-dependent scattering model was used, μ_{opt} was calculated using the value of Γ_{Dr} at the Drude frequency ω_{n}.

For the calculation of numerical data from these fitting results, constant carrier effective masses of $0.3m_{\mathrm{e}}$ and $0.35m_{\mathrm{e}}$ were assumed for ZnO and In_2O_3, respectively. Full fitting logs including estimated errors for fit parameters are shown in Appendix F.

5.4.3 Deposition Temperature Dependence

Optical and Hall effect carrier concentrations for ITO and IZO as a function of deposition temperature are shown in Figure 5.17. Note that the error bars on n_{opt} for ITO are significantly larger than those for IZO due to the different fitting approach used. The corresponding carrier mobility values are given in Figure 5.18. Keeping in mind that exact values for n_{opt} and μ_{opt} can vary depending on the choice of effective mass used for their calculation, the way these values *trend* across each temperature series is the most informative aspect in this case.

For each material, Figure 5.17 shows that the trends (and values) in optical and Hall carrier concentrations are similar. This is as expected, since all free carriers (even those trapped within a grain) can be displaced by the influence of external electric and magnetic fields, contribute to a measured direct current Hall voltage, and thus be included as part of a Hall carrier concentration.[54] In this way, the optical frequency measurements provide some independent corroboration of the generally higher carrier concentrations observed in ITO, as well as the larger temperature dependence of n in ITO initially seen using direct current measurements.

However, since Hall mobility is calculated using the direct current resistivity, its value reflects the fraction of total free carriers that are able to participate in *inter*-grain conduction. In other words, the measured DC Hall mobility of a sample with some of its free carriers trapped inside grains will be lower than the actual carrier mobility within a grain. In contrast, the optical mobility mostly senses the local environment around a charge carrier and is relatively insensitive to whether the carriers are trapped in grains or not.

For IZO (Figure 5.18a), the optical and Hall mobilities clearly diverge as the deposition temperatures of the samples decrease. μ_{Hall} drops from $\sim$13.6 $\text{cm}^2\,\text{V}^{-1}\,\text{s}^{-1}$ to nearly zero as T_{dep} is decreased from $\sim$417 to 292 °C. Meanwhile, the optical mobility stays basically flat in a band between about 30–40 $\text{cm}^2\,\text{V}^{-1}\,\text{s}^{-1}$. This is a very strong indication that the decrease in the direct current electrical performance of polycrystalline IZO prepared at lower deposition temperatures is not mostly due to changes *within* the grains, but instead, changes in *inter*-grain electronic transport.

Even though the Hall mobility of ITO also decreases with decreasing deposition temperature, optical frequency transport measurements reveal that the underlying

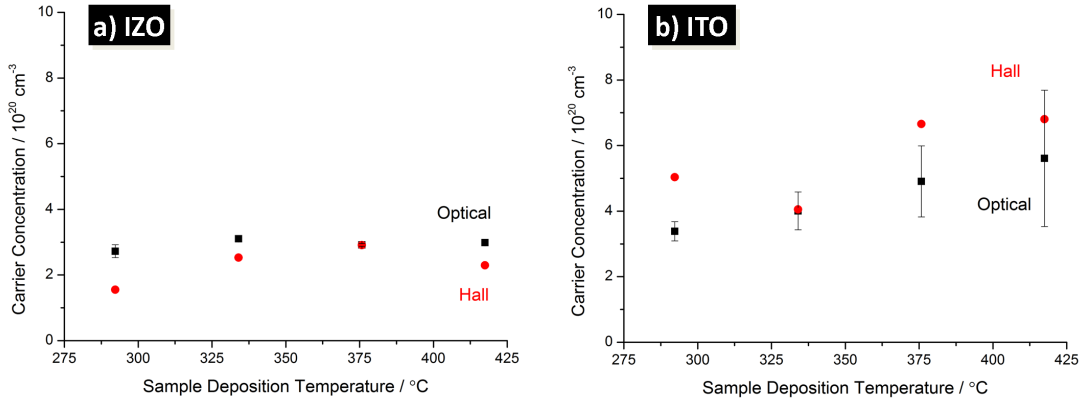

Figure 5.17: Optical (black) and Hall effect (red) carrier concentrations measured for a) 5 at% IZO and b) 5 at% ITO thin film samples deposited by spray pyrolysis as a function of deposition temperature. Error bars for optical transport properties reflect estimated 90 % confidence interval based on estimates from fitting software.

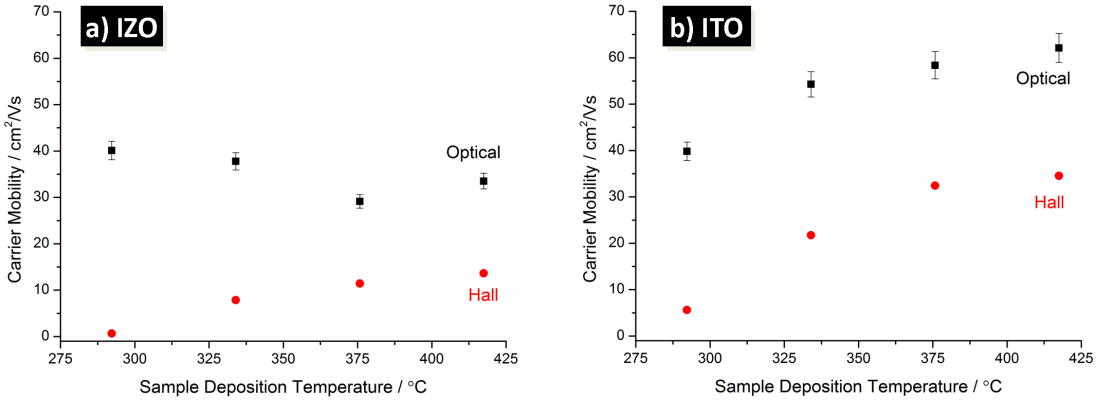

Figure 5.18: Optical (black) and Hall effect (red) carrier mobilities measured for a) 5 at% IZO and b) 5 at% ITO thin film samples deposited by spray pyrolysis as a function of deposition temperature. Error bars for optical transport properties reflect estimated 90 % confidence interval based on estimates from fitting software.

situation is entirely different from that of IZO. Figure 5.18b shows that the trend in Hall mobility is almost exactly matched by the trend in optical mobility. This suggests that the changes leading to reduced carrier mobility here are due to intrinsic differences within the grains of the TCO. While spray pyrolyzed ITO has not been studied enough in this present work to conclusively determine a mechanism, sensible possibilities include incomplete precursor decomposition at lower temperatures, or that higher T_{dep} provides more energy for the effective incorporation of tin impurities into the In_2O_3 lattice.

5.4.4 Proposed Future Measurements

These optical frequency measurements show quite strongly that just considering single crystal, grain interior processes is inadequate to fully explain the temperature-dependent electrical properties of polycrystalline IZO thin films. Furthermore, these data also suggest that these additional grain boundary factors are a key part of the differences between the doped ZnO and In_2O_3 samples.

It would be of great interest to perform analogous optical measurements and modeling on undoped ZnO and In_2O_3 samples to see if similar trends are observed. Starting from these simpler cases, it would also be useful to see what trends emerge as various types of perturbations are introduced, for example, changes in doping level, oxygen partial pressure during deposition, or lattice mismatch with the substrate. This could provide an indication of whether there are in fact intrinsic differences in the way the transport properties of ZnO and In_2O_3 thin films change in response to disorder, as has been implied by some of the evidence cited earlier in Section 5.2.

Since the plasma frequency is proportional to the square of the carrier concentration, performing such measurements on undoped and lightly doped samples will require data from the mid- and far-infrared.[vii] Since most common and non water-soluble substrate materials absorb strongly in the lower energy parts of this range, variable angle reflectance or spectroscopic ellipsometry may be the most straightforward ways of obtaining the minimum of two independent datasets needed to fully define the dielectric function. Unfortunately, due to a variety of equipment failures

[vii] For example, a carrier concentration of $\sim 10^{18}\,\mathrm{cm}^{-3}$ commonly seen in undoped ZnO would imply a Drude frequency of about $546\,\mathrm{cm}^{-1}$. Then, fully resolving the plasma edge would require a spectral range including even lower energies than that.

and access issues, it was not possible to perform such measurements for this thesis, and as such, these will have to be left to future work.

Similar dielectric modeling studies can also be performed using measurements in other frequency ranges, such as THz and microwave. Choosing an excitation in resonance with the characteristic frequency of a particular scattering mechanism could allow for the isolation and study of that mechanism in a TCO domain.

5.5 Conclusion

We have examined a range of physical processes related to electronic transport in single-crystal domains of transparent conducting oxides using results from both the literature and our current work. It is quite apparent that phenomena ranging from phonon and impurity scattering to the metal-non-metal transition have an important role in determining the electronic and optical properties of these materials.

Broadly speaking, the reasons for limited conductivity in single crystals are known and useful models exist to describe most of these processes. However, it is also clear that there remain cases where the details are not yet fully understood. We have attempted to highlight some areas where further work might be of significance in continuing efforts to expand the boundaries of TCO performance. It should also be recognized that many of the topics discussed here have relevance in solid-state physics as a whole, and can be applied to systems extending well beyond just the transparent conducting oxides.

At the same time, results have been presented to show that single-crystal behavior alone cannot come close to explaining the practical differences between ZnO and In_2O_3 thin films. Through both single-crystal data and optical frequency measurements, it is clear that the ordered domains of these two materials actually have extremely similar transport properties. Thus, it is very clear that a departure from this idealized picture is needed in order to properly understand the behavior of large-area, polycrystalline TCO thin films, and especially those made from low-cost ZnO.

5.6 Experimental

5.6.1 Deposition of Bromide-doped In_2O_3

Synthesis of Indium Bromide

A preparation based on one that has previously been reported was used.[55] In the fume hood, metallic indium shot (2.71 g, 23.6 mMol, Aldrich, 2–5 mm diameter, 99.999 % trace metals basis) was stirred vigorously in a warmed (∼50 °C) aqueous solution of excess hydrobromic acid (22 mL, Fisher Scientific, Analytical Reagent Grade, 37 %). Bubbles and a coppery sheen are observed on the surface of the metal shot as the indium metal dissolved overnight. The temperature of the solution is then raised to ∼75 °C and the solution boiled to dryness over 20 hours of heating and stirring. The resulting white crystals are collected and dried at room temperature under reduced pressure (approximately 9×10^{-2} mbar) for several hours until the isolated crystals are free-flowing. The crystalline white product is presumed to be indium(III) bromide (7.75 g, 354.52 g/mol, 21.8 mMol, 92.7 % isolated yield).

Precursor Solution for Bromide-doped In_2O_3

The precursor solution is prepared and used as in the standard deposition of In_2O_3 from chloride precursors (Section 4.7.1) except for the replacement of indium(III) chloride with indium(III) bromide and hydrochloric acid with hydrobromic acid.

5.6.2 Geometry Optimization of In_2O_3 and IBrO

Computational modeling of undoped In_2O_3 and bromide-doped indium oxide were carried out at the level of fully-periodic density functional theory using the plane-wave CASTEP code.[56] The $2 \times 2 \times 2$ supercells used for this calculation were generated from literature crystallographic data.[57] A plane wave cutoff of 300 eV was specified for each calculation, with k-point sampling performed on a $2 \times 2 \times 2$ Monkhorst-Pack house grid. The Perdew, Burke, and Ezerhoff functional[58] was used and an ultrasoft pseudopotential was optimized by the code for each iteration. The geometry of the 640 ions in each supercell was allowed to optimize within a fixed cubic volume with a side length of 20.238 Å. A maximum ionic displacement of 10^{-3} Å and a maximum

ionic force of 10^{-2} eV Å^{-1} were used as convergence criteria. The optimization for undoped In_2O_3 was constrained by the symmetry operations of the Ia$\bar{3}$ space group. No symmetry constraints were placed on the optimization of the bromide-doped In_2O_3.

5.6.3 10 K Resistance Measurements

Electrical resistance measurements between ∼11–300 K were made using a four-point technique. Conductive silver paint (Electrolube) was used to affix a 2 mm × 9 mm piece of thin film to a holder with four polished indium pads in a linear arrangement. The sample holder was fitted into a socket on a brass-backed, heated circuit board, which was inserted into a vacuum-jacketed, single-stage, closed-cycle helium cryostat. I-V measurements were used to calculate the resistance of the sample at various temperatures; these were then normalized to resistivity based on values previously obtained using measurements in the van der Pauw geometry.

5.6.4 Acknowledgments

Dr. Andrew Seel performed the DFT geometry optimizations of the structures of IBrO and In_2O_3 using CASTEP.

References

[1] Ellmer, K. *Electrical Properties*; Ellmer, K.; Klein, A.; Rech, B., Eds.; Transparent Conductive Zinc Oxide: Basics and Applications in Thin Film Solar Cells; Springer-Verlag: Berlin, 2008; pp 35–78.

[2] Ellmer, K. *Transparent Conductive Zinc Oxide and Its Derivatives*; Ginley, D. S.; Hosono, H.; Paine, D. C., Eds.; Handbook of Transparent Conductors; Springer: New York, NY, 2010; pp 193–263.

[3] Hutson, A. R. *Phys. Rev.* **1957**, *108*, 222–230.

[4] Weiher, R. L. *J. Appl. Phys.* **1962**, *33*, 2834–2839.

[5] Conwell, E.; Weisskopf, V. F. *Phys. Rev.* **1950**, *77*, 388–390.

[6] Erginsoy, C. *Phys. Rev.* **1950**, *79*, 1013–1014.

[7] Dingle, R. B. *Philos. Mag. (1798-1977)* **1955**, *46*, 831–840.

[8] Ridley, B. K. *J. Phys. C: Solid State Phys.* **1977**, *10*, 1589–1593.

[9] Chattopadhyay, D.; Queisser, H. J. *Rev. Mod. Phys.* **1981**, *53*, 745–768.

[10] Bellingham, J. R.; Phillips, W. A.; Adkins, C. J. *J. Mater. Sci. Lett.* **1992**, *11*, 263–265.

[11] Ellmer, K. *J. Phys. D: Appl. Phys.* **2001**, *34*, 3097–3108.

[12] Ashkenov, N.; Mbenkum, B. N.; Bundesmann, C.; Riede, V.; Lorenz, M.; Spemann, D.; Kaidashev, E. M.; Kasic, A.; Schubert, M.; Grundmann, M.; Wagner, G.; Neumann, H.; Darakchieva, V.; Arwin, H.; Monemar, B. *J. Appl. Phys.* **2003**, *93*, 126–133.

[13] Hamberg, I.; Granqvist, C. G. *J. Appl. Phys.* **1986**, *60*, R123–R160.

[14] Luong, M.; Shaw, A. W. *Phys. Rev. B* **1971**, *4*, 2436–2441.

[15] Masetti, G.; Severi, M.; Solmi, S. *IEEE Trans. Electron Devices* **1983**, *30*, 764–769.

[16] Sclar, N. *Phys. Rev.* **1956**, *104*, 1559–1561.

[17] Li, S. S.; Thurber, W. R. *Solid-State Electron.* **1977**, *20*, 609–616.

[18] Ashcroft, N. W.; Mermin, N. D. *Solid State Physics*; Harcourt, Inc.: Orlando, FL, 1976.

[19] Ellmer, K.; Mientus, R. *Thin Solid Films* **2008**, *516*, 4620–4627.

[20] Marezio, M. *Acta Crystallogr.* **1966**, *20*, 723–728.

[21] Shannon, R. D. *Acta Crystallogr., Sect. A: Cryst. Phys., Diffr., Theor. Gen. Crystallogr.* **1976**, *32*, 751–767.

[22] Meng, Y.; Yang, X. L.; Chen, H. X.; Shen, J.; Jiang, Y. M.; Zhang, Z. J.; Hua, Z. Y. *J. Vac. Sci. Technol., A* **2002**, *20*, 288–290.

[23] Yoshida, Y.; Wood, D. M.; Gessert, T. A.; Coutts, T. J. *Appl. Phys. Lett.* **2004**, *84*, 2097–2099.

[24] van Hest, M. F. A. M.; Dabney, M. S.; Perkins, J. D.; Ginley, D. S. *Thin Solid Films* **2006**, *496*, 70–74.

[25] van Hest, M. F. A. M.; Dabney, M. S.; Perkins, J. D.; Ginley, D. S.; Taylor, M. P. *Appl. Phys. Lett.* **2005**, *87*, 032111.

[26] Rauf, I. A. *Mater. Lett.* **1993**, *18*, 123–127.

[27] Leenheer, A. J.; Perkins, J. D.; van Hest, M. F. A. M.; Berry, J. J.; O'Hayre, R. P.; Ginley, D. S. *Phys. Rev. B* **2008**, *77*, 115215.

[28] Nomura, K.; Ohta, H.; Takagi, A.; Kamiya, T.; Hirano, M.; Hosono, H. *Nature* **2004**, *432*, 488–492.

[29] Nomura, K.; Kamiya, T.; Ohta, H.; Uruga, T.; Hirano, M.; Hosono, H. *Phys. Rev. B* **2007**, *75*, 035212.

[30] Hosono, H. *J. Non Cryst. Solids* **2006**, *352*, 851–858.

[31] Robertson, J. *Phys. Status Solidi B* **2008**, *245*, 1026–1032.

[32] Walsh, A.; Da Silva, J. L. F.; Wei, S.-H. *Chem. Mater.* **2009**, *21*, 5119–5124.

[33] Robertson, J. *Adv. Phys.* **1983**, *32*, 361–452.

[34] Bellingham, J. R.; Phillips, W. A.; Adkins, C. J. *J. Phys.: Condens. Matter* **1990**, *2*, 6207–6221.

[35] Buchholz, D. B.; Ma, Q.; Alducin, D.; Ponce, A.; Jose-Yacaman, M.; Khanal, R.; Medvedeva, J. E.; Chang, R. P. H. *Chem. Mater.* **2014**, *26*, 5401–5411.

[36] Kingery, W. D.; Mickelsen, R. A.; *Amorphous Zinc Oxide Semiconductor and Method of Making; US Patent 3294660*; 1966.

[37] Theissmann, R.; Bubel, S.; Sanlialp, M.; Busch, C.; Schierning, G.; Schmechel, R. *Thin Solid Films* **2011**, *519*, 5623–5628.

[38] Chandra, R. D.; Rao, M.; Zhang, K.; Prabhakar, R. R.; Shi, C.; Zhang, J.; Mhaisalkar, S. G.; Mathews, N. *ACS Appl. Mater. Interfaces* **2014**, *6*, 773–777.

[39] Huang, C.-I.; Chin, H.-A.; Wu, Y.-R.; Cheng, I.-C.; Chen, J. Z.; Chiu, K.-C.; Lin, T.-S. *IEEE Trans. Electron Devices* **2010**, *57*, 696–703.

[40] Cohen, D. J.; Barnett, S. A. *J. Appl. Phys.* **2005**, *98*, 053705.

[41] Yoo, J.; Lee, C.-H.; Doh, Y.-J.; Jung, H. S.; Yi, G.-C. *Appl. Phys. Lett.* **2009**, *94*, 223117.

[42] Ohtomo, A.; Tsukazaki, A. *Semicond. Sci. Technol.* **2005**, *20*, S1–S12.

[43] Ellmer, K.; Vollweiler, G. *Thin Solid Films* **2006**, *496*, 104–111.

[44] Moriga, T.; Edwards, D. D.; Mason, T. O.; Palmer, G. B.; Poeppelmeier, K. R.; Schindler, J. L.; Kannewurf, C. R.; Nakabayashi, I. *J. Am. Ceram. Soc.* **1998**, *81*, 1310–1316.

[45] Lee, K.; Kim, S. W.; Toda, Y.; Matsuishi, S.; Hosono, H. *Nature* **2013**, *494*,

336–340.

[46] Bhachu, D. S.; Scanlon, D. O.; Sankar, G.; Veal, T. D.; Egdell, R. G.; Cibin, G.; Dent, A. J.; Knapp, C. E.; Carmalt, C. J.; Parkin, I. P. *Chem. Mater.* **2015**, *27*, 2788–2796.

[47] Miyata, T.; Ida, S.; Minami, T. *J. Vac. Sci. Technol., A* **2003**, *21*, 1404–1408.

[48] Ganguly, P.; Vasanthacharya, N. Y.; Rao, C. N. R.; Edwards, P. P. *J. Solid State Chem.* **1984**, *54*, 400–406.

[49] Shanthi, E.; Dutta, V.; Banerjee, A.; Chopra, K. L. *J. Appl. Phys.* **1980**, *51*, 6243–6251.

[50] Edwards, P. P.; Lodge, M. T. J.; Hensel, F.; Redmer, R. *Phil. Trans. A* **2010**, *368*, 941–965.

[51] Vai, A. T.; Kuznetsov, V. L.; Jain, H.; Slocombe, D.; Rashidi, N.; Pepper, M.; Edwards, P. P. *Z. Anorg. Allg. Chem.* **2014**, *640*, 1054–1062.

[52] Ioffe, A. F.; Regel, A. R. *Prog. Semicond.* **1960**, *4*, 237.

[53] Graham, M. R.; Adkins, C. J.; Behar, H.; Rosenbaum, R. *J. Phys.: Condens. Matter* **1998**, *10*, 809–819.

[54] Jerhot, J.; Šnejdar, V. *Thin Solid Films* **1978**, *52*, 379–395.

[55] Forsberg, H. E. *Acta Chem. Scand.* **1956**, *10*, 1287–1297.

[56] Clark, S. J.; Segall, M. D.; Pickard, C. J.; Hasnip, P. J.; Probert, M. I. J.; Refson, K.; Payne, M. C. *Z. Kristallogr.* **2005**, *220*, 567–570.

[57] Marezio, M. *Acta Crystallogr.* **1966**, *20*, 723–728.

[58] Perdew, J.; Burke, K.; Ernzerhof, M. *ACS Symp. Ser.* **1996**, *629*, 453–462.

Chapter 6

Limitations on Impurity Doping

In the free-electron description of electronic conduction in TCOs, where $\sigma = ne\mu$, conductivity is directly proportional to the concentration of free charge carriers in a material. While even nominally undoped samples of ZnO and In_2O_3 will contain some free carriers due to their tendency to form with an oxygen-deficient stoichiometry, it is almost always necessary to add extrinsic impurity atoms, or *dopants*, in order to raise the carrier concentration and achieve the high levels of conductivity needed for most TCO applications.

Most of the existing literature on TCOs treats doping more or less just as a means to an end, rather than a topic worthy of much study in its own right. Thus, while there have been many works aimed at empirically finding the "best" dopants for achieving highly conductive TCOs, most discussions of the doping *process* begin and end with the simple substitutional model first introduced in Section 2.2.3. In this model, where charge carriers are generated (or consumed) because of differences in valency between the impurity atom and that of the atom for which it is substituted in the host lattice, carrier concentration would be a linear function of dopant concentration.

The real picture is not nearly so straightforward. Even a cursory examination of experimental data will show that the properties of a TCO do not change in a linear or even monotonic fashion as more and more dopant is added. In practice, this fact that arbitrarily high carrier concentrations cannot be achieved simply by using large amounts of dopant is a key restriction on the maximum electrical conductivity of a given system. For this reason, an exploration of the mechanisms and limitations of impurity doping feeds directly into the larger goal of improving optoelectronic performance in TCO thin films.

Here, the process of impurity doping in indium-doped zinc oxide (IZO) films prepared by spray pyrolysis will be examined in detail as a function of dopant concentration. The trends observed in IZO will be explained in both chemical and structural terms, including via the use of X-ray absorption spectroscopy to confirm that indium substituted for zinc is an electrically active defect and also to provide some of the first direct experimental evidence showing a mechanism that limits doping efficiency in IZO. These results will also be examined using a more general description of inefficient carrier generation in TCOs and used to highlight a fundamental structural advantage that In_2O_3 may have over ZnO with respect to its ability to be doped.

We will also consider that doping limitations can occur not only due to properties of the TCO itself, but also because of factors in the chosen thin film deposition process. In particular, the surprisingly important effects of solution chemistry on the preparation of the all earth-abundant TCO silicon-doped zinc oxide (SiZO) will be discussed, along with a new and highly practical method for overcoming one of the most significant problems inherent in using silicon as a dopant in solution-based thin film depositions.

6.1 Finding the Limits of Indium-doped ZnO

In the simple doping picture, indium should act as a one electron donor when substituted for zinc in the ZnO lattice. Indeed, its effectiveness as an n-type donor in ZnO has been demonstrated through the numerous real examples of IZO films that have been prepared using a wide range of deposition techniques.[1–3] In particular, indium-doped ZnO has produced the most highly conductive ZnO-based films that have been reportedly prepared using solution-based techniques.[4]

Furthermore, as a model system for fundamental studies on doping and impurities in ZnO, IZO possesses several key advantages. Particularly compared to other potential dopants like aluminum or silicon, indium has a very low environmental background. The high contrast in atomic number between Zn and In also simplifies the study of samples by many characterization techniques. And as has been noted above, a well-established and tested procedure for the preparation of IZO by spray pyrolysis has previously been reported, which has been amenable to quick and straightforward adaptation to the present experimental apparatus.

The emphasis in this study will be on understanding the behavior of the indium impurity in the Zn-rich portion of the ZnO-In_2O_3 phase system. To do so, a series of IZO thin films were prepared with indium concentrations ranging from 0 to about 20 at%.[i] This range was chosen to include samples both near and well past the indium concentrations where the approximation of simple, substitutional donor doping would be expected to break down, which will permit examination of how and why a departure from the idealized situation occurs.

It should be noted that referring to all of these samples as indium-doped ZnO, which typically implies a host structure that is only slightly perturbed by impurities, is something of an abuse of nomenclature. As will be seen, the samples with higher indium concentrations can no longer be adequately described as just ZnO with some carrier-generating modifications. Indeed, the formation of additional structures and phases within the sample as the indium concentration increases is central to answering the question of why the idealized doping picture does not hold.

It would be possible to use the more general term "indium-zinc oxides" to describe these samples. However, this term is often used to refer to materials with compositions towards the middle and indium-rich portions of the Zn-In oxide phase space, particularly where the wurtzite structure of ZnO is no longer observed. There is no question that phases such as the amorphous In-Zn oxides or the homologous $Zn_kIn_2O_{k+3}$ series have many interesting properties.[5–7] However, a full characterization of the structure and behavior of these is beyond the primary scope of this study to understand the limitations of indium doping in zinc oxide. For these reasons, we will persist in referring to the present set of samples as indium-doped ZnO, even while admitting that doing so is not entirely descriptive.

6.1.1 Preliminary Characterization

Confirmation of Compositional Variation

Ultimately, compositional variation in spray pyrolyzed TCO films is achieved by changing the composition of the precursor solution. Thus, before any analysis and

[i] Following the convention used throughout this thesis, the concentration or doping level refers to a proportion of *total* metals within the oxide sample. For instance, reference to 20 at% indium-doped ZnO (*i.e.*, 20IZO) indicates an In/Zn ratio of 1/4.

interpretation of optoelectronic properties, it is important to determine how the composition of the precursor solutions translates into that of the deposited films. A range of precursor solutions with nominal indium concentrations of 0 to 40 at% were used to prepare thin film samples by spray pyrolysis. It must be noted that these concentrations are nominal values because two important factors are not accounted for in their calculation. The first is the fact that as received indium acetate is almost always partially hydrolyzed to insoluble indium hydroxides, thus leading to the loss of some indium during filtration of the precursor solution. Second, the number of water molecules that can be incorporated into the crystal structure of indium acetate is not well characterized; thus, for consistency, the molecular weight of anhydrous indium acetate was always used for calculations. However, not accounting for the weight of possible crystalline (and adsorbed) waters also may mean that the actual amount of indium used is lower than the quoted nominal value.

Energy-dispersive X-ray spectroscopy (EDX) was used to determine the average indium content of films in this series.[ii] An accelerating voltage of 10 kV for the primary beam was chosen as a compromise between achieving reasonable signal intensity while at the same time minimizing the interaction of the beam with the substrate. After correcting for the minor contribution of the glass substrate to the EDX signal, the measured indium content was calculated and plotted against the nominal indium content of the precursor solution from which each sample was deposited (Figure 6.1).

Figure 6.1 shows that the relationship between nominal precursor and actual film doping levels is very close to linear in this range, with the actual doping level being just about half of the corresponding nominal value. Additionally, it is reassuring that the y-intercept of the fit line is (0,0) to within experimental error. These data essentially show that bulk indium concentration is behaving in a simple, linear fashion throughout the entire composition range that is of interest for this study. Therefore, based upon these results, the indium content of IZO films prepared using this precursor system is taken to be 0.5 of the "nominal" precursor solution value for all further analyses.[iii]

[ii] Additionally, a 1.5 at% IZO sample was examined at higher spatial resolution using TEM, and no evidence of dopant clustering or grain boundary segregation was observed on length scales larger than the EDX spot size of ~2 nm in TEM.

[iii] Samples deposited from precursor solutions containing a nominal indium concentration of 0.5 at% or less had indium concentrations below the detection limits of the EDX spectrometer

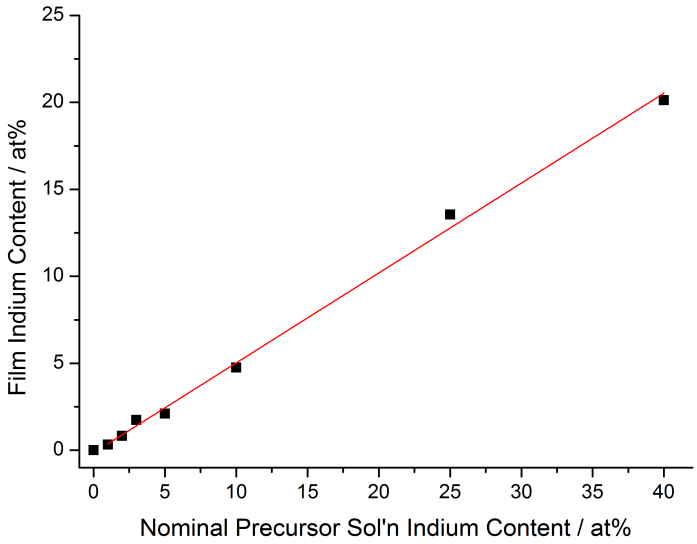

Figure 6.1: Indium content measured by EDX of a series of IZO thin films deposited using spray pyrolysis, as a function of the nominal indium content of the precursor solution from which each film is deposited. A best-fit linear trendline to the data is shown in red ($R^2 = 0.996$). The slope of the fit line is 0.517 ± 0.013, while the y-intercept is -0.15 ± 0.24 at%.

Gross Structural Characterization

As part of the groundwork for more detailed characterization to come, it is also useful to first describe in broad terms the structural nature of this series of samples. Figure 6.2 shows the X-ray diffraction patterns of a representative selection of the thin films in this series. All of the patterns, even the one from the sample with the highest indium concentration of 20 at%, show only diffraction peaks consistent with the presence of hexagonal, wurtzite ZnO crystallites within the samples. There is no clear evidence for the presence of any other crystalline phases.

The samples with 2.5 at% indium and lower demonstrate the same strong preference for growth with the (002) direction perpendicular to the substrate that is seen in undoped ZnO samples deposited at this temperature. If anything, the degree of preferred orientation appears to be even stronger in the samples with 1.5 and 2.5 at% indium than for the undoped ZnO. For IZO samples containing 5 or greater at% indium, the (100) and (101) peaks appear while the relative intensity of the (002) re-

used. However, since the electrical property data presented later clearly shows that indium is being incorporated into these samples and that carriers are being generated, the actual doping levels for these samples are assumed to follow the same trend determined using the rest of series.

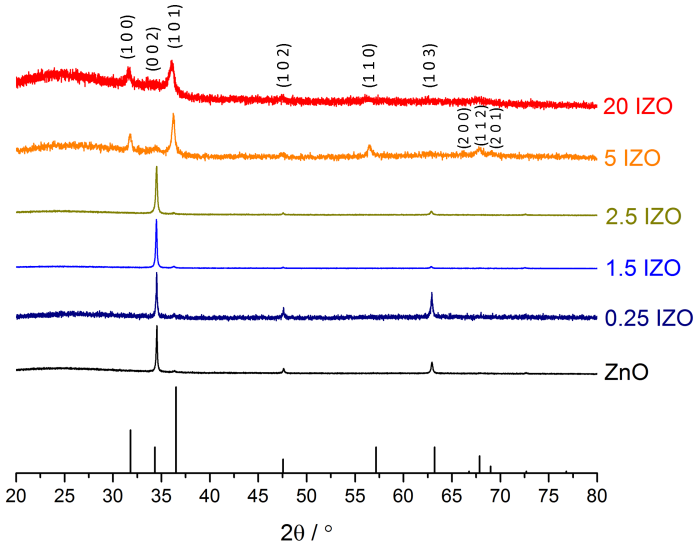

Figure 6.2: X-ray diffraction patterns of ZnO and IZO thin films deposited by spray pyrolysis at a substrate temperature of ∼376 °C. The indium content of each IZO sample is shown as at% of total metals in the sample. A reference pattern for pure ZnO powder is also shown as a stick chart.

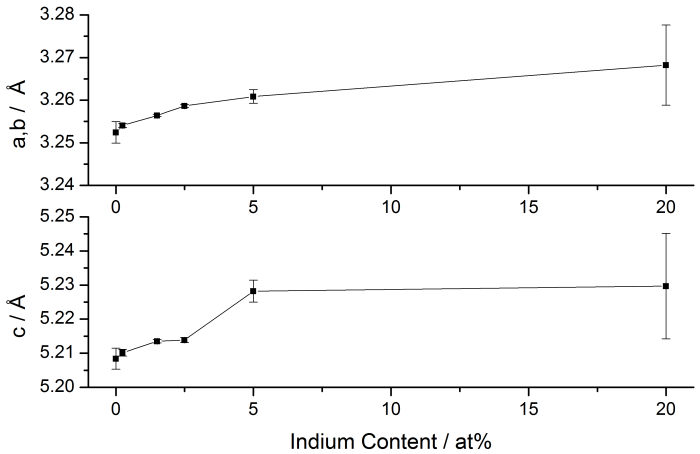

Figure 6.3: Lattice parameters $a(=b)$ and c for wurtzite phase in IZO films as a function of indium doping level.

flection is significantly diminished, suggesting that the distribution of ZnO crystallite orientations within these heavily doped IZO samples has changed substantially.

Additionally, as the indium content is increased, the breadth of the XRD peaks increases and their height decreases. This is consistent with a reduction in average crystallite size and/or an increase in lattice strain with increasing impurity concentration.[8,9] The broad, low features in the 20 at% IZO pattern could also be indicative of X-ray scattering due to the presence of amorphous material or very small crystallites.

The lattice parameters of the ZnO phase determined using Pawley refinement of the data are shown in Figure 6.3. The fits themselves are presented in Appendix E. The lattice parameters of the undoped sample are close to literature values of $a = 3.250\,\text{Å}$ and $c = 5.207\,\text{Å}$ reported for ZnO in the wurtzite structure.[10] As expected for the incorporation of an In^{3+} cation that is relatively large compared to Zn^{2+} ($\sim$94 pm vs. 74 pm[11]), the lattice parameter increases as the doping level increases. However, this increase does not happen linearly with respect to indium content, which argues against continual, uniform incorporation of indium in one structural environment.

A significant jump in c (and to a lesser extent, a) lattice parameter is observed for the 5 at% and 20 at% indium samples. It should be noted that the estimated errors for these samples are much larger than for the others because of the low signal-to-noise ratios of the spectra from which they are derived, especially for peaks associated with planes with a large ℓ component. It is not clear whether this apparent discontinuity in lattice parameter is a real effect, or just an artifact from the fitting of noisy data.

A direct observation of surface morphology using SEM confirms several of the key observations made using XRD (Figure 6.4). Characteristic hexagonal grains are visible in the undoped and lightly doped samples, while being entirely absent from the higher indium concentration samples. There appears to be a correlation between the presence of these grains and a strong (002) reflection in the X-ray pattern. The size of the hexagonal grains is broadly similar for all samples where they appear, which is consistent with the uniform peak width in the corresponding XRD data. Similarly, a significant reduction in average grain size can clearly be seen as the impurity level increases, which can be linked with the broader XRD peaks observed for these samples.

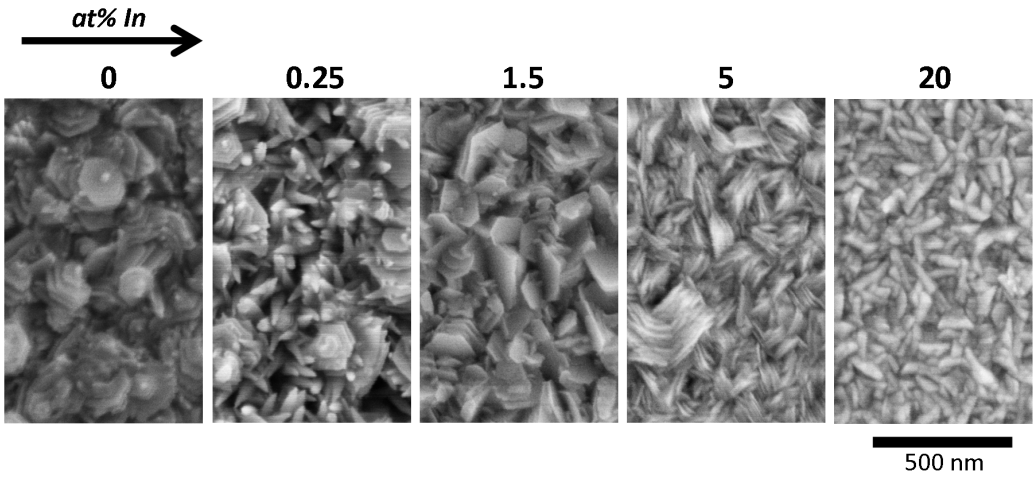

Figure 6.4: Changes in surface morphology of a selection of ZnO and IZO thin films deposited by spray pyrolysis as the doping level is increased. All samples shown here were deposited at a substrate temperature of ∼376 °C and the doping level of each sample (in at%) is noted above the corresponding image.

Taken together, these data show that all samples are in a composition regime where material having the wurtzite structure of ZnO is still present. However, while the most lightly doped samples appear to have broadly similar structures to their undoped counterparts, there is, as expected, a clear and increasing deviation from the baseline case as the indium content of the thin films increases.

6.1.2 Optoelectronic Properties and Doping Efficiency

Electrical Properties

Now, having a sense of the chemical and structural nature of these IZO samples, their electrical and optical properties can be considered. Figure 6.5 shows the electrical transport properties for a series of IZO samples deposited at ∼376 °C as a function of indium content.

Starting from the undoped ZnO samples, which have an average carrier concentration (n) of about 1.7×10^{18} electrons per cm^{-3}, the addition of indium initially leads to an increase in n up to a maximum value of about $4.1 \times 10^{20}\,\mathrm{cm}^{-3}$ for the 5 at% indium sample. However, unlike what would be expected from the simple model of doping where each indium atom substitutes for a zinc and contributes one electron, the increase in carrier concentration over this range clearly shows diminishing returns.

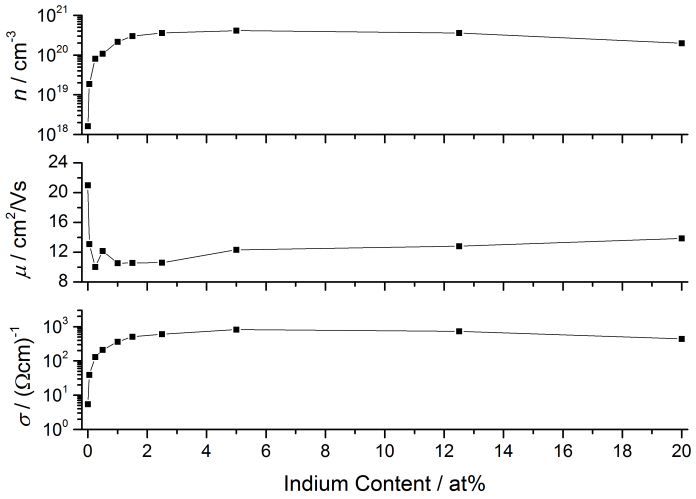

Figure 6.5: Carrier concentration (n), carrier mobility (μ), and electrical conductivity (σ) for a series of indium-doped ZnO films deposited by spray pyrolysis at ∼376 °C as a function of indium content.

Furthermore, n even decreases slightly as the indium content continues to increase above 5 at%.

The extent to which reality deviates from the substitutional model of doping can be quantified by calculating a *doping efficiency* as a function of doping level:

$$\text{Doping Efficiency} = \frac{n_{\text{doped}} - n_{\text{undoped}}}{k|\text{dopant}|}, \tag{6.1}$$

where n_{doped} and n_{undoped} are the carrier concentration of the doped and undoped samples, respectively, |dopant| is the concentration of the impurity (in units of atoms per cm^3), and k is the number of carrier electrons that should be generated for each ideal substitution of a host atom with that impurity. The concentration of dopant can be estimated by assuming that the appropriate atoms in the host structure have equal probability of being substituted by the dopant atoms, and that the atomic number density of the host structure is maintained. Note that the doping efficiency multiplied by k would be an estimate of the average number of free electrons contributed per dopant atom.

In the case of IZO, $k = 1$. Furthermore, the wurtzite structure of undoped ZnO has a theoretical density of $5.61\,\text{g}\,\text{cm}^{-3}$ and a molecular weight of $81.41\,\text{g}\,\text{mol}^{-1}$, which corresponds to 4.15×10^{22} cations per cubic centimeter. The concentration of indium in these indium-doped ZnO samples can then be estimated as this latter value multiplied by the indium doping level.

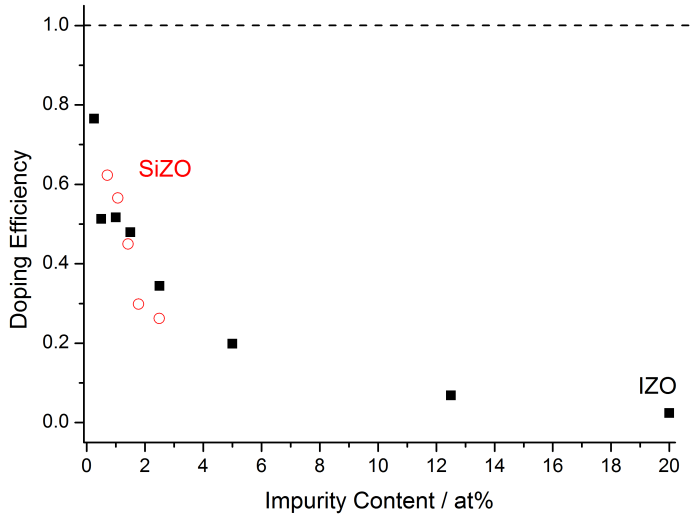

Figure 6.6: Calculated doping efficiency in a series of IZO films (black squares) and SiZO films (red circles) prepared by spray pyrolysis with different doping levels. The doping efficiency of unity expected if the simple substitutional picture of doping were fully correct is indicated with a dashed line.

Figure 6.6 shows the results of applying Equation 6.1 to the data from this set of IZO films, as well as from a series of silicon-doped ZnO films that will be discussed later in Section 6.3. Clearly, the doping efficiency is below one for all samples, with the extent of the deviation increasing as the doping level increases. These data are enough to demonstrate that if the simple one-indium, one-electron picture of doping ever holds, it only does so near the limit of infinitely low dopant concentrations. Even for the lowest indium concentration sample shown here, a clear deviation from pure substitutional doping can be observed.

Importantly, the fact that almost the same trends hold for both silicon and indium dopants is emblematic of the fact that this behavior is almost entirely general when it comes to doped TCO materials. For example, the diminishing returns in n that result from adding more and more dopant have also been observed in ITO, aluminum-doped ZnO, and fluoride-doped SnO_2.[12–14] This decreasing effectiveness of additional dopant represents one of the overall limits to TCO performance. We shall return to the question of why this occurs in general, and then for IZO specifically, in Section 6.2.

Turning now to the mobility data also shown in Figure 6.5, increasing indium content up to about 2.5 at% can be correlated with a drop in carrier mobility. This is

more or less as expected, since the addition of indium should lead to the creation of defects in the base ZnO structure that can act as scattering centers and thus reduce mobility.

What is surprising and apparently particular to these IZO films is that the mobility trend with doping reverses direction and tends to *increase* as the indium content is increased beyond 2.5 at%. At higher doping levels, even if additional dopant atoms were not leading to the effective creation of carriers, they would still be present in the film and should be scattering centers if acting as defects in a host lattice. The fact that these additional impurity atoms are not increasing scattering rate is further evidence that the picture of added defects merely perturbing a host structure is failing to properly describe the material in this composition range. Indeed, the structural characterization of Section 6.1.1 has also hinted at the formation of secondary structures at higher indium concentrations. This too, is something that will be more thoroughly studied and discussed using information from additional characterization techniques in the following section.

Optical Properties

UV-Vis-NIR transmission spectra of these IZO samples, and the corresponding average transparency values over the visible range are shown in Figure 6.7. The blueshift in bandgap energy and the decrease in near-infrared transmittance that are associated with an increasing carrier concentration are clearly visible, and line up very well with the direct current Hall effect measurements in Figure 6.5.

The transparency of these IZO films is encouraging. Despite having thicknesses on the order of 400 nm, the most transparent of these samples have average transparencies in the visible range of ∼89 % when corrected for the presence of the glass substrate (82 % uncorrected). Conveniently, the most conductive samples with 5 at % indium are also the most transparent. Furthermore, for this sample, the light transmission values are relatively uniform from 400 to 1200 nm,[iv] which should allow for excellent color rendition through this sample.

Another notable feature of Figure 6.7b is the sharp increase in transparency that occurs at an indium concentration of about 1.5 at%. Examination of the raw trans-

[iv] Barring, of course, the effect of the interference fringes, which can in principle be engineered out in a real device architecture.

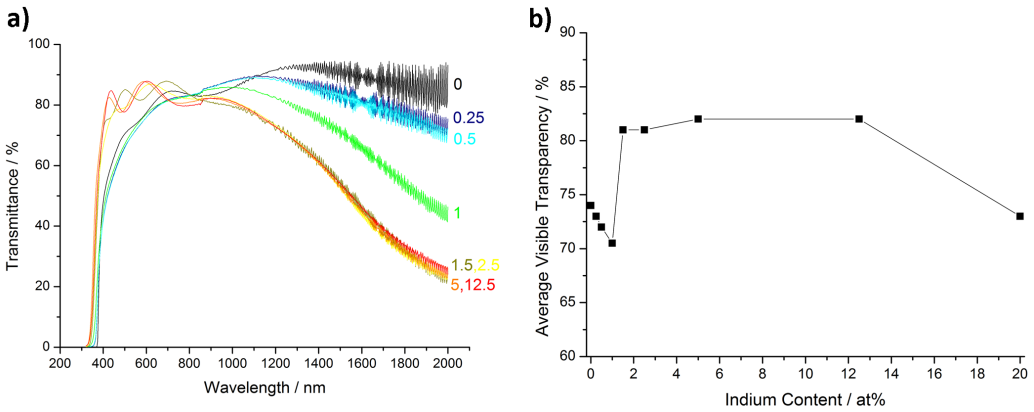

Figure 6.7: a) UV-Vis-NIR transmission spectra recorded from IZO films deposited by spray pyrolysis. The corresponding indium content for each dataset is indicated in at%. The glitch visible in some spectra near 860 nm is due to a detector change in the spectrometer. b) Average visible transparency (400–750 nm) extracted from the raw data in part (a). These values are not corrected for the presence of substrate.

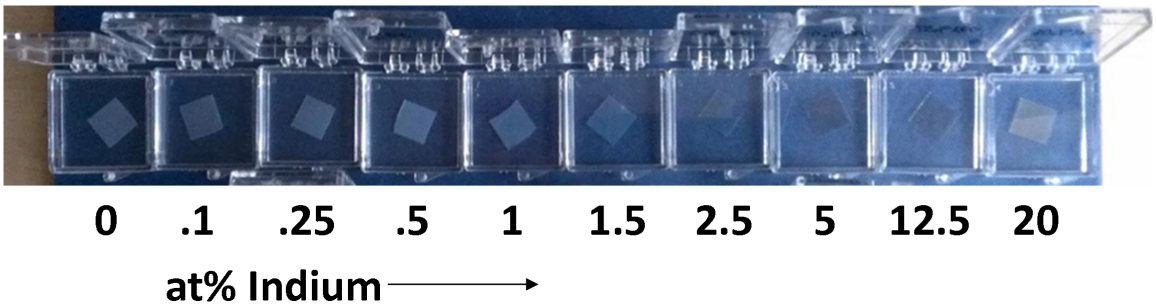

Figure 6.8: Visual appearance of IZO thin film samples as a function of indium doping level. The indium content of each sample is indicated in at% of total metals. As the indium content increases, a noticeable decrease in haze can be seen starting with 1.5 at% IZO sample.

mission spectra and visual inspection of the samples (Figure 6.8) show that the lower average transparency of the lightly doped and undoped samples is mostly due to haze and not intrinsic absorption. This can clearly be seen by the gradual loss of transmittance as the wavelength is decreased, which is characteristic of wavelength-dependent light scattering (Section 3.2). The SEM images in Figure 6.4 do imply a reduction in surface roughness and average feature size as the doping level increases, which would qualitatively explain this trend. However, it must be admitted that the sharpness of the hazy-to-non-hazy transition is somewhat surprising.

6.2 The Nature of Compensating Defects

6.2.1 General Thermodynamic Limits to Doping

A vast array of different structural defects is possible in doped oxides. Some of these will lead to the net creation of free electrons, while others will lead to their localization. These defect formation processes can be thought of in the same framework as chemical reactions. Since the extended solid oxide is capable of stabilizing a population of free conduction electrons, in this context, the free electrons can simply be treated as one of the reactants. For instance, it might be possible to (crudely) express a donor-forming defect reaction as

$$\text{Donor}^{n-} \rightleftarrows \text{Donor} + n(e^-_{\text{free}})\,. \tag{6.2}$$

An increase in free electron concentration will lead to a corresponding increase in the Fermi level E_{F}, which is also the chemical potential of these free electrons. Le Châtelier's principle would then suggest that the forward, electron-donating equation will become increasingly disfavored. Conversely, any acceptor forming (*i.e.*, electron localizing) defect reactions of the general form

$$n(e^-_{\text{free}}) + \text{Acceptor} \rightleftarrows \text{Acceptor}^{n-} \tag{6.3}$$

would become increasingly favored. This creates a general scenario where the equilibrium concentration of free electrons cannot be increased above a certain value by doping because of the spontaneous formation of compensating defects that consume electrons. Incidentally, this same reasoning also sets a lower bound on the equilibrium values of E_{F} and n, below which donor defects will spontaneously form and raise them.

The result is that the values of E_F at which the formation of the most stable acceptor and donor defects become spontaneous will define a finite range of E_F values that can be achieved in the material at thermodynamic equilibrium, as illustrated schematically in Figure 6.9. This of course does not rule out the possibility that non-equilibrium defect concentrations could be achieved by some specialized means, for instance, ion implantation[15,16] or plasma annealing.[17] However, such treatment steps would only add cost and complexity to a TCO deposition process, even if the kinetic stability of the resulting samples was enough to be useful.

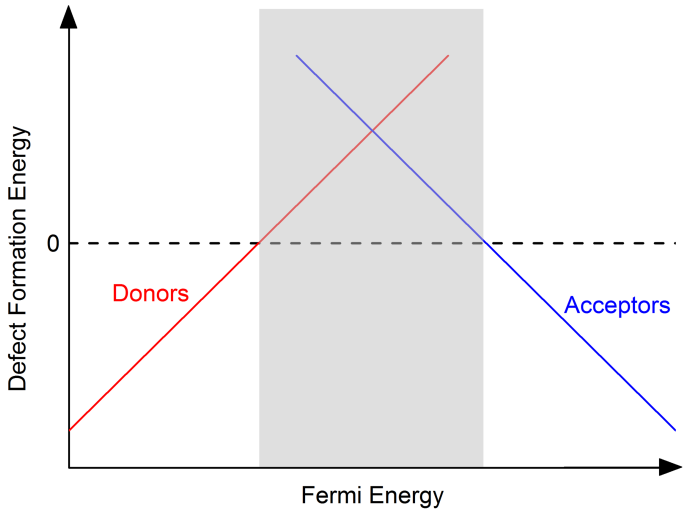

Figure 6.9: Schematic illustrating how the formation energies of donor and acceptor defects define a range of Fermi energy values (shaded gray) that can be achieved in a given material at thermodynamic equilibrium. Outside of this range, the spontaneous formation of defects will tend to push the Fermi energy back into this range.

Simply knowing that there will be a range of stable E_F values does not by itself provide any information on what the implications are for the behavior of any given material. To know this, it is necessary to consider how the range of stable E_F values lies in energy relative to the electronic bands of the material. Robertson and Clark have computationally analyzed a range of semiconductors assuming only intrinsic compensating defects.[18] A selection of their results is shown in Figure 6.10.

For ZnO and SnO_2, the two n-type TCOs in this figure for which the calculation has been made, the range of stable E_F begins in the higher energy part of the bandgap and extends into the conduction band. This is very much consistent with available experimental evidence on n-type TCOs. It is well established that ZnO (and In_2O_3)

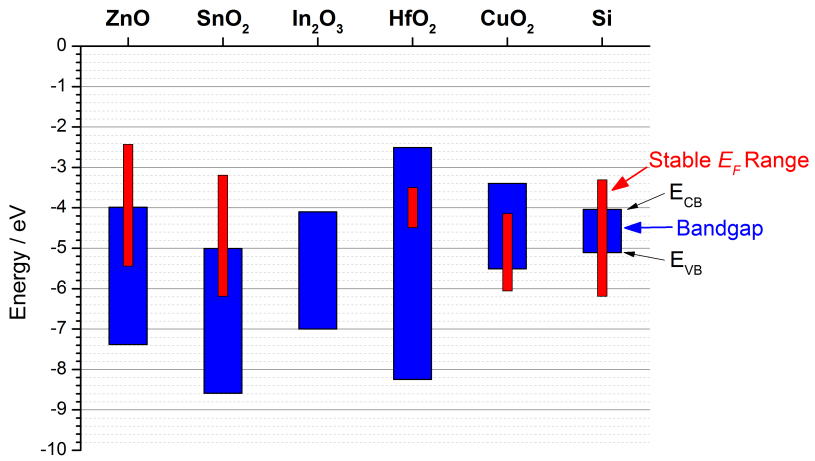

Figure 6.10: Band diagrams of various materials aligned with the vacuum level chosen as the zero of energy. For each material, the band gap is shown as a range in blue, while the Fermi levels that are thermodynamically stable against the formation of intrinsic defects as calculated by Robertson and Clark are shown in red.[18] The E_F range calculation has not been performed for In_2O_3, so only its bandgap is shown.

have a strong tendency to form with an oxygen-deficient stoichiometry. Even nominally pure samples almost always possess some degree of n-type conductivity due to the presence of spontaneously formed donor defects (such as V_O). This can now be explained in terms of the fact that stoichiometric samples of these oxides, where E_F is in the center of the bandgap, are not thermodynamically stable against spontaneous donor formation at such low electron concentrations. This also explains why it has been so difficult to consistently produce ZnO samples with persistent p-type behavior; such a material would have to be kinetically stabilized.

While the analogous calculations have apparently not yet been performed for In_2O_3, it is almost certain that the positioning of its stable E_F range is qualitatively similar to that of ZnO, especially given that both are n-type TCOs. However, it should be pointed out that any differences in the formation energy of acceptor defects could lead to different doping limits, and thus differences in the highest thermodynamically stable carrier concentration. Any future work that demonstrated such a difference between ZnO and In_2O_3 could well be very useful for explaining why these two TCO materials perform differently.

Figure 6.10 also allows a simple explanation for why the doping behavior of other materials differs from that of the n-type TCOs. For instance, the fact that the stable E_F range of CuO_2 extends into its valence band explains why this material can exhibit

degenerate p-type conduction. Si can be doped both n- and p-type because its E_F range straddles the entire bandgap and extends into both its conduction and valence bands. In contrast, this calculation suggests that HfO_2 will not permit degenerate band conductivity of either sign because the range of allowable E_F is entirely within its bandgap, thus explaining its status as a commonly-used dielectric.

This type of model is very conceptually useful for understanding the basic idea of why there should be limitations on effective doping. However, because the calculations described only include intrinsic defects, they cannot be entirely accurate when used to describe the behavior of a system like IZO as a function of doping level. In addition to changes in E_F, the changing chemical potential of the impurity species will also certainly be important. In this more general situation, there is also the possibility of electronically inactive defects whose formation can slow down, but not reverse, efforts to increase n by impurity doping. Nevertheless, the basic idea of a cap on carrier concentration and Fermi level imposed by the spontaneous formation of non-donor defects still holds. Given this, the challenge now is to understand the mechanisms that limit doping efficiency in the more complex, real-world case of IZO.

6.2.2 Dopant Disposition in IZO: An XAS Study

The combination of bulk chemical analysis and electrical property measurements have shown that some fraction of the indium present in IZO must be in one or more electrically inactive forms and that this fraction increases as the indium content is raised. As such, determining the structural and chemical role of the indium impurity in IZO as a function of doping level would be very useful information for understanding why these changes in doping efficiency occur.

For this task, analysis of the Extended X-ray Absorption Fine Structure (EXAFS) region of X-ray absorption spectra can be very illuminating, because it is one of very few characterization methods capable of providing element-specific local structure information about a dilute impurity in a chemically-distinct matrix without any requirements for long-range ordering. This technique has been successfully applied to the study of tin in ITO, as well as to several other dopant/TCO combinations.[19–21] However, such studies on doped ZnO, and IZO in particular, are comparatively rare. The only study that to our knowledge applies EXAFS to IZO reports on results for

5 at% IZO nanoparticles, and not thin films across a range of indium doping levels as would be most relevant to the problem at hand.[22]

For these reasons, we have elected to study a selection of the IZO thin film samples in this series using X-ray absorption spectroscopy. In K-edge spectra were collected from thin film samples with 0.5, 1.5, 5, and 12.5 at% indium in order to span a full range from relatively light to extremely heavy doping. The reduced and normalized data is plotted in Figure 6.11 along with reference data for pure In_2O_3 powder and Zn K-edge data for ZnO powder.

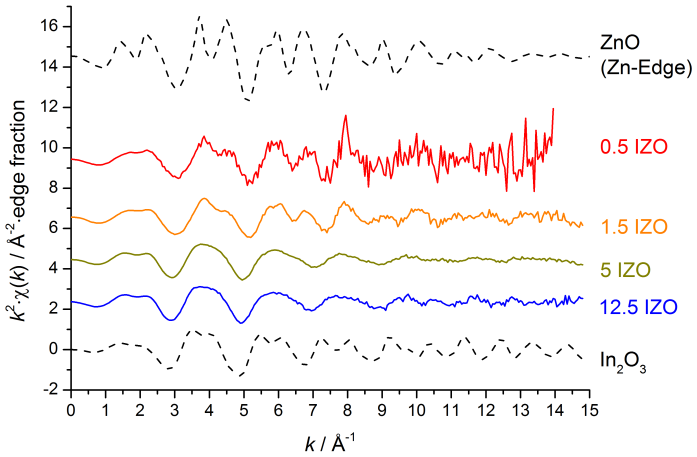

Figure 6.11: Normalized and background-subtracted In K-edge EXAFS data (k^2-weighted) for a series of IZO thin films with indium contents ranging from 0.5 to 12.5 at%. Reference data collected from pure In_2O_3 powder and Zn K-edge data from pure ZnO powder are also shown as dashed curves for comparison. The data have been offset for clarity.

Because the IZO samples are thin films with relatively low indium concentrations, the data quality is not as good as that for the reference powders. This arises simply from the geometry of the experimental samples, which means that a less-than-ideal number of indium absorbers is being interrogated by the beam. Due to the fact that the signal decays exponentially with increasing k (Equation 3.23), the noise is most evident in the high k portion of the data. While these data are not ideal (especially that for the 0.5 at% IZO sample) and some of the noisiest high k data will need to be excluded from later analysis, it will be seen that they are good enough to provide some very useful information about the structural disposition of indium in IZO.

Before proceeding, it is worth commenting briefly on a few qualitative features of Figure 6.11. Given the rather different structures of wurtzite (ZnO) and bixbyite

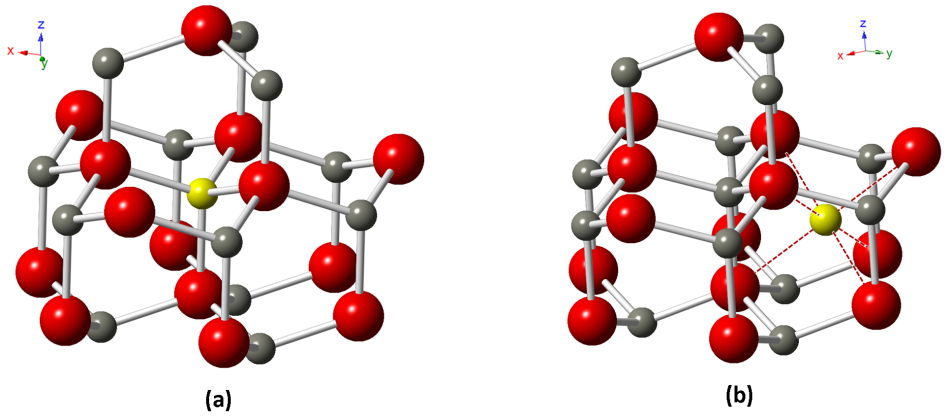

Figure 6.12: Local structure around a) tetrahedral substitutional and b) octahedral interstitial positions for indium defects in indium-doped ZnO, as used for EXAFS modeling. Indium atoms are shown in yellow, zinc in grey, and oxygen in red.

(In_2O_3) it should come as no surprise that the Zn environment in ZnO gives a markedly different EXAFS signal than that which arises from the combination of the In environments in In_2O_3.[v] While none of the IZO spectra are a precise match with the reference patterns, there is a visible transition of the indium environment in IZO from more ZnO-like to more In_2O_3-like as the indium content increases. Just as one example, the pair of maxima in the ZnO signal at approximately 3.7 and 4.5 $Å^{-1}$ are clearly also seen in the data for 0.5 and 1.5 at% IZO. However, for the 5 and 12.5 at% IZO, these two peaks have to a large extent merged into a single broad peak and shifted to slightly lower k, as is seen in the reference data for In_2O_3.

The idea that indium at low concentrations primarily substitutes for zinc in the ZnO lattice, and that this is the electrically active donor defect, is consistent with the fact that doping efficiencies are the highest for the low indium samples. Then, as other non-doping active environments for indium become more prevalent, it would be expected that doping efficiency would fall. This is the basic hypothesis that will be explored through more rigorous modeling of these data, as presented below.

[v]Strictly speaking, there are two crystallographically distinct indium environments in the bixbyite structure of In_2O_3. However, from a local structure point of view, both indium environments are very similar, with the main difference between the two being the fact that there is a small splitting of nearest-neighbor oxygen distances at one of the sites. For the purposes of EXAFS modeling, the fact that In_2O_3 is well represented by using just one indium environment with slightly higher than usual disorder in the In-O distance has been verified by the successful modeling of the reference powder data using this approach.

Local Structure Models for Lightly Doped IZO: 0.5 and 1.5 at%

For the IZO samples with relatively low doping levels and relatively high doping efficiency, assuming that all indium present is substituted at Zn sites is a reasonable first approximation. The local structure model for this case was created by starting from literature crystallographic data for ZnO,[23] replacing one of the zinc atoms with an indium, and then considering the local environment around the substitution (Figure 6.12a). The experimental and simulated EXAFS data using the five strongest single-scattering paths in this model are shown in Figure 6.13. For this and subsequent EXAFS fits in this section, full fitting logs, including details of the path parameters and error estimates, are provided in Appendix G.

Both of the data sets are reproduced with reasonable success by the substitution-only model. Furthermore, it is fairly safe to suggest that most of the apparent fitting error for the 0.5 at% sample is due to suboptimal data quality rather than any fundamental difficulties with the chosen structural model. This confirms the initial guess that a model containing only substitutional indium is a reasonable starting point.

However, it has been found that the fit for 1.5 at% IZO can be significantly improved by also including a contribution from indium located at the octahedral interstitial positions defined by the hexagonal close-packed oxide sublattice of ZnO (Figures 6.12b and 6.14). This improvement manifests itself in the steep reduction of both R-factor and χ^2_{red} compared to the model with only substitutional indium. Only the octahedral holes in the hexagonal close-packed oxide lattice of ZnO were considered as positions for interstitial indium because In^{3+} does not fit into the available tetrahedral holes (at least not without major structural distortion of the host ZnO structure, which is not evident in XRD data).

By analogy to DFT work performed on aluminum interstitial defects, the indium interstitial in ZnO can be hypothesized to be a deep donor, and thus electrically inactive under normal conditions.[24] The ratio of indium in interstitial and substitutional positions was an unconstrained fit parameter in this model and found to be 0.76 ± 0.46 to 1. This implies that 43.2 % (range: 23.2 to 54.9 %) of the indium in the sample is in the electrically-inactive interstitial position, which is entirely consistent with the just over 50 % doping efficiency for this sample shown in Figure 6.6. The excellent

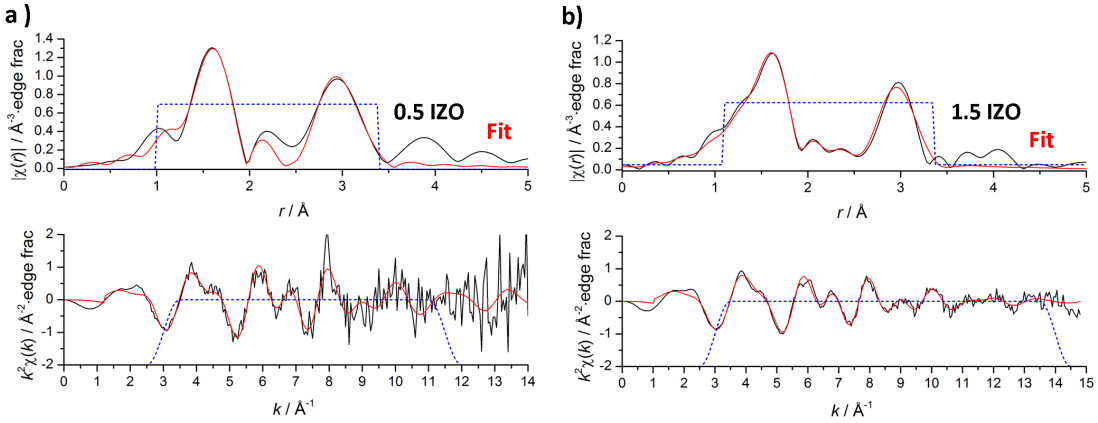

Sample	Model	Variables Used	N_{idp}	R-Factor	χ^2_{red}
a) 0.5 IZO	In_{Zn} Only	8	12.2	.0303	7.974
b) 1.5 IZO	In_{Zn} Only	8	15.6	.0145	13.384

Figure 6.13: Normalized EXAFS data (k^2-weighted) for a) 0.5 at% IZO and b) 1.5 at% IZO, and Fourier transform magnitude (black), along with data simulated for a theoretical model consisting of indium substituted at zinc sites only (red). The Hanning windows defining the fit ranges in k- and r-space are shown in blue.

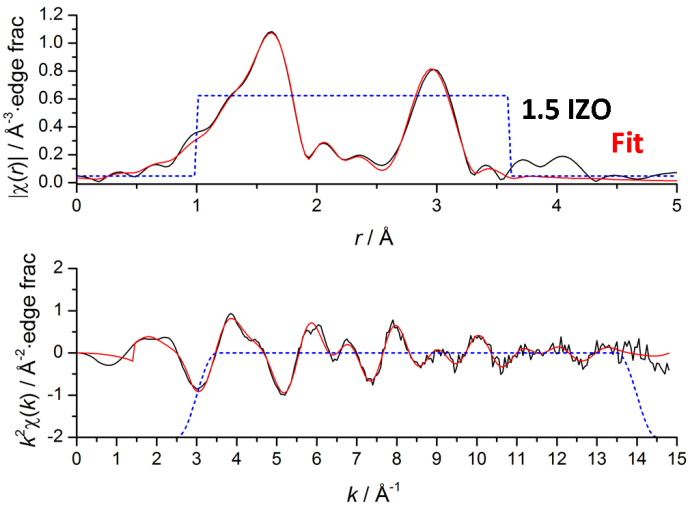

Sample	Model	Variables Used	N_{idp}	R-Factor	χ^2_{red}
1.5 IZO	In_{Zn} and In_{int}	13	18.0	.0053	6.933

Figure 6.14: Normalized EXAFS data for 1.5 at% IZO (k^2-weighted) and Fourier transform magnitude (black), along with data simulated for a theoretical model consisting of In substituted at Zn sites and In at octahedral holes in ZnO (red). The Hanning windows defining the fit ranges in k- and r-space are shown in blue.

agreement of this fitted range with independent electrical measurements is certainly evidence in favor of this proposed model.

Unfortunately, it was not possible to fit the data for 0.5 at% IZO using the model including both interstitial and substitutional positions because the information content of this noisier data set was smaller than the number of independent parameters required. However, it is reasonable to assume that better data would likewise show that the substitution-only model can be improved by also considering the presence of indium at interstitial sites. Presumably, the percentage of interstitial indium would be around 25 %, to account for the ∼75 % doping efficiency in these samples.

The fitting results for these lower doping level samples are consistent with the classic idea that cation-substituted indium is the active species when it comes to contributing free carriers to IZO. However, they also show that even at a doping level as low as 1.5 at% In, a significant fraction of the indium present may already be at electrically-inactive interstitial sites.

Local Structure Models for Heavily Doped IZO: 12.5 at%

The highest indium concentration IZO sample studied using EXAFS here was one with a doping level of 12.5 at%. Both the structural characterization of Section 6.1.1 and very low doping efficiency have already implied that "doped ZnO" is probably not a very complete description of this sample. Thus, for these data, local structure models based on In_2O_3 should also be introduced (Figure 6.15).

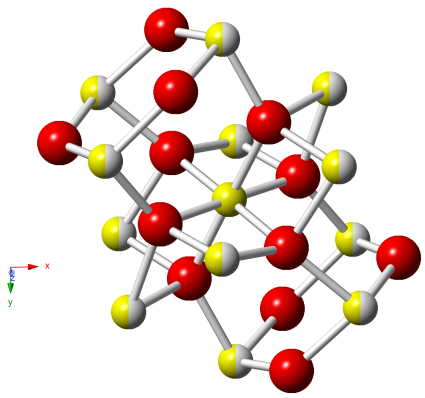

Figure 6.15: Local structure around the indium absorber in In_2O_3 (yellow) used for the theoretical model described in the main text. The other neighboring indium sites are colored both yellow and gray to reflect that some fraction of these sites are also occupied by zinc in some models. Oxygen is shown in red.

Figure 6.16 shows the results of fitting the EXAFS data for this sample with three candidate local structure models: a) Substitutional with contribution from interstitial indium (the same used to describe 1.5 at% IZO), b) the indium local structure found in In_2O_3,[25] and c) the indium local structure found in In_2O_3, but with additional perturbation from zinc scattering in the second nearest-neighbor shell.

It is obvious that the ZnO-based model used in Figure 6.16a reproduces the data from this heavily doped sample only very approximately. The fact that there is still some general resemblance, especially in the first peak in r at around 1.6 Å, is probably only a consequence of the fact that both sample and theoretical model are metal oxides. The In_2O_3-based model b is much more successful, despite using fewer independent parameters, and shows that a change of base model from the lightly doped case is needed.

As such, the best-fitting model we have found starts from an In_2O_3 local environment, but introduces additional zinc scattering in the second nearest-neighbor shell. This modification leads to dramatically improved fit quality, with both R-factor and reduced-χ^2 falling by more than a factor of two compared to the unmodified In_2O_3 structural model. The best fit was achieved using a zinc-to-indium ratio in the second shell of 0.21:1.

The lack of significant signal intensity in r beyond about about 3.9 Å, while not proof, is suggestive of a lack of long-range structural order around most indium atoms in the sample. This agrees with the X-ray diffraction data (Figure 6.2) which also did not detect any large domains of crystalline indium oxide in these samples.

Several possibilities can be proposed that would be consistent with the present data. One is that the increasing concentration of indium defects leads to their association and the formation of nanoclusters that locally have an indium oxide structure, but are too small to cause discernible XRD diffraction peaks. One intriguing variant of this could be the formation of fragments of the $InO_{1.5}$ bi-layers that have been reported in the high-temperature In-Zn oxide phases with the general formula $Zn_kIn_2O_{k+3}$.[7] In either case, a tightly limited spatial extent in one or more dimensions for the In_2O_3 region would explain the requirement for substantial zinc to be present in the neighborhood of the average indium scatterer. Another plausible scenario would be the formation of an amorphous indium-zinc oxide phase as has been

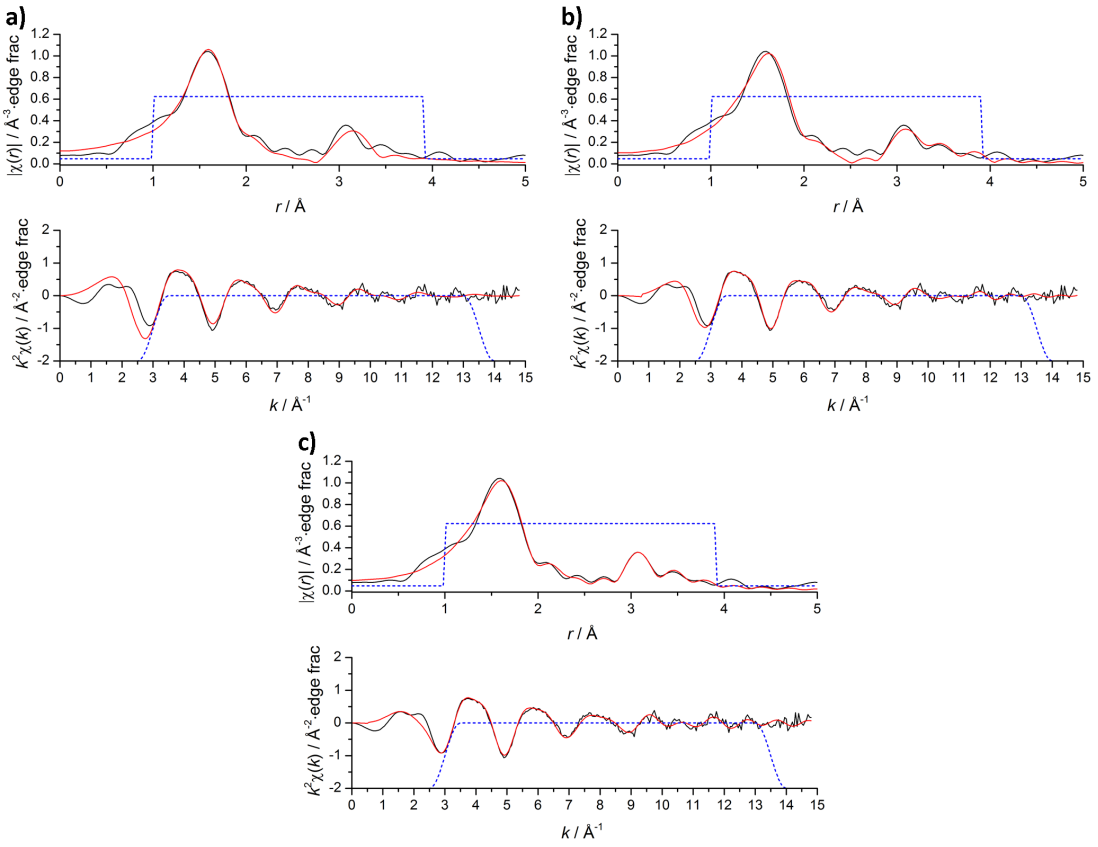

Sample	Model	Variables Used	N_{idp}	R-Factor	χ^2_{red}
12.5 at% IZO	a) In_{Zn} and In_{int}	13	19.2	.0489	125.930
	b) In_2O_3-like	10	19.2	.0341	60.279
	c) In_2O_3-like w/ Zn	13	19.2	.0104	28.186

Figure 6.16: Normalized EXAFS data for 12.5 at% IZO (k^2-weighted) and Fourier transform magnitude (black), along with data simulated for the indicated theoretical models (red). The Hanning windows defining the fit ranges in k- and r-space are shown in blue.

reported in some other contexts.[5,26,27]

A cation in its own "native" oxide environment would not be expected to be associated with free carriers, as there is no longer an excess of valency to be balanced by the presence of free electrons. In fact, if any zinc were to be present in an indium oxide environment, it should be expected to act as an acceptor. Thus, the low and decreasing doping efficiency can be readily explained by this apparent tendency for indium to adopt In_2O_3-like environments at higher doping levels. This being said, there is almost certainly still electrically active indium substituted at zinc sites in 12.5 at% IZO; this much is clear from the high carrier concentration of these samples. However, these EXAFS results clearly show that substitutional indium is no longer the dominant state of indium in this material. In fact, the poor fit of the model in Figure 6.16a suggests that indium substituting for zinc in ZnO-like regions must now be a relatively small minority of the total indium present.

Local Structure Models for Moderately Doped IZO: 5 at%

Based on the analysis of the previous two cases, it might be expected that the 5 at% IZO is transitional between the ZnO-like and In_2O_3-like cases. And indeed, Figure 6.17 shows that best results by far are achieved by modeling the 5 at% IZO as a linear combination of the models used for 1.5 and 12.5 at% IZO, rather than using either of these models individually. To do this, it was necessary to drop a few of the highest r ($r > 3.6$ Å) scattering paths from each of the component models in order to reduce the number of independent variables. The fact that this did not reduce the quality of the fit (and indeed, improved it), suggests that there is substantial disorder further than this distance from the scattering center.

The ratio of the substitutional and In_2O_3-like scattering paths was one of the independent fit parameters. The population of the substituted indium was found to be 0.19 ± 0.076 of the population of indium in In_2O_3-like environments. The implication is that 16 % (range: 10–21 %) of indium present is in an electrically active substitutional defect, which again is consistent to within experimental error with the measured doping efficiency of just under 20 %. This correspondence also helps confirm that indium substituted at the zinc site is indeed likely to be the main electrically active defect.

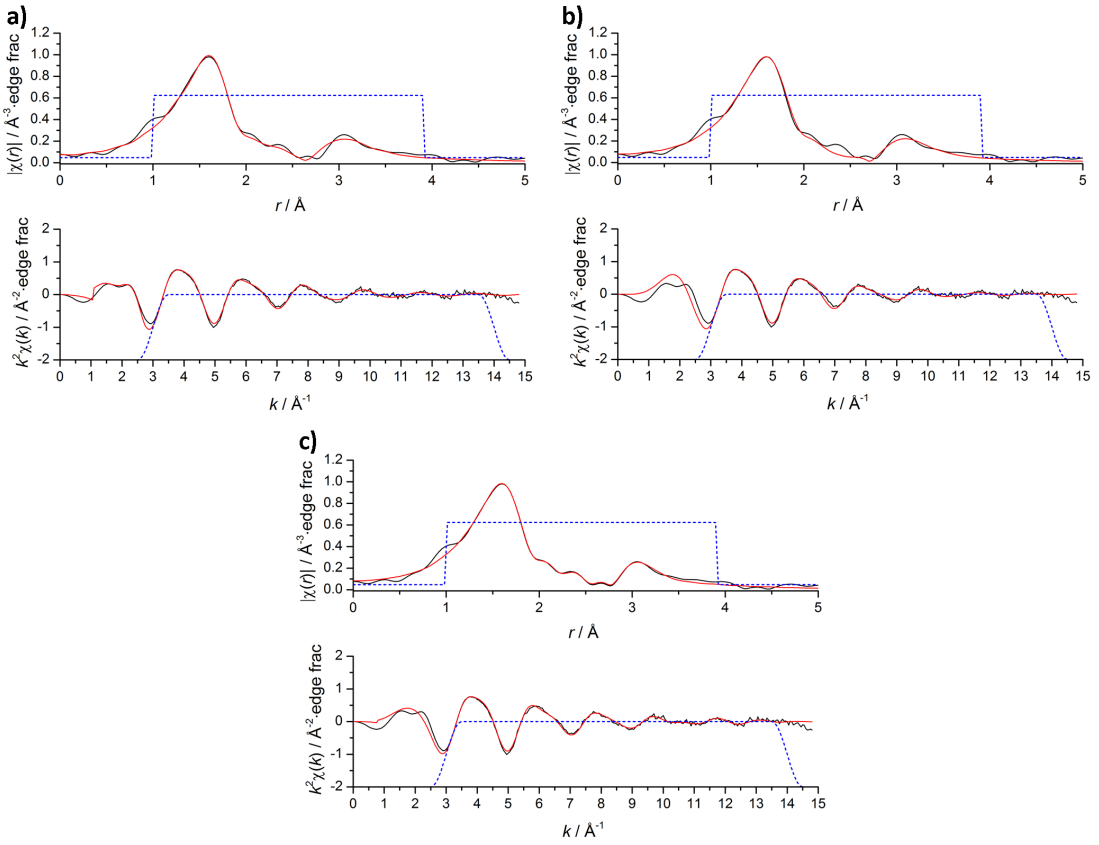

Sample	Model	Variables Used	N_{idp}	R-Factor	χ^2_{red}
5 at% IZO	a) In_{Zn} and In_{int}	11	20.1	0.0163	69.898
	b) In_2O_3-like	10	20.1	.0182	80.059
	c) In_{Zn} and In_2O_3-like	13	20.1	.00275	21.315

Figure 6.17: Normalized EXAFS data for 5 at% IZO (k^2-weighted) and Fourier transform magnitude (black), along with data simulated for the indicated theoretical models (red). The Hanning windows defining the fit ranges in k- and r-space are shown in blue.

Trends Across the IZO Series

At this point, it is useful to summarize this journey across the composition range of indium-doped zinc oxides. Fortunately, the results of these EXAFS studies allow for the development of a quite coherent proposal regarding the means, mechanisms, and limits of indium doping in spray-pyrolyzed IZO.

In the limit of light doping, the evidence suggests that most of the indium atoms substitute for zinc, as in the classic, simple doping picture. This accounts for the doping efficiency near 100 % as well as the initially rapid rise in carrier concentration upon doping. However, in principle, there should be a thermodynamically defined maximum number of zinc atoms in ZnO that can be stably replaced by indium, which can perhaps be termed a *substitutional solubility limit*. Based on the saturation of the carrier concentration around $4.15 \times 10^{20}\,\mathrm{cm}^{-3}$, it can be estimated that the limit is around 1 at% in the present system.

However, even before the substitutional solubility limit is reached, the decreasing favorability of the indium substitution reaction allows other defects to form in appreciable quantities. For instance, when the total indium concentration reaches 1.5 at%, the EXAFS results are consistent with about half of the indium being in octahedral interstitial sites. This interstitial defect is quite reasonable given that In^{3+} adopts six-fold oxygen coordination in all of its common oxide forms. Assuming that such defects are electrically inactive (perhaps because they are deep donors), it is now easy to see that the carrier concentration plateaus because of the increasing relative rate of non-substitutional defect formation.

There is an additional fact about In_2O_3 that is relevant to the question of what happens as the indium concentration is further increased. There exists a stable (albeit, high-pressure) phase of In_2O_3 in the corundum structure, which consists of a hexagonal close-packed lattice of oxide with cations in two-thirds of the octahedral holes. Recalling that the oxide ions in ZnO are also hexagonally close-packed, as the octahedral interstices are increasingly filled with indium, a natural structural relaxation would be for the interstitial indiums to associate and locally form an In_2O_3-like structure. Given that the EXAFS data are better represented by the indium local environment in cubic bixbyite, it would seem that the hexagonal corundum phase might represent a low-energy path to the cubic phase, rather than a stable phase in

its own right under these conditions. In any case, the In_2O_3-like environments are certainly apparent by 5 at% In and dominant by 12.5 at% In.

This formation of In_2O_3-like regions at higher doping levels can also help to explain the unexpected rise of carrier mobility seen in Figure 6.5. It is known that In_2O_3, even in a disordered or amorphous form can support high carrier mobilities due to the large spatial extent and low directionality of its In 5s-dominated conduction band.[28] In this sense, even small In_2O_3-like regions within the material could act as islands of higher carrier mobility, whose increasing density would facilitate the transport of carrier electrons initially generated in the lower mobility doped-ZnO portions of the sample.

Figure 6.18 presents the structural trends just described in another way. Shown here are values for the average In-O bond distance and indium coordination number calculated from first shell fits to the EXAFS data shown earlier in Figures 6.13-6.17. There is clearly a lengthening of the average In-O bond as the indium content increases and as more of the indium relaxes into In_2O_3-like environments from more tightly compressed substitutional or interstitial environments. The fact that the value has not reached 2.161 Å (that found from the In_2O_3 powder reference data) is probably a reflection of the fact that true, large area In_2O_3 domains are not present, and that the small In_2O_3-like areas that have formed are still heavily distorted by their surroundings.

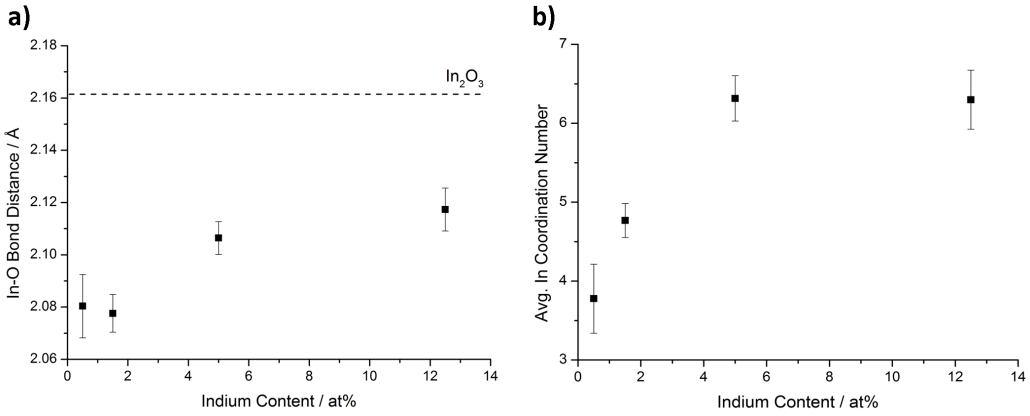

Figure 6.18: a) Average In-O bond distance and b) average In coordination number in IZO films with different indium contents as determined from the fitting of the first nearest-neighbor shells of the EXAFS datasets presented in Figures 6.13-6.17. The In-O distance found for the reference In_2O_3 powder sample is shown as a dotted line in (a).

Likewise, Figure 6.18b shows that the average first shell coordination number for indium increases from about four to about six as the indium content of the IZO samples increases. This too is what would be expected for a transition from indium being primarily at tetrahedral ZnO sites, to indium being in its preferred octahedral coordination. In terms of the trend, the coordination number rapidly deviates from ∼4 in the lightly doped parts of the range, showing again just how quickly the placement of additional indium at tetrahedral substitutional sites becomes disfavored as the indium concentration increases.

Finally, it should be noted that a very interesting contrast can be made between IZO and ITO with respect to doping. It has been observed in general that In_2O_3-based TCOs can support higher carrier concentrations than ZnO-based ones.[29] Analysis of these EXAFS results allows the proposal of a structural basis for this difference. A low-energy corundum pathway to stable In_2O_3-like environments would serve as a means of diverting indium away from electrically active substitution, and thus limiting indium's substitutional solubility in ZnO. However, for ITO, Parent, *et al.* have suggested that stability of the hexagonal phase of In_2O_3 (which has different In-O bond lengths than the cubic phase) provides the In_2O_3 lattice with the structural flexibility necessary to accommodate a comparatively large concentration of tin in substitutional positions.[20]

The solubility of tin in the In_2O_3 lattice is often found to be around 6 at% or greater in ITO powders and single crystals, and may be even higher in some thin film samples.[20,30,31] Likewise corresponding values of carrier concentration in thin films of ITO do not reach a maximum until 5 or 10 at% tin.[12] Indeed, in our own limited work on spray pyrolyzed ITO samples, carrier concentrations in excess of $6 \times 10^{20}\,\mathrm{cm}^{-3}$ and doping efficiencies near or in excess of 100 % are often observed even for ITO samples with nominal doping levels as high as 5 at%, which would be consistent with full involvement of the tin at this doping level *plus* an additional contribution from other donor defects, such as oxygen vacancies.

All of this indicates far higher values of substitutional solubility than what has been observed for indium (and silicon) in ZnO. While loss of visible transparency does place a limit on the maximum usable carrier concentration in a practical TCO, it would seem that this contrasting dopability may be one of the key differences between

ZnO and In_2O_3, and further, that this arises from the fundamental structural natures of the two materials.

6.3 Doping Limits from Solution Chemistry: The Fluoride-enhanced Silicon doping of ZnO

In addition to indium-doped ZnO, silicon-doped ZnO (SiZO) has also been studied as a promising ZnO-based TCO material. From the point of view of cost and resource availability, SiZO is particularly interesting because it is indium-free and composed entirely of elements with high earth abundance and low cost. Silicon has been shown to be an effective *n*-type dopant in samples deposited by a variety of deposition techniques.[32,33] Furthermore, Si^{4+} would be a two-electron dopant when substituted for Zn^{2+}, allowing for the possibility of a higher carrier concentration than indium at a given doping level and efficiency (Figure 6.6).[34]

In previously reported work, our research group has used spray pyrolysis and 4 at% silicon tetraacetate as the silicon source to prepare SiZO samples with an average visible transparency of 89 % and an electrical conductivity of $\sim 210\,(\Omega\,\mathrm{cm})^{-1}$.[35]

More recently, we have observed that the addition of fluoride to the precursor solution substantially increases the maximum electrical conductivity that can be achieved by SiZO made using spray pyrolysis. For instance, when 30 at% of ammonium fluoride is added to precursor solutions containing 4 at% silicon tetraacetate, the average electrical conductivity of the resulting samples is more than tripled to $\sim 670\,(\Omega\,\mathrm{cm})^{-1}$.[36] Remarkably, despite these being *as deposited* conductivity values for an entirely indium-free TCO material, they closely approach the highest ever reliably reported values for doped ZnO thin films prepared by spray pyrolysis ($\sigma \approx 770\,(\Omega\,\mathrm{cm})^{-1}$), which were achieved only by using costly indium as the dopant, and in one case, after vacuum annealing.[37,38]

A more general view of the increase in thin film conductivity that occurs when fluoride is added to precursor solutions while holding the silicon concentration constant can be seen in Figure 6.19a. As can be seen from the very similar shape of the two curves, most of the increase in conductivity is due to the increase in carrier concentration that results from the addition of fluoride (Figure 6.19b). For the precursor solutions containing 3 at% silicon, the rate of conductivity improvement begins

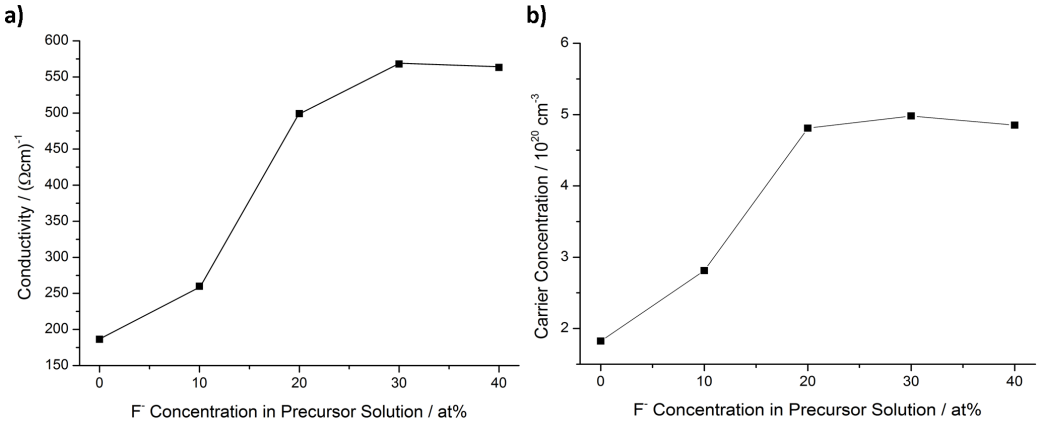

Figure 6.19: a) Conductivity and b) Hall effect carrier concentration of SiZO thin films prepared by spray pyrolysis at a deposition temperature of ∼376 °C using a constant 3 at% silicon and varying concentration of fluoride in the precursor solution.

to decrease around 20 at% fluoride, and the maximum conductivity value is reached at around 30 at% fluoride. The conductivity decreases if the fluoride concentration is further increased beyond the range shown here.

6.3.1 Ruling out Co-Doping

Given that fluoride would be expected to act as a donor if it substitutes for oxide in ZnO, the first and most obvious way to explain these observations would be to suggest that the increased carrier concentration in these films results from Si and F co-doping. This could be verified if the total increase in n from the undoped case is close to the sum of that when each of the two dopants is used individually.

To isolate the effect of fluoride, precursor solutions containing varying amounts of fluoride and no intentionally added silicon were used to prepare ZnO thin films. Surprisingly, so long as these precursor solutions were handled only using plastic and metal implements, the addition of fluoride was found to have no appreciable effect on the electrical properties of the resulting films. The ZnO samples with no added fluoride had an average carrier concentration of about $1.4 \times 10^{19}\,\mathrm{cm}^{-3}$, while corresponding values after the addition of 10 to 40 at% fluoride varied from about $1.2–1.6 \times 10^{19}\,\mathrm{cm}^{-3}$ with no systematic pattern. Recalling the reproducibility study in Section 4.5.1, which showed a standard deviation in n of about 26.5 % of value due to random experimental errors, it is safe to conclude from these values that the addition of fluoride alone has no statistically significant effect on film performance. Note that

these SiZO thin films are prepared using zinc acetylacetonate instead of zinc acetate as the ZnO precursor, explaining the different baseline value of carrier concentration.

Furthermore, even if all of the $\sim 1 \times 10^{19}$ carriers per cm^3 in these samples were attributed to the addition of fluoride (a highly dubious proposition), this contribution would not be nearly enough to explain the more than 3×10^{20} cm^{-3} increase in carrier concentration observed with the addition of fluoride when silicon is present (Figure 6.19b).

The point that fluoride alone is not acting as an effective dopant in this spray pyrolysis process can be further confirmed by chemical analysis of the prepared TCO films. A series of samples prepared from precursor solutions containing 3 at% Si and varying amounts of fluoride were analyzed using XPS. Figure 6.20 shows that even the addition of 50 at% fluoride to the precursor solution leads to no detectable fluorine in either the surface or the interior of the deposited films. To provide a point of reference, even assuming perfect doping efficiency, a 3×10^{20} cm^{-3} increase in carrier concentration would require approximately 0.7 at% fluorine in the sample, which should be significantly above the detection limit of the instrument used.

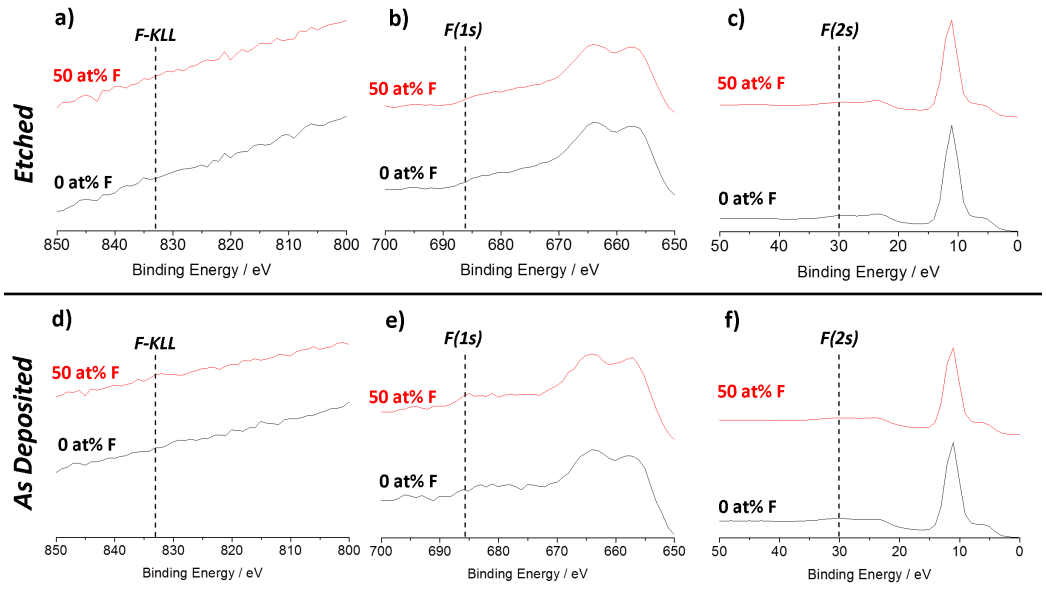

Figure 6.20: XPS spectra of SiZO films prepared by spray pyrolysis with solutions containing 50 at% F$^-$ and 3 at% Si (red lines) and 0 at% F$^-$ and 3 at% Si (black lines) in three energy ranges where a signal would be expected if fluorine were present in the sample: F-KLL Auger (a,d), fluorine 1s (b,e), and fluorine 2s (c,f). Data is shown for both an argon-plasma etched surface (a–c) and an *as deposited* surface (d–f).

Instead of acting as a dopant by itself, fluoride apparently increases the efficiency with which silicon is incorporated into the SiZO films. For a series of samples prepared using precursor solutions with a fixed silicon concentration of 3 at%, it was found that increasing the concentration of fluoride in the solution led to a monotonic increase in silicon incorporation into the films up to at least 50 at% fluoride (Figure 6.21).

This fluoride-induced increase in silicon incorporation is of the correct order of magnitude to explain the observed changes in carrier concentration, and would be by far the most straightforward explanation for the improved electrical performance of these SiZO samples. However, it is worth noting that the increase in carrier concentration is proportionally smaller than the increase in silicon concentration, implying that some part of this newly incorporated silicon is present in an electrically inactive form, harkening back to the discussions of Sections 6.1 and 6.2.

Additionally, the XPS elemental analyses show that the concentration of silicon in the samples is sometimes much lower than the nominal concentration of Si in the precursor solution, implying that a significant fraction of dopant is being lost during the deposition. While the activity of fluoride does significantly increase the efficiency of silicon transfer from precursor solution to film, the highest value of silicon incorporation is still only just over 50 %.

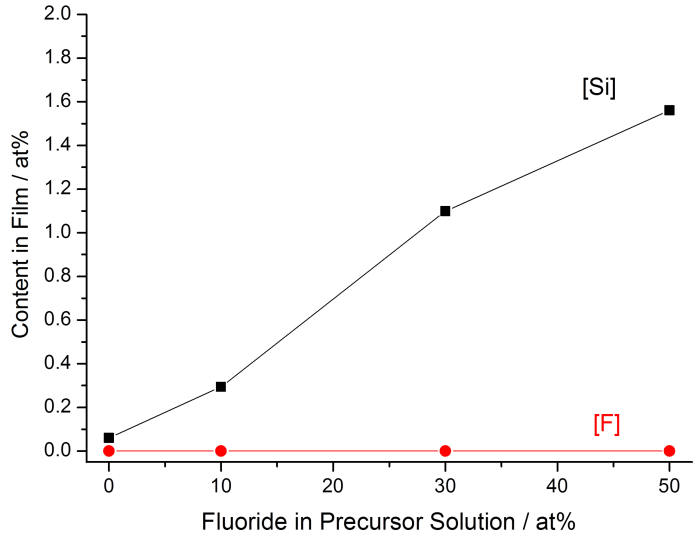

Figure 6.21: Silicon content (black) of SiZO films deposited by spray pyrolysis using precursor solutions containing 3 at% Si and varying amounts of fluoride, as determined by integration of Si 2p and Zn 3p XPS signals collected after the surfaces of the films were etched. Fluorine is below detection limits in all samples (red).

6.3.2 The Solution Chemistry of Silicon and Fluoride

These results do not challenge the fact that fluorine can be an *n*-type dopant in ZnO under the right circumstances. There have been several studies on fluorine-doped ZnO prepared using vacuum-based techniques, where a connection between fluorine incorporation and an improvement in electrical properties has been clearly demonstrated.[39–41]

However, it is now apparent that the situation for spray pyrolysis may not be so straightforward. There are indeed a number of literature reports on an increase in electrical conductivity that supposedly occurs upon fluoride doping of ZnO prepared using spray pyrolysis.[42,43] This would seem to be contrary to the results of Section 6.3.1, which clearly show the addition of only fluoride to a precursor solution has virtually no effect on the resulting ZnO samples, as long as the solutions are carefully prevented from contacting any material made of glass during handling. In fact, only by using conventional glassware have we been able to reproduce the increase in electrical conductivity that is allegedly due to "fluoride doping".

On this basis, it can be suggested that the reported increases in electrical conductivities from "fluoride doping" probably arise from the unintentional extraction of glass components into the precursor solution by the aqueous fluoride ion. Importantly, since silicon is one of the major constituents of glass, previous reports of "fluoride doping" may well actually be a case of accidental silicon doping. One of the published reports indicated that adding hydrofluoric acid to the precursor solution and then using long solution aging times (up to 12 days) in glassware increased the effect of fluoride, which is entirely consistent with our proposed mechanism.[43]

The solution chemistry of silicon and fluoride can also be used to explain the increase in electrical conductivity that occurs when fluoride is added to precursor solutions already containing intentionally added silicon tetraacetate. In aqueous solutions, dissolved silicon is present in the form of silicic acid, $Si(OH)_4$, which can participate in reversible self-condensation reactions to form various oligomers, colloidal silica, or extended-network gels, depending on the conditions. Polymerization is favored when the concentration of silicon is high and at slightly acidic pH, both of which are conditions that hold for these precursor solutions.[44,45]

Previous work in our group has found that, in the absence of fluoride, neither colloidal silica (in commercially-available preparations like Ludox^{TM}) nor macroscopic pieces of glass (*i.e.*, the typically used borosilicate beakers) are effective silicon sources for the preparation of SiZO films by spray pyrolysis. This would suggest that silicon is most easily incorporated into a ZnO film when present in solution as a monomeric or small oligomeric species. Perhaps similar is the case seen in the colorimetric analysis for dissolved silica, in which polymerized forms of silica do not readily react with ammonium heptamolybdate to form the yellow silico-12-molybdate polyoxometalate that is sensed by the measurement.[46]

It is well known that silicates can react with fluoride in acidic aqueous solutions to form the water-soluble and relatively stable hexafluorosilicate ($[SiF_6]^{2-}$) anion via

$$SiO_2 + 6HF \rightarrow [SiF_6]^{2-}_{(aq)} + 2H_3O^+_{(aq)} \,. \tag{6.4}$$

This reaction is the basis for the use of hydrofluoric acid to etch glass, which has been applied in a wide range of artistic, scientific, and industrial endeavors. The formation of $[SiF_6]^{2-}$ would reduce the concentration of silicon oxy and hydroxy species available to participate in polymerization reactions, and thus shift solution equilibria in favor of monomeric, doping-active forms of silicon (of which $[SiF_6]^{2-}$ itself is apparently one).

The first experimental evidence observed for this mechanism was that the precursor solutions for SiZO differ in visual appearance depending on whether any fluoride has been added. Precursor solutions prepared using silicon tetraacetate alone are usually slightly cloudy, which is indicative of silica polymerization and the formation of particles large enough to scatter visible light. Adding fluoride quickly causes these polymerized particles to be redissolved and the solution to become clear and colorless (Figure 6.22).

To further verify this hypothesis, ^{19}F NMR experiments were performed on a series of model solutions designed to approximate those used for spray pyrolysis. These were prepared with different ratios of fluoride to silicon: 1-to-0 (pure fluoride), 12-to-1 (excess fluoride), and 3-to-1 (excess silicon). The model solutions were prepared in plastic laboratory ware and FEP NMR tube liners were used to prevent the solutions from interacting with the glass NMR tubes. Figure 6.23 shows the NMR spectra acquired after allowing these samples to equilibrate.

Figure 6.22: Precursor solutions for the preparation of silicon-doped ZnO. The clear and colorless solution on the left contains both fluoride and silicon, while the cloudy solution on the right contains only silicon and no fluoride.

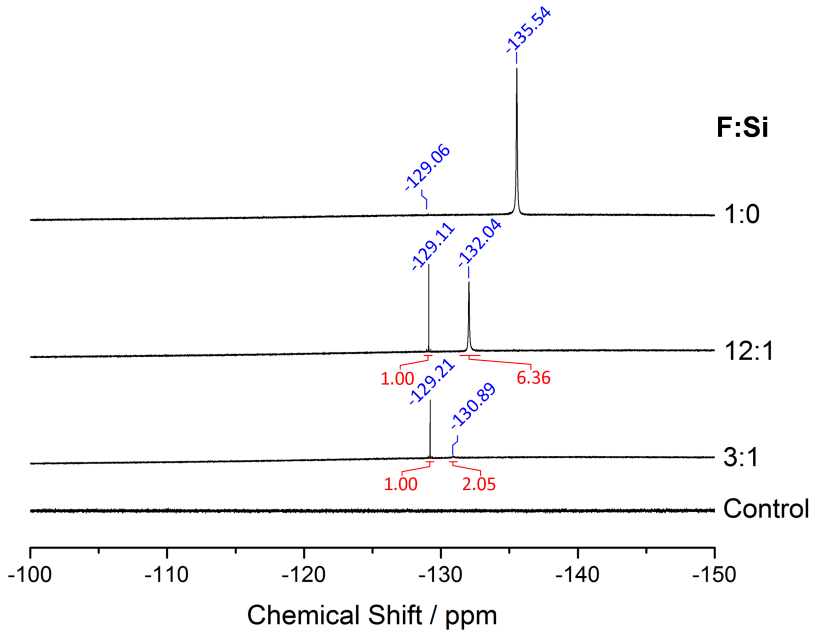

Figure 6.23: ^{19}F NMR of solutions containing the indicated ratio of ammonium fluoride to silicon tetraacetate in 2:1 ethanol:(7 vol% acetic acid in D_2O). The small impurity signal at $\delta = -129.06$ ppm in the pure fluoride spectrum (1:0, top) is due to $[SiF_6]^{2-}$ and may reflect the presence of a small amount of silicon impurity in one of the reagents. A control sample of only solvent is also shown at bottom.

Aqueous fluoride participating in the F^-/HF equilibrium is known to have a pH dependent chemical shift ranging from $\delta = -160$ to -120 ppm. The signals observed at -135.54, -132.04, and -130.89 ppm are consistent with fluoride in solutions with pH varying between 3.2 and 3.5.[47] The sharp signal appearing at $\delta = -129.1 \pm 0.1$ ppm is assigned as that of the $[SiF_6]^{2-}$ anion based on reported values for this species in aqueous solution.[48] This assignment also has been verified by the independent addition of zinc hexafluorosilicate to the solutions, which did not produce any additional peaks.

The $[SiF_6]^{2-}$ signal appears quickly whenever *both* fluoride and silicon are present in the precursor solution. This occurs equally if the silicon is intentionally added, or if the fluoride-containing precursor solutions are handled using glassware or allowed to contact an unlined NMR tube during analysis. This confirms a strong Si-F interaction in the precursor solutions that explains both the earlier reports on "fluoride-doped" ZnO, as well as our observation that fluoride substantially increases the extent of silicon incorporation into the thin films.

It should be noted that even with an excess of silicon, as in the sample with a 3:1 F:Si ratio, free fluoride is not entirely consumed, suggesting that $[SiF_6]^{2-}$ is in an equilibrium with free F^-. This probably explains why addition of excess fluoride beyond a 6-to-1 ratio with silicon is needed to achieve the highest electrical conductivities (Figure 6.19a, for example). Similarly, this would also explain why the silicon incorporation efficiency is still never 100 % (Figure 6.21), as the addition of even large amounts fluoride can only shift these reversible equilibria to a finite extent, and not entirely prevent the loss of silicon into polymerized forms.

6.3.3 Implications for Process Design

From a practical perspective, adding fluoride to SiZO precursor solutions increases the fraction of Si atoms in the precursor that eventually become electrically active to a level approximating that which can be achieved using vacuum-based processes like pulsed-laser deposition (Figure 6.24). These values reflect a combination of both the intrinsic doping efficiency once an impurity atom is actually incorporated into the TCO material, as well as the transfer efficiency of impurity atoms from the precursor into the prepared film. Obviously, fluoride addition cannot by itself improve the

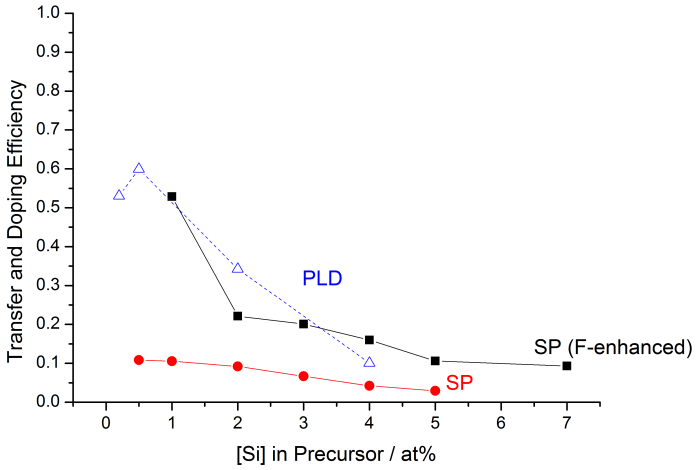

Figure 6.24: Fraction of silicon in precursor that becomes electrically active in SiZO films prepared using standard spray pyrolysis (red), fluoride-enhanced spray pyrolysis (black), and pulsed-laser deposition (blue) as a function of Si concentration in the precursor materials. This value combines both the transport of atoms from precursor to film, as well as the intrinsic doping efficiency of silicon in ZnO.

performance of spray pyrolyzed films to the levels of those prepared using vacuum-based techniques (see Section 7.3.3), however, it does solve one of the key problems inhibiting the preparation of high-quality, silicon-doped films using solution-based techniques.

Furthermore, these insights about the role of silicon and fluoride solution chemistry have the potential to improve significantly the cost and flexibility of the process for producing SiZO by spray pyrolysis. In particular, the generality of the fluoride-silicon interaction to form $[SiF_6]^{2-}$ should greatly expand the range of potential silicon precursors.

For some time, silicon tetraacetate has been the primary silicon source used in the preparation of SiZO films, mostly because many other potential silicon sources did not lead to effective silicon doping.[vi] Unfortunately, silicon tetraacetate is not ideal for large-scale production due to the fact that it is relatively expensive, not readily available in high purity, moisture-sensitive in storage, and very prone to hydrolysis.

Using fluoride to enhance the solubility and doping efficiency of silicon opens up a range of other potential silicon sources, many of which would have otherwise been ineffective given the abovementioned tendency of dissolved silica to polymerize under

[vi] It could be speculated that the acetate ligands have some role in limiting silicon self-polymerization.

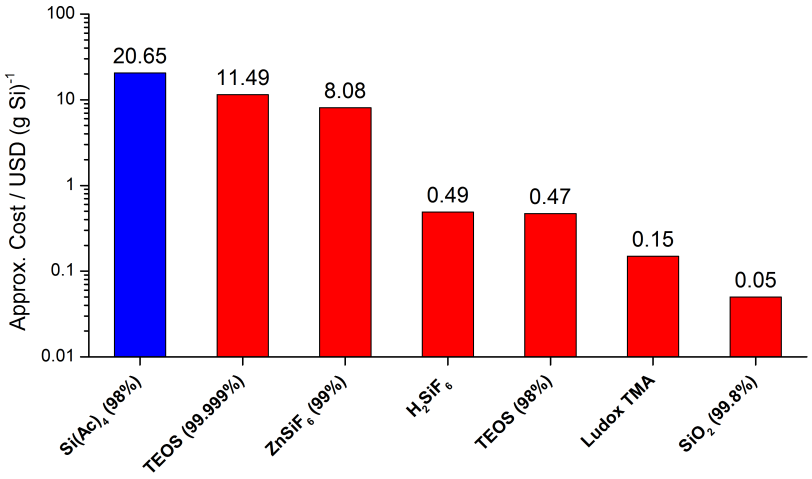

Figure 6.25: Estimated costs for various potential silicon sources in USD per gram of silicon (note the logarithmic scale). TEOS is tetraethylorthosilicate and LUDOX^{TM} TMA is a nominally inorganic cation-free colloidal suspension of silica. The current incumbent precursor, silicon tetraacetate is shown in blue. Where known, the purity of the material is indicated in parenthesis. Costs are estimated based on Sigma-Aldrich pricing in September 2015.

the conditions in the precursor solutions used. Figure 6.25 estimates the monetary cost of some of the silicon precursors that would become viable when used in conjunction with fluoride, and compares those values with the cost of silicon tetraacetate. The values in this figure are based upon retail pricing available through Sigma-Aldrich; much better pricing could almost certainly be obtained for bulk quantities through wholesale suppliers. Nevertheless, this analysis, albeit crude, is enough to illustrate how much dopant cost optimization is now possible given the wider selection of silicon precursors enabled by fluoride.

While this work is still ongoing, it has now been demonstrated that colloidal suspensions of silica (TMA-series Ludox^{TM}) can act as a silicon source in the preparation of SiZO. This has produced samples with electrical conductivities as high as $460\,(\Omega\,\mathrm{cm})^{-1}$. While conductivity matching that of the optimized system based on silicon tetraacetate has not yet been achieved, it is very encouraging that even these preliminary experiments have more or less already proven the concept. Interestingly, it seems possible that the most cost-effective solution-processed SiZO may ultimately be achieved by simply stirring a fluoride-containing precursor solution over pieces of quartz glass, in perhaps something of an amusing throwback to the accidental silicon-

doping already caused by the handling of fluoride-containing precursor solutions in glassware.

It cannot be emphasized enough that when it comes to the preparation of TCO films, the problem of getting a dopant into the film is just as important as what happens once the dopant atom is present there. In the drive to produce the highest performance films, the nature, behavior, and influence of chemical species in precursor solutions has unfortunately often been overlooked. Hopefully, these results on the fluoride-enhanced silicon doping of ZnO will further help to dispel the too-often held assumption that the composition of starting materials will translate simply and directly into the composition of a finished TCO. This work hopefully also serves as a reminder that solution chemistry can indeed be a powerful tool worthy of continued study in efforts to tune the properties of solution-processed TCO materials.

6.4 Conclusion

This chapter has considered the examples of indium-doped and silicon-doped zinc oxide, which together illustrate two broadly different types of limitations on impurity doping in ZnO. Together, these illustrate the general challenges of impurity doping in TCOs, where potential losses at each step mean that the concentration of electrically-active impurities in the finished product is often substantially lower than the originally intended doping level (Figure 6.26).

One class of doping limits arises from the thermodynamics of defect formation in oxides. We have examined a detailed set of electrical and structural data on indium-doped zinc oxides across a wide composition range which shows that the classic one substitution-one electron picture of doping is a drastic oversimplification of the real situation in IZO. As part of this, one of the first ever applications of EXAFS to this material has been used to reveal a much more complete picture of doping in ZnO.

While the substitutional defect is indeed likely to be the active electron donor and the most favored site for indium at low doping levels, its formation is rapidly outstripped first by the formation of electrically inactive indium interstitials, and then by the formation of In_2O_3-like local environments at higher doping levels. The structural flexibility of In_2O_3 and its relationship to the ZnO structure have been

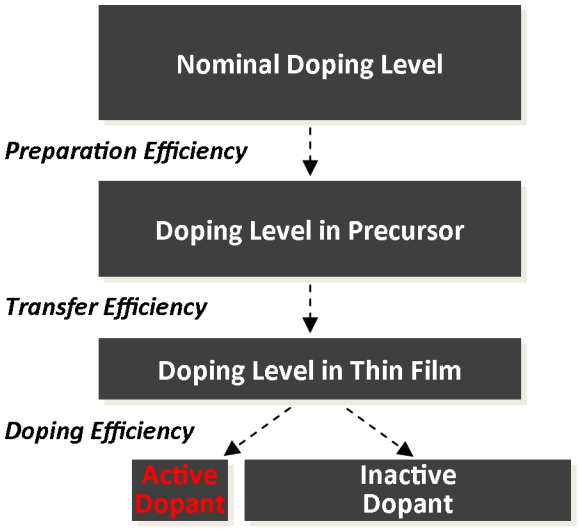

Figure 6.26: Summary of a general doping process in TCOs. Due to imperfect efficiency at each step, the final concentration of electrically active dopant in the thin film is often much less than original nominal doping level.

identified as potentially important factors for explaining the relative ease with which these electrically-inactive defects form. This places a relatively low limit on the substitutional solubility of indium in ZnO of around 1 at% for these samples prepared using spray pyrolysis. The situation is entirely different with ITO, where the structural flexibility of In_2O_3 instead facilitates the high substitutional solubility of tin, and consequently allows much higher doping levels and electrical conductivity to be obtained. This represents a fundamental difference between ZnO and In_2O_3 that must be overcome in the search for high performance ZnO-based TCOs.

Another class of limitations are those that are not fundamental to the material, but instead arise from the choice of deposition process and parameters. The case of the entirely earth-abundant material silicon-doped ZnO spotlights the surprisingly important role that precursor solution chemistry can have in determining the properties of TCO films prepared by spray pyrolysis. An improved mechanistic understanding has led to a fluoride-enhanced deposition process that dramatically improves doping efficiency in this system. Furthermore, this work has potentially important future implications for process optimization, cost-reduction, and scale-up of solution-based preparation of SiZO thin films.

6.5 Experimental

6.5.1 Preparation of Indium-doped ZnO (IZO)

The base solution for the preparation of undoped ZnO films using zinc acetate precursor is as described in Chapter 4. For indium doping, a ratio of indium acetate (Alfa-Aesar, 99.99 %) to zinc acetate is calculated based on the anhydrous molecular weight of each precursor. The nominal concentration of indium plus zinc in the aqueous portion of the precursor solution remains 0.225 M, which gives a nominal metal concentration of 0.075 M in the final precursor solution after addition of alcohol. The indium acetate does not dissolve completely, probably due to hydrolysis to insoluble hydroxides, and suspended particles are often visible even after extended stirring. For this reason, the aqueous solution is gravity-filtered before being combined with alcohol and used for a deposition run. As noted in the main text, the indium doping level of a prepared film is approximately half the nominal indium doping level of the precursor solution.

The deposition process itself proceeds as previously described, using a deposition temperature of 376 °C and a nitrogen carrier gas. The only exception is that the amount of solution sprayed must be adjusted to maintain samples of approximately the same thickness (∼400 nm) across the composition series. Larger amounts of solution are required to achieve the same sample thickness at higher indium concentrations.

6.5.2 EDX Analysis of IZO Films

The basic instrumentation and software for EDX analysis is described in Chapter 3. A primary beam acceleration voltage of 10 kV was used to minimize the amount of signal from the substrate while achieving sufficient signal intensity to allow reliable quantification of small amounts of indium in a reasonable time. A large analysis area of at least 50 μm × 100 μm was used for each acquisition to obtain an average concentration over the film independent of any possibility of localized inhomogeneity. Several different spots were measured for some of the samples and no significant large-scale gradients in composition were observed. Signal deconvolution and quantification was carried out semi-automatically using the AZtec software.

A portion of the measured signal is from the substrate, as evidenced by the presence of a silicon peak, which should not be seen in an analysis of the IZO films alone. Based on EDX measurements of the bare glass substrates used, it is known that they contain a small amount of zinc, which in principle would affect the measured In-to-Zn ratio in the films. The fraction of the zinc signal that is due to the substrate can be estimated using the known Si-to-Zn atom ratio in the glass (13.88 to 1.88) and the magnitude of the Si signal, which is entirely due to the substrate. This (small) excess in Zn magnitude is subtracted from the total signal prior to calculation of the film indium content.

6.5.3 EXAFS Data Collection and Modeling

Zinc and indium K-edge X-ray absorption spectra were measured on Beamline B18 at the Diamond Light Source (Harwell, Didcot, UK).[49,50] The beamline is equipped with a water-cooled vertically collimating Si mirror, a double crystal monochromator with Si(111) and Si(311) crystals, and several additional mirrors for beam focusing and harmonic rejection at low energies.

Thin film IZO samples on D263T glass substrates were measured in fluorescence mode using a multiple-element, solid-state Ge detector. The thin film samples were positioned to allow for grazing beam entry. Reference powder samples containing a calculated optimum amount of absorber were mixed with cellulose, uniaxially pressed into pellets, and then measured in transmission mode using ion chambers to determine incident and transmitted beam intensity. The beamline is also equipped with a range of reference metal foils, maintained in vacuum, for the purpose of energy calibration. Data collection for each sample was generally carried out as multiple shorter scans that were first aligned using the reference foils for energy calibration and then averaged to produce the final data set.

Data reduction and modeling were carried out using the Athena and Artemis components of the IFEFFIT software suite.[51] Theoretical standards were developed from literature crystallographic data and calculated using FEFF6.[52] Although data are only plotted here with a k^2 weighting, the fits were carried out simultaneously against k, k^2, and k^3 weightings in r space. The amplitude reduction factor S_0^2 was a fit parameter and constrained to be the same for all paths of an absorber in a given

environment. ΔE was a fit parameter and constrained to be the same for all paths in a given dataset. Full details of each reported fit are provided via fitting logs in Appendix G.

The R-factor for quantifying fit mismatch is calculated using

$$R = \frac{\sum_{i=1}^{N}(\text{data}_i - \text{fit}_i)^2}{\sum_{i=1}^{N}(\text{data}_i)^2}\,, \tag{6.5}$$

where the summation is over all N points of fitted data. A lower value of R represents a better fit.

χ^2_{red} is another parameter for measuring goodness-of-fit that includes both fit mismatch and the number of independent parameters in the model needed to achieve that fit. The definition of χ^2_{red} used by the software is

$$\chi^2_{\text{red}} = \frac{N_{\text{idp}}}{N(N_{\text{idp}} - N_{\text{vars}})\epsilon^2}\sum_{i=1}^{N}[Re(\text{data}_i - \text{fit}_i)^2 + Im(\text{data}_i - \text{fit}_i)^2]\,, \tag{6.6}$$

where N_{idp} is the information content of the fitted data set (Equation 3.24), N is the number of data points used, N_{vars} is the number of independent variables in the model, ϵ is the measurement uncertainty, and the sum is over all data points used for the fit. A more general definition uses different values of ϵ for each data point. However, the determination of ϵ is somewhat problematic in general and the software uses a single value for all of the data points in a given set.

Although the bixbyite structure is cubic and isotropic expansion/contraction of the unit cell is sometimes assumed to reduce the number of independent model parameters in cubic systems, we have chosen to not use this constraint because the In_2O_3-like local environments in this sample have surroundings that may impose anisotropic boundary conditions.

6.5.4 Silicon-doped ZnO (SiZO)

Deposition by Spray Pyrolysis

The basic procedure for the spray pyrolysis deposition of oxide thin films is as described in Chapter 4. A desired quantity of ammonium fluoride (Sigma-Aldrich, 99.99+ % metals basis) was added to a prepared base precursor solution of zinc acetylacetonate hydrate (Aldrich, 99.995 % trace metals basis) and (optionally) silicon tetraacetate (Aldrich, 98 %). All additive/dopant amounts are reported as at%

of the total metal and metalloid concentration (including Zn and Si), which in the finished solution is kept constant at 0.15 M for the samples reported here. Films were deposited at a substrate surface temperature of 376 °C using nitrogen as the carrier gas.

The results for solutions prepared in glass and those prepared entirely in plastic have been compared and no statistically significant difference in the properties of the films was found in the cases where silicon is added intentionally as silicon tetraacetate. Thus, the reported properties for films deposited from solutions containing intentionally added silicon are an average including samples deposited from solutions prepared in both plastic and glass laboratory ware. In contrast, results for films deposited from precursor solutions containing fluoride without added silicon are of those prepared using plastic labware only.

Additionally, some samples were also deposited with the same procedure, but instead using either zinc hexafluorosilicate hydrate (Sigma Aldrich, 99 %) or Ludox^{TM} TMA colloidal silica (34 wt% suspension in water) as the silicon source.

XPS Analysis

X-ray photoelectron spectroscopy (XPS) data were collected on a Thermo Scientific K-Alpha XPS with an Al-K_α X-ray source (1486.7 eV). All spectra were acquired with a 0.4 mm diameter X-ray spot size and with charge compensation. The polished (111) surface of a phosphorus-doped silicon wafer (Pi-KEM, Ltd.) was used as a reference sample. Spectra were recorded from as received samples, as well as after ∼600 seconds of etching using 4 keV argon ions from a MAGCIS ion source.

The silicon content of these samples was determined by examining the average of 10 high resolution scans over a binding energy range of 110 to 75 eV, which includes the Si(2p) and Zn(3p) signals. The Si(2p) signal is centered at ∼102.9 eV, while the Zn(3p) signal consists of 2 broad peaks centered at ∼92.3 and ∼89.5 eV, corresponding to the spin-orbit split $3p_{3/2}$ and $3p_{1/2}$ resonances, respectively. Using the CasaXPS software package, the peak areas were integrated using a linear baseline and normalized by the relative scattering factors tabulated in the built-in Scofield Element Library (0.817 for Si(2p) and 2.83 for Zn(3p)) to calculate the doping level. The doping efficiencies presented in Figure 6.6 are calculated using the silicon contents

experimentally measured from the interior of the SiZO films prepared from precursor solutions containing 30 at% fluoride.

To determine whether fluorine has been substantially incorporated into the films prepared using these deposition conditions, the XPS spectra of samples prepared with 0 % and 50 % F^- (with constant 3 at% Si) in the precursor solutions were compared near binding energies of 29.2 eV, 685.7 eV, and 833.0 eV, which are the expected locations of the F(2s), F(1s), and F-KLL Auger signals, respectively.[53]

6.5.5 NMR Analysis of Model Precursor Solutions

Proton-decoupled ^{19}F NMR (376.50 MHz) spectra were recorded on a Bruker AVIII400 Nanobay spectrometer at room temperature. Samples containing 3:1, 12:1, and 1:0 molar ratios of ammonium fluoride and silicon tetraacetate were dissolved in a mixture of acetic acid (Fisher Scientific, Analytical Reagent Grade), deuterium oxide (Apollo Scientific Limited, 99.92 at%D), and ethanol (Sigma-Aldrich, absolute, ≥99.8 %) in a 7:93:200 volume ratio designed to simulate the spray pyrolysis solvent, except with water replaced by deuterium oxide to assist in locking of the spectrometer and to provide an internal frequency reference. Chemical shifts are measured based on the deuterium lock frequency, and are reported relative to $CFCl_3$. Unless otherwise noted, solutions were handled in plastic labware and FEP NMR tube liners (Wilmad) were used to prevent interaction of the solutions with the glass NMR tubes.

Monitoring over time revealed that the mixtures had largely reached equilibrium within 30–40 minutes after preparation, with only very minor changes thereafter.

6.5.6 Acknowledgments

Some of the EXAFS data acquisitions on the 1.5 and 5 at% IZO samples were run by Dr. Andy Dent (Beamline B18 Principal Scientist, Diamond Light Source) as part of a remote, rapid-access session.

Dr. Josh Makepeace assisted with the extraction of lattice parameters from the IZO XRD data using Topas.

The work on fluoride-enhanced silicon doping was performed in collaboration with other members of my research group. Some of the SiZO samples reported on were prepared and characterized by Dr. Nazanin Rashidi.

References

[1] Harding, G. L.; Window, B.; Horrigan, E. C. *Sol. Energy Mater.* **1991**, *22*, 69–91.

[2] Nishino, J.; Kawarada, T.; Ohshio, S.; Saitoh, H.; Maruyama, K.; Kamata, K. *J. Mater. Sci. Lett.* **1997**, *16*, 629–631.

[3] Machado, G.; Guerra, D. N.; Leinen, D.; Ramos-Barrado, J. R.; Marotti, R. E.; Dalchiele, E. A. *Thin Solid Films* **2005**, *490*, 124–131.

[4] Major, S.; Banerjee, A.; Chopra, K. L. *Thin Solid Films* **1983**, *108*, 333–340.

[5] Kumar, B.; Gong, H.; Akkipeddi, R. *J. Appl. Phys.* **2005**, *98*, 073703.

[6] Naghavi, N.; Dupont, L.; Marcel, C.; Maugy, C.; Laïk, B.; Rougier, A.; Guéry, C.; Tarascon, J. M. *Electrochim. Acta* **2001**, *46*, 2007–2013.

[7] Moriga, T.; Edwards, D. D.; Mason, T. O.; Palmer, G. B.; Poeppelmeier, K. R.; Schindler, J. L.; Kannewurf, C. R.; Nakabayashi, I. *J. Am. Ceram. Soc.* **1998**, *81*, 1310–1316.

[8] Patterson, A. L. *Phys. Rev.* **1939**, *56*, 978–982.

[9] Langford, J. I.; Wilson, A. J. C. *J. Appl. Crystallogr.* **1978**, *11*, 102–113.

[10] Jagadish, C.; Coleman, V. A. *Basic Properties and Applications of ZnO*; Jagadish, C.; Pearton, S., Eds.; Zinc Oxide Bulk, Thin Films and Nanostructures; Elsevier, Ltd.: Kidlington, UK, 2006; pp 1–20.

[11] Shannon, R. D. *Acta Crystallogr., Sect. A: Cryst. Phys., Diffr., Theor. Gen. Crystallogr.* **1976**, *32*, 751–767.

[12] Frank, G.; Köstlin, H. *Appl. Phys. A: Solids Surf.* **1982**, *27*, 197–206.

[13] Kim, K. H.; Park, K. C.; Ma, D. Y. *J. Appl. Phys.* **1997**, *81*, 7764–7772.

[14] Rakhshani, A. E.; Makdisi, Y.; Ramazaniyan, H. A. *J. Appl. Phys.* **1998**, *83*, 1049–1057.

[15] Ali, E. B.; Sorensen, G.; Ouerfelli, J.; Bernéde, J. C.; Maliki, H. E. *Appl. Surf. Sci.* **1999**, *152*, 1–9.

[16] Hong, S.-J.; Heo, G.-S.; Park, J.-W.; Lee, I.-H.; Choi, B.-H.; Lee, J.-H.; Park, S.-Y.; Shin, D.-C. *J. Nanosci. Nanotechnol.* **2007**, *7*, 4077–4080.

[17] Ryoken, H.; Sakaguchi, I.; Ohashi, N.; Sekiguchi, T.; Hishita, S.; Haneda, H. *J. Mater. Res.* **2005**, *20*, 2866–2872.

[18] Robertson, J.; Clark, S. J. *Phys. Rev. B* **2011**, *83*, 075205.

[19] Nadaud, N.; Lequeux, N.; Nano, M. *J. Solid State Chem.* **1998**, *135*, 140–148.

[20] Parent, P.; Dexpert, H.; Tourillon, G.; Grimal, J. M. *J. Electrochem. Soc.* **1992**,

139, 282–285.

[21] González, G. B. *Materials* **2012**, *5*, 818–850.

[22] Brehm, J. U.; Winterer, M.; Hahn, H. *J. Appl. Phys.* **2006**, *100*, 064311.

[23] Sawada, H.; Wang, R.; Sleight, A. W. *J. Solid State Chem.* **1996**, *122*, 148–150.

[24] Bazzani, M.; Neroni, A.; Calzolari, A.; Catellani, A. *Appl. Phys. Lett.* **2011**, *98*, 121907.

[25] Marezio, M. *Acta Crystallogr.* **1966**, *20*, 723–728.

[26] Socol, G.; Craciun, D.; Mihailescu, I. N.; Stefan, N.; Besleaga, C.; Ion, L.; Antohe, S.; Kim, K. W.; Norton, D.; Pearton, S. J.; Galca, A. C.; Craciun, V. *Thin Solid Films* **2011**, *520*, 1274–1277.

[27] Kuznetsov, V. L.; O'Neil, D. H.; Pepper, M.; Edwards, P. P. *Appl. Phys. Lett.* **2010**, *97*, 262117.

[28] Hosono, H. *Thin Solid Films* **2007**, *515*, 6000–6014.

[29] Bellingham, J. R.; Phillips, W. A.; Adkins, C. J. *J. Mater. Sci. Lett.* **1992**, *11*, 263–265.

[30] Frank, G.; Köstlin, H.; Rabenau, A. *Phys. Status Solidi A* **1979**, *52*, 231–238.

[31] Kanai, Y. *Jpn. J. Appl. Phys.* **1984**, *23*, L12–L14.

[32] Minami, T.; Sato, H.; Nanto, H.; Takata, S. *Jpn. J. Appl. Phys.* **1986**, *25*, L776–L779.

[33] Clatot, J.; Campet, G.; Zeinert, A.; Labrugére, C.; Nistor, M.; Rougier, A. *Sol. Energy Mater. Sol. Cells* **2011**, *95*, 2357–2362.

[34] Körner, W.; Elsässer, C. *Phys. Rev. B* **2011**, *83*, 205306.

[35] Rashidi, N.; Kuznetsov, V. L.; Dilworth, J. R.; Pepper, M.; Dobson, P. J.; Edwards, P. P. *J. Mater. Chem. C* **2013**, *1*, 6960–6969.

[36] Rashidi, N.; Vai, A. T.; Kuznetsov, V. L.; Dilworth, J. R.; Edwards, P. P. *Chem. Commun.* **2015**, *51*, 9280–9283.

[37] Major, S.; Banerjee, A.; Chopra, K. L. *J. Mater. Res.* **1986**, *1*, 300–310.

[38] Biswal, R.; Castañeda, L.; Moctezuma, R.; Vega-Pérez, J.; de la Luz Olvera, M.; Maldonado, A. *Materials* **2012**, *5*, 432–442.

[39] Noirfalise, X.; Godfroid, T.; Guisbiers, G.; Snyders, R. *Acta Mater.* **2011**, *59*, 7521–7529.

[40] Thimont, Y.; Clatot, J.; Nistor, M.; Labrugére, C.; Rougier, A. *Sol. Energy Mater. Sol. Cells* **2012**, *107*, 136–141.

[41] Yoon, H. S.; Lee, K. S.; Lee, T. S.; Cheong, B.; Choi, D. K.; Kim, D. H.; Kim, W. M. *Sol. Energy Mater. Sol. Cells* **2008**, *92*, 1366–1372.

[42] de la L. Olvera, M.; Maldonado, A.; Asomoza, R.; Solorza, O.; Acosta, D. R. *Thin Solid Films* **2001**, *394*, 241–248.

[43] Biswal, R. R.; Velumani, S.; Babu, B. J.; Maldonado, A.; Tirado-Guerra, S.; Castañeda, L.; de la L. Olvera, M. *Mater. Sci. Eng. B-Adv.* **2010**, *174*, 46–49.

[44] Weres, O.; Yee, A.; Tsao, L. *J. Colloid Interface Sci.* **1981**, *84*, 379–402.

[45] Chan, S. H. *Geothermics* **1989**, *18*, 49–56.

[46] Coradin, T.; Eglin, D.; Livage, J. *Spectroscopy* **2004**, *18*, 567–576.

[47] Gerken, J. B. *J. Fluorine Chem.* **2011**, *132*, 68–70.

[48] Finney, W. F.; Wilson, E.; Callender, A.; Morris, M. D.; Beck, L. W. *Environ. Sci. Technol.* **2006**, *40*, 2572–2577.

[49] Dent, A. J.; Cibin, G.; Ramos, S.; Smith, A. D.; Scott, S. M.; Varandas, L.; Pearson, M. R.; Krumpa, N. A.; Jones, C. P.; Robbins, P. E. *J. Phys.: Conf. Ser.* **2009**, *190*, 012039.

[50] Dent, A. J.; Cibin, G.; Ramos, S.; Parry, S. A.; Gianolio, D.; Smith, A. D.; Scott, S. M.; Varandas, L.; Patel, S.; Pearson, M. R.; Hudson, L.; Krumpa, N. A.; Marsch, A. S.; Robbins, P. E. *J. Phys.: Conf. Ser.* **2013**, *430*, 012023.

[51] Newville, M. *J. Synchrotron Radiat.* **2001**, *8*, 322–324.

[52] Rehr, J. J.; de Leon, J. M.; Zabinsky, S. I.; Albers, R. C. *J. Am. Chem. Soc.* **1991**, *113*, 5135–5140.

[53] Crist, B. V. *Handbook of monochromatic XPS spectra: The elements and native Oxides*; XPS International, Inc., 1999; Vol. 1.

Chapter 7

Grain Boundary Effects in Transparent Conducting Oxides

The performance limits that arise in a polycrystalline thin film due to grain boundaries could be seen as somehow less intrinsically important than those imposed by the physics of single-crystal electronic transport or the effects of impurity doping. Perhaps, this is because grain boundary effects are not just related to the chemical identity of the TCO, but are also profoundly affected by film morphology and microstructure, as well as the interactions of the material with its environment. Even so, this cannot be an excuse for overlooking the critical role that grain boundaries play. Indeed, this chapter will show that grain boundaries can sometimes have such a dominating effect on conduction in polycrystalline TCO films that they can obscure many of the within-grain processes discussed in the previous two chapters.

It could be argued that an obvious solution to any grain boundary problem would be to prepare epitaxial films without any grain boundaries, which thus have the potential to possess electrical properties comparable to those in single crystals.[1–4] However, this "solution" overlooks the practical reality that easily up-scaled deposition techniques, like spray pyrolysis or magnetron sputtering, almost inevitably produce TCO thin films that are polycrystalline. Since large-area films are ultimately required for most end uses of TCOs, until such time as cost-effective, large-scale preparation of epitaxial films can be demonstrated, the understanding of how grain boundaries affect electronic conduction in these materials will remain absolutely essential to the progress of the field.

In this chapter, a comparative study of polycrystalline ZnO and In_2O_3 thin films

prepared by spray pyrolysis will confirm that their performance mostly differs due to grain boundary processes. These grain boundary differences will be traced to a variety of factors, some fundamental to the chemistry of the two materials, and others which can be substantially influenced by changes in the film deposition process. Taking advantage of these insights, a variety of approaches for mitigating the deleterious effects of grain boundaries will be introduced and discussed, with the goal of suggesting how it might be possible, at least in principle, to produce ZnO-based films on a large scale with properties approaching those currently demonstrated by ITO.

7.1 Basic Concepts

7.1.1 Polycrystallinity

The fact that a given thin film sample is polycrystalline can usually be very easily seen from either X-ray diffraction (XRD) or scanning electron microscopy (SEM) data. An example of such data for an In_2O_3 thin film prepared by spray pyrolysis is presented in Figure 7.1.

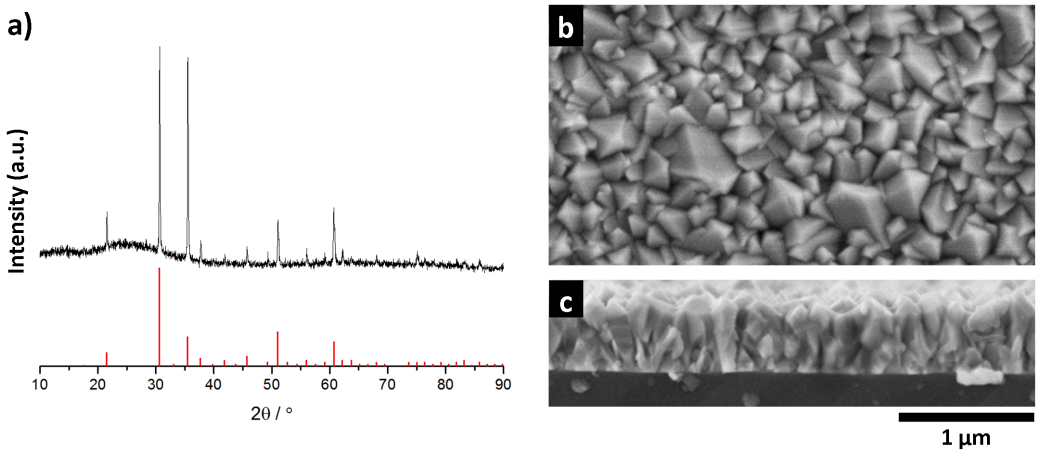

Figure 7.1: Representative evidence for the polycrystallinity of an In_2O_3 thin film prepared by spray pyrolysis: a) Experimental X-ray diffraction data (black) and a reference stick chart for randomly oriented In_2O_3 (red), b) secondary electron SEM of film surface, and c) SEM of a cleaved film cross-section. The scale bar applies to both b and c.

In these XRD data, the appearance of reflections corresponding to many different planes clearly shows that many crystallites with different orientations are present in the sample. In a case of very strong preferred orientation, where signals corresponding

to only one diffraction plane are visible, it may not be so obvious from XRD alone that the sample is polycrystalline. In such cases, it is sensible to also examine the electron micrographs of either the film surface or cross-section, from which the granular nature of the sample is usually quite obvious. In general, a combination of these two types of data is more than enough to demonstrate convincingly that a given sample is not an exception to the nearly universal rule that spray pyrolysis and sputtering produce polycrystalline TCO samples.[i]

Polycrystalline samples can be thought of as consisting of many domains of finite extent, individually possessing a relatively high degree of internal structural order. Whenever domains meet, there will necessarily be a transitional boundary layer between the differently ordered regions. Similarly, layers with structure and properties distinct from the ordered crystalline material will also arise at oxide–air, or oxide–substrate interfaces. High-resolution TEM can be used to observe the differently-ordered and less-ordered regions of a sample directly (Figure 7.2).

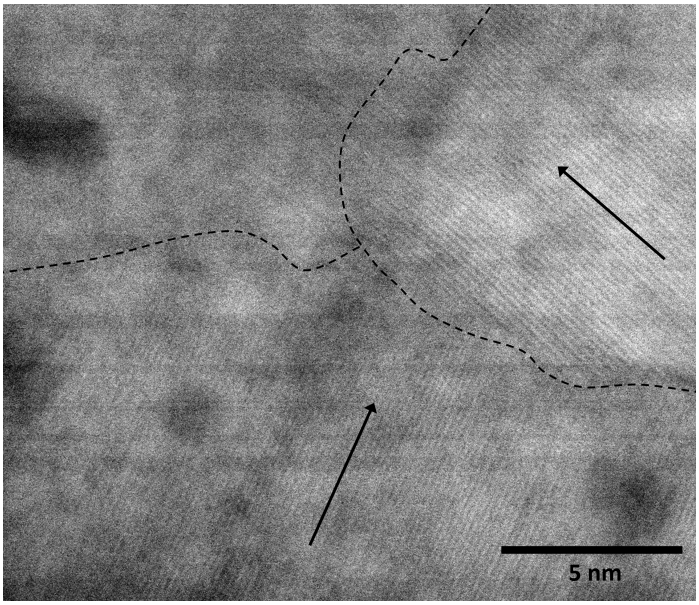

Figure 7.2: Cross-sectional high resolution scanning TEM image of a silicon-doped ZnO sample prepared by spray pyrolysis. Approximate boundaries between differently-oriented domains are indicated with dashed lines. The top left region of the image is apparently less ordered or amorphous since individual lattice planes are not as clearly defined as they are in the other two regions.

[i]One exception worth mentioning regards the preparation of amorphous samples which can sometimes be achieved by sputtering on substrates near or below room temperature.[5] The subject of conduction in amorphous TCOs was briefly discussed in Chapter 5.

Since there seem to be some differences in usage amongst various workers in this area, a brief clarification of terminology is appropriate. The SEM images in Figure 7.1b and c show faceted particles with length scales on the order of tens to hundreds of nanometers. For this thesis, such larger scale particles will be termed *grains*, and the interfaces between them, as well as their surfaces, will be called *grain boundaries*. However, it is not necessarily the case that each grain consists of a single, ordered crystalline domain. In some samples, it is possible that grains may in turn be composed of multiple smaller regions of crystalline order that are themselves separated by boundaries or dislocations. Where necessary, these will be referred to as *domains* and *domain boundaries* to draw a clear distinction between them and their larger scale counterparts.

As will shortly be discussed at length, the exchange of chemical species between the film surface and the atmosphere is of great importance to the electronic properties of some TCO thin films. On this basis, it probably fair to infer that the relatively exposed and open grain boundaries are active in such behavior. Unfortunately, there is little hard evidence at present to judge how much of a role is played by the domain boundaries within grains. Thus, the generic term "grain boundary effects" will be used simply for convenience without any attempt to imply anything either way regarding the possible contribution of domain boundaries to them.

7.1.2 Defects at Grain Boundaries

Due to their transitional nature, grain boundaries will usually contain a high concentration of dangling or distorted bonds, vacancies, or other defects relative to the host structure. These disordered boundaries and surfaces also provide ample sites for the chemisorption of outside species upon interaction of the sample with the atmosphere. As with defects in the bulk, grain boundary defects capable of donating electrons to the system are referred to as donors and result in the creation of filled electronic states. Conversely, defects whose formation requires the localization of electrons are acceptors and lead to the creation of unfilled states in the band structure.

In general, how a grain boundary affects electronic transport is dictated by the relative concentration of donor and acceptor defects. Thus, there can be a continuous range of behaviors from donor-dominated to acceptor-dominated, and the position

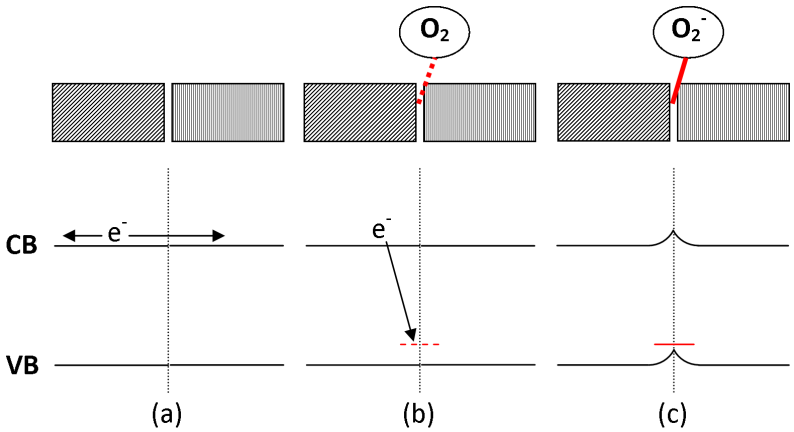

Figure 7.3: Schematic illustrating the localization of electrons due to chemisorption at TCO grain boundaries. a) In a "clean" oxide grain boundary the conduction band and the valence band of the bulk are relatively undisturbed. b) Physisorption of a species from the atmosphere leads to the creation of a low-lying, unfilled electronic state into which a conduction electron can relax and become localized. c) The filling of the defect state is equivalent to chemisorption of the adsorbate onto the oxide surface. This localization of negative charge also leads to the formation of a potential barrier centered at the grain boundary.

of a sample along this spectrum can be influenced by changing the concentration of either defect type.

In the case of undoped, as-deposited ZnO and In_2O_3, grain boundaries tend to be dominated by defects capable of creating acceptor states and trapping free electrons.[6,7] A class of such acceptor defects particularly relevant to the present discussion is chemisorbed, oxygen-containing species. Should the physisorption of an atmospheric species (such as O_2) to the oxide surface lead to the creation of an unfilled, low-lying electronic state, it will act as a trap into which free conduction electrons can relax to lower the energy of the system (Figure 7.3b). This net localization of an otherwise free electron leads to a dipolar interaction that in the limiting case is chemically equivalent to the formation of a chemisorption bond between the oxide surface and the adsorbed species (Figure 7.3c).

Another common example of grain boundary acceptors can be found in ZnO-based varistors with non-linear I-V characteristics.[8] In such devices, these defects result from a choice of preparation conditions that allow carefully chosen impurities to preferentially segregate to grain boundaries. The presence of these impurities leads to the creation of acceptor states at grain boundaries, which then leads to the trapping

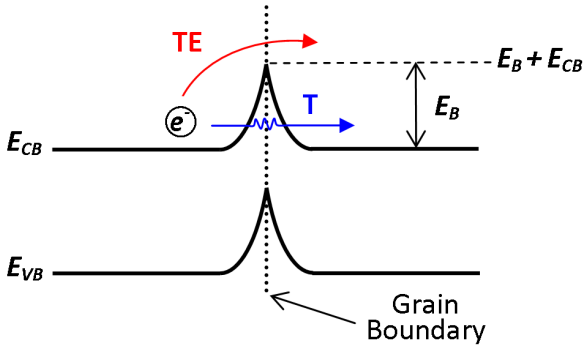

Figure 7.4: A carrier electron that is free within a grain can traverse a grain boundary energy barrier of height E_b by either quantum-mechanical tunneling (T, blue) or thermionic emission (TE, red).

of charge carriers in a similar fashion as chemisorbed species.

The fact that such acceptor defects provide a site for the localization of conduction electrons leads to a buildup of negative charge at the grain boundaries, and a corresponding depletion of negative charge from nearby regions of the ordered grain. Such an electrostatic charge distribution leads to a distortion of the electronic band structure of the host oxide near the grain boundary (often referred to as *band bending*), and the creation of a potential barrier that can inhibit charge transport.

Carriers can only move from one grain to another by having or gaining enough energy to cross over the barrier by thermionic emission, or by quantum-mechanical tunneling through the barrier (Figure 7.4). This can lead to situations where carrier electrons have high enough energy to occupy delocalized conduction band states and be free *within* a grain, but not enough energy to traverse the potential barrier and participate in electronic conduction across macroscopic distances.

While acceptor-dominated grain boundaries are the most common in *n*-type TCOs, it is reportedly possible to prepare samples which have, at least transiently, an excess of *donor* defects at surfaces, either through partial reduction of the oxide surface or the electron donation that occurs upon the binding of atomic hydrogen.[9–11] In such a scenario, the grain boundary defects will lead to a net increase in the number of free electrons in the system and no potential barriers will occur.[12] In our experience, a relatively donor-rich ZnO surface can be produced by annealing thin film samples at modest temperatures (∼350 °C) under a 5 % hydrogen atmosphere. However, these donor states do not appear stable under air, and we have observed that the increases

in conductivity achieved by this method decay over time.

7.1.3 Models for Electronic Transport in Polycrystalline Materials

Grain boundary barriers in polycrystalline materials are typically modeled in one-dimension, with all changes occurring along a direction locally normal to the boundary. Within this framework, grain boundary potential barriers are then typically treated as two symmetric Schottky barriers arranged back-to-back.[13]

Electrons are fermions, and as such, their population distribution as a function of energy and temperature will be described by Fermi-Dirac statistics. Tarng, and then Prins, *et al.* have both analyzed this scenario for a polycrystalline material assuming that quantum-mechanical tunneling has a negligible contribution to conduction.[14,15] In our TCO materials, we find this to be true except at low measurement temperatures ($\lesssim$115 K), and thus that the predominance of thermionic transport is a justifiable assumption for most of the data we consider in this chapter.

Following the form of the result given by Prins, *et al.*, the temperature-dependent, grain boundary-limited mobility is given by

$$\mu_{gb}(T) = \frac{4\pi e m^* \alpha_{\text{eff}} L}{h^3 n_{\text{gb}}} \frac{\ell}{\ell + \frac{3}{4}w} k_{\text{B}} T \ln[1 + \exp(-\frac{\Phi}{k_{\text{B}}T})] \,, \tag{7.1}$$

where n_{gb} is the carrier concentration near the grain barrier, α_{eff} is a correction factor that accounts for spatially non-uniform current distribution due to variations in barrier heights, L is the average grain size, ℓ is the mean free path of carriers, w is the width of the potential barrier, and $\Phi = (E_{\text{B}} + E_{\text{CB}}) - E_{\text{F}}$ is the difference between the Fermi level E_{F} and the top of an average barrier (Figure 7.5).[15]

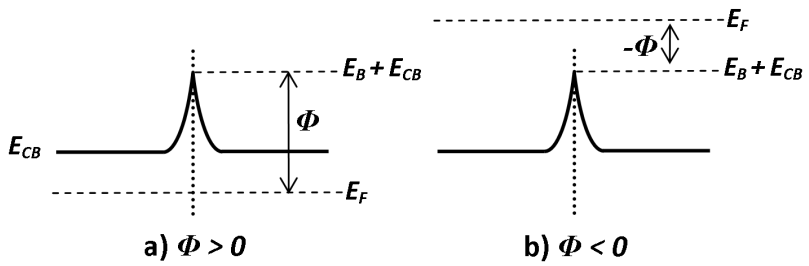

Figure 7.5: Schematic illustrating band structures for different signs of Φ, a) $\Phi > 0$ and b) $\Phi < 0$.

One of the potentially counterintuitive implications of Equation 7.1 is that carrier mobility can still be thermally activated even if Φ is negative. This can be understood by first noting that all free carriers within a grain will contribute to the DC Hall voltage and hence the measured carrier concentration n, even if they do not have enough energy to traverse over a grain boundary. In contrast, a measurement of the direct current conductivity σ will only sense carriers with enough energy to participate in intergrain conduction.[16] Since the measured n is higher than the actual density of carriers contributing to σ, in order for the free-electron description $\sigma = ne\mu$ to still hold, the measured Hall carrier mobility μ must be lower than the *intra*grain mobility by some factor related to the fraction of total free carriers trapped within grains by potential barriers.

Where Φ is not much less than $-k_{\mathrm{B}}T$, thermal excitation can still excite carriers from states below the top of a barrier to states above, increasing the fraction of total carriers participating in intergrain conduction, and thus the measured Hall mobility. Only in the limit where $\Phi \ll -k_{\mathrm{B}}T$ does the effect of the grain boundary potential barrier become insignificant and μ_{gb} become independent of temperature.

Equation 7.1 has the downside that it contains several mathematically coupled terms (for instance, α_{eff}, L, ℓ, and w) that cannot be independently determined from just a measurement of Hall mobility as a function of temperature. Additionally, near the low barrier limit ($\Phi \ll -k_{\mathrm{B}}T$), Equation 7.1 reduces to

$$\mu_{gb}(T) = \frac{4\pi e m^* \alpha_{\mathrm{eff}} L}{h^3 n_{\mathrm{gb}}} \frac{\ell}{\ell + \frac{3}{4}w} |\Phi| \,. \tag{7.2}$$

In this case, the now insignificant barrier height becomes coupled to the rest of the physical parameters and also can no longer be independently determined from the temperature dependence of carrier mobility. In this scenario, a qualitative assessment of whether the experimental carrier mobility increases with increasing temperature can still be used to judge whether grain boundary effects are of significance for a given sample, as no other major scattering mechanism would lead to a mobility with this sign for temperature dependence in degenerately conducting samples.

For these reasons, it can sometimes be convenient and useful to adopt a further simplification. If the grain boundary barrier is much higher than the Fermi level, only electrons with $E \gg E_{\mathrm{F}}$ can traverse the barrier by thermionic emission, and their

energy distribution can then be approximated using Boltzmann, instead of Fermi-Dirac statistics.[17] In the context of polycrystalline TCOs, this represents the case of low carrier concentration and non-degenerately conducting samples.

Seto (building on the earlier work of Petritz[18]) has analyzed the situation for grains of uniform size L with a boundary trap density of Q_t, and applied this model to the analysis of doped polycrystalline silicon with carrier concentrations as high as $5 \times 10^{19}\,\mathrm{cm}^{-3}$. In the regime where the boundary trap density is not sufficient to completely deplete the grains of carriers ($Q_t < nL$), as is true for all TCO samples in this study, the temperature-dependent, grain boundary-limited carrier mobility is

$$\mu_{gb}(T) = Le(\frac{1}{2\pi m^* k_B T}) \exp(-\frac{E_B}{k_B T}) \,, \tag{7.3}$$

where m^* is the electron effective mass, E_B is the height of the grain boundary barrier relative to the bulk conduction band minimum (Figure 7.4), and k_B is Boltzmann's constant.[19] Given that the effective mass can be determined independently or assumed using literature values, L is the only unknown physical parameter among the leading terms to the exponential.

As the Fermi level begins to approach closer to the top of the grain boundary barriers and the minimum energy for electrons capable of surmounting the barrier becomes closer to E_F, the Boltzmann distribution will increasingly overestimate the population of electrons with enough energy to cross over the barrier. Consequently, Equation 7.3 will tend to *overestimate* the height of the potential barrier when used to model experimental data.

Combining Intragrain and Grain Boundary Effects

For DC electronic conduction to take place across a polycrystalline film, charge carriers must necessarily traverse a path that includes many grains and grain boundaries. It follows easily that, in general, the macroscopic electrical resistivity of a sample will depend on the properties of both grain boundaries and those of the more ordered bulk material within grain interiors.

Under the approximation that all significant carrier scattering mechanisms act independently, the effect of grain boundary scattering can be accounted for in the total

scattering model simply as an additional term in the Matthiessen's Rule summation of scattering mechanisms:

$$\tau^{-1} = \sum_i \tau_i^{-1} \tag{7.4}$$

where τ_i is the average time between scattering events for the ith mechanism acting individually.[20]

Another useful way of thinking about how grain boundary and grain interior properties contribute to the overall electrical properties of the sample is to consider an equivalent circuit description of the system. A variety of models of varying complexity have been used in the literature, and here, only the very simplest will be considered as a means to illustrate some conceptual points.[21] Figure 7.6 shows an equivalent circuit representing grain interiors as a resistor with resistance R_{g} in series with a resistor R_{gb} and a capacitor with capacitance C_{gb} in parallel, which represent the resistive grain boundaries and the fact that an applied bias can cause charge to build up along them, respectively.

The equivalent circuit picture is particularly useful as a qualitative guide for how a sample will behave in response to an oscillating electric field. Given that the impedance of a capacitor is given by $-1/i\omega C$, where ω is the angular frequency of the excitation, the capacitor is a short circuit at infinite frequency, and an open circuit to DC. Thus, the measured DC resistance of the whole system is $R_{\mathrm{g}} + R_{\mathrm{gb}}$, while the resistance as frequency tends to infinity is just R_{g}. In other words, such a picture is a simple method for illustrating why optical frequency measurements (Chapter 5) sample mostly the grain interiors, whereas the DC resistivity that is of interest for most TCO applications must also consider the conductivity-limiting effects of the

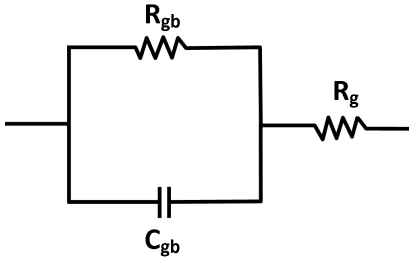

Figure 7.6: A simple R-RC equivalent circuit model showing one approach for combining the effects of grain boundary (C_{gb} and R_{gb}) and within grain electronic transport (R_{g}).

grain boundaries.

Finally, a critical point that is particularly transparent from this type of equivalent circuit model is that the grains and the grain boundaries act *in series*. Because resistances in series add, a relatively unconductive part will dominate the overall behavior of the system. Thus, in the quest to achieve high DC conductivity, it does not matter how conductive the grain interiors are if highly resistive grain boundaries are preventing good grain-to-grain electrical contacts. We have already seen this principle demonstrated in Chapter 5, where a doping-induced metal-to-non-metal transition occurs within the grains, but is partially obscured in DC electrical measurements by the influence of grain boundaries. Thus, in samples that are polycrystalline like most TCO thin films, conductive grain boundaries are *required* to achieve good overall electrical performance.

7.2 Grain Boundaries in ZnO and In_2O_3

Thinking back to the problem first posed in Section 1.3, a comparison of ZnO and In_2O_3 samples prepared by spray pyrolysis vividly highlights the challenges of trying to replace the latter with the former. It is relatively straightforward to prepare indium oxide and ITO samples by spray pyrolysis with stable electrical conductivities matching or even exceeding those seen in commercial sputtered samples.[22] The performance of ZnO, however, is highly sensitive to deposition conditions and environmental influences, and thus often struggles to reach levels that are industrially useful. We can now show that this divergence is due in large part to the differing behavior of grain boundaries in these polycrystalline TCO materials.

7.2.1 Room Temperature Properties

When the electrical conductivity of undoped ZnO and In_2O_3 thin films deposited at various temperatures are compared (Figure 7.7), two significant qualitative differences are obvious. First, the electrical conductivity of any In_2O_3 sample is at least 10 times higher than that of any ZnO sample. Second, the conductivity of In_2O_3 appears to be relatively constant, or perhaps even slightly increasing with decreasing deposition temperature, whereas the conductivity of ZnO falls sharply as the deposition temperature decreases below 334 °C.

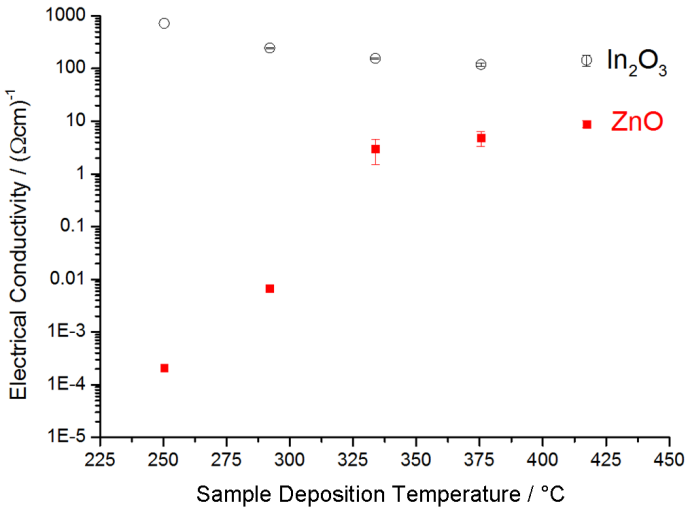

Figure 7.7: Electrical conductivity of undoped In_2O_3 (black circles) and ZnO (red squares) thin films deposited by spray pyrolysis as a function of deposition temperature. Figure adapted from Vai, *et al.*[23]

The sample in the indium series deposited at 209 °C was not measurably conducting. This is due to incomplete decomposition of the indium chloride precursor at this low temperature, which resulted in a film composed primarily of insulating indium oxide chloride (InOCl) instead of indium oxide (Figure 7.8). Ergo, this sample will not be discussed further here. The decreasing conductivity of ZnO with decreasing T_{dep} cannot be explained by a similar mechanism, as the performance drop-off in this case occurs at temperatures well above those where there is any evidence of incomplete precursor decomposition.

It is very interesting to note that the In_2O_3 sample deposited at 250 °C remains highly conducting despite containing some InOCl as a secondary phase and being very near the low temperature edge of the spray pyrolysis temperature window for the indium chloride precursor.

Room-temperature Hall effect measurements reveal that the sharp decrease in ZnO conductivity with decreasing deposition temperature is primarily due to a reduction in mobility, while carrier concentrations are constant to within experimental error (Figure 7.9). The samples deposited at 292 °C and below were too resistive for reliable Hall effect measurements, likely due to the even lower carrier mobilities ($\ll 1\,\mathrm{cm}^2/\mathrm{Vs}$) that result at these low deposition temperatures.

Carrier mobilities range between roughly 40–50 $\mathrm{cm}^2\,\mathrm{V}^{-1}\,\mathrm{s}^{-1}$ for the indium oxide

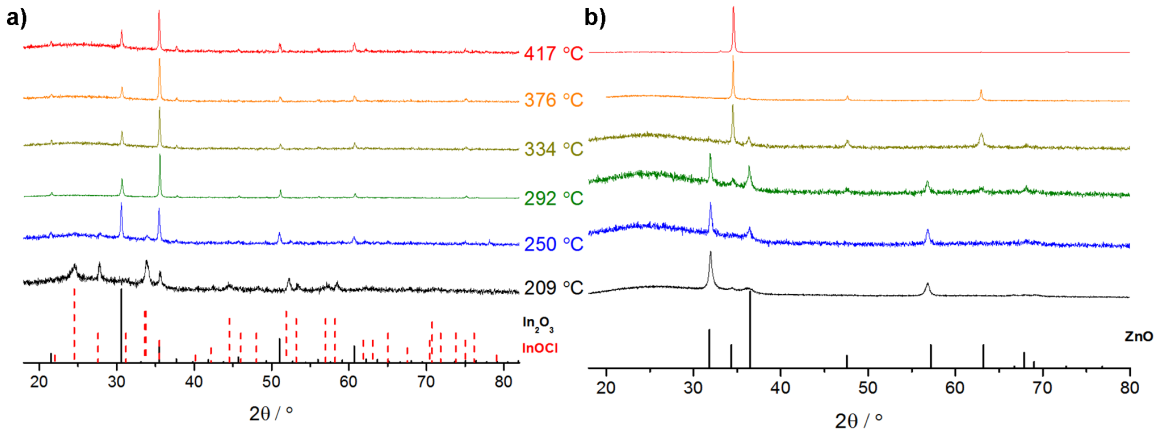

Figure 7.8: X-ray diffraction patterns of a) indium oxide and b) zinc oxide films deposited by spray pyrolysis at various temperatures. The 209 °C and 250 °C patterns in (a) show incomplete decomposition of the indium chloride precursor, leading to indium oxide chloride. Reference stick charts for In_2O_3 (a, black), InOCl (a, red), and ZnO (b, black) are also shown. Figure adapted from Vai, *et al.*[23]

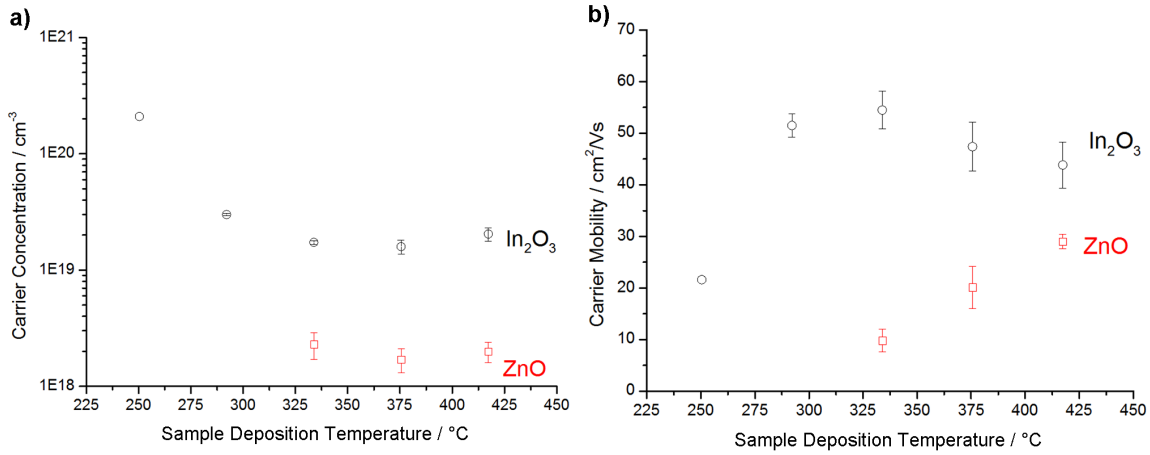

Figure 7.9: Room-temperature Hall effect (a) carrier concentration and (b) carrier mobility of In_2O_3 (black circles) and ZnO (red squares) thin films deposited by spray pyrolysis as a function of deposition temperature. Data is omitted for lower temperature ZnO samples too resistive for reliable Hall effect measurements. Figure adapted from Vai, *et al.*[23]

films deposited at 292 °C and above. These values are markedly higher than those observed for the ZnO samples. A slight increase in carrier concentration for the sample deposited at 292 °C accounts for its higher conductivity. The sample deposited at 250 °C is found to have a much higher carrier concentration and lower mobility than its higher temperature counterparts. This behavior would be consistent with doping by increasing amounts of residual chloride left in the sample as the deposition temperature decreases. This is further evidenced by the presence of a crystalline InOCl impurity in the sample deposited at 250 °C (Figure 7.8a).

SEM Surface Morphology

SEM images of the surfaces of the two series of samples are shown in Figure 7.10. The ZnO samples show a gradual change from a higher T_{dep} morphology consisting of stacked horizontal platelets, to a more porous, feather-like structure characteristic of low decomposition temperatures. The most significant structural transition occurs between the samples deposited at 334 and 292 °C, which also corresponds well with sharp changes in preferred orientation (Figure 7.8b) and electrical conductivity (Figure 7.7) that occur around these deposition temperatures.

With the notable exception of the sample deposited at 250 °C, which contains indium oxide chloride as an impurity, all of the In_2O_3 thin films consist of polyhedral grains with roughly the same shape. However, the size of the grains diminishes quite dramatically with a reduction in the deposition temperature, from some grains larger than 500 nm visible in the sample deposited at 417 °C to grains mostly ∼50 nm or smaller for the sample deposited at 292 °C.

7.2.2 Variable Temperature Hall Effect

As implied by Equation 7.3, the effect of grain boundaries on electronic transport can be quantified by analyzing how the carrier mobility of a sample varies as a function of temperature. Mobility data collected from the two series of samples between approximately 80–360 K is presented as the colored symbols in Figure 7.11.

For modeling the grain-boundary limited mobility, Seto's result (Equation 7.3) is used in preference to that of Prins, *et al.* (Equation 7.1) because all phase pure

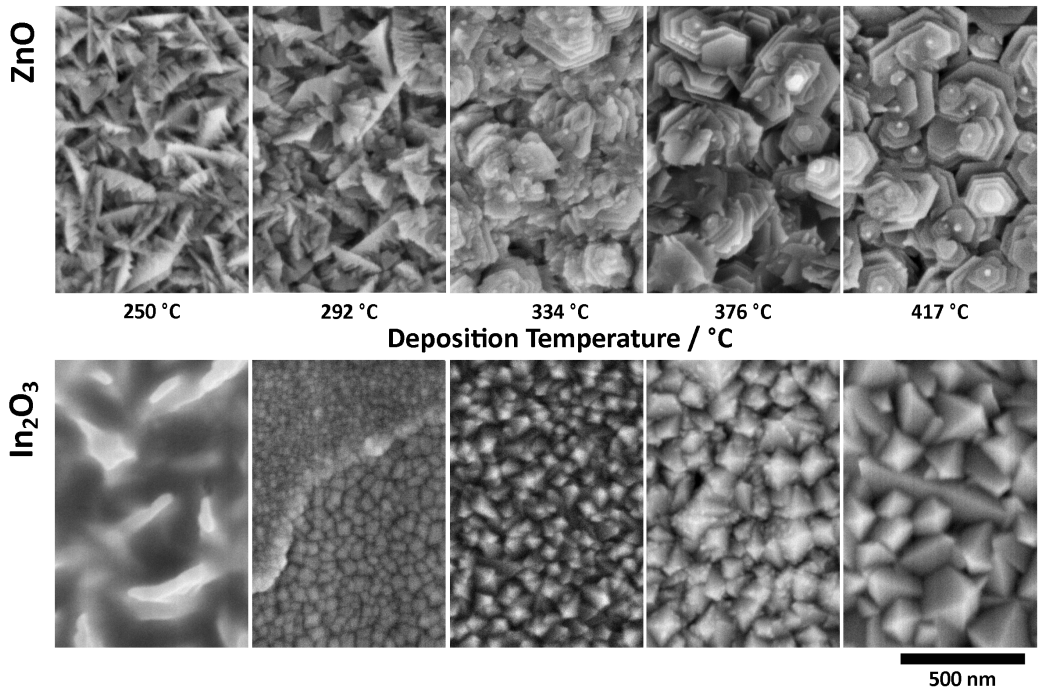

Figure 7.10: Representative SEM micrographs showing the surface morphology of nominally undoped ZnO (top) and In_2O_3 (bottom) thin films deposited by spray pyrolysis at various deposition temperatures. Figure reproduced from Vai, *et al.*[23]

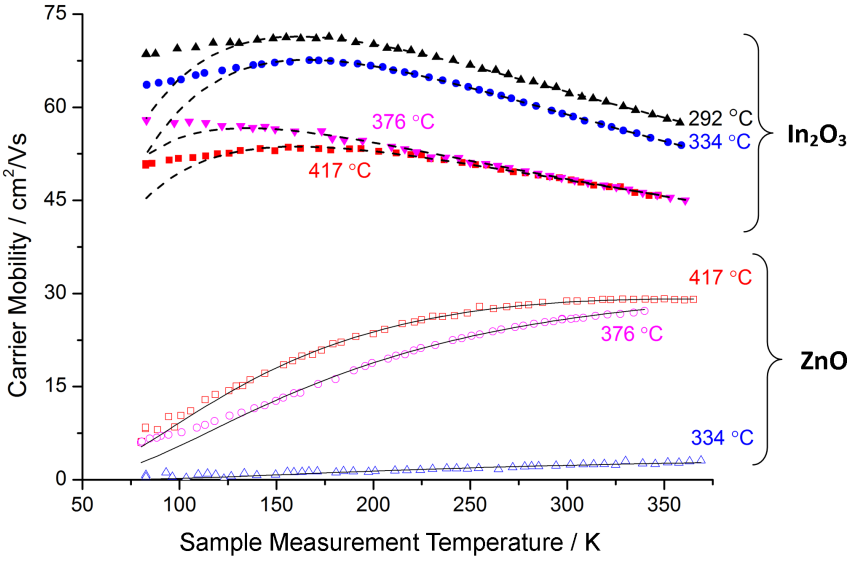

Figure 7.11: Hall carrier mobilities as a function of sample temperature for nominally undoped ZnO (open symbols) and In_2O_3 (closed symbol) samples deposited by spray pyrolysis at the T_{dep} shown. The black curves are theoretical values calculated using Equation 7.7 and the best-fit parameters given in Table 7.1. Figure adapted from Vai, *et al.*[23]

samples here have carrier concentrations less than the Mott critical density of 2–$7 \times 10^{19}\,\mathrm{cm}^{-3}$ previously found for ZnO in Chapter 5 and are thus expected to be non-degenerate conductors.

However, grain boundary scattering alone cannot account for the decrease in mobility that is observed as the temperature increases; to do so requires that the effects of electron-phonon scattering also be considered, since these are the only major scattering mechanisms that lead to a decrease in mobility with increasing temperature.[24] For the samples and conditions presently under study, and assuming reasonable literature values for the relevant physical constants of ZnO and In_2O_3, acoustic phonon modes are found to be dominant over optical and piezoelectric modes. In this case, the classic result of Bardeen and Shockley can be used to approximate the acoustic phonon limited mobility as

$$\mu_{\mathrm{ph}}(T) = A * T^{-3/2}\,, \tag{7.5}$$

where

$$A = \frac{(8\pi)^{1/2} e \hbar^4 c_{\mathrm{ii}}}{3 E_1^2 m^{*5/2} k_{\mathrm{B}}^{3/2}} \tag{7.6}$$

and $\hbar = h/2\pi$ is the reduced Planck's constant, c_{ii} is the elastic constant in the direction of phonon propagation, and E_1 is a parameter with units of energy related to the magnitude of energy band shifts upon physical deformation of the crystalline lattice.

Equations 7.3 and 7.5 can then be combined using Equation 7.4 to yield

$$\mu_{\mathrm{Hall}}(T)^{-1} \approx \mu_{\mathrm{ph}}(T)^{-1} + \mu_{\mathrm{gb}}(T)^{-1} \tag{7.7}$$

as a model for describing temperature-dependent mobility.

The black lines in Figure 7.11 show the theoretical mobility as a function of temperature calculated using this model and the best-fit parameters listed in Table 7.1.

This model should describe the data best at higher temperatures, where the thermionic transport assumed by Equation 7.3 dominates over thermally-assisted tunneling through the barriers. Indeed, the mobility data collected above ∼115 K is very satisfactorily represented for both data sets. Below this temperature, Equation 7.3 underestimates the carrier mobility in the samples, as would be expected as the relative contribution of electron tunneling to inter-grain carrier transport (and hence

Table 7.1: Best-fit parameter values used to generate the theoretical fits to each data set in Figure 7.11 using the model given by Equation 7.7. An effective mass of $m^* = 0.3\,m_e$ was assumed for both materials based on literature values.[25,26]

	T_{dep} / °C	A / 10^6 $cm^2K^{3/2}V^{-1}s^{-1}$	L / nm	E_B / meV
In_2O_3	417	2.8	3.8	7.8
	376	1.3	5.9	9.8
	334	1.8	5.6	8.8
	292	3.0	3.6	6.4
ZnO	417	1.4	4.1	23.2
	376	2.4	4.4	28.6
	334	2.1	0.52	37.3

carrier mobility) increases. If this measurement were to be performed at even lower temperatures, additional processes such as ionized impurity scattering or electron-electron scattering might become significant and have a substantive effect on the observed carrier mobility.

The significantly different electronic transport properties of ZnO and In_2O_3 can be largely explained by differences in the average height of the grain boundary potential barrier E_B across the two data sets. The calculated indium oxide E_B values range from 6.4–9.8 meV, which are substantially smaller and less variable than the analogous values for ZnO. For ZnO, E_B increases markedly from 23.2 meV for the sample deposited at 417 °C to 37.3 meV for the sample deposited at 334 °C. These trends correspond well with room-temperature electrical properties presented in Figures 7.7 and 7.9, which show that In_2O_3 has relatively high and steady conductivity across the range of deposition temperatures, whereas ZnO has a lower overall conductivity that is highly sensitive to a decrease in T_{dep}.

The L parameter, which in Seto's model corresponds to the effective size of the grains, was calculated from the best-fit parameters assuming a constant effective electron mass in both materials of $m^* = 0.3m_e$.[25,26] L is relatively constant across all samples, except for the ZnO sample deposited at 334 °C. This change can be correlated with the sharp change in both morphology and room-temperature electrical properties

that begins around this deposition temperature.

Finally, the best-fit values of A are also presented for reference. The values vary somewhat, but not in a systematic way, suggesting that the extent of acoustic phonon scattering is not strongly dependent on sample deposition temperature. In any case, A is a function of two independent physical parameters (c_{ii} and E_1) that cannot be uniquely determined from these data alone.

7.2.3 X-ray Photoelectron Spectroscopy of ZnO Surfaces

Since grain boundary potential barriers are closely related to the chemical state of oxide surfaces, X-ray Photoelectron Spectroscopy (XPS) is a surface-sensitive characterization tool that can provide additional information about the types of species that are potentially involved. Experimental oxygen 1s XPS signals collected from the series of ZnO samples can be reproduced extremely well using 3 pseudo-Voigt components constrained to have the same full-width at half-maximum.[ii] These three components are centered at approximately 530.5, 531.8, and 532.7 eV (for example, Figure 7.12). This deconvolution of the oxygen 1s photoelectron spectrum into three component signals has also been adopted in several other previous works.[27,28]

There is little question that the lowest binding energy component arises from the oxide in locally well-ordered regions of the ZnO lattice.[29] The literature consensus regarding the two higher binding energy components is more tentative, primarily because a wide range of oxygen-containing species could potentially have binding energies in this range. Nevertheless, with this caveat in mind, we will note that the middle component centered at ∼531.8 eV has often been associated with oxygen near oxygen vacancies,[30,31] and that the highest binding energy component at ∼532.7 eV has previously been correlated with a variety of adsorbed oxygen-containing species, such as water or hydroxide.[28,32,33]

Some authors have suggested that carbon plays an important role in ZnO photoconductivity,[6,34,35] either as part of the active species being adsorbed/desorbed or as a catalyst for other speciation changes. It has also been demonstrated that signals for

[ii] It should be noted that the choice to represent the experimental data with three components is not likely to be unique and that valid deconvolutions can probably be found with four or more components. However, in the absence of independent evidence as to the "correct" number of components, this work elects to use three, the minimum number of components needed to satisfactorily reproduce the data.

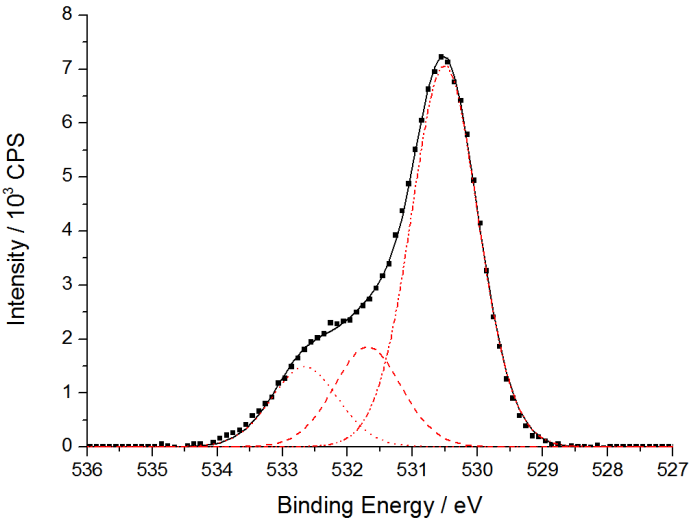

Figure 7.12: Example experimental O(1s) XPS data (black squares) for a ZnO thin film deposited at 334 °C and measured without any further treatment. The model fit to the data is shown as a black curve and consists of three pseudo-Voigt components centered at approximately 530.5, 531.8, and 532.7 eV (red curves).

oxygen in carbonates would also occur near the highest binding energy component observed here. However, we could not find any obvious correlations between these oxygen 1s and the carbon 1s photoelectron spectra that were also recorded from these samples. While the involvement of carbon in grain boundary effects cannot be conclusively ruled out on this basis, it does not seem to be a major contributor to the behavior of the system under study.

Oxygen 1s XPS data for the series of ZnO films deposited at different temperatures were normalized to the height of the largest, lowest binding energy signal (corresponding to lattice oxygen), as shown in Figure 7.13. A clear decrease in the relative size of the higher binding energy components with increasing deposition temperature can be seen. This indicates that the proportion of surface oxygen associated with defects is greatest for the lowest T_{dep} samples. Assuming that this highest binding energy component does indeed result from various adsorbed acceptor species, this would be further evidence supporting the proposal that the low conductivity of low deposition temperature ZnO samples is due to grain boundary potential barriers.

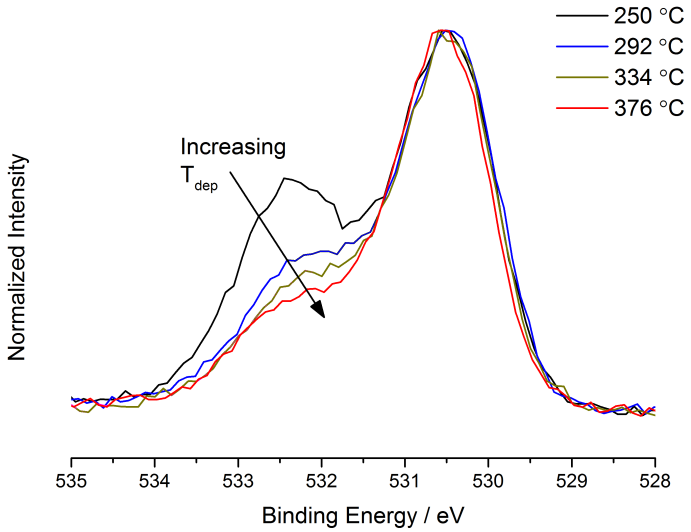

Figure 7.13: Experimental O(1s) XPS data for ZnO thin films deposited by spray pyrolysis at deposition temperatures ranging from 250 to 376 °C. The spectra are all normalized to the height of the main oxide peak at ~530.5 eV. The decrease in the area of the higher binding energy components with increasing T_{dep} is clearly visible.

7.2.4 Photoconductive Response

It has been known for quite some time that some semiconductors, most notably zinc oxide, exhibit a phenomenon known as *persistent photoconductivity*, where the electrical conductivity of a sample increases upon exposure to light with energy exceeding that of the material's bandgap.[36,37] This effect is called "persistent" because the conductivity changes can last for many hours or even days after the irradiation ceases with the sample in air. In fact, the increase in conductivity can be made essentially permanent if the sample is kept under a good vacuum or a rigorously inert atmosphere.[38] This effect is reversible and a given sample can be cycled many times between its dark and irradiated states.[39]

Data showing how the electrical conductance of a ZnO thin film deposited at 292 °C changes with exposure to light and various flowing atmospheres are shown in Figure 7.14. Starting from a dark conductance of $<5 \times 10^{-10}\,\Omega^{-1}$ (beyond the range of the multimeter used), irradiation using a handheld UV blacklight causes at least a five-to-six order of magnitude increase in electrical conductivity. With the sample in a container under flowing nitrogen, the photoconductivity decays very slowly. Indeed, most of the photoconductivity decay observed is probably due to the small amount of

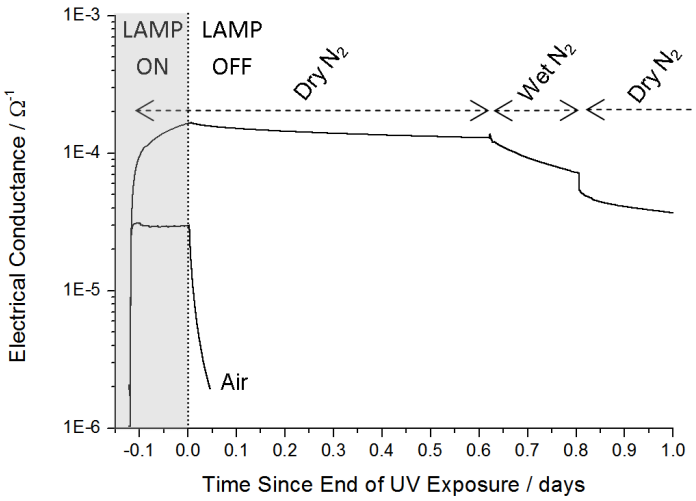

Figure 7.14: Changes in electrical conductance of a ZnO sample ($T_{\text{dep}} \approx 292\,^{\circ}\text{C}$) under the indicated conditions of UV irradiation and composition of flowing atmosphere. The zero of time is when the UV lamp is switched off. The conductance of this sample after being stored in the dark under air for ~2 days was $<5 \times 10^{-10}\,\Omega^{-1}$. Reproduced from Vai, *et al.*[40]

air introduced to the system during gas changeovers. Even for the sample kept under flowing air, the photoconductivity has only decayed by about an order of magnitude in an hour.

Persistent photoconductivity occurs because of light-driven changes to chemical equilibria at grain boundaries. Photons with energy greater than the bandgap can excite electrons into the conduction band, while leaving corresponding holes in the valence band (Figure 7.15a). These positively charged holes can be drawn towards the excess of negative charge trapped by acceptor states at the grain boundary. Once in the vicinity, the holes can then neutralize electrons trapped there, reducing the net charge and hence the height of the potential barrier. At the same time, this breaks the chemisorption bonds between adsorbed molecules and the oxide surface (Figure 7.15b). Now only physisorbed, the species can easily desorb at room temperature, thus reducing the density of acceptor states. In addition to reducing the height of the potential barrier and increasing mobility in this way, each photo-induced desorption of an acceptor also leads to the net generation of one or more conduction electrons (Figure 7.15c). Both the increases in mobility and carrier concentration lead to a higher electrical conductivity for the sample.

As long as illumination persists, the continual supply of photo-generated holes

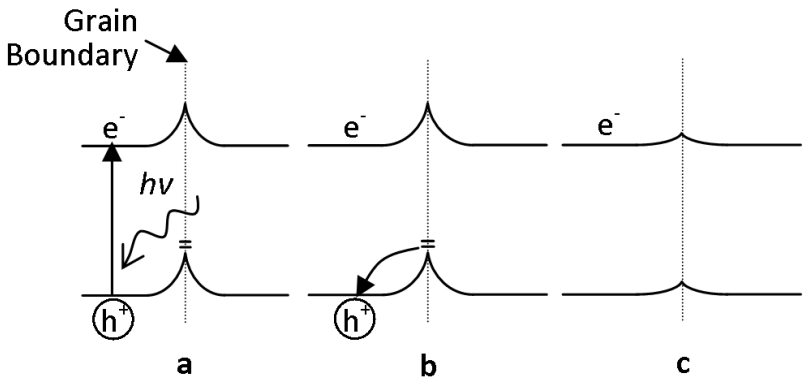

Figure 7.15: Schematic illustrating how grain boundary acceptor states can be neutralized by UV irradiation, thus reducing the height of the potential barrier and leading to the net generation of free carrier electrons.

disfavors the chemisorption of species from the atmosphere that would lead to the formation of acceptors. However, once irradiation ceases, the supply of holes ends and the sample will tend back towards its pre-irradiation equilibrium. If the sample is in air, oxygen and water will gradually re-adsorb over the course of hours or days until the sample comes back into equilibrium with the ambient humidity and temperature. Naturally, if there is no water or oxygen in the environment, there can be no re-adsorption and the photoconductivity will be stable.

Notably, it is this fact that conductivity is controlled by relatively slow chemical processes, rather than fast electronic ones, which ultimately gives rise to the apparent "persistence" of this effect.

This type of mechanism has been verified in ZnO by several different groups with measurements that directly correlate light-induced changes in conductivity with the desorption of gases from the surfaces of the material.[6,41] There remains controversy over the exact chemical species involved. Proposed candidates have included chemisorbed O^-,[39] O_2^-, O_2^{2-},[42] and CO_2^-.[6] In our own work, we have found wet nitrogen leads to a noticeably faster decay of photoconductivity than dry nitrogen, which suggests that the dissociative adsorption of atmospheric moisture, perhaps as hydroxide, also makes an appreciable contribution to the formation of acceptor states (Figure 7.14). Li, *et al.* have also noted the important role played by humidity in modulating the photoconductive response of ZnO.[43]

Photoconductivity as a Probe of Grain Boundary Barriers

Besides being of fundamental interest, the phenomenon of persistent photoconductivity has also been developed as a tool for assessing the extent to which conduction in a given TCO sample is limited by the adsorption of species from the atmosphere at grain boundaries. Since the net effect of irradiation is to induce the desorption of labile species that lead to acceptor defects, the larger the conductivity change upon irradiation, the more limiting such species are to electronic conduction in the dark state. Figure 7.16 shows the relative photoconductive responses for ZnO and In_2O_3 samples deposited by spray pyrolysis at various deposition temperatures. The fact that all of these samples show a measurable photoconductive response implies that similar physics are happening in both of these materials, albeit to greatly varying extents.

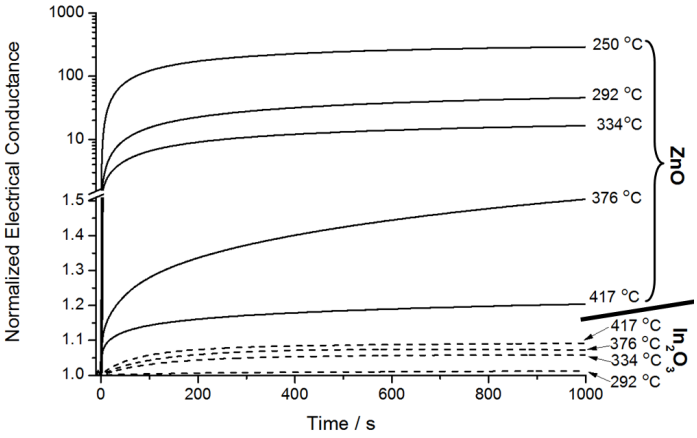

Figure 7.16: Normalized photoconductive response of ZnO (solid curves) and In_2O_3 (dashed curves) thin films deposited at the indicated T_{dep}. Note the break where the y-axis changes from linear to logarithmic. The zero of time is when the sample is first exposed to UV light. All conductance values are normalized to the $t = 0$ value for a given sample. Figure reproduced from Vai, *et al.*[23]

Figure 7.16 clearly shows that the photoconductive response of each ZnO sample is larger than that for any of the In_2O_3 samples. Furthermore, the magnitude of the response in ZnO increases significantly as the deposition temperature decreases. Both of these observations are in close agreement with earlier results. It can be concluded that labile species at grain boundaries limit electronic conduction in ZnO far more than for any of the In_2O_3 samples. It is also confirmed that the low deposition

temperature ZnO samples suffer much more from the effect of air-derived species adsorbed at grain boundaries than their higher T_{dep} counterparts.

A few more important inferences can be drawn from these data. With the temporary reduction of grain boundary potential barriers by UV light, all of the ZnO samples deposited at 292 °C and above have electrical conductivities that vary by at most a few tens of percent. Even the sample deposited at ∼250 °C, which was at least four-to-five orders of magnitude more resistive in the dark than the most conductive ZnO, is only about five times more resistive during irradiation. These data show unequivocally that the effect of labile, atmospheric species adsorbed at grain boundaries accounts for the vast majority of the *as deposited* conductivity difference between low and high T_{dep} ZnO thin films, even if they are not the *only* relevant factor.

At the same time, even with grain boundary effects suppressed, the best ZnO films only have carrier mobilities of at most $\sim 35\,\text{cm}^2\,\text{V}^{-1}\,\text{s}^{-1}$(black curves in Figure 7.23b). This is still substantially lower than the carrier mobilities seen in the In_2O_3 series, even though the In_2O_3 samples have higher carrier concentrations. In other words, the effect of labile air-derived acceptors alone does not fully explain the differences between zinc and indium oxide films prepared by spray pyrolysis. This is a point to which we will return in Sections 7.2.5 and 7.2.6.

Combining Photoconductivity with XPS

More information about the changes underlying persistent photoconductivity in ZnO can be obtained by a comparison of the oxygen 1s XPS signals for a sample in the dark and while the same sample undergoes UV irradiation in the vacuum chamber of the XPS spectrometer.

Figure 7.17a shows oxygen 1s spectra for a ZnO sample deposited at low T_{dep} for which the changes upon UV irradiation are most obvious. With the spectra normalized to the height of the largest peak (due to lattice oxide), an obvious reduction in the area of the highest binding energy peak can be observed upon irradiation, which is consistent with the photo-induced desorption of oxygen-containing species. A more modest, but still distinct change is also observed for samples prepared at higher deposition temperatures (Figure 7.17b), from which a general trend of decreasing surface speciation change — and hence photoconductive response — with increasing T_{dep} can be seen.

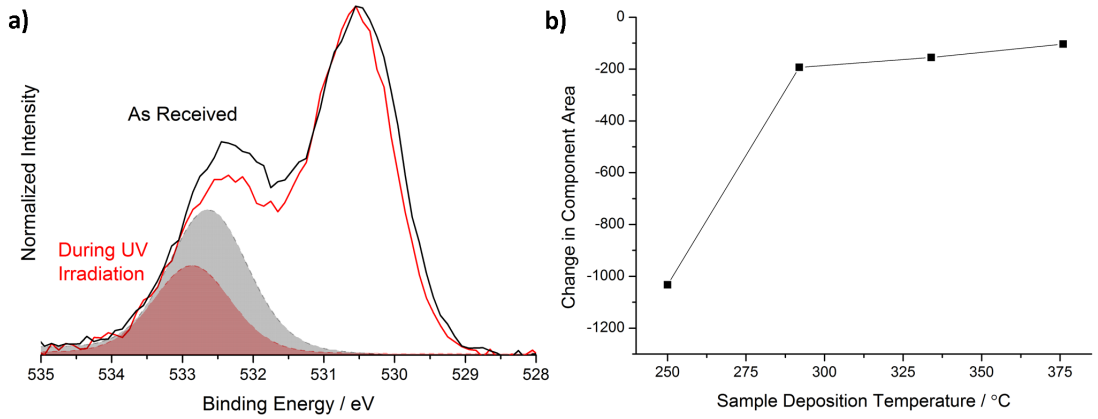

Figure 7.17: a) Oxygen 1s XPS data for a ZnO sample deposited at 250 °C measured in the dark (black) and during irradiation with 365 nm UV light (red), normalized to the height of the largest component and with the highest binding energy component highlighted. b) Absolute change in the area of the highest binding energy oxygen 1s component of ZnO upon post-deposition UV irradiation.

The sample deposited at $T_{dep} = 250\,°C$ does appear to be somewhat outside the trend set by its higher temperature counterparts. This apparent anomaly can potentially be rationalized in terms of temperature-dependent morphology changes, which will be covered in Section 7.2.6.

It may also be noted that the change in XPS signal upon UV irradiation (Figure 7.17a) is only a fraction of that which occurs as the deposition temperature is varied (Figure 7.13). This is clear evidence that more than one class of oxygen-containing species is represented among the highest binding energy components of the signal, and that only some of these species will desorb upon irradiation.

7.2.5 Intrinsic Differences between ZnO and In_2O_3

Clearly, when compared to ZnO, electronic conduction in polycrystalline In_2O_3 is hindered very little by the adsorption of atmospheric species at grain boundaries. Given this, it is sensible to examine some of the presently available evidence on the surface chemistry of these two materials to try to determine why these differences might exist. This comparison is particularly relevant to the basic question of why In_2O_3 exhibits such excellent performance as a TCO compared to ZnO, and is furthermore an important prerequisite for both developing and understanding the various mitigation approaches that will be discussed in Section 7.3.

Temperature-programmed desorption measurements of ZnO have shown that the desorption of water from grain surfaces occurs in two distinct steps with peaks occurring at 220 °C and 270 °C.[44] A similar measurement on ITO likewise reports surface water loss in two steps upon heating, but at the lower temperatures of 150–165 °C and ∼242 °C.[45] A couple of other workers have also reported hydroxide desorption from indium oxide films at less than 200 °C.[46,47] Regardless of the variation in exact values, the higher desorption temperatures from ZnO surfaces imply a stronger water-surface interaction than is present in In_2O_3. This would be consistent with a greater tendency for the dissociative chemisorption of water from the atmosphere, which in turn would lead to more significant grain boundary potential barriers in ZnO

In addition to water, the adsorption of a range of other species to ZnO surfaces has been reported, particularly in the numerous studies on the applications of ZnO as a catalyst.[34,35,48–50] However, while an active surface chemistry is indeed a useful property for a catalyst, many such adsorbates also lead to the formation of acceptor defect states and would be detrimental to the performance of ZnO as a transparent conductor.

These observations should not be taken as evidence that the electrical conductivity of In_2O_3 cannot be significantly changed by the effects of adsorbed species at grain boundaries. Indeed, gas sensors based on In_2O_3 have been reported which rely precisely on the conductivity changes caused by such effects.[51–53] However, such works have also shown that the preparation of highly resistive, grain boundary-limited In_2O_3 thin films is quite challenging and in general requires very strongly oxidizing conditions, such as sputtering deposition in a pure oxygen atmosphere[54] or post-deposition annealing with ozone.[55] These are much harsher conditions than are needed to substantially reduce the conductivity of ZnO samples. As noted in Section 4.4.2, we have found that depositing ZnO samples in air as opposed to high purity nitrogen leads to a more than 1000× decrease in conductivity, while In_2O_3 prepared under the same conditions only suffers a four-fold reduction in conductivity.

The conditions needed to produce highly resistive In_2O_3 are so aggressive that they probably go beyond merely increasing the concentration of adsorbed acceptors at grain boundaries. Instead, they may well lead to a filling of near-surface oxygen vacancies and thus a reduction in the concentration of surface donors. At this point,

it bears repeating that both surface donor and acceptor concentrations go into determining the height of the grain boundary potential barriers. Given this, the differences in the formation energy of surface oxygen vacancies in ZnO and In_2O_3 may also have an important role to play in distinguishing their behavior.

For instance, DFT calculations have been made showing that the most easily formed oxygen vacancy (from out of six symmetry-inequivalent oxygen sites) on the (111) surface of indium oxide has a formation energy of about 0.95 eV.[9] The result of a different calculation on ZnO showed that the energy cost to remove one-quarter of the oxygens in an ordered array from an oxygen-terminated surface was more than 50% greater, at between 1.54 and 1.75 eV per vacancy.[56]

It must be admitted that these results may not be directly comparable because of the different vacancy concentrations implied by the two calculations. Furthermore, the effect of surface reconstruction in real materials, especially that of polar surfaces, may significantly affect the applicability of these calculated results.[48] Nevertheless, a study of defect formation energies in these two materials using the same computational approach could still be of interest. And, if the already calculated formation energies are taken at face value or are even qualitatively correct, they would be consistent with the fact that surface donors form much more easily in In_2O_3 than in ZnO, and would thus be present in the former at higher concentrations under any given set of conditions. The net result would be a lower potential barrier in In_2O_3, even if the surface acceptor density of both materials was similar.

Another calculation that could also provide insight into differences between In_2O_3 and ZnO would be to determine how charge density is distributed across In-O and Zn-O polyhedra with various boundary conditions. The bonding between transition metals and oxygen is in general rather complex and often involves substantial π character, making broader periodic trends difficult to identify.[57] Differences in the electron-richness of near-surface oxide ions and metals in ZnO and In_2O_3 that stem from factors like electronegativity difference, preferred coordination geometry, and ion density may well have the power to at least qualitatively explain differences in their surface chemistry. To our knowledge, this is an aspect of TCO chemistry that has not yet been carefully considered.

7.2.6 T_{dep}-dependent Morphological Changes

How strongly a given sample is affected by grain boundary effects will be closely related to the geometry of the grain-to-grain contacts within the polycrystalline film.[58]

Consider two hypothetical contacts between grains, one with a small area and the other large. For the small area contact, even a small depletion depth due to the presence of surface acceptor states can extend far enough into the grains to choke off electronic transport through the narrow "neck" between them (Figure 7.18a).[iii] This is true even if adsorbed acceptors do not penetrate directly into the area of intimate grain-grain contact and are restricted to nearby accessible surfaces. In contrast, for conduction through a large area boundary to be substantially limited, much spatially wider potential barriers or significant diffusion of the acceptor species into the actual contact area would be needed (Figure 7.18b).

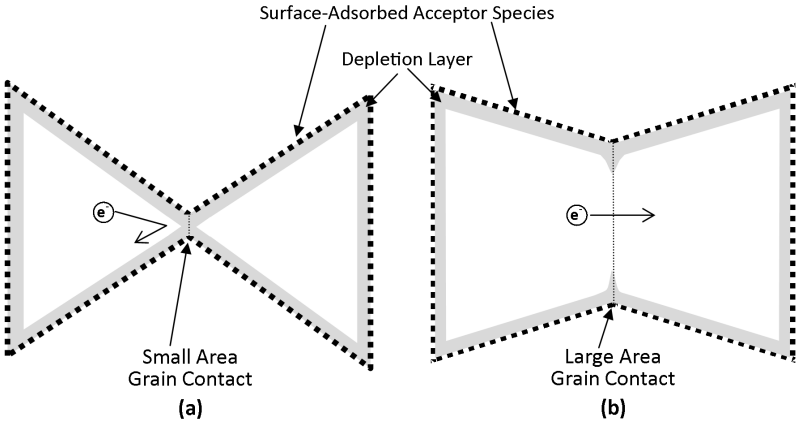

Figure 7.18: A two dimensional schematic contrasting a) small and b) large area contacts between grains in a polycrystalline material. Conduction through small area contacts can be strongly affected by the depletion layer (shaded) resulting from the presence of surface acceptors, even if the acceptors are not present in the grain-grain contact itself.

This morphology-dependent modulation by adsorbed species will occur on top of any potential barrier that may be present due to defects in the contact area itself. The height of this "baseline" barrier will depend on factors like the extent of disorder or concentration of defects at the boundary itself, the size and shape of the boundary, and also the intrinsic sensitivity of conduction in the TCO material to disorder (Chapter 5). In other words, this leads to a situation where the overall grain

[iii] Or, for that matter, a narrow point within a single grain.

boundary effect is a function of both the intrinsic properties of the material and its morphology.

This idea is very important for explaining the changes in the electrical properties of ZnO that happen as a function of deposition temperature. Both the room-temperature conductivity (Figure 7.7) and magnitude of the photoconductive response (Figure 7.16) show distinct higher ($T_{\text{dep}} \geq 376\,^{\circ}\text{C}$) and lower ($T_{\text{dep}} \leq 292\,^{\circ}\text{C}$) temperature behavior, with the sample deposited at 334 °C being transitional between the two regimes. It is probably not coincidental that the most significant changes in crystallite orientation and surface morphology also occur near the same transitional temperature, as can be seen in the XRD and SEM data of Figures 7.8b and 7.10, respectively.

The significance of the loosely-packed, feathery grains observed in the ZnO sample deposited at 250 °C can now be stated explicitly. These grains appear to have a high exposed surface area compared to the stacked hexagonal platelets in the higher T_{dep} samples. This by itself would lead to a larger photoconductive response. However, in addition, it can also be suggested that the feathery shapes of the grains lead to smaller grain-grain contacts, which would effectively magnify any photoconductive effect, and be consistent with the large response observed in these samples.

Even if the material within the grains was similar (as has been implied by some of the results in Section 5.4), differences in grain contact area across the series can be used to explain the trend in underlying transport properties after labile grain boundary acceptor species have been desorbed using UV light. Since small area contacts are simply more resistive than analogous large area contacts due to geometry, it would not be surprising for the lower temperature samples to start from a higher resistance baseline.

Given that there are also changes in preferred orientation across the deposition temperature series, the distribution of in-contact and exposed faces differs from sample to sample. For instance, the higher deposition temperature samples grow with a preference for polar (002) faces parallel to the substrate, which would imply that most of the grain-grain contacts in the direction of current flow are made up of two non-polar faces. On the other hand, crystallites in the lower deposition temperature samples mostly have their (002) faces *perpendicular* to the substrate surface, which

also allows for current to flow through polar/polar and polar/non-polar grain contacts. Work on ZnO has shown that the energetics of near-surface defect formation can depend quite strongly on which surface is involved; hence, it is certainly plausible that these various combinations would lead to different baseline barrier heights and thus different underlying conductivities.[48,59] Studies of bicrystals, like those used to characterize ZnO-based varistors, would be very useful for quantifying the effect of grain orientation on the formation and height of potential barriers.[60,61]

Turning now to the series of In_2O_3 samples, there are significant changes in grain size across the phase-pure members of the series ($T_{dep} \geq 292\,^{\circ}C$), which significantly affects both the size and the number of grain boundaries that must be traversed by a conduction electron traveling across the film. Given this, perhaps the most surprising observation is how *little* the photoconductive response in In_2O_3 changes as a function of grain size. Indeed, the change in conductivity with irradiation is in all cases less than 10 %, a dramatically smaller response than that observed for most of the ZnO samples (Figure 7.16).

More than anything, this strongly suggests the high conductivity and stability of the In_2O_3 films do not result from a specific favorable sample morphology, but instead, an innately lower sensitivity to grain boundary and surface influences as compared to ZnO. While certainly not the only relevant factor, this clear difference in how easily intrinsic conductivity is reduced by environmental influences is clearly among the most important features distinguishing these materials, and a large part of what has made In_2O_3 and its derivatives so successful as engineering materials.

To conclude, we have ended up at a rather complex picture of grain boundaries in polycrystalline TCOs, whose effects ultimately depend on several interacting factors. Some of these factors are clearly dependent on the morphology of the sample, including the geometry of grain contacts and the amount of grain surface exposed to atmosphere. Then, aspects of the TCO surface chemistry, such as the relative formation energies of various acceptor and donor defects, must also be considered. In particular, it has been shown that the chemisorption of oxygen-containing acceptor species from the air has a particularly dominating influence on the behavior of ZnO, but much less so on that of In_2O_3. And finally, it is quite clear that grain boundary issues cannot be entirely divorced from the intrinsic transport properties of the bulk

TCO, such as the sensitivity of electronic conduction to disorder and the ability to use doping to modify the Fermi energy relative to the height of the potential barriers.

At the same time, the existence of many influential factors also implies that there may exist many different approaches for the mitigation of grain boundary limits to conductivity, with each targeting varying aspects of the problem. Thus, a variety of approaches will be introduced and discussed in the following section, with the goal of answering the question of how In_2O_3-like conductivity might be achieved using a ZnO-based thin film.

7.3 Mitigating Grain Boundary Effects in ZnO

Thinking back to Chapter 1, one of the overarching goals in current TCO research is to develop inexpensive ZnO-based materials whose performance as transparent conductors as closely approaches that of In_2O_3 and ITO as possible.

The previous section has clearly shown that grain boundaries are one of the most important differences between these two materials. And while some of the difference is almost certainly due to intrinsic materials differences that cannot be easily modified, it is also encouraging to note the existence of phenomena like persistent photoconductivity, which show that important features of grain boundary behavior can be dramatically modified by externally controllable parameters like exposure to light or varying atmospheres. Likewise, the idea that changing thin film morphology can lead to significant differences in performance is also useful, particularly since sample morphology is something that can also be substantially modified through appropriate process design.

Now that many of the key considerations and insights have been laid out, it is possible to evaluate critically a range of potential strategies that could be used to minimize the grain boundary problem in ZnO. It seems that many potentially useful pieces that could be part of a solution already exist, even if they have not yet been integrated into a final, demonstrated form. And so, the primary goal here is to highlight a set of approaches that if sufficiently developed and used together in right way should make it technically possible to prepare ZnO-based thin films on a large scale with performance rivaling that of class-leading, incumbent materials. Developing an idea of what would be required to achieve this also positions us well

for tackling the question of whether such mitigation strategies are ultimately worth pursuing further.

7.3.1 *in situ* UV: A New and Permanent Photoconductive Effect

Despite its name, the "persistent photoconductivity" discussed in Section 7.2.4 is not truly permanent and decays over time if the samples are exposed to air. However, in the course of investigating this phenomenon in polycrystalline ZnO thin films, we discovered an entirely new and apparently permanent photoconductive effect.

Instead of irradiating a sample after deposition is entirely finished, it was found that exposing a ZnO sample to UV light prior to its first exposure to air led to a statistically significant and long-lasting increase in its electrical conductivity. Among the samples prepared using this approach was one with a mobility of $44.3\,\mathrm{cm^2\,V^{-1}\,s^{-1}}$, which to our knowledge is the highest ever reported for a ZnO-based film prepared by spray pyrolysis. This value is easily competitive with the best carrier mobilities reported for ZnO films of comparable carrier concentration prepared using industrially-relevant vacuum-based techniques.[24] We have also found that this approach lowers the deposition temperature needed to produce the most conductive ZnO films by more than 80 °C, which could be useful in allowing the use of temperature-sensitive flexible substrates.

For the purposes of the discussion in this section, the conventional post-deposition irradiation of samples will be termed *ex situ* irradiation, while the UV treatment of samples prior to their first removal from the nitrogen-purged deposition chamber will be termed *in situ* irradiation (Figure 7.19).

The increase in electrical conductivity due to *in situ* irradiation of ZnO samples with UV light having energy exceeding that of ZnO's electronic bandgap ($\sim$3.4 eV) as compared to samples deposited in the dark (or while exposed to longer wavelength light) is plotted in Figure 7.20. With *in situ* irradiation, a maximum electrical conductivity of $13.3 \pm 3.0\,\Omega^{-1}\,\mathrm{cm}^{-1}$ was obtained at a deposition temperature of 334 °C. For the sake of comparison, the highest conductivity dark samples required a higher deposition temperature of 417 °C, and even then only had a conductivity of $8.9 \pm 1.3\,\Omega^{-1}\,\mathrm{cm}^{-1}$.

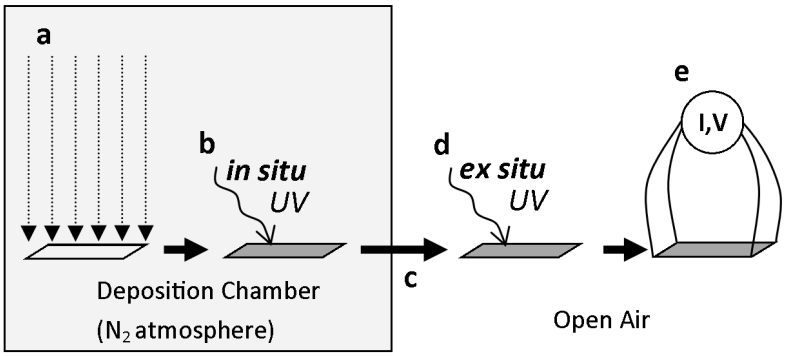

Figure 7.19: Scheme describing a spray pyrolysis process potentially incorporating two different UV irradiation treatments. (a) A ZnO sample is deposited by spray pyrolysis in a nitrogen-filled deposition chamber. (b) Either during or after deposition, the film can be exposed to UV radiation *in situ* while still under inert atmosphere. (c) The sample is then taken out of the deposition chamber into normal air. (d) An *ex situ* irradiation can be performed prior to e) electrical characterization of the sample. Depending on the situation, steps (b) and/or (d) may be omitted. Figure reproduced from Vai, *et al.*[40]

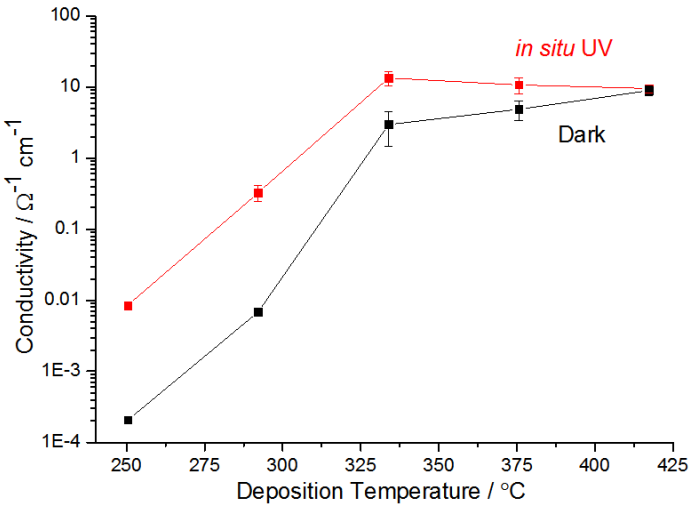

Figure 7.20: Electrical conductivity of ZnO thin films deposited by spray pyrolysis at various deposition temperatures with *in situ* UV irradiation (red) and in the dark (black). Figure adapted from Vai, *et al.*[40]

In stark contrast to classic "persistent" photoconductivity (Figure 7.14), Figure 7.21 shows that the conductivity increase due to *in situ* UV irradiation is more or less stable over at least 90 days. The small variation in measured conductivity about the trendline probably results from changes in the equilibrium chemical speciation on the sample surface due to small variations in laboratory lighting and humidity conditions.

Room-temperature Hall effect measurements (Figure 7.22) show that most of the difference in electrical conductivity between the two series is due to changes in carrier mobility. The largest absolute improvement in mobility upon *in situ* irradiation occurs for the samples deposited at 376 °C, which is also the temperature at which the sample with the record-setting mobility value of $44.3\,\mathrm{cm^2\,V^{-1}\,s^{-1}}$ was prepared.

In order to show the statistical significance of these changes, 18 separate films were deposited at this temperature using *in situ* irradiation. The average mobility of this set was $37.4\,\mathrm{cm^2\,V^{-1}\,s^{-1}}$ with a standard deviation of $3.5\,\mathrm{cm^2\,V^{-1}\,s^{-1}}$. Conveniently, the dark analogues of this set were used for the reproducibility study in Section 4.5.1 and had an average mobility of $20.1 \pm 4.1\,\mathrm{cm^2\,V^{-1}\,s^{-1}}$. Thus, for this set of deposition conditions *in situ* irradiation leads to a $4.2\,\sigma$ increase in mobility which is extremely unlikely to be due to chance.

In situ irradiation has also made the Hall effect measurements of samples deposited at 376 °C and above indistinguishable. However, there remains a drop in mobility as the deposition temperature decreases below this temperature, indicating that one or more factors that limit carrier mobility in low T_{dep} ZnO samples are not being resolved by *in situ* irradiation. It should be noted that the approximate doubling of the carrier concentration in the samples deposited at 334 °C due to *in situ* irradiation compensates for their lower mobility, and is what allows these samples to have a higher average conductivity than those prepared at higher T_{dep}.

A Grain Boundary Mechanism

Variable temperature carrier mobility data for representative ZnO samples deposited at 376 °C with and without *in situ* irradiation were analyzed using Equation 7.3. On this basis, it was determined that the increase in mobility was due to a UV-induced reduction of the grain boundary potential barrier from 27.0 meV to 19.5 meV. The fit did not show significant differences in effective grain size between the two samples, suggesting little change in gross morphology with irradiation.

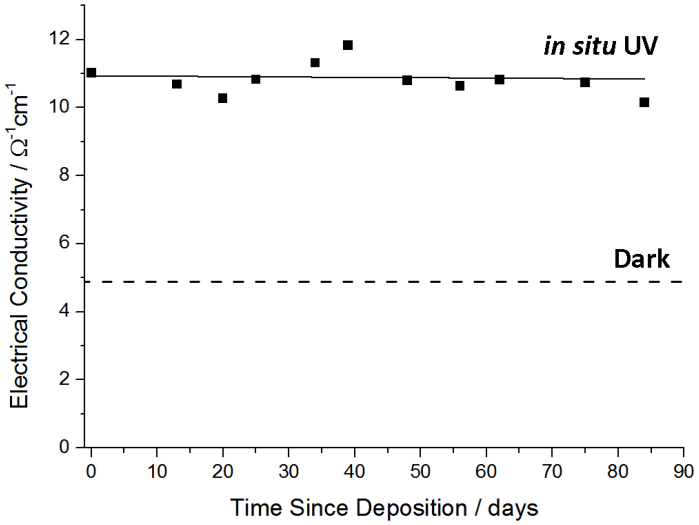

Figure 7.21: Electrical conductivity of a ZnO thin film deposited at ∼376 °C with *in situ* UV irradiation as a function of time since initial exposure to air. The solid line is a best-fit linear trendline to the conductivity data, while the dashed line represents the average conductivity of ZnO samples deposited under the same conditions but in the dark. Figure reproduced from Vai, *et al.*[40]

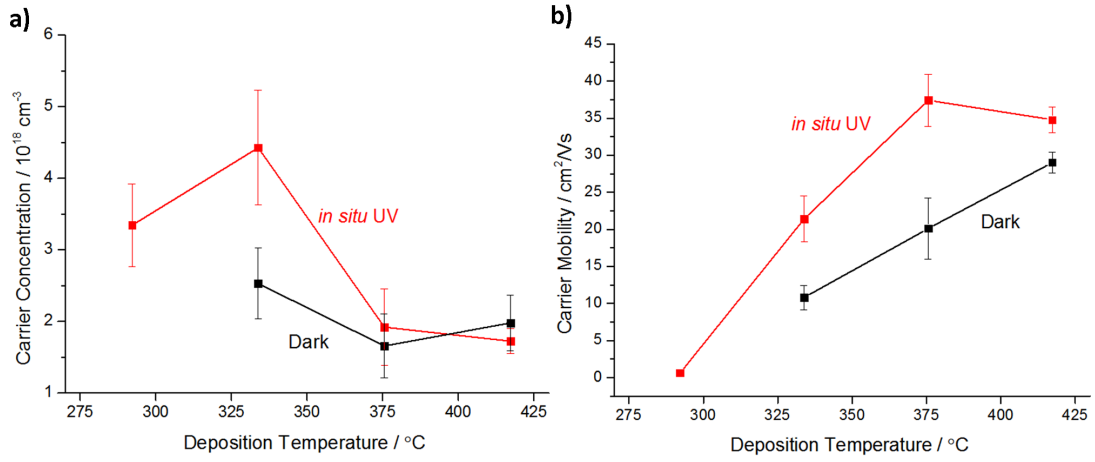

Figure 7.22: Room-temperature Hall effect a) carrier mobility and b) carrier concentration of ZnO thin films deposited by spray pyrolysis using *in situ* UV irradiation (red) and in the dark (black). Data from samples that were too resistive for reliable Hall measurements are not shown. Figure adapted from Vai, *et al.*[40]

Likewise, neither X-ray diffraction nor SEM show any appreciable structural differences between samples deposited at the same temperature in the dark and with *in situ* irradiation. Furthermore, the handheld blacklight used is of very modest power; a flux of $<150\,\mu\mathrm{W\,cm^{-2}}$ is enough to fully saturate the *in situ* UV effect. The light source does not produce photons with energies anywhere close to the binding energy of the bulk ZnO lattice ($\sim$7.4 eV).[62] It has also been noted that an improvement in conductivity still occurs even if a sample is exposed to UV light *in situ* only at temperatures below 100 °C. It is extremely unlikely that any substantial structural changes are being caused by such mild irradiation or at these low temperatures.

Together, these observations strongly suggest that the new permanent photoconductive effect is, like classic persistent photoconductivity, related to the surface and grain boundary chemistry of the ZnO thin films.

These two effects do appear to happen in addition to, and not in place of, each other. This is emphasized by the fact that appreciable *ex situ* photoconductivity is still observed for samples that had been irradiated *in situ*, especially those prepared at lower T_{dep}. To better separate the two effects, Hall effect measurements were taken immediately after *ex situ* irradiation so that the effect of loosely-bound grain boundary acceptors is suppressed (Figure 7.23). These results show that *in situ* irradiation increases the carrier concentration of the underlying material for all deposition temperatures, while mobility is most greatly enhanced in samples prepared at moderate deposition temperatures.

Additional insight into the mechanism of *in situ* irradiation can be obtained by comparing the oxygen 1s XPS data collected from the surface of samples deposited at 292 °C with and without this treatment. Figure 7.24 shows that the most significant difference between the two spectra is the size of the highest binding energy component relative to that of the lowest energy component. Under the interpretation scheme discussed in Section 7.2.3, these components are assigned as weakly adsorbed oxygen-containing species and lattice oxide, respectively.

The UV photons used to treat the samples should have sufficient energy to cause the formation of *surface* oxygen vacancies (Section 7.2.5), which are likely to be at least metastable in the oxygen-deficient conditions of the nitrogen-purged deposition chamber.[56] Both theory and experiment have been used to suggest that chemisorbed

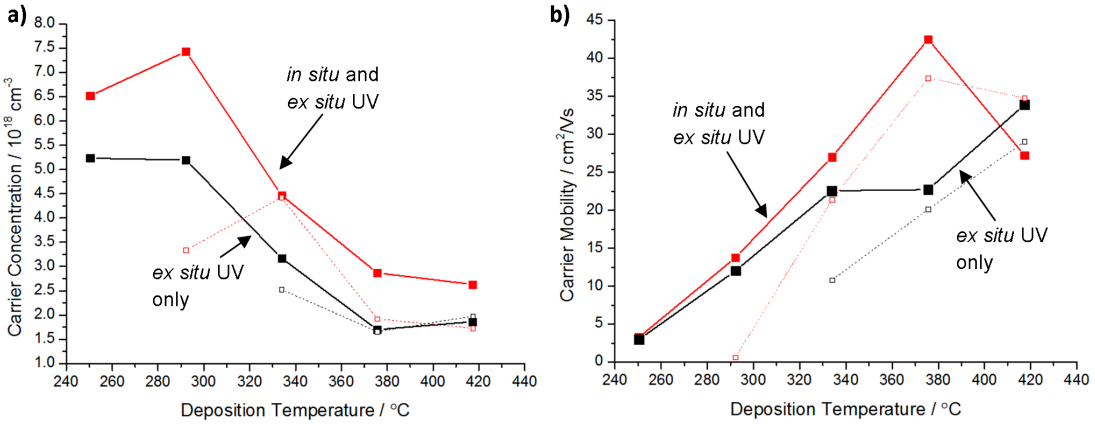

Figure 7.23: Hall effect a) carrier mobility and b) carrier concentration of ZnO thin films deposited by spray pyrolysis using *in situ* UV irradiation (red) and in the dark (black) and measured immediately following an additional *ex situ* UV treatment. Data for these samples without the latter *ex situ* treatment is shown in smaller symbols for comparison. Figure adapted from Vai, *et al.*[40]

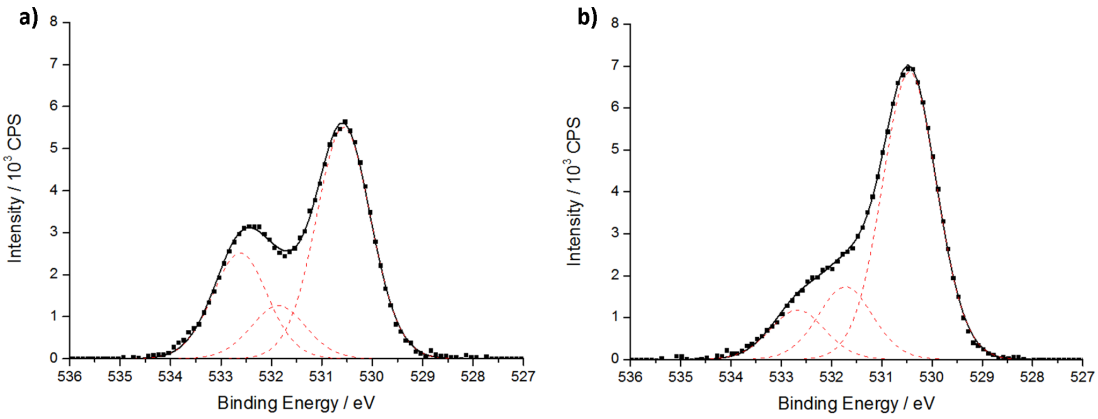

Figure 7.24: Experimental oxygen 1s XPS spectra (black squares) for ZnO thin film samples deposited by spray pyrolysis (a) in the dark, and (b) with *in situ* UV irradiation. A fitted spectrum (solid black line) composed of three components (dashed red lines) is shown for each dataset. Figure adapted from Vai, *et al.*[40]

species will bind to a ZnO surface differently depending on the local defect environment.[42,63,64] For example, it is plausible that a species such as hydroxide might adsorb weakly in a locally stoichiometric area of the ZnO surface (which contributes to the high binding energy XPS signal), or more strongly in the event that the hydroxide oxygen is filling a surface oxygen vacancy (which would contribute to the lowest energy XPS signal). In the former case, the adsorbed acceptor leads to the net trapping of an electron, whereas in the latter case, the acceptor is merely compensating a UV-induced donor, and the net change to carrier concentration is zero.

While an atom-level mechanism for the effect of *in situ* irradiation cannot be determined using these data alone, all available evidence is consistent with the hypothesis that the benefits of this treatment derive from its ability to make the oxide surface that underlies any adsorbed species more oxygen-deficient and donor-rich. This then partially compensates for the effect of chemisorbed acceptors that form upon exposure of the sample to air.

Once the sample is exposed to air, the further formation of oxygen vacancies is inhibited by the high chemical potential of oxygen in this environment. Under these conditions, only loosely bound species can be desorbed by irradiation, which leads to the temporary conductivity changes of persistent photoconductivity but not the permanent changes of *in situ* irradiation.

The possible filling of surface oxygen vacancies by oxygen or moisture from the air can also explain why the effects of this *in situ* treatment apparently cannot be achieved by *returning* a sample to an inert environment before irradiation. It has been reported that the stability of a well-ordered oxide surface increases the formation energy of defects.[65] Thus, as surface vacancies are filled during the initial exposure to air, the non-stoichiometry of the surface is decreased and further vacancy formation is made more unfavorable.

Scope and Applicability

In summary, *in situ* irradiation with UV significantly increases the maximum carrier mobility, and hence conductivity, that can be achieved in ZnO films made by spray pyrolysis. At the same time, it significantly reduces the temperature required to produce the most conductive undoped ZnO films from ∼417 to ∼334 °C. Effectively,

this treatment appears to alleviate most of the conductivity-limiting mechanisms that differentiate higher T_{dep} ZnO samples. While this treatment clearly also benefits lower temperature samples, the effect of *in situ* irradiation in this regime is overwhelmed by the large influence of the air-derived acceptor states associated with persistent photoconductivity, and by the conductivity limits imposed by the low-temperature morphology of spray-pyrolyzed ZnO films.

Unfortunately, this effect has so far only been observed in undoped ZnO samples. In particular, attempts to replicate this phenomenon with doped ZnO samples were not successful. This may be due to the already diminished effect of grain boundary barriers that comes with a raised Fermi level (Section 7.3.2). Alternatively, it may also be true that the presence of dopant changes defect formation energies in ZnO and reduces the feasibility of these UV-induced changes.

Despite this narrow scope, *in situ* irradiation could be of significant practical interest to the preparation of semiconducting channel layers for transparent thin-film transistors (TFTs) of the type found in active-matrix electronic displays, which specifically require thin film materials with high mobility and low carrier concentrations.[66] Thus, if an appropriate technique can be found to suppress the carrier concentration of these ZnO samples, the high mobility values and moderate spray pyrolysis deposition temperatures made possible by *in situ* irradiation may well be useful in such applications.

As for transparent conductor applications, it must be admitted that the phenomenon as currently described is not likely to be of significant practical use, simply because doping is generally required to obtain useful levels of conductivity. For this reason, the greatest significance of this result is that it re-emphasizes the usefulness of working from an understanding of the mechanisms that limit electronic conduction in TCOs. It also shows that there are still new and undiscovered ways to modify the grain boundary behavior of ZnO, even using something as mundane and well-studied as the exposure of a TCO film to UV light.

7.3.2 Doping

As has been mentioned at several points in this chapter, it is not the absolute height of the grain boundary barrier (*i.e.*, the E_{B} term in Figure 7.4) that determines its

effect. Instead, it is the position of the top of the barrier relative to the Fermi energy E_F within the grains (namely, Φ in Equation 7.1 and Figure 7.5) that is most directly relevant to how much a barrier limits conductivity. The higher E_F is relative to the top of the barrier, the less thermal excitation is needed for electrons to gain enough energy to go over it. At some point, when E_F becomes significantly higher than the top of the barrier, most electrons participating in conduction will have sufficient energy to cross over the barrier even in their ground state, and conductivity will no longer be thermally activated near room temperature.

Seto also points out that an increasing free electron density within the grains will narrow the width of the barrier, since a lower volume of the bulk must be depleted of electrons to fill a given number of acceptor states at the grain boundary. This narrowing reduces the dipole moment associated with the boundary and also reduces the absolute height of the barrier.[19]

It is undoubtedly true that increasing the carrier concentration of a TCO by doping reduces the effect of grain boundary potential barriers. This can be seen by examining changes in carrier mobility with sample temperature for a series of ZnO samples prepared with different carrier concentrations (Figure 7.25a). The mobility of the undoped sample with the lowest carrier concentration of $0.13 \times 10^{19}\,\mathrm{cm}^{-3}$ shows the strongest thermal activation, increasing by more than $20\,\mathrm{cm}^2\,\mathrm{V}^{-1}\,\mathrm{s}^{-1}$ as the sample temperature increases from about 90 to 350 K. This magnitude of this change decreases monotonically as the carrier concentration is raised. When n is $34 \times 10^{19}\,\mathrm{cm}^{-3}$ — approaching the maximum carrier concentration that we have been able to achieve in ZnO prepared by spray pyrolysis — the increase in carrier mobility over this temperature range of 0.1–0.2 $\mathrm{cm}^2\,\mathrm{V}^{-1}\,\mathrm{s}^{-1}$ is barely visible on the scale of the figure and amidst the noise in the signal.

Nevertheless, the fact that the ZnO films all display a thermally activated carrier mobility shows that inter-grain barriers still have a noticeable effect on electronic transport, even for samples with rather high carrier concentrations.

When similar data are examined for polycrystalline In_2O_3-based samples (Figure 7.25b), rather different behavior is observed. Even the lowest carrier concentration, nominally undoped In_2O_3 sample only shows a thermally activated mobility at lower temperatures. By the time room temperature is reached, the effects of grain bound-

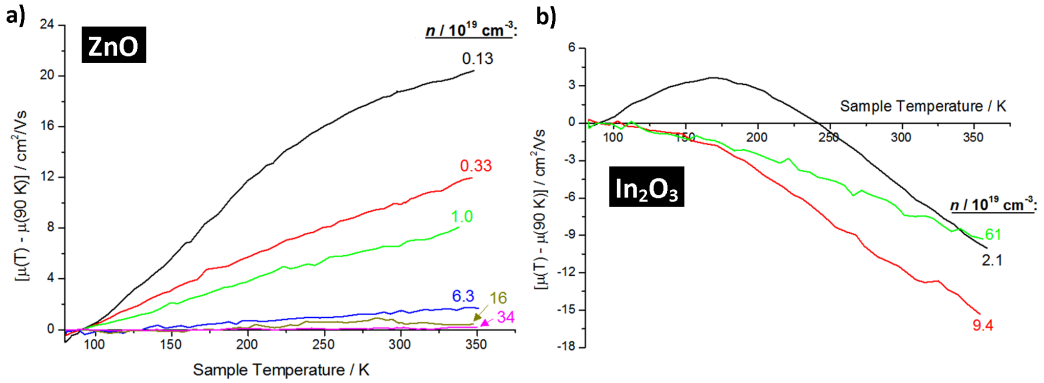

Figure 7.25: Change in Hall effect carrier mobility value relative to the value at ∼90 K as a function of temperature over a range of 80 to 350 K. Each dataset for a) ZnO and b) In_2O_3 is accompanied by an annotation indicating the room temperature carrier concentration of the corresponding sample in units of 10^{19} cm^{-3}. The black curves in each figure are data for nominally undoped samples.

ary scattering have become small in comparison to carrier-phonon scattering, which causes the observed decrease in mobility with increasing temperature. For the doped samples, mobility is no longer thermally activated at all in this temperature range; the only conclusion that can be drawn is that these samples are in the limit where the Fermi level is much more than k_BT greater than the top of the barriers (that is, $-\Phi \ll k_BT$), and that these barriers now represent an insignificant hindrance to conduction.

The simplest explanation for these observations is that the absolute height of the barriers in these In_2O_3-based materials is lower, as has been previously demonstrated (Figure 7.1). Thus, a higher Fermi level is required to achieve the same value of Φ in ZnO than is required for In_2O_3. And of course, Chapter 6 has already shown that there are limits to the extent that carrier concentration can be increased in a given material by doping.

Here too, the phenomenon of photoconductivity is useful for reinforcing the important differences between indium-doped ZnO (IZO) and tin-doped indium oxide (ITO). Table 7.2 shows the relative UV photoresponse for samples of these two materials deposited at different temperatures. Recalling that a large change in conductivity upon irradiation indicates that species adsorbed at grain boundaries have a large effect on conduction (Section 7.2.4), it can be seen that doping has markedly reduced the magnitude of these effects in both materials compared to the corresponding undoped

Table 7.2: Relative photoconductive response for ITO and IZO samples deposited at 292 and 376 °C. $G_{t=0}$ is the conductance when the 8 W, 365 nm UV blacklight is switched on and $G_{\max}$ is the maximum conductance achieved during irradiation.

	T_{dep} / °C	$G_{t=0}$ / Ω^{-1}	$G_{\max}$ / Ω^{-1}	Relative Photoresponse
5 at% ITO	376	3.717×10^{-2}	3.722×10^{-2}	1.116×10^{-3}
	292	2.557×10^{-2}	2.599×10^{-2}	1.664×10^{-2}
5 at% IZO	376	8.882×10^{-3}	9.005×10^{-3}	1.387×10^{-2}
	292	5.843×10^{-6}	1.879×10^{-4}	31.17

cases (Figure 7.16). Further, doping has narrowed the gap somewhat between ZnO and In_2O_3.

However, even at these relatively high doping levels, the effect of air-derived grain boundary barriers is still significantly larger for ZnO-based materials than In_2O_3-based materials deposited at the same temperature. The dramatic effect that deposition temperature has on ZnO films can also still be seen, whereas the temperature-dependence is much smaller for In_2O_3.

In short, the effect of grain boundary barriers in ZnO thin films prepared by spray pyrolysis can be substantially reduced by doping, but not entirely eliminated. When it comes to spray pyrolysis, even at the highest achievable carrier concentrations, the performance of doped ZnO samples, especially those made at lower deposition temperatures, cannot be made to match that of ITO. As has also been implied by these results on photoconductivity, even with the effect of grain boundary barriers suppressed as much as possible by doping and irradiation, there must remain important underlying differences in these spray pyrolyzed films that contribute to their differences in performance.

And so, in order to examine these differences and further improve the performance of ZnO-based materials, it is necessary to expand the scope of the discussion to include deposition techniques besides spray pyrolysis.

7.3.3 Deposition Technique

In the previous two sections, it has been shown that one of the main difficulties with ZnO is the sensitivity of its electrical conductivity to environmental conditions like light, air, and humidity, especially in contrast to the relative stability displayed by In_2O_3-based thin films. As useful and powerful a deposition technique as spray pyrolysis is in some situations, it does use aqueous solutions in order to prepare TCO thin films, meaning that the deposition process itself must also be considered as a source of potential contamination. For this reason, vacuum-based deposition techniques like pulsed-laser deposition or magnetron sputtering capable of more rigorous compositional control of deposited films do have important advantages when it comes to the preparation of ZnO thin films.

Furthermore, evidence shows that the morphology of the ZnO samples can have a substantive effect on grain boundaries and thus film performance. Within the deposition technique of spray pyrolysis, it has been challenging to find ways to systematically modify film morphology independent of T_{dep}.[iv] This also is a reason to compare spray pyrolyzed samples with those prepared using other techniques that lead to different morphologies.

With the caveat that the vacuum-deposition processes described in this section have not yet been not fully optimized, and that sample properties will almost certainly vary as process parameters are changed, this comparison is meant to show just how important the choice of technique is to the preparation of highly conducting ZnO-based thin films.

For instance, using silicon-doped zinc oxide (SiZO) as an example, Figure 7.26 shows dramatic changes in the surface morphology of thin films that arise with the use of different deposition techniques. The sample prepared using spray pyrolysis (Figure 7.26a) is characterized by large, clearly-defined grains whose growth is made possible by solvent- and thermally-assisted mass transport during the deposition process. It may be speculated that the relatively loose packing of the grains and the well-defined gaps between them contribute to the particular susceptibility of these films to grain boundary effects. It is also plausible that the as deposited grain surfaces in such

[iv] Section 4.3.3 presents some concepts that would be of interest for future work in this area.

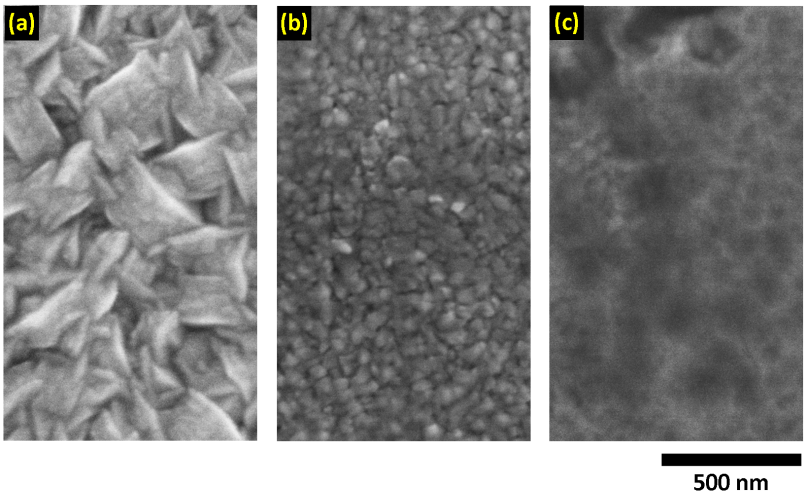

Figure 7.26: Scanning electron micrographs showing the surface morphology of silicon-doped ZnO thin films prepared using (a) spray pyrolysis, (b) RF magnetron sputtering, and (c) pulsed-laser deposition.

Table 7.3: Approximate properties of "best" silicon-doped ZnO films prepared by our group using various thin film deposition techniques. The best results reported by Minami, *et al.*[67] are also shown for comparison purposes.

Deposition Technique	Doping Level[a]/ at%	n / 10^{20} cm^{-3}	μ / cm^2 V^{-1} s^{-1}	σ / Ω/cm	Thick. / nm	R_s / $\Omega/\square$
Spray Pyrolysis	4	4.0	9.6	610	520	32
RF Sputtering (Present Work)	2	1.4	9.3	210	360	132
RF Sputtering (Minami, *et al.*)	2	12	13.7	2630	445	8.5
Pulsed-laser Deposition	2	5.9	27.2	2580	275	14

[a] All quoted doping levels are nominal values.

samples have some quantity of adsorbed water simply because the deposition process involves the use of aqueous solutions.

The sputtered film shown in Figure 7.26b consists of much smaller and more densely-packed, but still well-defined grains. Given this, it should come as no surprise that appreciable grain boundary barriers, persistent photoconductivity, and a thermally-activated conductivity are still observed in these samples. The sputtered film has a marginally more thermally activated mobility than seen in the best spray pyrolysis samples (Figure 7.27). However, this, as well as the slightly lower absolute mobility, may be because of the as yet unoptimized sputtering process used here (Table 7.3).

Reports from the literature do show that it is possible (though certainly not easy) to design sputtering processes for producing aluminum- or silicon-doped ZnO samples with electrical conductivities approaching $10^4\ \Omega^{-1}\,\mathrm{cm}^{-1}$ and thus comparable to commercial ITO.[67,68] However, while the solvent-free deposition conditions of such sputtered films allow the possibility of higher starting conductivities than spray pyrolysis, even these films generally still do not possess long-term environmental stability when confronted with the heat and humidity levels typically used in the lifespan testing of consumer electronics.[69–72] As it stands, it is probably safe to suggest that the denser microstructure that may result from a carefully engineered sputtering process can retard, but not entirely stop the penetration of air-derived grain boundary acceptors into the sample, which eventually leads to degradation of the optoelectronic properties of the film.

Only by using pulsed-laser deposition have we been able to achieve a dense, relatively smooth morphology without grain boundaries that are clearly visible using SEM (Figure 7.26c). This more limited access of potential contaminants to the interior of the film allows for excellent, ITO-competitive electrical conductivity (Table 7.3). At the same time, Figure 7.27 shows the decreasing mobility with increasing temperature that would be expected for metallic samples where grain boundary barriers are insignificant, and where within-grain processes like phonon-carrier scattering dominate. Furthermore, these samples have had stable electrical properties even after several years of storage under ambient conditions.

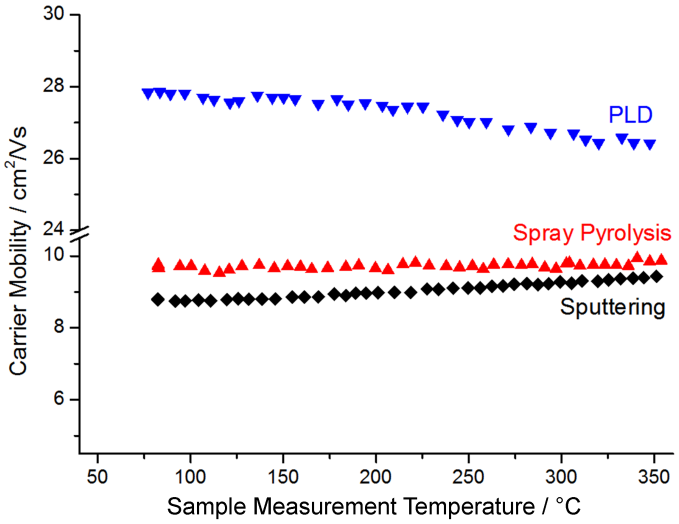

Figure 7.27: Hall effect carrier mobility as a function of sample temperature for nominally 2 at% silicon-doped ZnO prepared by PLD (blue) and RF magnetron sputtering (black), and a film prepared by spray pyrolysis using a 4 at% silicon-doped precursor solution (red).

This difference in the long-term stability of electrical performance in thin films prepared using various deposition techniques can clearly be seen in the results of an accelerated aging test, where the resistance of samples is monitored over several hundred hours of storage at 60 °C and 100 % relative humidity (Figure 7.28).

For both SiZO and ZnO, pulsed-laser deposition produces samples with the lowest conductivity fade rate. Indeed, for SiZO produced by PLD, where the benefits of doping and deposition technique come together, the fade rate is zero to within experimental error. This test also shows well the particularly large environmental sensitivity of undoped ZnO prepared by spray pyrolysis, which has a fade rate of nearly $10\,\%\,\mathrm{hr}^{-1}$. However, even for this highly sensitive material, the dense morphology created by PLD is capable of slowing down conductivity fade by nearly a factor of 80. Interestingly, the SiZO and IZO samples show very similar degradation behavior, despite being quite different in sample thickness.

Finally, as a brief aside, it is worth noting again the impressive insensitivity of indium oxide to environmental degradation, even when it is prepared using spray pyrolysis. Its fade rate is several times better than that of doped ZnO prepared by the same method, and comparable to doped ZnO prepared using sputtering. While there was no opportunity to test this directly, it is fairly safe to assume that a sputtered

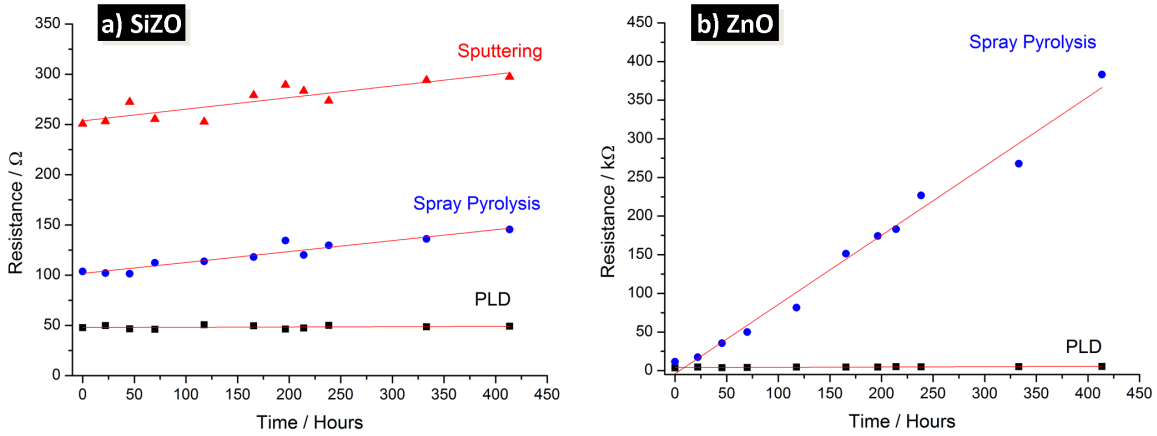

Material	Deposition Technique	Thickness / nm	σ Fade Rate / % hr^{-1}
SiZO	Spray Pyrolysis	610	$1.0 \pm 0.1 \times 10^{-1}$
	Sputtering	400	$4.6 \pm 0.9 \times 10^{-2}$
	PLD	275	$5.6 \pm 8.5 \times 10^{-3}$
Undoped ZnO	Spray Pyrolysis	410	7.7 ± 0.3
	PLD	275	$1.1 \pm 0.2 \times 10^{-1}$
5 at% IZO	Spray Pyrolysis	340	$1.0 \pm 0.1 \times 10^{-1}$
5 at% ITO	Spray Pyrolysis	230	$3.9 \pm 2.0 \times 10^{-2}$

Figure 7.28: Electrical resistance of a) silicon-doped ZnO and b) undoped ZnO samples prepared using various deposition techniques as a function of exposure time to moisture-saturated, 60 °C air. The conductivity fade rates determined from the linear fits to these data (red lines) are shown in the table below, along with equivalent data for 5 at% tin-doped indium oxide (ITO) and 5 at% indium-doped zinc oxide (IZO) prepared by spray pyrolysis for comparison.

ITO film would have even better environmental stability.

From these results, there is little doubt that the choice of deposition technique profoundly affects the properties of TCO films. Using our spray pyrolysis process, we are able to consistently match the best reliable literature reports on ZnO samples made using solution-based techniques. However, despite the extensive (and perhaps nearly exhaustive) optimization efforts that have taken place, there is currently no clear path for how to use spray pyrolysis to match the best vacuum-deposited ZnO. At this time, it would seem that clean, solvent-free deposition conditions are needed to produce ITO-competitive doped zinc oxide, while the highly dense morphology that can be obtained using PLD is needed to protect the samples from degradation over time.

Of course, if it is possible to produce highly and stably conductive doped ZnO thin films using PLD, then a logical follow-up question is how such results might be achieved using a more scalable and industrially-relevant deposition technique. A handful of modifications to standard deposition approaches have been proposed with the aim of achieving this goal. For instance, there are reports that the stability of doped ZnO produced by magnetron sputtering can be improved by the use of specific dopants.[73] Another example is research on high-power, pulsed sputtering equipment that can be used to produce denser, more PLD-like film morphologies.[74]

However, in lieu of examining such specific process modifications, the final section of this chapter will instead discuss a more general approach that might be considered a logical consequence of all the ideas that have been introduced and discussed so far.

7.3.4 Encapsulation

A common thread throughout this chapter has been that the most significant grain boundary-related performance problems in ZnO can ultimately be traced back to the exposure of samples to air and moisture. Whether this happens primarily during deposition (as with spray pyrolysis) or over time after deposition (as with sputtered films), the adsorption of oxygen or water onto ZnO surfaces forms electron traps and grain boundary potential barriers that inhibit electronic transport.

Since the interaction of ZnO's chemically active surface with the environment is the root cause of the problem, perhaps the most conceptually straightforward solution

would be to encapsulate or passivate the ZnO surfaces to prevent these interactions from happening. The problem of protecting air or moisture-sensitive materials is not an uncommon one, and this approach has already been applied to ZnO itself in a range of non-TCO applications. Reported techniques include the use of polymers,[75,76] inorganic oxides or nitrides,[77–79] and thiocyanates as barrier materials.[80]

One of the appealing features of encapsulation is that it can be used in combination with many of the ideas already discussed. For instance, Section 7.2 showed that ZnO samples prepared at low deposition temperatures compatible with some polymer substrates can be made almost as conductive as higher T_{dep} samples by exposure to UV light. Both our work and that of other groups have demonstrated that light-induced improvements can be made permanent if the sample is maintained under an inert atmosphere. So far, protection of persistent photoconductivity has generally been achieved using vacuum chambers or purged containers, but it is certainly plausible that an appropriate encapsulation design might achieve similar results.

Likewise, highly conductive and ITO-competitive doped ZnO thin films have been prepared by scalable sputtering techniques, only to degrade upon exposure to heat and humidity. Encapsulation again would be a very sensible solution to consider for protecting the acceptable intrinsic performance of ZnO thin films in the face of negative environmental influences.

It is worth highlighting that the idea of encapsulating undoped ZnO films has already been reduced to practice. Illiberi, *et al.* have reported that using atomic layer deposition to apply a 75 nm conformal coating of aluminum oxide on top of a ZnO film acts as an effective moisture barrier and substantially reduces the increase in resistivity experienced by the TCO upon exposure to damp heat.[81] The same type of barrier layer is also reportedly able to make the effects of persistent photoconductivity effectively stable over at least 1000 hours.[82] There are also reports of technical developments that may make encapsulation by atomic layer deposition a scalable industrial process, and at least one patent on this general topic.[83,84]

It should also be noted that full encapsulation of device stacks is precisely the approach currently used to protect the sensitive active layers in devices such as organic light-emitting diodes or liquid crystal displays. Techniques for producing alternating thin layers of polymers and inorganic materials as flexible barriers with extraordinarily

low moisture and oxygen transmission rates are well known and in commercial use today.[85,86] Certainly, with such devices that must be encapsulated anyway, protection of a ZnO-based electrode may even be achievable at no extra cost.

Although an assessment of various barrier schemes is beyond the work that has been done for this thesis, the evidence would seem to suggest that protection of a highly-conductive ZnO-based transparent electrode is entirely plausible and feasible with existing technology. And if the choice is ultimately made to pursue such a route, then it would be an excellent example of applying mechanistic knowledge to circumvent performance limitations in a material.

7.4 Conclusion: Revising the Central Question

A careful investigation has shown that one of the most significant challenges facing ZnO-based TCOs is that they are far more sensitive to the grain boundary effects that inhibit electronic conduction than In_2O_3-based materials. Using a range of characterization techniques, including a new type of grain-boundary probe based on photoconductivity, it has been shown specifically that adsorption of oxygen-containing chemical species derived from the air is primarily to blame for these effects in ZnO.

Taking advantage of this insight, a clear chain of evidence has been laid out to show that producing ZnO-based transparent electrodes with optoelectronic performance approaching that of ITO should be technically possible. And in this sense, at least, grain boundary problems could be classed as practical, and not fundamental, limitations.

However, the intrinsic sensitivity of ZnO to grain boundary effects means that these solutions will necessarily be exacting and complicated, requiring very careful management of deposition conditions, sample composition, film morphology, exposures to light and air, and likely in the end, some type of encapsulation. What is more, it cannot be denied that all of this complexity would only be to approach (and perhaps not even to match) ITO, which can simply be deposited by spray pyrolysis at moderate temperatures, very easy by comparison. Surely, there is a point when fighting against the fundamental characteristics of ZnO will become so difficult as to make these "practical" solutions not very practical at all. And the ground truth of ZnO's lack of market penetration so far speaks volumes about this final point.

And so, we will now take the question originally posed at the beginning of this thesis to the next and final chapter in a somewhat revised and more focused form: *Can we reasonably expect that more research effort will make these fundamental differences between ZnO and In_2O_3 easier to bridge?*

7.5 Experimental

7.5.1 Photoconductivity Measurements

Hall Effect after *ex situ* Irradiation

Pieces of film were attached to a Hall effect sample holder as for a standard Hall effect measurement (Section 3.5.1). The samples were then irradiated with an 8 W UVP EL Series blacklight with emission centered at 365 nm (3.4 eV) from a distance of ∼10 cm until a multimeter showed the sample was at constant resistance (after about 5 minutes). The samples were then quickly loaded into the Hall effect apparatus, with measurements being taken within 15 seconds of the sample being removed from the light.

Time Dependence of Photoconductivity

An approximately 2 mm × 7 mm piece of sample previously stored in the dark for several days was wired for a four-point resistance measurement using soldered indium contacts.

Where the effect of various atmospheres was of interest, a custom circuit board providing connection points for a two-point resistance measurement, and that could be enclosed in a plastic chamber with Luer ports for the supply of various flowing gases was used. Dry house nitrogen, nitrogen passed through a water bubbler, and compressed air were flowed through the chamber at a rate of approximately 15 L min^{-1} during measurements.

In all cases, an Agilent 34401A 6.5 digit multimeter was used to measure and record the resistance of the samples before, during, and after irradiation with the handheld blacklight.

7.5.2 *in situ* Irradiation during Spray Pyrolysis

The base spray pyrolysis procedure is as described in Section 4.7.2.

For depositions carried out in the dark, precautions were taken to exclude ambient light from the spray chamber. For depositions incorporating *in situ* irradiation, a modified chamber front with a 65 mm diameter fused quartz window was used to permit the UV irradiation of the film inside the chamber. The 365 nm EL Series handheld blacklight was used to illuminate the film from an angle of approximately 45 degrees and at a distance of approximately 10 cm, resulting in a total radiative flux of $\sim$140 μW cm^{-2}. For standard depositions, the light source was on from the end of solution spraying until just before the chamber was opened to ambient atmosphere at a temperature of less than 50 °C.

7.5.3 Vacuum-based Thin Film Deposition Techniques

RF Magnetron Sputtering

A Lesker PVD75 sputtering unit located at the London Center for Nanotechnology (University College London) was used to deposit thin films by RF magnetron sputtering using a 3-inch diameter $(ZnO)_{0.98}(SiO_2)_{0.02}$ ceramic target prepared by slipcasting. The substrate was a cleaned piece of borosilicate glass heated from behind using halogen lamps to a temperature of approximately 305 ± 5 °C. The substrate was rotated at 10 rpm during deposition in order to improve film uniformity.

Sputter deposition was carried out at a pressure of 3 mTorr in pure argon gas, with an RF power density of approximately 3.2 W/cm^2.

Pulsed-Laser Deposition

Deposition targets were prepared by the pressing and sintering of phase homogeneous silicon-doped ZnO powders synthesized using a sol-gel technique.

Then using equipment in the Department of Metallurgy and Materials at the University of Birmingham, thin films were deposited by pulsed-laser deposition onto borosilicate glass substrates held at a temperature of 350 °C. The substrates had been sequentially cleaned with ethanol and acetone in an ultrasonic bath and then blown dry with purified nitrogen gas before use. Target ablation was performed using a KrF excimer laser (Lambda Physik LPX 300, $\lambda = 248$ nm). For a thin film deposition, 5000

pulses with energy of 250–400 mJ per pulse were used at a frequency of 10 Hz. The deposition chamber was initially evacuated to 5×10^{-6} Torr and then backfilled with pure oxygen gas to a dynamic partial pressure of 2 mTorr which was held constant during deposition.

7.5.4 Preparation of Tin-doped In_2O_3 Thin Films

The same basic preparation was used as for undoped In_2O_3 (Section 4.7.1). For tin doping, a portion of the indium chloride was replaced with anhydrous tin(II) chloride (Sigma-Aldrich, ≥99.99 % trace metals basis) to achieve the desired doping level, while maintaining the same total nominal metal concentration (0.025 M in the final spraying solution after addition of alcohol).

7.5.5 Accelerated Aging Test

A wide-necked HDPE bottle was filled to a depth of 1 cm with deionized water, closed with an air-tight cap, and placed inside a drying oven to create an environmental chamber. A thermocouple was used to determine power settings for the heating elements that would create a stable temperature of 60 °C inside the chamber with the doors closed.

Small pieces of thin film samples (approx. 3 mm × 10 mm) to be tested were attached to a larger glass slide with epoxy in a grid pattern for easy and consistent handling. Each sample was marked on the back with permanent marker to indicate two fixed points across which resistance measurements were made using handheld multimeter probes. Samples were stored in the moisture-saturated headspace of the bottle and taken out at regular intervals for resistance measurements. Because perfectly consistent contacts were not possible with this method, each reported data point is the average of at least four measurements. The standard deviation among a set of measurements was always less than 10 % of value and more typically around 5 %. All data points were equally weighted in the linear fits used to determine conductivity fade rate.

7.5.6 Acknowledgments

A number of the samples referenced in this chapter were prepared by other members of my research group, however, all analysis and discussion of these is my own work. I am grateful to Dr. Nazanin Rashidi for the preparation of some spray pyrolyzed SiZO samples, Dr. Vladimir Kuznetsov for providing SiZO samples prepared using PLD, and Mr. Yiwen Fang for some of the undoped In_2O_3 samples.

I also thank Dr. Dosten Baluch for preparing the SiZO sputtering target and Mr. Steve Etienne for training and guidance with the cleanroom and sputtering equipment at the London Centre for Nanotechnology.

References

[1] Kim, H.; Horwitz, J. S.; Qadri, S. B.; Chrisey, D. B. *Thin Solid Films* **2002**, *420-421*, 107–111.

[2] Kaidashev, E. M.; Lorenz, M.; von Wenckstern, H.; Rahm, A.; Semmelhack, H. C.; Han, K. H.; Benndorf, G.; Bundesmann, C.; Hochmuth, H.; Grundmann, M. *Appl. Phys. Lett.* **2003**, *82*, 3901–3903.

[3] Ohta, H.; Orita, M.; Hirano, M.; Tanji, H.; Kawazoe, H.; Hosono, H. *Appl. Phys. Lett.* **2000**, *76*, 2740–2742.

[4] Opel, M.; Geprägs, S.; Althammer, M.; Brenninger, T.; Gross, R. *J. Phys. D* **2014**, *47*, 034002.

[5] Xiao, Y.; Gao, F.; Dong, G.; Guo, T.; Liu, Q.; Ye, D.; Diao, X. *Thin Solid Films* **2014**, *556*, 155–159.

[6] Shapira, Y.; McQuistan, R. B.; Lichtman, D. *Phys. Rev. B* **1977**, *15*, 2163–2169.

[7] Lichtman, D.; Shapira, Y. *CRC Crit. Rev. Solid State Mater. Sci.* **1978**, *8*, 93–118.

[8] Gupta, T. K. *J. Am. Ceram. Soc.* **1990**, *73*, 1817–1840.

[9] Walsh, A. *Appl. Phys. Lett.* **2011**, *98*, 261910.

[10] King, P. D. C.; Veal, T. D.; Payne, D. J.; Bourlange, A.; Egdell, R. G.; McConville, C. F. *Phys. Rev. Lett.* **2008**, *101*, 116808.

[11] Heiland, G.; Kunstmann, P. *Surf. Sci.* **1969**, *13*, 72–84.

[12] Litton, C. W.; Reynolds, D. C.; Collins, T. C. *Zinc Oxide Materials for Electronic and Optoelectronic Device Applications*; Capper, P.; Kasap, S.; Willoughby, A., Eds.; Materials for Electronic and Optoelectronic Applications; Wiley: Chichester, UK, 2011.

[13] Russell, J. D.; Halls, D. C.; Leach, C. *J. Mater. Sci. Lett.* **1995**, *14*, 676–678.

[14] Tarng, M. L. *J. Appl. Phys.* **1978**, *49*, 4069–4076.

[15] Prins, M. W. J.; Grosse-Holz, K. O.; Cillessen, J. F. M.; Feiner, L. F. *J. Appl. Phys.* **1998**, *83*, 888–893.

[16] Jerhot, J.; Šnejdar, V. *Thin Solid Films* **1978**, *52*, 379–395.

[17] Sze, S. M.; Ng, K. K. *Physics of Semiconductor Devices*; Wiley-Blackwell: New York, NY, 2006.

[18] Petritz, R. L. *Phys. Rev.* **1956**, *104*, 1508–1516.

[19] Seto, J. Y. W. *J. Appl. Phys.* **1975**, *46*, 5247–5254.

[20] Saxena, A. K.; Gurumurthy, K. S. *J. Phys. Chem. Solids* **1982**, *43*, 801–808.

[21] Chiou, B.-S.; Lin, S.-T.; Duh, J.-G.; Chang, P.-H. *J. Am. Ceram. Soc.* **1989**, *72*, 1967–1975.

[22] Benamar, E.; Rami, M.; Messaoudi, C.; Sayah, D.; Ennaoui, A. *Sol. Energy Mater. Sol. Cells* **1999**, *56*, 125–139.

[23] Vai, A. T.; Rashidi, N.; Fang, Y.; Kuznetsov, V. L.; Edwards, P. P. *J. Phys.: Condens. Matter* **2015**, (In Press).

[24] Ellmer, K. *J. Phys. D: Appl. Phys.* **2001**, *34*, 3097–3108.

[25] Preissler, N.; Bierwagen, O.; Ramu, A. T.; Speck, J. S. *Phys. Rev. B* **2013**, *88*, 085305.

[26] Morkoç, H.; Özgür, Ü. *Zinc Oxide: Fundamentals, Materials and Device Technology*; Wiley-VCH: Weinheim, Germany, 2009.

[27] Park, S.-M.; Ikegami, T.; Ebihara, K. *Thin Solid Films* **2006**, *513*, 90–94.

[28] Lee, S.; Bang, S.; Park, J.; Park, S.; Jeong, W.; Jeon, H. *Phys. Status Solidi A* **2010**, *207*, 1845–1849.

[29] Coppa, B. J.; Davis, R. F.; Nemanich, R. J. *Appl. Phys. Lett.* **2003**, *82*, 400–402.

[30] Fan, J. C. C.; Goodenough, J. B. *J. Appl. Phys.* **1977**, *48*, 3524–3531.

[31] Pugel, D. E.; Vispute, R. D.; Hullavarad, S. S.; Venkatesan, T.; Varughese, B. *Appl. Surf. Sci.* **2008**, *254*, 2220–2223.

[32] Barr, T. L. *J. Phys. Chem.* **1978**, *82*, 1801–1810.

[33] Major, S.; Kumar, S.; Bhatnagar, M.; Chopra, K. L. *Appl. Phys. Lett.* **1986**, *49*, 394–396.

[34] Au, C. T.; Hirsch, W.; Hirschwald, W. *Surf. Sci.* **1988**, *199*, 507–517.

[35] Au, C. T.; Hirsch, W.; Hirschwald, W. *Surf. Sci.* **1988**, *197*, 391–401.

[36] Mollwo, E.; Breckendridge, R. G.; Russell, B. R.; Hahn, E. E., Eds.; Photoconductivity Conference (Atlantic City); John Wiley and Sons: New York, NY, 1954; p 509.

[37] Melnick, D. A. *J. Chem. Phys.* **1957**, *26*, 1136–1146.

[38] Heiland, G. *J. Phys. Chem. Solids* **1961**, *22*, 227–234.

[39] Bao, J.; Shalish, I.; Su, Z.; Gurwitz, R.; Capasso, F.; Wang, X.; Ren, Z. *Nanoscale Res. Lett.* **2011**, *6*, 404–410.

[40] Vai, A. T.; Kuznetsov, V. L.; Dilworth, J. R.; Edwards, P. P. *J. Mater. Chem. C* **2014**, *2*, 9643–9652.

[41] Medved, D. B. *J. Chem. Phys.* **1958**, *28*, 870–873.

[42] Barry, T. I.; Stone, F. S. *P. Roy. Soc. Lond. A Mat.* **1960**, *255*, 124–144.

[43] Li, Y.; Valle, F. D.; Simonnet, M.; Yamada, I.; Delaunay, J.-J. *Appl. Phys. Lett.* **2009**, *94*, 023110.

[44] Morishige, K.; Kittaka, S.; Moriyasu, T.; Morimoto, T. *J. Chem. Soc., Faraday Trans. 1* **1980**, *76*, 738–745.

[45] Sawada, Y.; Seki, S.; Sano, M.; Miyabayashi, N.; Ninomiya, K.; Iwasawa, A.;

Tsugoshi, T.; Ozao, R.; Nishimoto, Y. *J. Therm. Anal. Calorim.* **2004**, *77*, 751–757.

[46] Barraud, L.; Holman, Z. C.; Badel, N.; Reiss, P.; Descoeudres, A.; Battaglia, C.; Wolf, S. D.; Ballif, C. *Sol. Energy Mater. Sol. Cells* **2013**, *115*, 151–156.

[47] Koida, T.; Shibata, H.; Kondo, M.; Tsutsumi, K.; Sakaguchi, A.; Suzuki, M.; Fujiwara, H. *J. Appl. Phys.* **2012**, *111*, 063721.

[48] Wöll, C. *Prog. Surf. Sci.* **2007**, *82*, 55–120.

[49] Dutta, G.; Sokol, A. A.; Catlow, C. R. A.; Keal, T. W.; Sherwood, P. *ChemPhysChem* **2012**, *13*, 3453–3456.

[50] Strunk, J.; Kähler, K.; Xia, X.; Muhler, M. *Surf. Sci.* **2009**, *603*, 1776–1783.

[51] Korotcenkov, G.; Ivanov, M.; Blinov, I.; Stetter, J. R. *Thin Solid Films* **2007**, *515*, 3987–3996.

[52] Gurlo, A.; Ivanovskaya, M.; Bârsan, N.; Schweizer-Berberich, M.; Weimar, U.; Göpel, W.; Diéguez, A. *Sens. Actuators, B* **1997**, *44*, 327–333.

[53] Yamaura, H.; Jinkawa, T.; Tamaki, J.; Moriya, K.; Miura, N.; Yamazoe, N. *Sens. Actuators, B* **1996**, *36*, 325–332.

[54] Bender, M.; Katsarakis, N.; Gagaoudakis, E.; Hourdakis, E.; Douloufakis, E.; Cimalla, V.; Kiriakidis, G. *J. Appl. Phys.* **2001**, *90*, 5382–5387.

[55] Xirouchaki, C.; Kiriakidis, G.; Pedersen, T. F.; Fritzsche, H. *J. Appl. Phys.* **1996**, *79*, 9349–9352.

[56] Meyer, B. *Phys. Rev. B* **2004**, *69*, 045416.

[57] Armentrout, P. B.; Halle, L. F.; Beauchamp, J. L. *J. Am. Chem. Soc.* **1981**, *103*, 6501–6502.

[58] Xu, C.; Tamaki, J.; Miura, N.; Yamazoe, N. *Sens. Actuators, B* **1991**, *3*, 147–155.

[59] Kaneti, Y. V.; Zhang, Z.; Yue, J.; Zakaria, Q. M. D.; Chen, C.; Jiang, X.; Yu, A. *Phys. Chem. Chem. Phys.* **2014**, *16*, 11471–11480.

[60] Ataev, B. M.; Bagamadova, A. M.; Mamedov, V. V.; Makhmudov, S. S.; Omaev, A. K. *Crystallogr. Rep.* **2002**, *47*, 1049–1050.

[61] Leach, C.; Freer, R.; Azough, F.; Ling, Z. *Interface Sci.* **2000**, *8*, 141–146.

[62] Gurwitz, R.; Cohen, R.; Shalish, I. *J. Appl. Phys.* **2014**, *115*, 033701.

[63] Li, H.; Schirra, L. K.; Shim, J.; Cheun, H.; Kippelen, B.; Monti, O. L. A.; Bredas, J.-L. *Chem. Mater.* **2012**, *24*, 3044–3055.

[64] Peers, A. M. *J. Phys. Chem.* **1963**, *67*, 2228–2229.

[65] Studenikin, S. A.; Golego, N.; Cocivera, M. *J. Appl. Phys.* **1998**, *84*, 2287–2294.

[66] Edwards, P. P.; Porch, A.; Jones, M. O.; Morgan, D. V.; Perks, R. M. *Dalton Trans.* **2004**, *19*, 2995–3002.

[67] Minami, T.; Sato, H.; Nanto, H.; Takata, S. *Jpn. J. Appl. Phys.* **1986**, *25*, L776–L779.

[68] Kim, K. H.; Park, K. C.; Ma, D. Y. *J. Appl. Phys.* **1997**, *81*, 7764–7772.

[69] Minami, T.; Miyata, T.; Ohtani, Y.; Kuboi, T. *Phys. Status Solidi RRL* **2007**, *1*, R31–R33.

[70] Theelen, M.; Dasgupta, S.; Vroon, Z.; Kniknie, B.; Barreau, N.; van Berkum, J.; Zeman, M. *Thin Solid Films* **2014**, *565*, 149–154.

[71] Lin, W.; Ma, R. X.; Xue, J.; Kang, B. *Sol. Energy Mater. Sol. Cells* **2007**, *91*, 1902–1905.

[72] Greiner, D.; Gledhill, S. E.; Köble, C.; Krammer, J.; Klenk, R. *Thin Solid Films* **2011**, *520*, 1285–1290.

[73] Minami, T. *Thin Solid Films* **2008**, *516*, 5822–5828.

[74] Aiempanakit, M.; Helmersson, U.; Aijaz, A.; Larsson, P.; Magnusson, R.; Jensen, J.; Kubart, T. *Surf. Coat. Technol.* **2011**, *205*, 4828–4831.

[75] Qin, L.; Shing, C.; Sawyer, S.; Dutta, P. S. *Opt. Mater.* **2011**, *33*, 359–362.

[76] Xu, X.; Feng, L.; He, S.; Jin, Y.; Guo, X. *IEEE Electron Device Lett.* **2012**, *33*, 1420–1422.

[77] Schmidt, O.; Geis, A.; Kiesel, P.; van de Walle, C. G.; Johnson, N. M.; Bakin, A.; Waag, A.; Dhler, G. H. *Superlattices Microstruct.* **2006**, *39*, 8–16.

[78] Hong, D.; Wager, J. F. *J. Vac. Sci. Technol., B* **2005**, *23*, L25–L27.

[79] Seo, H.-S.; Bae, J.-U.; Kim, D.-H.; Park, Y.; Kim, C.-D.; Kang, I. B.; Chung, I.-J.; Choi, J.-H.; Myoung, J.-M. *Electrochem. Solid-State Lett.* **2009**, *12*, H348–H351.

[80] Jalali, N.; Briscoe, J.; Woolliams, P.; Stewart, M.; Weaver, P. M.; Cain, M.; Dunn, S. *J. Phys.: Conf. Ser.* **2013**, *476*, 012131.

[81] Illiberi, A.; Scherpenborg, R.; Theelen, M.; Poodt, P.; Roozeboom, F. *J. Vac. Sci. Technol., A* **2013**, *31*, 061504.

[82] Illiberi, A.; Grob, F.; Frijters, C.; Poodt, P.; Ramachandra, R.; Winands, H.; Simor, M.; Bolt, P. J. *Prog. Photovoltaics* **2013**, *21*, 1559–1566.

[83] Poodt, P.; Cameron, D. C.; Dickey, E.; George, S. M.; Kuznetsov, V.; Parsons, G. N.; Roozeboom, F.; Sundaram, G.; Vermeer, A. *J. Vac. Sci. Technol., A* **2012**, *30*, 010802.

[84] Makoto, K.; Tomoshige, T.; Kazuaki, M.; *Transparent Conductor; Patent JPH085352*; 1996.

[85] Park, J. S.; Chae, H.; Chung, H. K.; Lee, S. I. *Semicond. Sci. Technol.* **2011**, *26*, 034001.

[86] Yang, Y. Q.; Duan, Y. *J. Phys. Chem. C* **2014**, *118*, 18783–18787.

Chapter 8

Conclusions: Where Next for ZnO?

8.1 Current Status of ZnO-based TCOs

It is worth repeating a simple fact first stated in the introduction: At the time of this writing, ITO coatings continue to hold more than 90 % of the total market for transparent conducting thin films. And while some prognosticators have projected a modest decline in ITO market share over the coming years, this is almost entirely due to the emergence of non-oxide technologies like metal nanowires, and not due to any predicted breakthroughs on the part of low cost, ZnO-based TCOs.[1] This inability of ZnO thin films to gain substantial acceptance in real applications, despite compelling advantages in raw material cost, is ultimately due to their inferior environmental stability and electrical performance when compared to analogous films based on In_2O_3.

These downsides are present in ZnO samples prepared using any highly-scalable deposition technique, but are magnified when spray pyrolysis and other solution-based methods are used. Nevertheless, spray pyrolysis has been demonstrated as a simple and versatile technique capable of producing TCO thin films with sufficient reliability and reproducibility to elucidate a wide range of physical phenomena. Furthermore, the fact that ZnO-specific limits are highlighted in samples prepared using this deposition technique has been extremely useful for the task of identifying and understanding the mechanisms that limit performance.

This work clearly shows that the differences between ZnO and In_2O_3 are not just due to specific choices made during the course of film deposition, but that they occur because of fundamental differences in the chemistry of these two oxides. Even

though carefully-prepared single crystals of ZnO and In_2O_3 exhibit remarkably similar electronic transport properties, differences begin to emerge almost as soon as any departure is made from this ideal situation. Some of these are observable even when just considering the single crystal-like domains inside the grains of a polycrystalline sample.

As with all semiconductors, there are thermodynamic constraints in TCOs that limit the extent to which impurity doping can be used to raise the carrier concentration, and hence, the electrical conductivity. A detailed local structure characterization of the changing disposition of dopant in indium-doped ZnO has shown several ways in which both host and impurity structures govern doping efficiency; these in turn lead to potentially important differences between the doping behavior of ZnO- and In_2O_3-based materials. There are also process specific limits to doping, such as those relating to the preparation of solution-processed silicon-doped ZnO films. These have been overcome using knowledge obtained from studying the chemistry of various precursor species in solution.

Grain boundaries can have a dramatic and sometimes overwhelming effect on the electrical properties of TCO films that are polycrystalline, which almost every sample with practical commercial relevance will be. While it is apparent that the same types of grain boundary processes can happen in both ZnO and In_2O_3, it is also obvious that they generally occur to a much greater extent in ZnO. In fact, such effects appear to explain both the lower maximum performance of ZnO-based samples prepared by spray pyrolysis, as well as the much stronger sensitivity of ZnO to both deposition and environmental conditions.

However, even taking into account all of these intrinsic difficulties with ZnO, it is not technically impossible to make ZnO-based thin films with performance approaching, or even matching that of ITO. In fact, by carefully considering all of the relevant limits and applying insights obtained from these studies, a line of reasoning showing just how such might be done has been presented. Thus, the appropriate question now is not one of whether it *can* be done, but rather whether it is *worth it* to do so.

Many of the requirements for high conductivity in polycrystalline TCO thin films, including high carrier concentration, high mobility, and minimal grain boundary potential barriers are almost trivially achieved in In_2O_3-based materials, even those

prepared using spray pyrolysis. On the other hand, obtaining ZnO with these properties will require careful consideration in almost every aspect, including the use of specialized vacuum deposition methods, the selection of appropriate dopant(s), the possible use of non-equilibrium doping, and the design of an encapsulation method to protect deposited films from the deleterious effects of environmental exposure.

Ultimately, whether ZnO-based TCOs will ever be substantially adopted depends on the trade-off between the much lower starting material costs for ZnO and the requirements for a much more complicated and exacting deposition process. As technology progresses, this is a question that must be repeatedly decided by the manufacturers and end users for each of the many possible applications of transparent conductors. Given what this thesis has shown about the challenges facing ZnO as a TCO material, it is not that surprising that, to date, most commercial assessments of this balance have come down squarely against the use of ZnO.

8.2 Opportunities for Future Research

If future research and development work on ZnO-based TCOs aims to make these materials more attractive, then it is this cost-complexity calculation that must be shifted significantly by some means. The track record of empirical optimization for doing this has thus far been rather poor, perhaps because the difficulties of ZnO have meant that most work has started too far from any "optimum" that might exist. Instead, now that the critical features that differentiate ZnO from In_2O_3 have been laid out with some specificity here, the goal of future work should be to see what new methods can be found to affect these known differences in a positive way.

The prospective ZnO researcher should not harbor any illusions that such a task will be easy or straightforward. ZnO is far enough away from competing successfully with In_2O_3 in most cases that further incremental improvements will not likely be sufficient. Something resembling a revolutionary step-change will be needed. And as has been seen here, In_2O_3 has demonstrated a truly remarkable (and thus far, a nearly unique) suitability as a TCO material, which sets a very high bar to overcome.

Ergo, our approach here will be to highlight some currently understudied areas of the deposition and materials chemistry of TCOs that would be of substantial use in gaining an improved fundamental understanding of these systems. There is of course

no guarantee that any of these will lead to near-term practical applications. However, we do believe these are the types of research ideas most likely to generate new and useful approaches for improving TCO performance, if any of these exist to be found. Some of these concepts may not only apply to ZnO-based systems, but may even be of use for better understanding and improving ITO.

The Chemistry of Precursor Solutions

There can be very little doubt that solution chemistry plays an essential role in the deposition of oxide films by spray pyrolysis. For example, data have been shown suggesting that metal hydroxides are likely to be the "active" species that lead directly to the formation of metal oxides when water is present. If this hypothesis can be confirmed, it would provide a theoretical method for predicting whether a given precursor solution will lead to the successful or efficient deposition of an oxide, and thus be of use in the design of new precursor systems for specific desired materials.

It has also been shown that the morphology of a film can have a substantial influence on the size of grain boundary potential barriers due to adsorbed species. At the same time, preliminary work has clearly shown that the choice of counter anion can substantially alter the morphology of a film deposited by spray pyrolysis. However, many aspects of how the presence of ligand can direct the growth of a TCO crystallite remain to be elucidated.

Finally, there is a question of whether the aqueous nature of most spray pyrolysis solvents is itself a contributing factor to the lower performance of sprayed ZnO thin films. There do exist a number of reports on the thermal spray deposition of TCO thin films from non-aqueous systems.[2,3] The mechanism(s) of precursor decomposition under such conditions remain an open question, but this could represent an approach for avoiding one of the built-in sources of contamination that reduces the performance of solution-processed ZnO films.

A Closer Look at Impurity Doping

The study of impurity doping in TCOs now needs to extend far beyond the basic idea of differences in valence leading to the generation of electrons. Combining local structural techniques like X-ray absorption spectroscopy and EXAFS with classic electrical characterization should make it possible to determine if any particular dopants

stand out as having a particularly high substitutional solubility or a low tendency to form electrically inactive defects. The application of computational methods could also provide very useful complementary information, such as trends in the formation energies of various types of defects.

Our work has shown that doping can retard the conductivity decay of ZnO films exposed to high temperature and humidity environments. It has also been suggested that different dopants might alter the formation energy of intrinsic defects in TCO materials and thus change how quickly they degrade over time.[4] This is a possibility that has received relatively little attention; given the importance of such phenomena with ZnO, accelerated aging tests should certainly form part of the standard characterization package when the many different examples of doped ZnO are under study.

With regards to co-doping, the idea that simultaneously using two or more dopants might achieve results that cannot be achieved using just one has been repeatedly advanced, whether the goal has been the preparation of metastable *p*-type ZnO,[5,6] or to produce more conductive *n*-type samples.[7,8] The ease with which precursor solutions can be mixed in arbitrary ratios gives spray pyrolysis immense potential for use in combinatorial screens that can be used to detect combinations of dopants and conditions that might not be readily predictable from first principles. Work to develop chemically compatible libraries of dopant precursors for a given host precursor would go a long way towards allowing this type of rapid materials discovery to occur.

Engineering Aspects and Precursor Decomposition

One of the major limitations of spray pyrolysis is the high temperature needed to decompose most precursors to oxide. This substantially limits the range of substrates that can be used with this deposition technique.

Traditionally, spray pyrolysis apparatuses have been designed using hotplates that heat substrates from the back. It may be useful to also consider apparatus designs which selectively heat at the top of the substrate where decomposition occurs. This could reduce the maximum temperature to which the bulk of the substrate is subjected. Concepts which may be of interest range from the combination of top-down halogen lamp heating with substrate cooling to using microwaves to selectively heat precursor solutions and not the substrate.

Other members of our group have used the example of zinc to show that there is significant scope for modifying the decomposition temperature of organometallic complexes using coordination chemistry.[9] Applying such ideas to In_2O_3 films may be particularly useful since the need to decompose the current halide precursors appears to define the lowest temperatures at which highly conductive films of this material can be prepared using spray pyrolysis.

Identifying the Right Applications

Given the great diversity of TCO applications, more thought should be given to identifying those which favor the distinguishing features of ZnO. For instance, even if the direct current conductivity of spray pyrolyzed ZnO films is limited by grain boundary effects, these films could still be very attractive in applications where grain interior properties are dominant. One example is in heat-reflective glass coatings, where the IR reflectivity does not depend on inter-grain carrier transport, but mostly on the carrier concentration and mobility within the grains. In order to expand its penetration, it would be sensible to focus on such applications where ZnO's key attributes of low cost, easy scalability, and excellent transparency are the most important.

Finding and Exceeding "Fundamental" Boundaries

Section 5.4 showed an example of how frequency-dependent transport measurements can be used to probe the interiors of grains within doped polycrystalline films. This is a potential tool that could be applied to more clearly reveal fundamental processes like the metal-to-non-metal transition in polycrystalline samples. It would also be very interesting to examine transport properties in various TCOs as a function of factors like stoichiometry, doping, or strain, which can often be varied more readily in polycrystalline or powdered samples than in true single crystals. This could reveal differences in the way electronic transport in these materials respond to disorder.

Finally, we note that some doped indium oxide samples, including the bromide-doped In_2O_3 that we have reported here and the molybdenum-doped In_2O_3 reported by Bhachu, *et al.*, have surprisingly good electrical performance, reaching and even exceeding the limits to carrier mobility that would be implied by ionized impurity scattering in single crystals.[10] Clearly, the ideas that appropriate structural distortions (including amorphousness) or the use of anion doping might represent potential

workarounds to the intrinsic performance limitations in such materials are very interesting. They are certainly worthy of being the targets of a more focused investigation, particularly into how electronic conduction here would be different than in more traditional cases. And of course, such work would also help to show if these concepts can be applied in practical contexts.

8.3 Concluding Remarks

The Transparent Conducting Oxides are indeed a remarkable class of materials. This is true from the very basic physics of how their unusual combination of properties arises, all the way to the very pragmatic task of trying to preserve these useful properties even when the materials are deposited as thin films on a very large, industrial scale.

In many respects, it is commercial interest and the array of both realized and developing applications that has driven the tremendous volume of research on TCOs. Yet, the very desire to meet these commercial interests has led us back to the importance of studying the fundamental processes of electronic transport, carrier generation, and surface chemistry in these oxides. We have tried to highlight the basic mechanisms that limit the performance of practical TCOs, and especially those acting with particular vigor in the case of zinc oxide, on the thesis that these must first be known before they can be overcome.

By this point, nobody should enter this field with the presumption that further work in this area will inevitably lead to the low-cost, earth-abundant, high-performance, best-of-all-worlds TCO that has long been sought. Yet, surely, we have also demonstrated that further study of this wonderful example of optoelectronic materials holds the promise of rich scientific rewards, with many open questions to be answered, and many new ideas to be tried.

And so, to conclude, we sincerely hope that the ideas and results presented here will be applied, not *only* with the goal of producing better technological materials, but also in a continuing exploration of the fascinating chemistry and physics embodied in these transparent conducting oxides.

References

[1] Ghaffarzadeh, K.; Das, R.; *Transparent Conductive Films (TCF) 2014-2024: Forecasts, Technologies, and Players*; Tech. Rep.; IdTechEx; 2014.

[2] Lokhande, B. J.; Patil, P. S.; Uplane, M. D. *Mater. Chem. Phys.* **2004**, *84*, 238–242.

[3] Natarajan, C.; Fukunaga, N.; Nogami, G. *Thin Solid Films* **1998**, *322*, 6–8.

[4] Minami, T.; Miyata, T.; Ohtani, Y.; Kuboi, T. *Phys. Status Solidi RRL* **2007**, *1*, R31–R33.

[5] Yamamoto, T. *Phys. Status Solidi A* **2002**, *193*, 423–433.

[6] Joseph, M.; Tabata, H.; Kawai, T. *Jpn. J. Appl. Phys.* **1999**, *38*, L1205–L1207.

[7] Kim, J.-P.; Bae, J.-S.; Hong, T.-E.; Won, M.-S.; Yoon, J.-H.; Lee, B.-S.; Lee, H.-J. *Thin Solid Films* **2010**, *518*, 6179–6183.

[8] Nomoto, J.; Miyata, T.; Minami, T. *J. Vac. Sci. Technol., A* **2009**, *27*, 1001–1005.

[9] Rashidi, N.; *Cation and Anion Doping of ZnO Thin Films by Spray Pyrolysis*; Ph.D. thesis; University of Oxford; Oxford, UK; 2014.

[10] Bhachu, D. S.; Scanlon, D. O.; Sankar, G.; Veal, T. D.; Egdell, R. G.; Cibin, G.; Dent, A. J.; Knapp, C. E.; Carmalt, C. J.; Parkin, I. P. *Chem. Mater.* **2015**, *27*, 2788–2796.

Appendices

Appendix A

Swanepoel Calculator

The following is code written in Python 2.7 to provide a graphical interface for the semi-automatic determination of average visible transparency and film thickness from UV-Vis-NIR transmission data using the envelope method of Swanepoel (Section 3.2.1). This program was used routinely throughout this thesis work.

The code accepts .csv input files with an arbitrary number of header rows. The row immediately before the data begins must be of the format: "nm, [Units]", where [Units] is '%T' or 'A' (no quotations) depending on whether the data is in units of percent transmittance or absorbance. This is the default .csv output format for Perkin Elmer spectrophotometers.

```
from Tkinter import Tk
## Swanepoel Calculator
## Made by Alex T. Vai, Edwards Group
## Last Update: 2 April 2015

from tkFileDialog import askopenfilename, asksaveasfilename
from numpy import std, mean, array, linspace
import pylab
import scipy.interpolate as sp
import scipy.stats as stats

def main():

    print "What file do you want to process?"
    Tk().withdraw()
    datafile = askopenfilename()

    wave, trans = readFile(datafile)

    ## "Define T_max Curve"
    maxX, maxY = curveDefine(wave, trans, "Define T_max Curve")
    maxFunc, limMaxX = splineInterpolate(maxX, maxY)
```

```
## "Define T_min Curve"
minX, minY = curveDefine(wave, trans, "Define T_min Curve")
minFunc, limMinX = splineInterpolate(minX, minY)

## "Select Extrema"
exX, exY = curveDefine(wave, trans, "Select at least 2 Extrema (
    Recommend omitting outermost)")

## Do some math based on Swanepoel, R., J Phys E: Sci Instrum, 16,
    (1983)
ior = swanepoel_ior(minFunc, maxFunc, exX, 1.51)#Assumes IoR for
    glass = 1.51 and constant
thicknesses = swanepoel_thickness(exX, ior)

##### Outputs Block
print "\nResults for '" + str(datafile.split("/")[-1]) + "':\n"
print "Peaks:", exX
print ior
print "Average Index of Refraction:", round(mean(ior),2), "+/-",
    round(std(ior),2) #This is the average of IOR for the points
    chosen for the calculation.
print "Thicknesses:", thicknesses
print "Average Thickness:", round(mean(thicknesses),0), "+/-", round
    (std(thicknesses),0)
print "Average Transmittance (400-750 nm):", averageTrans(maxFunc,
    minFunc)

if len(exX) > 2:
    ## Kludgy way of  returning 0 if stage 2 is pointless...i.e. if
        not >2 extrema
    thick2, m = stage2(exX, ior)
else:
    thick2 = 0
    m = 0
    print "WARNING: Stage 2 not applicable with 2 or fewer peaks"

##Graphical Method here to get standard error (uses reflection order
     calculated in Stage 2)
n_over_lambda = []

for item in range(len(exX)):
    n_over_lambda.append(ior[item]/exX[item])

ls = range(len(exX)-1,-1,-1)

for i in range(len(ls)):
    ls[i] = ls[i]/2.0
slope, intercept, r, prob2, see = stats.linregress(n_over_lambda, ls
    )
########## End Graphical Method

print "Thickness - Stage 2:\n    " + str(round(mean(thick2),0)) + "
    nm +/- " + str(round(std(thick2),0)) + " nm"
```

```
    print "Order of highest wavelength peak:", m
    print "Graphical Method r^2:", r**2

    ### A bunch of gymanstics to plot visual check
    new_Max_x = linspace(limMaxX.min(), limMaxX.max(), 200)
    new_Min_x = linspace(limMinX.min(), limMinX.max(), 200)

    smoothMinY = minFunc(new_Min_x)
    smoothMaxY = maxFunc(new_Max_x)

    pylab.figure(1)
    pylab.plot(wave,trans)
    pylab.axis([300,wave[0],0,1])
    pylab.title("Results Graph: " + str(datafile.split("/")[-1]))
    pylab.text(500, .2, \
               "\n\nAv. Index of Refraction:\n    " + str(round(mean(ior
                   ),2)) + " +/- " + str(round(std(ior),2)) +\
               "\n\nAv. Vis Transmittance (400-750 nm):\n    " + str(
                   round(averageTrans(maxFunc, minFunc)*100,0)) + "%" +\
               "\n\nStage 2 Thickness:\n    " + str(round(slope/2,0)) +
                   " nm +/- " + str(round(see/2,0)) + " nm")
    pylab.plot(new_Min_x, smoothMinY, color = "r")
    pylab.plot(new_Max_x, smoothMaxY, color = "r")
    pylab.plot(exX, exY, "k*")

##    This code turns on verification plot of graphical method
    pylab.figure(2)
    pylab.plot(n_over_lambda, ls)
    pylab.title("slope:" + str(round(slope,1)) + "   intercept: " + str
       (round(intercept,1)) + "   nr^2: " + str(round(r**2,3)))


    pylab.draw()

    pylab.show()
    ### Plotting Gymnastics End

def stage2(exX2, ior2):
    """This function takes the picked peaks, the calculated index of
       Refraction at those peaks, and
    attempt to guess the order of refraction, m, that is responsible for
        said peaks.
    The order of refraction is chosen so that the resulting variance in
       the calculated thicknesses is minimized.
    This function should be used if there are 3 or more peaks"""

    bestdev = 1000000000.0
    revexX2 = exX2[::-1]
    revior2 = ior2[::-1]

    for m in
       [.5,1,1.5,2,2.5,3,3.5,4,4.5,5,5.5,6,6.5,7,7.5,8,8.5,9,9.5,10]:
        thick2 = []
```

```
        for peak in range(len(revexX2)):
            thick2.append((m+peak*.5)*revexX2[peak]/2.0/revior2[peak])

        if std(thick2) < bestdev:
            bestdev = std(thick2)
            bestThick = thick2
            bestM = m

    ### For now, not recalculating ior based on new estimated
        thicknesses

    return bestThick, bestM

def averageTrans(maxFunc, minFunc):
    """This function calcualtes the average transmittance in the visible
        range
    assumed to be 450-750 nm, which is the geometric mean of the T_max
        and T_min
    functions."""
    x = linspace(400,750) #assuming visible wavelengths are 400 to 750
        nm

    #Note that the interference free transmission is the geometric mean
        of T_max and T_min
    intFreeTrans = []

    for val in range(400,750):
        intFreeTrans.append((maxFunc(val)*minFunc(val))**(0.5))

    return round(mean(intFreeTrans),2)


def swanepoel_thickness(exX, ior):
    """Takes list of wavelengths and index of refractions at those
        wavelengths
    appropriately ordered, and returns the thickness based on swanepoel
        method of
    each succesive pair of extrema"""

    thickness = []

    for i in range(0,len(exX)-1):
        thickness.append(0.25*exX[i]*exX[i+1]/(exX[i+1]*ior[i] - exX[i]*
            ior[i+1]))
        #1/4 because using successive extrema, not successive maxima

    return thickness
def swanepoel_ior(minFunc, maxFunc, exX, n_sub):
    s = []
    ior = []
    for i in range(len(exX)):
        s.append((2*n_sub*(maxFunc(exX[i])-minFunc(exX[i]))/(maxFunc(exX
            [i])*minFunc(exX[i])))+((n_sub**2+1)/2))
```

```
    for i in range(len(s)):
        ior.append((s[i]+((s[i]**2)-(n_sub**2))**(.5))**(.5))

    return ior

def readFile(filepath):
    """Opens and orgaznizes data from the .csv export file from the
       PerkinElmer UV-Vis-NIR
    Input: filepath is the path of the file to be processed.
    Output: Two Lists, one of wavelengths, one of transmittance values.
    Function return wavelengths in increasing order, assuming normal
       output in decreasing order"""
    myfile = open(filepath, 'r')

    wavelengths = []
    transmittances = []
    cycleFlag = 0 #0 if first line (which is instruement data), 1 for
       headers, 2 else

    for line in myfile:
        if cycleFlag == 0:
            if line.split(",")[0].strip() == "nm": ##Checks to see if we
                are past any header lines that may be present above the
                column titles
                dataType = line.split(",")[1].strip() ##Records if the
                    data is absorbance or transmittance
                cycleFlag = 1
        else:
            parsedLine = line.split(",")
            wavelengths.append(float(parsedLine[0].strip()))
            if dataType == "A":
                transmittances.append(abs2trans(float(parsedLine[1].
                    strip()))) #This version assumes that the export
                    file has values in A
            if dataType == "%T":
                transmittances.append(float(parsedLine[1].strip())/100)
                   #This version assumes that the export file has
                    values in %T

    wavelengths.reverse()
    transmittances.reverse()

    return wavelengths, transmittances

def abs2trans(number):
    """Converts an absorbance to a transmittance. Both inputs and
       outputs are floats"""
    return 10**(-number)

def curveDefine(rawx, rawy, prompt):
    """Function plots raw data and asks user to select points along
       curve
    These selected points are stored as two lists of equal lengths, the
```

```
        first of x values
    the second of correspondingly indexed y values
    prompt is a string that displays on the graph telling the user what
        to do"""
    pylab.plot(rawx,rawy)
    pylab.title(prompt)
    pylab.axis([300,rawx[0],0,1])###############
    points = pylab.ginput(0,0)
    pylab.close()


    newx = []
    newy = []

    for i in range(len(points)):
        newx.append(points[i][0])
        newy.append(points[i][1])

    return newx, newy

def splineInterpolate(userx, usery):
    """Function takes a series of x,y datapoints and returns a cubic
        spline interpolation
    input should take the form of two lists of equal lengths, the first
        of x values
    the second of correspondingly indexed y values"""

    x = array(userx)
    y = array(usery)

    new_length = 2000 #This is the resolution of the interpolation.
        Pretty arbitrary, but it works.
    new_x = linspace(x.min(), x.max(), new_length)
    f = sp.UnivariateSpline(x,y, w=None, bbox=[None, None], k=2, s=0)
    return f, x

main()
```

Appendix B

Derivation of Electric Susceptibilities

A Lorentz oscillator follows the following equation of motion

$$\frac{d^2\vec{r}}{dt^2} + \Gamma\frac{d\vec{r}}{dt} + \omega_0^2\vec{r} = \frac{e}{m^*}\left[\vec{E}(\vec{r},t) + (\frac{d\vec{r}}{dt} \times \vec{B}(\vec{r},t))\right] , \tag{B.1}$$

where $\vec{r}$ is the displacement vector, Γ is the damping constant, and ω_0 is the characteristic frequency of the oscillator. The oscillating particle has charge e and mass m^* and is driven by a field with electric and magnetic components $\vec{E}$ and $\vec{B}$, respectively.

In the context of a charge in a rapidly oscillating electromagnetic field, the acceleration due the magnetic field is insignificant compared to that of the electric because the moving charge does not have the time to build up significant velocity. In this case, to a good approximation, we can neglect the magnetic acceleration term, leaving

$$\frac{d^2\vec{r}}{dt^2} + \Gamma\frac{d\vec{r}}{dt} + \omega_0^2\vec{r} = \frac{e}{m^*}\vec{E}(\vec{r},t) . \tag{B.2}$$

Assuming a spatially uniform, time-dependent, oscillating electric field of the form

$$\vec{E}(t) = \vec{E_0}e^{i\omega t} , \tag{B.3}$$

it is sensible to guess that displacement will have the same time dependence:

$$\vec{r}(t) = \vec{r_0}e^{i\omega t} . \tag{B.4}$$

By plugging Equations B.3 and B.4 into Equation B.2 and solving for $\vec{r_0}$ we obtain

$$\vec{r_0}\left[(i\omega)^2e^{i\omega t} + \Gamma(i\omega)e^{i\omega t} + w_0^2e^{i\omega t}\right] = \frac{e}{m^*}\vec{E_0}e^{i\omega t} \tag{B.5}$$

$$\vec{r_0}\left[-\omega^2 + i\Gamma\omega + w_0^2\right] = \frac{e}{m^*}\vec{E_0} \tag{B.6}$$

$$\vec{r_0} = \vec{E_0}\frac{e}{m^*}\frac{1}{-\omega^2 + i\Gamma\omega + \omega_0^2}\,. \tag{B.7}$$

Noting that electric polarization is proportional to charge displacement and the density of charge we can write

$$\vec{P}(t) = ne\vec{r}(t)\,, \tag{B.8}$$

where n is the density of particles each with charge e in the system. By substituting in Equations B.7 and B.4:

$$\vec{P}(t) = \vec{E_0}\frac{ne^2}{m^*}\frac{1}{-\omega^2 + i\Gamma\omega + \omega_0^2}e^{i\omega t}\,. \tag{B.9}$$

Then, by making the substitution $\frac{ne^2}{\epsilon_0 m^*} = \omega_n^2$, the time-dependent polarization becomes

$$\vec{P}(t) = \epsilon_0\vec{E_0}\frac{\omega_n^2}{-\omega^2 + i\Gamma\omega + \omega_0^2}e^{i\omega t}\,. \tag{B.10}$$

The definition of the electric displacement field $\vec{D}$ is

$$\vec{D} \equiv \epsilon_0\vec{E} + \vec{P}\,. \tag{B.11}$$

Assuming a linear, homogeneous, and isotropic material, $\vec{D}$ can also be expressed as

$$\vec{D} = \epsilon_0\epsilon_r\vec{E} = \epsilon_0(1+\chi)\vec{E} \tag{B.12}$$

where ϵ_r is the relative permittivity and χ is the electric susceptibility. Thus, after substituting Equation B.3 and B.10 into Equation B.11 we obtain

$$\vec{D} = \epsilon_0\vec{E_0}e^{i\omega t} + \epsilon_0\vec{E_0}\frac{\omega_n^2}{-\omega^2 + i\Gamma\omega + \omega_0^2}e^{i\omega t} \tag{B.13}$$

$$\vec{D} = \epsilon_0\vec{E}\left[1 + \frac{\omega_n^2}{-\omega^2 + i\Gamma\omega + \omega_0^2}\right]\,. \tag{B.14}$$

By comparison to Equation B.12 it follows easily that the electric susceptibility due to the Lorentz oscillator is

$$\chi_{Lor} = \frac{\omega_n^2}{-\omega^2 + i\Gamma\omega + \omega_0^2}\,. \tag{B.15}$$

The Drude oscillator is a special case of the Lorentz oscillator where there is no restoring force and the characteristic oscillation frequency $\omega_0 = 0$. Thus, the electric susceptibility for the Drude oscillator is

$$\chi_{Dr} = \frac{\omega_n^2}{-\omega^2 + i\Gamma\omega}\,. \tag{B.16}$$

Appendix C

Standard Equipment and Procedures for Spray Pyrolysis

This is a reproduction of SOP SP-1.3, Rev D (Last Major Revision: 15 July 2014), which is a procedure describing the standard method of producing and analyzing thin films by spray pyrolysis using a BETE XA pneumatic atomizing nozzle. The steps here represent the baseline procedure which is assumed unless specific deviations are recorded in the experimental notes. Photographs have been added to illustrate the actual equipment used for this work.

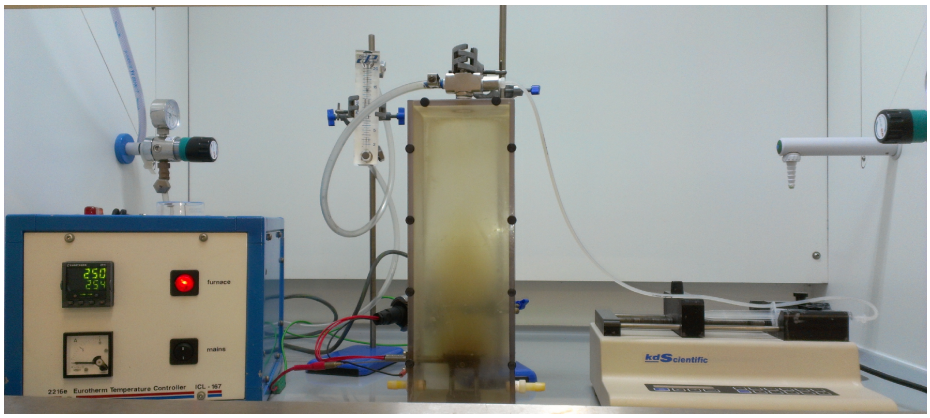

Figure C.1: Overview of spray pyrolysis apparatus showing polycarbonate spray chamber (120 mm W × 350 mm H × 94 mm D) in center of fume hood. The spray nozzle is mounted at the top of the chamber and connected to gas supply (left) and solution supply from a KDS-200-CE syringe pump (right). The furnace controller (Eurotherm 2416) is also shown (blue box, left) and connected to the heater stage located in the bottom of the chamber.

Relevant Risk Assessments (On File in ICL, F9):

1. Ecopia HMS-3000 Hall Effect Measurement System
2. Electrical Equipment
3. Furnace Operation
4. General Chemical Hygiene
5. Handling Glassware
6. Heated Reactions
7. Indium Soldering of TCO Samples
8. Spray Pyrolysis
9. Use of Fume Hoods
10. Use of Sonicator
11. Washing Up

C.1 Mount Compressed Gas Spray Nozzle

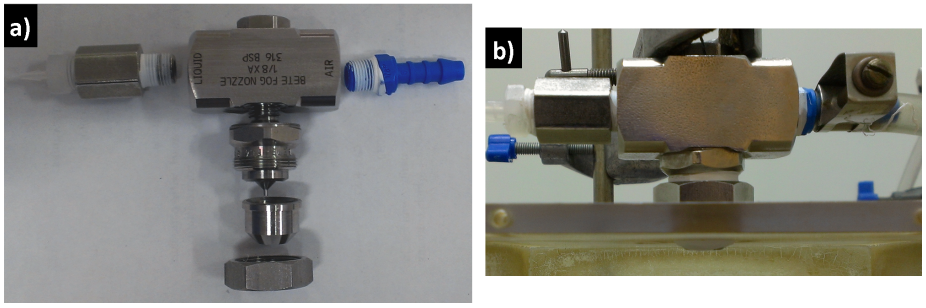

Figure C.2: a) Components of BETE XA PR-050 pneumatic spray nozzle and associated fittings for solution (left) and gas (right). b) Assembled nozzle mounted at top of spray chamber and connected to utilities.

1. If any components for the spraying process[i] are not known to be clean, follow the instructions in Section C.8 before proceeding.
2. Set the cleaned spray chamber inside the fume hood between the furnace controller and pump. Face the open side outwards. Make sure the two outlet adapters are attached to the spray chamber.
3. Screw the spray nozzle into the nozzle body firmly by hand.

[i]The liquid adapter consists of two parts, a metal fitting and a polypropylene hose barb (not typically disassembled). The BETE XA spray nozzle consists of a nozzle body with back cap (not typically disassembled), a spray nozzle, an air cap, and a retaining nut.

4. Attach the air cap to the spray nozzle using the retaining nut finger tight. Ensure that the back cap is fully seated.
5. Apply ∼2 turns of Teflon tape to the liquid adapter, then insert into the port marked liquid on the spray nozzle. Tighten fully by holding the body of the spray nozzle with an adjustable wrench and turning the fitting with a 9/16" wrench.
6. Apply ∼2 turns of Teflon tape to the gas supply line adapter, then attach the fitting to the port marked air on the spray nozzle. Hold the gas fitting in place with a 10 mm wrench and rotate the body of the spray nozzle to do this.
7. Apply 3–4 turns of Teflon tape to the circumference of the aircap. Do not obstruct the spray nozzle opening.
8. With the gas line perpendicular to the left side of the spray chamber, insert the tip of the spray nozzle into the hole on the top of the spray chamber. It should fit snugly with the Teflon tape forming a partial seal.
9. Fix nozzle firmly place with a lab stand and clamp around the hex on the back of the spray nozzle.
10. Attach the liquid feed line to the liquid adapter.

C.2 Prepare and Mount Glass Substrate

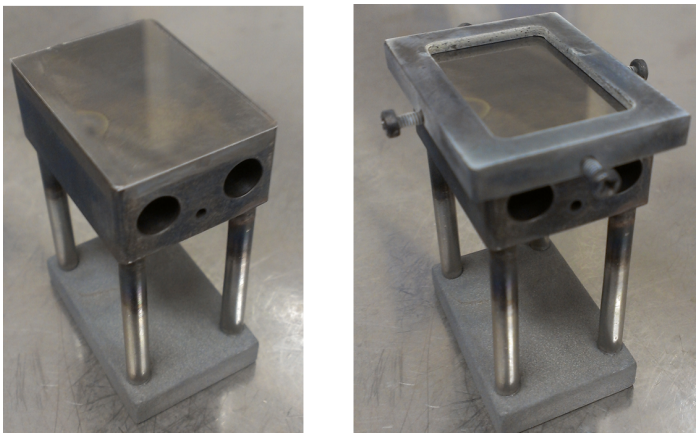

Figure C.3: Heater stage for spray pyrolysis substrate without (left) and with cap securing a cleaned glass cover slide (right). The surface area of the stainless steel heater block is 35 mm × 25 mm, and that of the window in the cap 30 mm × 20 mm. The overall height of the stage is 51 mm.

1. Substrates are made from pieces of material which are slightly smaller than the stage upon which they rest.
2. Verify that the top surface of the heater stage is clean, smooth, and free of contaminants, cleaning or polishing if necessary to achieve this.
3. After this step, the substrates should not be handled with ungloved hands. Sonicate the substrate in acetone for ∼5 minutes.
4. Carefully extract the substrate with tweezers and rinse both sides with fresh acetone.
5. Immediately, pat the substrate dry by sandwiching between two clean pieces of lens tissue on top of a flat surface covered with printer paper.
6. Blow the substrate dry with compressed nitrogen.
7. Record the experiment ID, operator, date, and time in the QC document.
8. By using an appropriate platform (such as a glass vial), measure and record the mass of the substrate at least four times and until consistent masses (i.e. ± 0.2 mg) are recorded. Also, record the substrate material.[ii]
9. Center the clean substrate on the top of the heater block.
10. Fit the substrate cap over the substrate onto the heater block, making sure that the retaining screws are withdrawn far enough to allow the cap to be fully seated.
11. Apply firm, vertical, downward pressure to the heater cap while the retaining screws are tightened with a mini screwdriver. Tighten each screw to the point of first resistance, then go back around to finish tightening just beyond this point. Listen for any sounds of cracking glass (if this occurs, remove the substrate cap and inspect the substrate for cracks, starting this section again if any are observed).
12. Use dry nitrogen from the spray nozzle to blow off any dust that may have settled on the substrate.

[ii]Take care not to shift the location of the platform on the weighing platform between taring and measuring, as this can affect the measurement.

C.3 Chamber Set-up

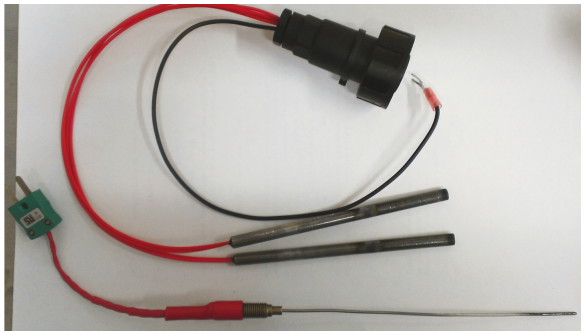

Figure C.4: Two Tempco HDC27831 (100 W, 240 V, 1/4" diameter) Incoloy-sheathed cartridge heaters wired with grounding cable and IP67 immersion-resistant connector (top). Ungrounded, stainless-steel sheathed Type-K thermocouple (bottom).

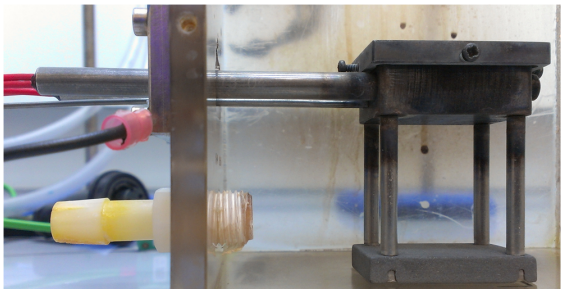

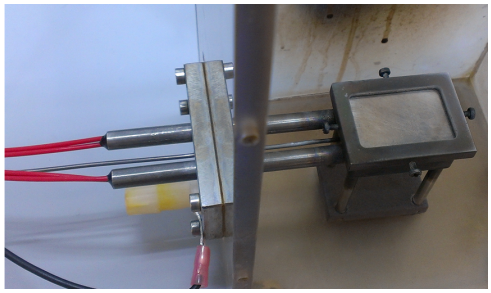

Figure C.5: The thermocouple and heater cartridges pass through a metal plate in the side of the chamber and are inserted into corresponding holes in the heater stage. Note the firmly attached grounding cable and ∼3 mm protrusion of the cartridge heaters past the end of the stage.

1. Verify that the Furnace switch on the heater controller is off.
2. Inspect the grounding wire to verify that the copper spade connector is in good condition and firmly connected to the rest of the wire.
3. Firmly affix the grounding wire to the heater mounting plate by securing the spade connector with one of the four mounting bolts.
4. Slide the heater cartridges through the 2 large holes in heater mounting plate.
5. Plug the heaters and thermocouple into the furnace controller.
6. Insert the two cylindrical heating elements into the corresponding holes in the stage. The side of the stage with the thermocouple well should point towards the heating elements.

7. Insert the thermocouple through small hole in the heater mounting plate, into the small well on the side of the stage. Do not press too hard and bend the thermocouple, but ensure that it is fully seated in the well.
8. Carefully adjust the cartridge heaters and thermocouple such that the stage is aligned with the marks on the bottom of the chamber.
9. Align the non-lead ends of the cartridge heaters flush protruding slightly from ($\sim$3 mm) the far side of the heater stage.
10. Clamp the heater plug in a position that minimizes strain on the leads.
11. Verify that the thermocouple is still fully seated and that the stage is still correctly positioned, making any adjustments as necessary.

C.4 Heat-up

1. Verify that the furnace program is set to 1) ramp to the target heater temperature at a rate of 30 °C/min, 2) dwell at temperature for at least 30 minutes, 3) ramp to 20 °C at a rate of 25 °C/min, 4) end. Record the target heater temperature.
2. Switch on the syringe pump and verify that the following settings on the syringe pumps are correct:
   (a) Syringe diameter
   (b) Sample volume
   (c) Solution delivery rate
3. Without moving the chamber, partially secure the front plate of the chamber by installing provided finger screws into the top two and bottom two positions.
4. Turn on the cooling gas and adjust until the target flow rate is achieved. Record the following information:
   (a) Gas identity
   (b) Gas flow rate
5. [***WARNING:*** *NEVER switch on the furnace without the thermocouple in place, as this will result in uncontrolled heating and destruction of the heaters. Never touch the thermocouple housing or attempt to adjust the position of the stage while the heaters may be energized. Attempting to do so may result in a*

dangerous electrical shock!] Run through the following checklist prior to switching the heater on:

(a) Thermocouple... visibly in heater block

(b) Heaters... both aligned with or just protruding from far side of block

(c) Gas Flow... On

(d) Front plate of chamber... at least 2 Top and 2 Bottom screws installed

6. Change the "Furnace switch on the controller to On. Start the furnace program and record the time.
7. Verify that the measured furnace temperature is increasing as expected prior to carrying out any further tasks.
8. Without moving the chamber, carefully install the remainder of the finger screws to finish securing the front plate.
9. While the heatup continues. Record the following information on the QC document:

(a) Chamber ID

(b) Precursor

(c) Precursor solvent

(d) Solution concentration

(e) Solution amount

(f) Solution batch date

(g) Pump type

(h) Pump Rate/Speed

(i) Atomizer type

10. Spray solution preparation may occur during heatup. Unless otherwise intended, it is desirable that solution be used as soon as possible after completion:

(a) Write down the details of the solution preparation in the notes section of the QC document.

(b) Draw the desired volume of solution + $\sim$2 mL into the appropriately sized syringe.

(c) Carefully eject as much air as possible from the syringe after inverting it (without losing solution).

(d) Mount the syringe into the syringe pump sideways so that the syringe outlet is at a middle height.

(e) Lock the driver block in position.

11. After the stage reaches the target temperature, make any adjustments necessary to achieve the target flow rate of carrier gas. Wait at least 5 minutes, then measure and record the range of furnace power being used to maintain the target heater temperature.
12. [***CAUTION:*** *While gas is flowing to the spray nozzle, the syringe may become substantially pressurized, especially if the spray nozzle becomes partially blocked. Do not switch off the gas flow or disconnect the syringe without first ensuring that no pressurized liquid is in a position to suddenly flow upon release of pressure. Do not release the driver block without accounting for the pressure inside the syringe.*] Using the Luer adapter, firmly attach the liquid tubing to the end of the syringe
13. Proceed immediately to Section C.5.

C.5 Spraying

1. During the spraying, monitor the apparatus. Any unusual events (such as uneven spraying, changes in carrier gas flow, etc.) should be noted in the comments.
2. Start the syringe pump. Watch as liquid moves up the tubing towards the liquid adapter.
3. Once the liquid first reaches the tubing adapter, listen carefully for the sound of liquid exiting the spray nozzle or watch for the spray (this typically takes ∼1 ml. If 1.25 mL elapses with no sign of spray, verify that the syringe pump is correctly configured before proceeding). When this occurs, stop and restart the spraying. [Note: It may be useful to start a stopwatch or timer at this time, to assist the execution of Step 5.5]
4. Hold the furnace program. Edit the dwell time of the second program step to "0" (zero).
5. Five (5) minutes after the designated amount of solution has been sprayed, proceed to Section C.6.

C.6 Cool-down

1. Un-hold the program. This should initiate the cooldown ramp.
2. When the furnace temperature a target temperature (350 °C in prior revisions), switch the "Furnace switch on the controller to Off.
3. Stop the program by holding the run/hold button for five seconds. Record the temperature at which the furnace power is switched off.
4. [***WARNING:*** *The stage may still be hot!*] When a target temperature is reached (250 °C in prior revisions) begin opening the spray chamber.
5. Put the front aside, and then record the time and temperature when the chamber was first opened.
6. Handling the stage by the base, which will be the coolest part, carefully extract the stage with attached substrate and set aside to continue cooling. Leave the heater cartridges and thermocouple balanced in the heater mounting plate.
7. [***CAUTION:*** *Perform this step cautiously as the syringe may have been pressurized during spraying, especially if the nozzle has become partially blocked.*] Release the syringe from the pump and use it to withdraw excess solution from the spray apparatus. When all solution has been removed, continue pulling back slowly on the syringe while simultaneously shutting off the cooling gas flow.
8. When the gas flow is completely off, disconnect spray solution syringe from the system.
9. If another film is to be prepared, clean the nozzle:
   (a) Make sure a beaker is present to catch liquid as it exits the spray nozzle.
   (b) Use a clean 20 mL syringe to push (an) appropriate solvent(s) (usually distilled water or dilute HCl followed by distilled water) into the solution supply line until it flows freely from the nozzle. Typically, ∼40–50 mL of each liquid is adequate.
   (c) Use the syringe to push ∼40–50 mL of air through the system.
   (d) Discard the collected solvents appropriately.
   (e) Again using the beaker to catch any liquid, slowly turn on the gas flow for at least 15 seconds to blow the spray nozzle and lines dry. Switch off the gas flow.

10. Remove the substrate cap and transfer the coated substrate to the clean weighboat. Place the other parts aside while the operations in Section C.7 are carried out.

C.7 Quick Analysis

1. By alternating weighboats, measure and record the mass of the coated substrate at least four times or until consistent masses (*i.e.*, ± 0.2 mg) are recorded.
2. Measure and record the approximate dimensions of the film (as defined by the substrate cap).
3. Wait until at least 5 minutes have elapsed from the time that the chamber was opened. Use a multimeter to measure and record the resistance across the middle of the in the long direction. Place the probes approximately 2 mm in from each edge.
4. Place the film inside a clearly labeled, snap top plastic container.
5. Write down any qualitative observations about the film, such as quality, uniformity, color, or transparency in the comments.
6. Store the film in the designated location and record the time that the procedure is finished. In the bottom right table of the QC document, list further analysis that should be performed on the sample.
7. If the parts are not to be reused with the same or compatible solution, immediately clean the apparatus as described in the following section.

C.8 Clean Apparatus

1. Use a clean syringe to run the following through the tubing. The rinsings can be disposed of down the sink:
   (a) At least 40 mL of water with a few drops of dilute HCl
   (b) At least 60 mL of distilled water
   (c) Enough air so that no more liquid can be obviously ejected from the tubing.
2. Unplug the heater cartridges and thermocouple from the furnace controller.
3. Disconnect the grounding wire by loosening the bolt, then extract the entire heater cartridge assembly.

4. Clean the stage, substrate cap, heater cartridges, and thermocouple (as well as components of the compressed gas spray nozzle, if applicable):
   (a) Place the disassembled pieces of the heater stage and spray nozzle in a suitably sized glass beaker.
   (b) Add enough tap water to completely cover the parts.
   (c) Add a ∼1 mL of dilute hydrochloric acid.
   (d) Dip the non-lead end of the heater cartridges and thermocouple into the beaker. Do not immerse the lead ends.
   (e) Place the beaker with parts and water into basket of the ultrasonic bath. Sonicate at room temperature for 5 minutes.
   (f) Take care not to lose any parts down the sink. When sonication is complete, decant as much water from the beaker as possible. The slightly acidified water may be disposed of down the sink.
   (g) Triple rinse the parts with tap water, then with distilled water.
   (h) Allow the parts dry completely (in air or in the drying oven). The parts may now be reused immediately or (except for the heater cartridges and thermocouple) stored in the oven for later use. An acetone rinse may be used to expedite drying of the parts.
5. [***CAUTION:*** *Do not use acetone to clean the chamber*] Clean the chamber and chamber front:
   (a) Thoroughly rinse the inside of the chamber with copious amounts of tap water.
   (b) Dilute HCl and scrubbing with non-abrasive materials may be used to remove stubborn deposits.
   (c) Rinse the inside of the chamber with distilled water.
6. Parts may be left to dry until needed.

C.9 Detailed Analysis

1. Any filenames generated by instrumentation during analysis should include the date of acquisition and the experiment ID in the format "YYYY-MM-DD - ID - [Optional Comments]".

2. Record the type of analysis and the date performed in the bottom right table of the QC document.
3. Record the UV-Vis-NIR Transmission Spectrum:
   (a) The spectrometer in Lab T10 should be for routine measurements.
   (b) Use the program "Thin Film.msc"
   (c) Use the purpose-designed sample holder to support the samples in and perpendicular to the beam path in the main sample chamber as close to the focal point as possible.
   (d) Save the data as .csv and process it using the Swanepoel Calculator program to obtain the optical constants and estimated thickness.
4. Room-temperature Hall effect should be recorded for all films of reasonable conductivity:
   (a) For standard measurements, ensure that the sample has been sitting in ambient lab light (no darkness or direct sunlight!) for at least 1 hour prior to making a measurement.
   (b) Using a diamond scribe, cut a square/rectangular piece of the film ∼5–10 mm on each side. Avoid using material from the very edge of a film.
   (c) Use a multimeter or other appropriate technique to identify the side of the substrate on which the film is deposited.
   (d) Place the piece, film side up, on the center of a Hall effect circuit board. Gently press the film piece into place using the tip of a plastic pipette.
   (e) Use a minimum amount of indium solder to attach the four lead wires to the four corners of the sample.
      i. A solder iron temperature of 170 °C and a gentle brushing motion are suitable for promoting adhesion of indium and most films
      ii. A droplet of indium should be placed first at each corner.
      iii. Use a pair of fine-tipped tweezers to melt the lead wires into the indium droplets. Take care to not solder the tweezers to the sample!
      iv. Check the connections by using a multimeter to measure the resistance across each pair of contacts at the end of the circuit board. Any contact showing consistently higher resistance than the others should be considered suspect and inspected. Remake the connection if necessary.

(f) Carefully insert the circuit board into the Hall effect machine. Follow the drawing to ensure the board is correctly oriented.

(g) Start the Hall Effect Measurement software. Enter your user name and the sample name in the appropriate boxes. Ensure the following settings are entered correctly:

i. B (Magnetic Field Strength) = 0.55 T

ii. D (Thickness) = Use result from Swanepoel Calculator in C9.3.d

iii. DT (Delay Time) = 0.1 seconds

iv. MN (Number of measurements) = 1000

v. I (Current) = Will depend on resistance of sample. Generally 1 milliamp or the highest current that does not result in "Contact Fail" error when measurement is started. Note that carrier concentration and mobility data will not be reliable if a current less than 20 microamps is used. If a very conductive sample is being measured, a current higher than 1 mA may be needed to generate high enough Hall voltage for a reliable measurement.

(h) Click Start Measurement and follow the onscreen instructions to the record Hall effect data.

(i) After the measurement is complete, save the data.

(j) Repeat the measurement at least twice more, saving the data to the same file. Despite the onscreen message, the system is NOT overwriting old data, but instead appending the new data.

5. If appropriate, additional characterization may be employed using more specialized measurements. These may be more time consuming and/or more difficult to access, and are not necessary for all samples. Examples include:

(a) XRD - Crystallite size, crystalline orientation, chemical identity

(b) XPS - Elemental composition, oxidation state

(c) SEM/TEM - Morphology, structure

(d) EDX - Elemental composition

(e) Variable-temperature Hall effect

6. Any files should be transferred as soon as reasonably possible to the appropriate subfolder in the sample folder in "Results".

7. Update the "Active Films Logbook" with information from the QC document and measurements for each film, as well as written summaries of purpose, results, and next steps.

Quality Control Document:

Notes:

Metric	Value	
Experiment ID		
Operator		
Date (yyyy/mm/dd)	/ /	
Time, Operation Start	:	
Substrate Mass, Pre Deposition	g	g
	g	g
Substrate Material		
Furnace Temperature		°C
Carrier Gas		
Gas Flow Rate		lpm
Time, Furnace On	:	
Chamber ID		
Precursor		
Precursor Solvent		
Solution Concentration		M
Solution Amount		mL
Solution Batch Date	*or*	□ Today
Pump Type		
Pump Rate/Speed		mL/min
Atomizer Type		
Furnace Power at Temperature		%
Temperature @ Furnace Power Off		°C
Time/Temp Chamber Open	:	°C
Substrate Mass, Post Deposition	g	g
	g	g
Film Length		mm
Film Width		mm
Resistance, Long Direction		Ω
Time, Procedure Finished	:	

Comments:

_____

_____

_____

_____

_____

Analysis	Date

Appendix D

Thermal Analysis of Precursors

D.1 TVA

As the samples are heated, the pressure inside the apparatus indicates the production of gaseous species from the material being analyzed. This pressure is shown as a function of temperature for the three zinc carboxylates studied using TVA (Figure D.1).

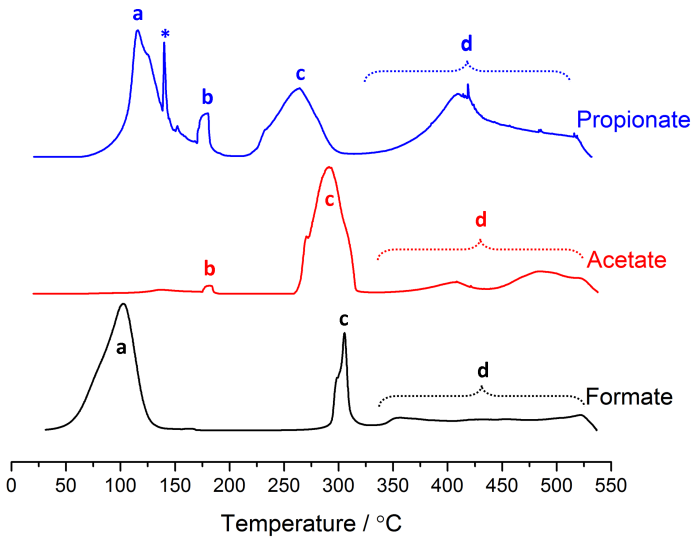

Figure D.1: System pressure as a function of sample temperature for TVA runs on zinc formate hydrate (blue), anhydrous zinc acetate (red), and zinc propionate hydrate (black). The heating rate used was 10 °C/min. Peaks associated with several processes are indicated: a) dehydration, b) possible volatilization as polymeric "basic zinc carboxylates", c) ketonic decarboxylation, d) high-temperature pyrolysis of residual organics. The sharp peak marked $*$ is an experimental artifact due to a change in valve position.

The lowest-temperature process (a) is assigned as dehydration, since this peak only has significant intensity for the hydrated starting materials. Process (b) has not been conclusively identified. However, both zinc acetate and propionate are known to volatilize as a tetrametric "basic zinc carboxylate" upon heating in vacuum. These species are not extremely volatile at ambient temperatures and would have quickly condensed in the cooled part of the system between the furnace and the cold trap, leading to the relatively small signals observed. The corresponding basic zinc formate was not reported by Gordon and Silver, who studied this series of compounds, which could explain the absence of this signal in the zinc formate trace.[1] Process (c) is the main decomposition process leading to ZnO. Ketonic decarboxylation is almost certainly active in all three cases, but there may be significant alternative pathways in the case of zinc propionate and formate. Process (d) is likely the higher temperature pyrolysis of residual organics under anoxic conditions which may not be directly related to the process of ZnO formation.

In-line mass spectrometry confirmed that the (a) peaks in Figure D.1 were primarily composed of water and the corresponding carboxylic acid. The remaining volatiles (generated above 150 °C) were collected in a liquid nitrogen cold trap. After the heating of the sample was over, the cold trap was slowly warmed and the components that were released at various temperatures were analyzed using mass spectrometry and gas-phase IR.

Figures D.2–D.4 are summaries of these results. In each figure, the heavy black curve at bottom is the total system pressure, which indicates the evaporation of gaseous species from the warming trap, whose temperature is shown as a dashed red line. The colored curves at the top of each figure represent the signal from specific channels of the mass spectrometer data, selected to represent the specific chemical species indicated. While the peaks are chosen to minimize interferences, it is inevitable that a peak may sometimes appear due to a species other than the one listed. In cases of potential ambiguity, the peak that is associated with the listed compound is marked with an asterisk. Some of the assignments are tentative, especially for species that are seen only in mass spectra, and are indicated as such.

It should be noted that this analysis is qualitative, and the magnitude of mass spectrometer signals cannot be easily correlated to the real concentration of various

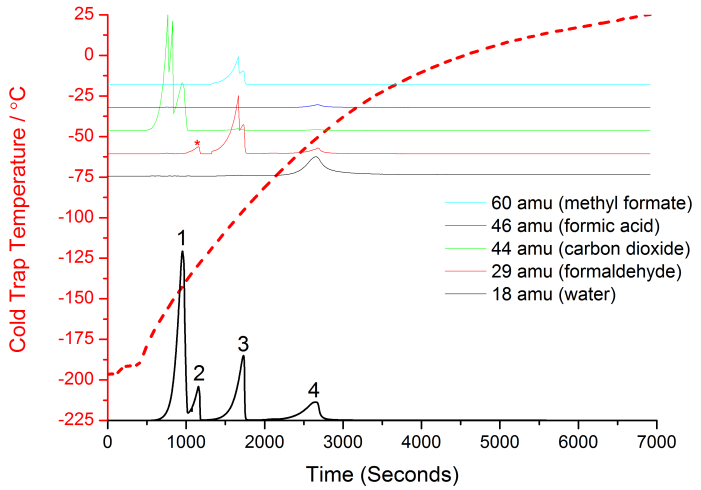

Figure D.2: Summary of mass spectrometry analysis of liquid nitrogen cold trap fractions collected from the thermal decomposition of zinc formate under vacuum between 150–550 °C. From left to right the main constituents of the pressure peaks observed are assigned as: 1) carbon dioxide, 2) formaldehyde, 3) methyl formate, 4) water and formic acid.

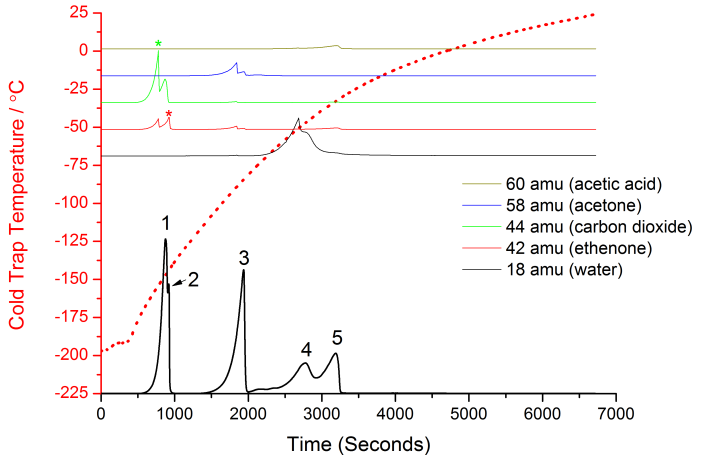

Figure D.3: Summary of mass spectrometry analysis of liquid nitrogen cold trap fractions collected from the thermal decomposition of zinc acetate under vacuum between 150–550 °C. From left to right the main constituents of the pressure peaks observed are assigned as: 1) carbon dioxide, 2) ethenone (tentative), 3) acetone, 4) water, and 5) acetic acid.

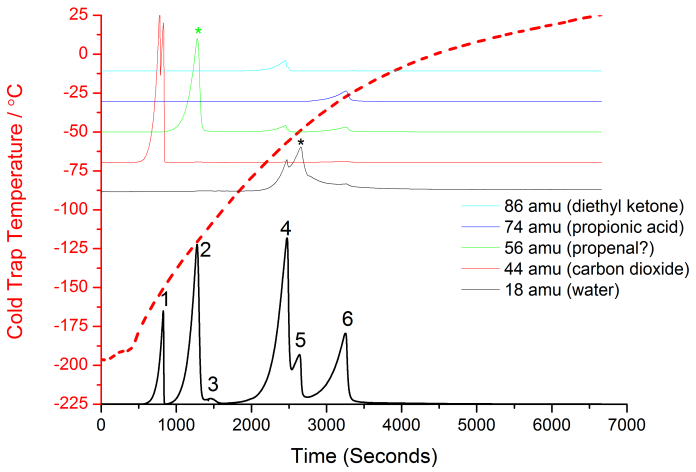

Figure D.4: Summary of mass spectrometry analysis of liquid nitrogen cold trap fractions collected from the thermal decomposition of zinc propionate under vacuum between 150–550 °C. From left to right the main constituents of the pressure peaks observed are assigned as: 1) carbon dioxide, 2) propenal (tentative), 3) unknown, 4) diethyl ketone, 5) water, and 6) propionic acid.

chemical species. Furthermore, the appearance of double peaks in the mass spectrometer signals is generally reflective of a range switch to avoid detector saturation, and is not a real feature of the experiment.

The assignments in Figures D.2–D.4 are derived from analysis of both the full mass spectra associated with each of the pressure signals as well as gas phase IR of samples taken from each of the fractions. For brevity, the full analysis of each peak will not be shown here. However, one example of this is provided in Figure D.5 which shows how infrared transmittance and mass spectrometry are used to identify acetone as the major component of Peak 3 in Figure D.3.

Finally, with most major decomposition products thusly identified, an additional experiment was performed to decompose zinc acetate without a cold trap, in order to determine the temperature at which the various products are produced. This experiment is summarized in Figure D.6. From this it is very clear that acetone and carbon dioxide are produced together in a process occurring between about 255 and 325 °C; this is consistent with ketonic decarboxylation being the primary pathway for the formation of ZnO. Other species are formed separately in a higher temperature process which has been broadly assigned as the pyrolysis of organics; for instance, ketene has previously been reported as a product of the pyrolysis of acetone.[2]

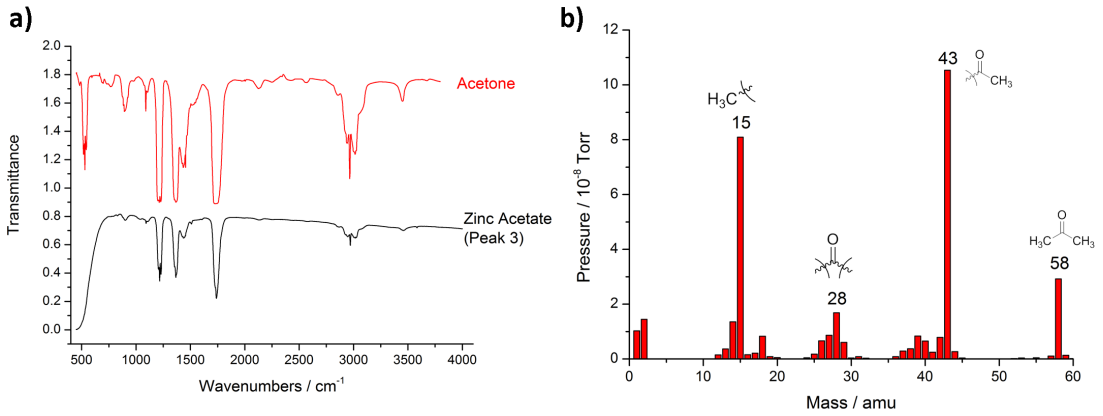

Figure D.5: a) Comparison of experimental gas phase infrared spectrum of fraction (black) and NIST reference spectrum for acetone (red). b) Mass spectra from open-ion source residual gas analyzer. The major mass peaks are labeled with the corresponding fragmentation products of acetone.

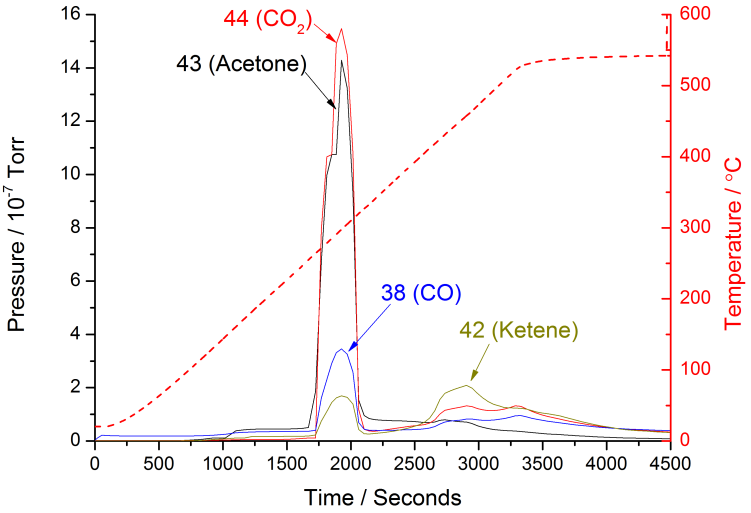

Figure D.6: Mass spectrometer data from the decomposition of anhydrous zinc acetate under vacuum for the indicated mass channels are shown, along with the chemical species primarily responsible. The temperature of the sample is shown as the dotted red curve.

D.2 Cold Trap and NMR Experiment

After a spray pyrolysis deposition of zinc acetate in deuterium oxide, proton NMR spectra were collected of the neat condensed exhaust and with various independent additions. The condensate shows a single single signal at $\delta = 1.98\,\text{ppm}$ and the addition of acetic acid does not lead to any additional signals, confirming that the original signal is due to aqueous acetic acid/acetate. The small shift in peak position is probably due to a decrease in solution pH with the addition of more acid (Figure D.7a).

Figure D.7b shows that the addition of zinc acetate also does not lead to additional NMR signals, however the signal is slightly broadened, perhaps due to the various coordination states for acetate made possible by the presence of zinc. The further addition of a small amount of acetone leads to the formation of a new signal at $\delta = 2.18\,\text{ppm}$, confirming that acetone was below detection limits in the original neat sample.

These results clearly show that the ketonic decarboxylation mechanism for the thermal decomposition of zinc acetate is not substantially active under spray pyrolysis conditions. Instead, the results shown here are consistent with zinc oxide formation by simple hydrolysis of the dissolved zinc salt.

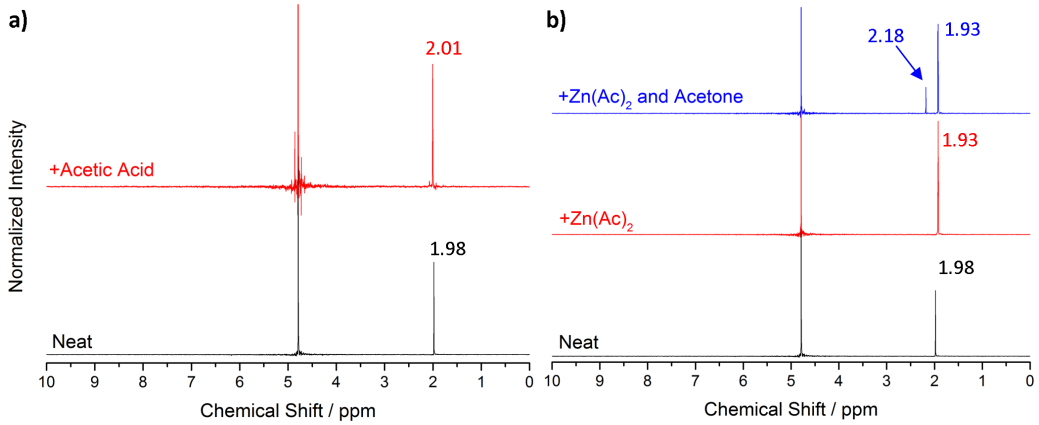

Figure D.7: Proton NMR spectra of condensed exhaust from spray pyrolysis deposition using zinc acetate in deuterium oxide. a) Neat condensate (black) and with independent addition of acetic acid (red). b) Neat condensate (black), with addition of zinc acetate (red), and with addition of zinc acetate and acetone (blue). Spectra are normalized and offset to show the acetate and acetone signals clearly. The peaks at $\delta = 4.79\,\text{ppm}$ are due to solvent and truncated due to scaling.

References

[1] Gordon, R. M.; Silver, H. B. *Can. J. Chem.* **1983**, *61*, 1218–1221.

[2] McNesby, J. R.; Davis, T. W.; Gordon, A. S. *J. Am. Chem. Soc.* **1954**, *76*, 823–827.

Appendix E

Pawley Refinements

In_2O_3 Prepared using Bromide and Chloride Precursors

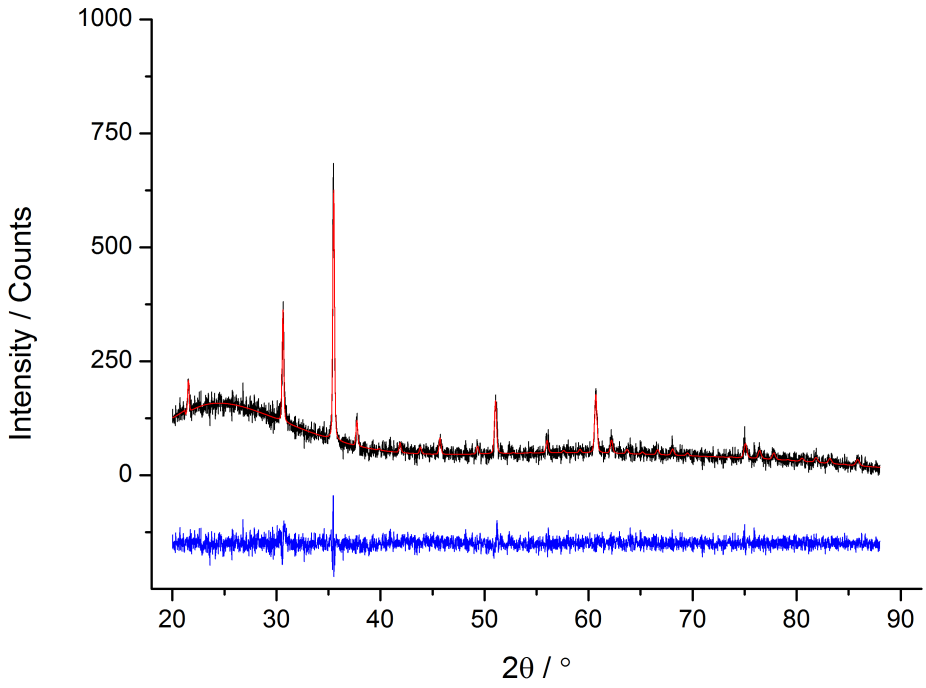

Figure E.1: Pawley fit (red) and residual (blue) for XRD pattern of an In_2O_3 thin film deposited using $InCl_3$ precursor (black). The residual is on the same vertical scale but is offset.

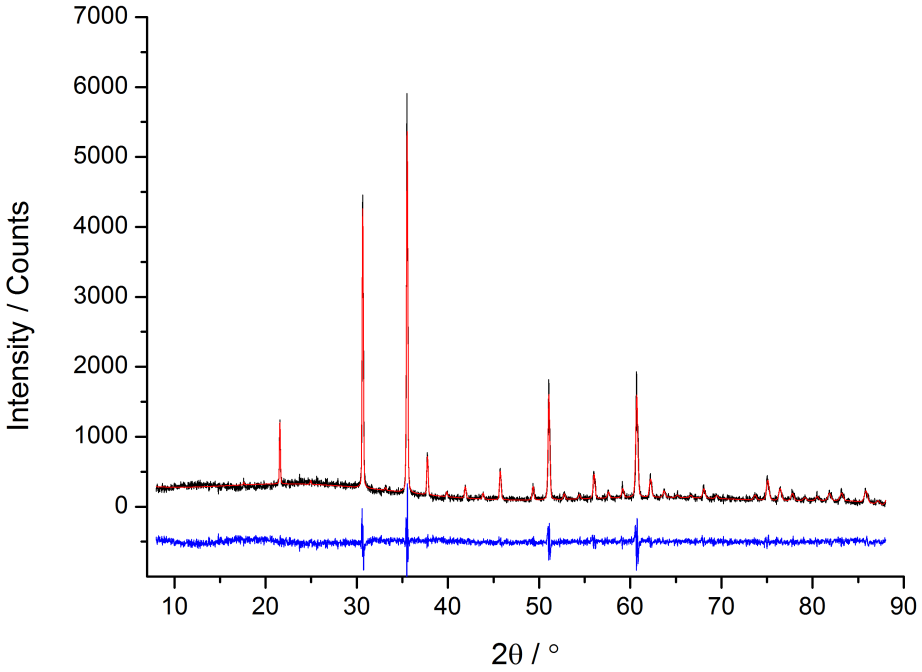

Figure E.2: Pawley fit (red) and residual (blue) for XRD pattern of an IBrO thin film deposited using $InBr_3$ precursor (black). The residual is on the same vertical scale but is offset.

Indium-doped ZnO

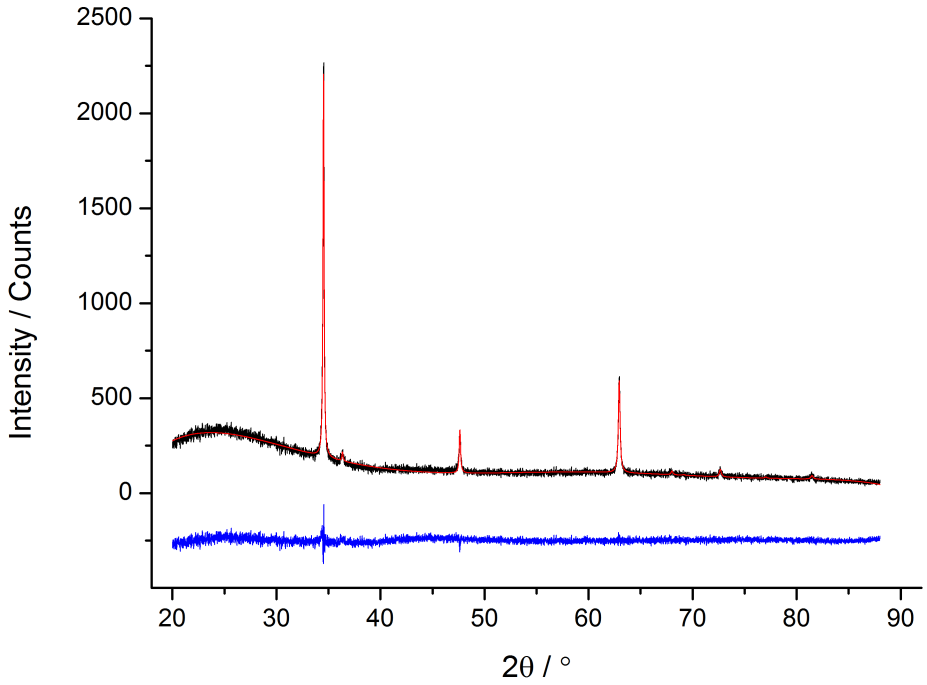

Figure E.3: Pawley fit (red) and residual (blue) for ZnO thin film XRD pattern (black). The residual is on the same vertical scale but is offset.

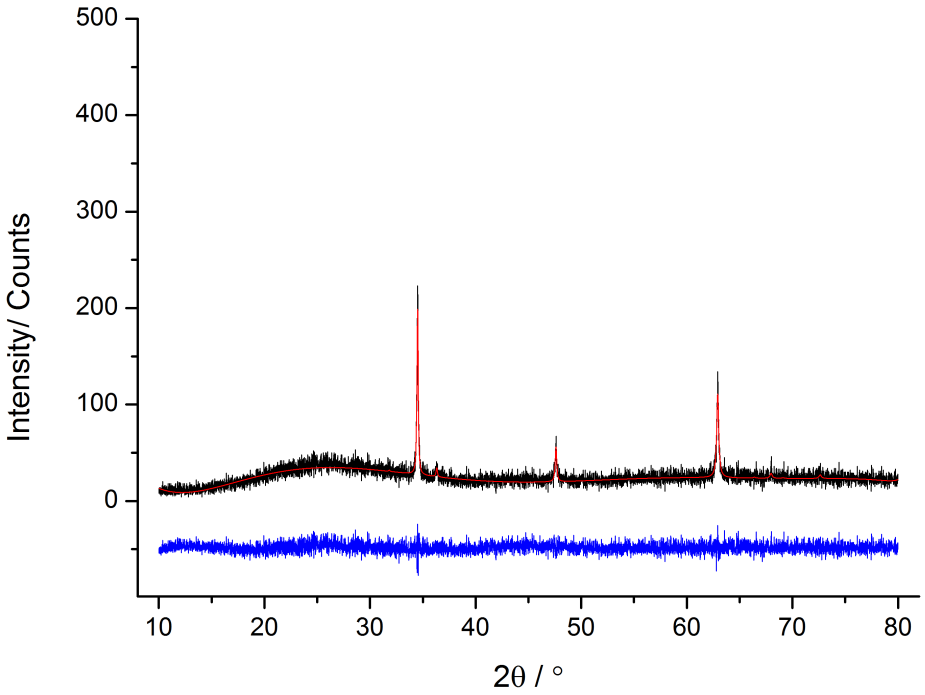

Figure E.4: Pawley fit (red) and residual (blue) for 0.25 at% IZO thin film XRD pattern (black). The residual is on the same vertical scale but is offset.

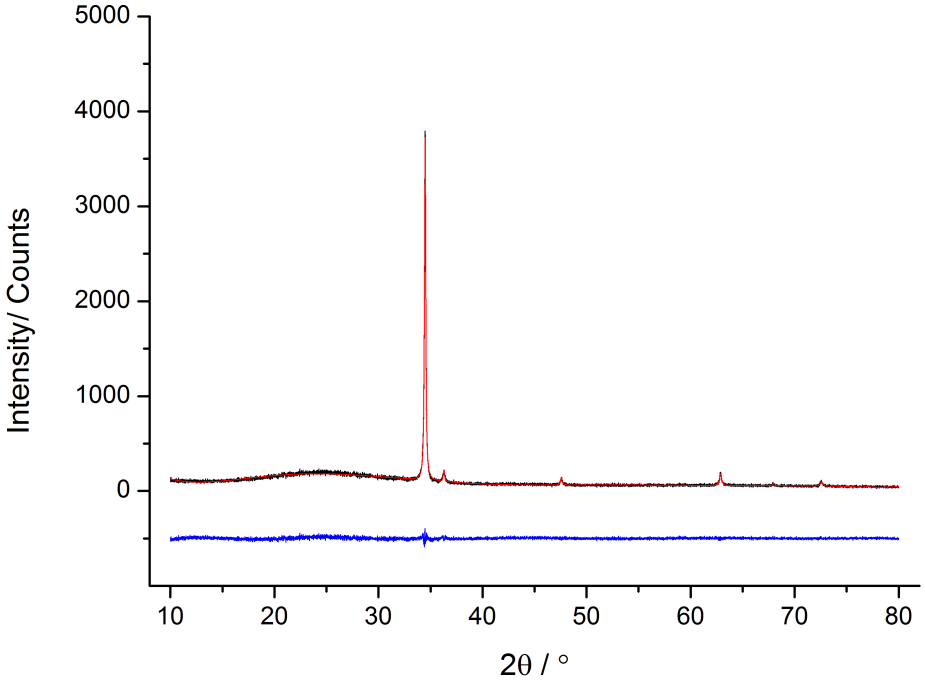

Figure E.5: Pawley fit (red) and residual (blue) for 1.5 at% IZO thin film XRD pattern (black). The residual is on the same vertical scale but is offset.

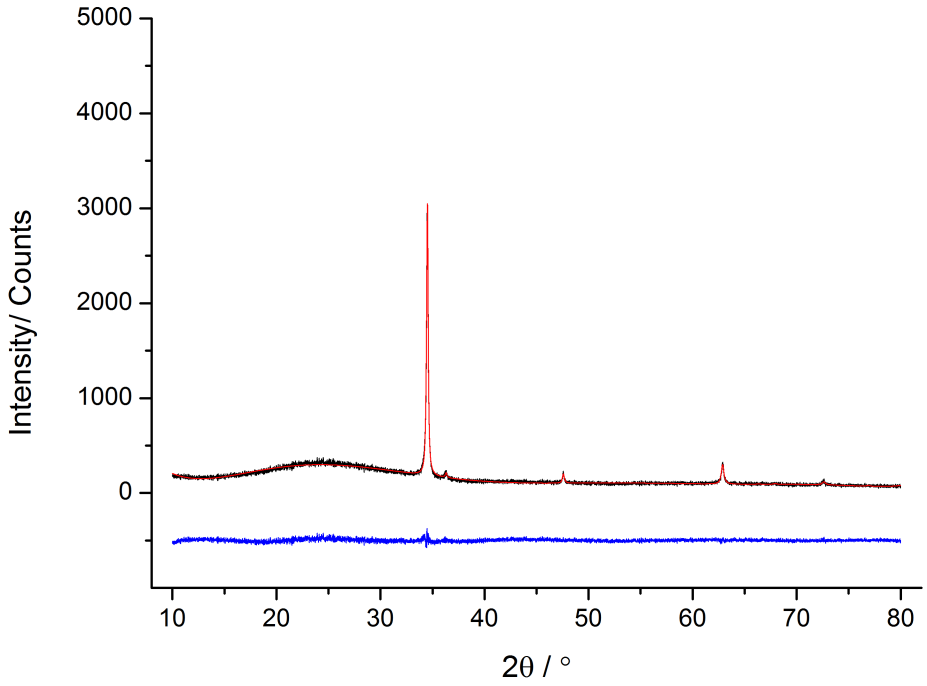

Figure E.6: Pawley fit (red) and residual (blue) for 2.5 at% IZO thin film XRD pattern (black). The residual is on the same vertical scale but is offset.

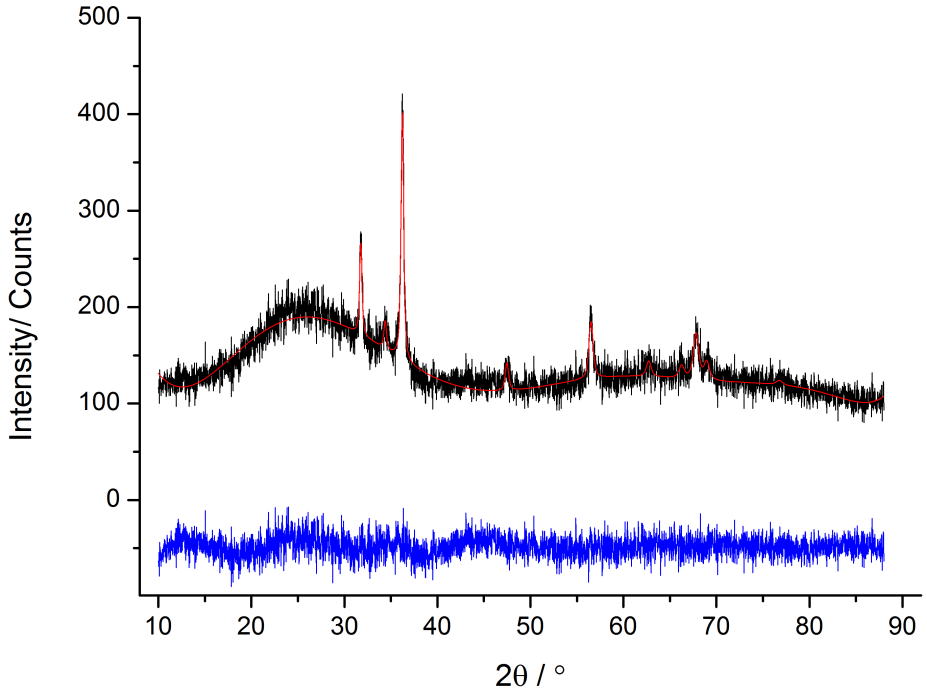

Figure E.7: Pawley fit (red) and residual (blue) for 5 at% IZO thin film XRD pattern (black). The residual is on the same vertical scale but is offset.

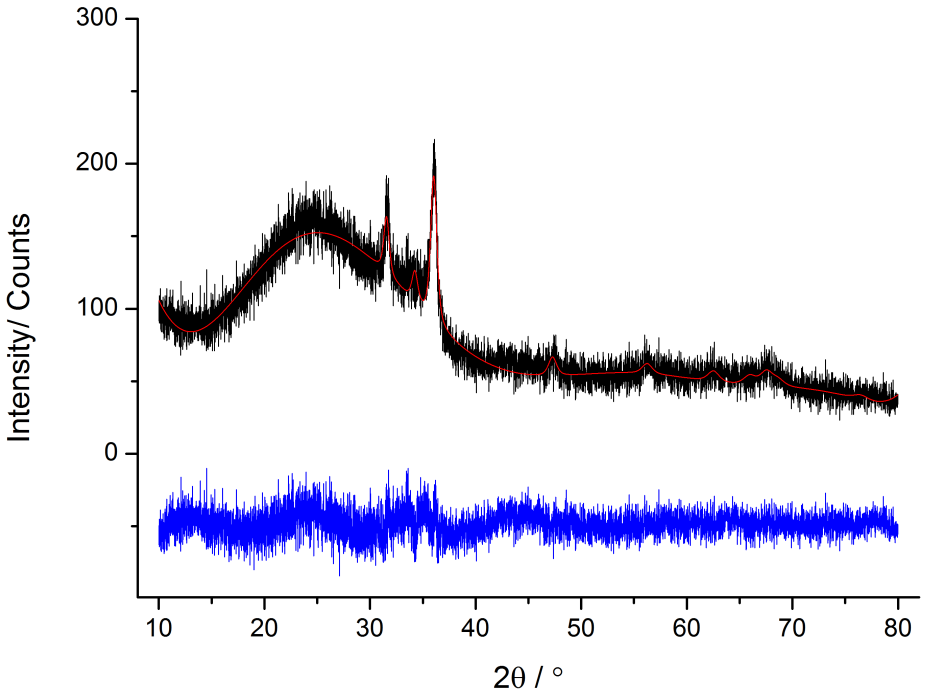

Figure E.8: Pawley fit (red) and residual (blue) for 20 at% IZO thin film XRD pattern (black). The residual is on the same vertical scale but is offset.

Appendix F

Optical Frequency Transport Modeling

F.1 Fits to 5 at% Indium-doped ZnO

Description of Parameters

IZO transmittance and reflectance spectra (between 320 nm and 2500 nm) were modeled using a Drude oscillator to describe the behavior of conduction electrons near the plasma edge and a Lorentz oscillator for the bandgap. The parameter names and corresponding descriptions are given in Table F.1. The substrate is modeled as a 0.17 mm thick layer of D263T borosilicate glass with literature dielectric properties.

Table F.1: Model parameters used for optical transport modeling of IZO transmittance and reflectance spectra.

Parameter Name	Units	Description
Thick.1	Å	Thickness of Uniform ITO layer
Thick.2	Å	Thickness of Surface Roughness Layer (50:50 Intermix of TCO and Air)
e1(inf).1		High Frequency Dielectric Constant (ϵ_∞)
wp.1	eV^2	Lorentz Oscillator Amplitude ($\omega^2_{n,Lor}$)
wt.1	eV	Lorentz Resonant Frequency ($\omega_{0,Lor}$)
G.1	eV	Lorentz Damping Factor (Γ_{Lor})
wp2.1	eV^2	Drude Frequency ($\omega^2_{n,Dr}$)
GL.1	eV	Low-Frequency Damping(Γ_L)
GH.1	eV	High-Frequency Damping(Γ_H)
k.1		Damping Midpoint $\Omega_{\Gamma Dr} = (k.1) * \omega_{n,Dr}$
ggw.1	eV	Damping Steepness ($\Gamma_{\Gamma w}$)

Graphical Fitting Results

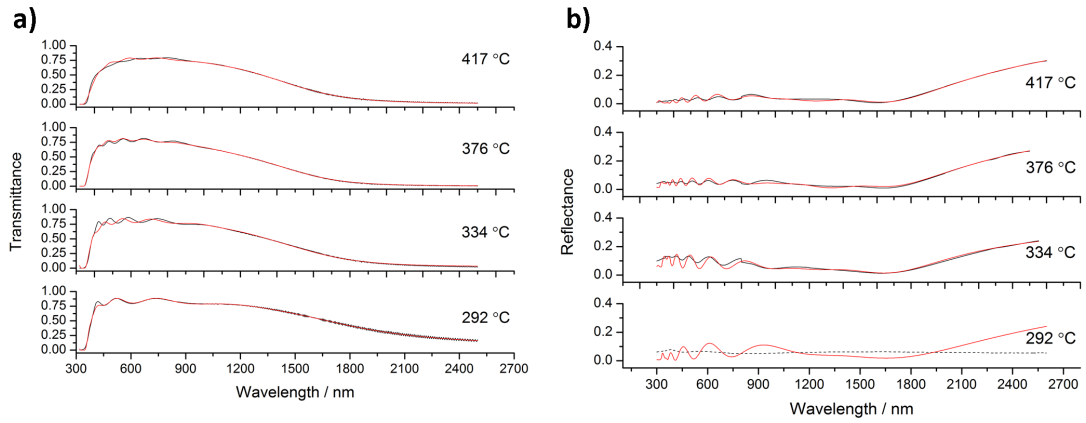

Figure F.1: Experimental a) transmittance and b) reflectance spectra of 5 at% IZO samples prepared by spray pyrolysis at various deposition temperatures are shown in black. The model fits are shown in red. Due to unforeseen issues it was not possible to obtain reliable reflectance data for the sample deposited at 292 °C and the fits shown were made to the transmittance data only.

Numerical Fitting Results

Samples are denoted by deposition temperature. For example, IZO417 refers to an IZO sample prepared at $T_{dep} = 417\,°C$.

```
IZO500
  Thick.2          546.18 +/- 7.86
  Thick.1          6724.41 +/- 25.2
  Einf.1           2.9796 +/- 0.0252
  wp.1             4.3761 +/- 0.211
  wt.1             3.9259 +/- 0.00914
  G.1              0.36588 +/- 0.016
  wp2.1            1.369 +/- 0.00958
  GL.1             0.37249 +/- 0.00791
  GH.1             0.083659 +/- 0.00384
  k.1              0.54876 +/- 0.0087
  ggw.1            0.21895 +/- 0.0126

IZO450
  Thick.2          356.93 +/- 6.23
  Thick.1          8043.06 +/- 22.7
  Einf.1           3.0237 +/- 0.0159
  wp.1             2.2104 +/- 0.0991
  wt.1             3.7758 +/- 0.00546
  G.1              0.19942 +/- 0.00871
```

```
  wp2.1           1.336 +/- 0.0069
  GL.1            0.4232 +/- 0.0124
  GH.1            0.095285 +/- 0.00339
  k.1             0.50393 +/- 0.0117
  ggw.1           0.24452 +/- 0.012

IZO400
  Thick.1         6049.26 +/- 18.6
  Einf.1          3.4403 +/- 0.0201
  wp.1            1.5899 +/- 0.0678
  wt.1            3.6666 +/- 0.00517
  G.1             0.23172 +/- 0.0132
  wp2.1           1.421 +/- 0.0084
  GL.1            0.76159 +/- 0.0833
  k.1             0.36358 +/- 0.0301
  GH.1            0.034325 +/- 0.00977
  ggw.1           0.27212 +/- 0.0142
  Thick.2         14.17

IZO350
  Thick.1         4013.15 +/- 62.4
  Einf.1          3.6768 +/- 0.123
  wp.1            3.0961 +/- 0.476
  wt.1            3.6763 +/- 0.00877
  G.1             0.17153 +/- 0.0319
  wp2.1           1.249 +/- 0.0363
  GL.1            0.4038 +/- 0.0645
  k.1             0.56051 +/- 0.0446
  GH.1            0.049184 +/- 0.0201
  ggw.1           0.24216 +/- 0.0474
  Thick.2         469.33 +/- 40.4
```

F.2 Fits to 5 at% Tin-doped In_2O_3

Description of Parameters

ITO transmittance and reflectance spectra (between 1000 nm and 2500 nm) were modeled using a Drude oscillator to describe the behavior of conduction electrons near the plasma edge. The parameter names and corresponding descriptions are given in Table F.2. The substrate is modeled as a 0.17 mm thick layer of D263T borosilicate glass with literature dielectric properties.

Table F.2: Model parameters for optical transport modeling of ITO transmittance and reflectance spectra.

Parameter Name	Units	Description
Thick.1	Å	Thickness of Uniform ITO layer
Thick.2	Å	Thickness of Surface Roughness Layer (50:50 Intermix of TCO and Air)
Am1.1	eV^2	Drude Frequency (ω_p^2)
Br1.1	eV	Drude Damping Constant (Γ)
e1(inf).1		High Frequency Dielectric Constant (ϵ_∞)

Graphical Fitting Results

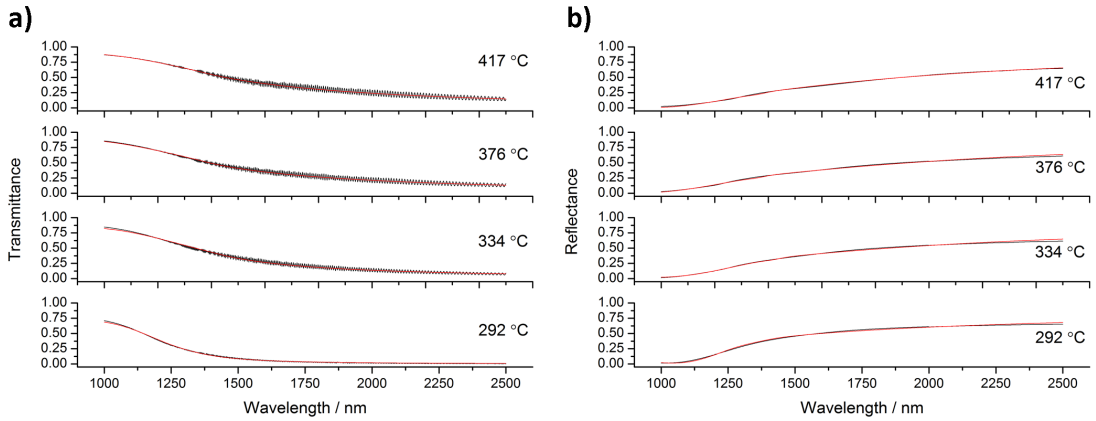

Figure F.2: Experimental a) transmittance and b) reflectance spectra of 5 at% ITO samples prepared by spray pyrolysis at various deposition temperatures are shown in black. The model fits are shown in red.

Numerical Fitting Results

Samples are denoted by deposition temperature. For example, ITO417 refers to an ITO sample prepared at $T_{dep} = 417\,^{\circ}\mathrm{C}$.

```
ITO417
  Thick.2          375.00 +/- 28.8
  Thick.1          2124.99 +/- 152
  Am1.1            2.2033 +/- 0.216
  Br1.1            0.062049 +/- 0.00369
  e1(inf).1        2.7033 +/- 0.19
```

```
ITO376
  Thick.2          503.31 +/- 26.2
  Am1.1            1.9273 +/- 0.129
  Br1.1            0.066009 +/- 0.00336
  Thick.1          2413.77 +/- 114
  e1(inf).1        2.3504 +/- 0.109

ITO334
  Thick.2          593.92 +/- 22.5
  Thick.1          3331.59 +/- 120
  e1(inf).1        2.0883 +/- 0.079
  Am1.1            1.5743 +/- 0.0841
  Br1.1            0.071005 +/- 0.00215

ITO292
  Thick.2          537.34 +/- 13.5
  Thick.1          5898.24 +/- 121
  e1(inf).1        1.6288 +/- 0.0513
  Am1.1            1.3287 +/- 0.0505
  Br1.1            0.096794 +/- 0.000897
```

Appendix G

EXAFS Fitting Logs

G.1 Defining Path Nomenclature

The scattering paths detailed in the following logs are named in accordance with the following figures. All paths used for these fittings are single-scattering paths. The absorber atom is shown in solid yellow in all cases.

Where paths from multiple environments are used in a single model, their relative intensity is varied by introducing a parameter ("doping") to allow the amplitude reduction factor S_0^2 to vary between environments. The variable "amp" is used for the amplitude reduction factor and "dele" is used for ΔE_0. "dr" parameters refer to the difference between the fitted scattering path length (R) and the theoretical path length based on the starting model (R_{eff}). "ss" parameters are for the σ^2 of paths. The names following the *dr* and *ss* do not necessarily correspond to the path names, however, a comparison of values should make it apparent which parameters are connected with a given path.

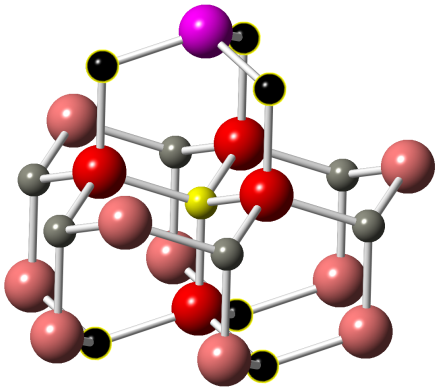

Figure G.1: Names of scattering paths for indium substituted at zinc sites: Red (O1.1), Light Grey (Zn1.1), Black (Zn1.2), Pink (O1.4), Purple (O1.3)

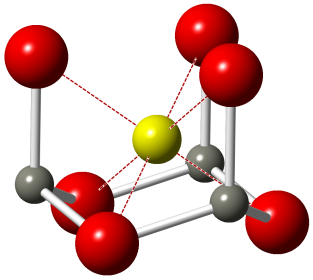

Figure G.2: Scattering paths for In located at octahedral holes in ZnO: Grey (Zn1.1_int), Red (O1.1_int)

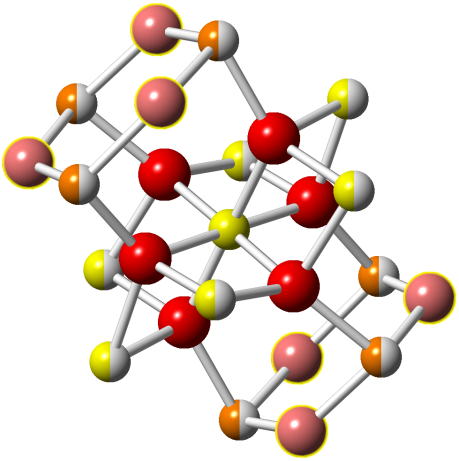

Figure G.3: Scattering paths for In at In_2O_3-like sites: Red (O1.1), Yellow/White (In2.1), Orange/White (In2.2), Pink (O1.2). Note that a fraction of the In2.1 or In2.2 paths may be replaced with the same path, but with a zinc scatterer and denoted Zn2 in some models.

G.2 Fitting Logs

G.2.1 Models for 0.5IZO

In_{Zn} Only

```
guess parameters:
  amp                =   0.76815826    # +/-   0.11941947     [.803]
  dele               =   5.51019498    # +/-   1.73531626     [5.65]
  drO2               =  -0.05774875    # +/-   0.05321697     [-.05]
  ssO2               =   0.00491725    # +/-   0.00629605     [.007]
  drZn1              =   0.07203664    # +/-   0.01523225     [0]
  drO1               =   0.10238431    # +/-   0.01287902     [.1]
  ssO1               =   0.00041204    # +/-   0.00169943     [.001]
  ssZn1              =   0.01000145    # +/-   0.00190634     [0.00300]

: k-range              = 3 - 11.5
: dk                   = 1
: k-window             = hanning
: k-weight             = 1,2,3
: R-range              = 1.1 - 3.4
: dR                   = 0.0
: R-window             = hanning
: fitting space        = r
: background function  = no
: phase correction     =
: R-factor by k-weight = 1 -> 0.01289,  2 -> 0.02803,  3 -> 0.04996
```

name	N	S02	sigma^2	e0	delr	Reff	R
O1.1	4.000	0.768	0.00041	5.510	0.10238	1.97730	2.07968
Zn1.1	6.000	0.768	0.01000	5.510	0.07204	3.20820	3.28024
Zn1.2	6.000	0.768	0.01000	5.510	0.07204	3.24880	3.32084
O1.4	9.000	0.768	0.00492	5.510	-0.05775	3.80490	3.74715
O1.3	1.000	0.768	0.00492	5.510	-0.05775	3.22210	3.16435

G.2.2 Models for 1.5IZO

In_{Zn} Only

```
guess parameters:
  amp                =   0.89463705    # +/-   0.05026425     [.803]
  dele               =   4.06844138    # +/-   0.76237115     [5.65]
  drO2               =  -0.12763019    # +/-   0.04400614     [-.05]
  ssO2               =   0.02699359    # +/-   0.00754428     [.007]
  drZn1              =   0.07836348    # +/-   0.00673868     [0]
  drO1               =   0.09888566    # +/-   0.00645336     [.1]
  ssO1               =   0.00428313    # +/-   0.00079159     [.001]
  ssZn1              =   0.01250005    # +/-   0.00072208     [.015]

: k-range              = 3 - 14
: dk                   = 1
```

```
: k-window             = hanning
: k-weight             = 1,2,3
: R-range              = 1.1 - 3.35
: dR                   = 0.0
: R-window             = hanning
: fitting space        = r
: background function  = no
: phase correction     =
: R-factor by k-weight = 1 -> 0.00269,  2 -> 0.00980,  3 -> 0.03105
```

name	N	S02	sigma^2	e0	delr	Reff	R
O1.1	4.000	0.895	0.00428	4.068	0.09889	1.97730	2.07619
Zn1.1	6.000	0.895	0.01250	4.068	0.07836	3.20820	3.28656
Zn1.2	6.000	0.895	0.01250	4.068	0.07836	3.24880	3.32716
O1.4	9.000	0.895	0.02699	4.068	-0.12763	3.80490	3.67727
O1.3	1.000	0.895	0.02699	4.068	-0.12763	3.22210	3.09447

$\mathbf{In_{Zn}}$ and $\mathbf{In}_{int}$

```
guess parameters:
  amp                =   0.54318181    # +/-   0.06734357     [1.00000]
  dele               =   7.74429576    # +/-   0.92236103     [7.26962]
  drZn1              =   0.09260317    # +/-   0.00662015     [0.08955]
  ssZn1              =   0.00871353    # +/-   0.00092137     [0.00300]
  drO1               =   0.11013769    # +/-   0.00937267     [0.10944]
  ssO1               =   0.00197032    # +/-   0.00109045     [0.00300]
  drO2               =   0.05308362    # +/-   0.03369662     [0.05144]
  ssO2               =   0.00908211    # +/-   0.00379951     [0.00300]
  drInZn             =   0.05278938    # +/-   0.06390201     [0.04504]
  ssInZn             =   0.01610789    # +/-   0.01062266     [0.00300]
  drO3               =  -0.07657923    # +/-   0.03856386     [-0.08296]
  ssO3               =   0.01080041    # +/-   0.01304959     [0.00300]
  doping             =   0.75935190    # +/-   0.45710285     [.1]

: k-range              = 3 - 14
: dk                   = 1
: k-window             = hanning
: k-weight             = 1,2,3
: R-range              = 1 - 3.6
: dR                   = 0.0
: R-window             = hanning
: fitting space        = r
: background function  = no
: phase correction     =
: R-factor by k-weight = 1 -> 0.00077,  2 -> 0.00312,  3 -> 0.01204
```

name	N	S02	sigma^2	e0	delr	Reff	R
O1.1	4.000	0.543	0.00197	7.744	0.11014	1.97730	2.08744
Zn1.1	6.000	0.543	0.00871	7.744	0.09260	3.20820	3.30080
Zn1.2	6.000	0.543	0.00871	7.744	0.09260	3.24880	3.34140
O1.4	9.000	0.543	0.00908	7.744	0.05308	3.80490	3.85798

```
[ZnO_InIn]  Zn1.1_Int      3.000   0.412   0.01611   7.744  0.05279  1.99580  2.04859
[ZnO_InIn]  O1.1_Int       6.000   0.412   0.01080   7.744 -0.07658  2.28290  2.20632
 O1.3                      1.000   0.543   0.00908   7.744  0.05308  3.22210  3.27518
```

G.2.3 Models for 5IZO

In_{Zn} and In_{int}

```
guess parameters:
  amp                =   0.41060525    # +/-   0.21722235     [1.00000]
  dele               =   4.28547291    # +/-   1.80112228     [0]
  drO1               =   0.03542364    # +/-   0.03727490     [0]
  ssO1               =   0.00484916    # +/-   0.00270113     [0.00300]
  drZn               =   0.09632311    # +/-   0.02442165     [0]
  ssZn               =   0.02429061    # +/-   0.00680019     [0.00300]
  drO2               =   0.07986179    # +/-   0.05927079     [0]
  ssO2               =   0.02197666    # +/-   0.02140411     [0.00300]
  doping             =   0.97338692    # +/-   1.29889183     [1.00000]
  drO3               =  -0.11405255    # +/-   0.04643694     [0]
  ssO3               =   0.01001108    # +/-   0.01024132     [0.00300]

: k-range              = 3 - 14
: dk                   = 1
: k-window             = hanning
: k-weight             = 1,2,3
: R-range              = 1 - 3.9
: dR                   = 0.0
: R-window             = hanning
: fitting space        = r
: background function  = no
: phase correction     =
: R-factor by k-weight = 1 -> 0.00330,  2 -> 0.00930,  3 -> 0.03649
```

name	N	S02	sigma^2	e0	delr	Reff	R
Zn1.1	3.000	0.400	0.02429	4.285	0.09632	1.99580	2.09212
O1.1	6.000	0.400	0.01001	4.285	-0.11405	2.28290	2.16885
O1.1	4.000	0.411	0.00485	4.285	0.03542	1.97730	2.01272
Zn1.1	6.000	0.411	0.02429	4.285	0.09632	3.20820	3.30452
Zn1.2	6.000	0.411	0.02429	4.285	0.09632	3.24880	3.34512
O1.4	9.000	0.411	0.02198	4.285	0.07986	3.80490	3.88476
O1.3	1.000	0.411	0.02198	4.285	0.07986	3.22210	3.30196

In_2O_3-like

```
guess parameters:
  amp                =   0.92456058    # +/-   0.16623428     [1.00000]
  dele               =  -0.18375581    # +/-   3.87558631     [0]
  drIn0              =  -0.06145295    # +/-   0.01608338     [0]
  ssIn0              =   0.00925834    # +/-   0.00180069     [0.00300]
  drIn1              =  -0.12866383    # +/-   0.04111517     [0]
  ssIn1              =   0.02085963    # +/-   0.00378247     [0.00300]
```

```
  drIn2              =  -0.09573512    # +/-   0.09285429     [0]
  ssIn2              =   0.04379567    # +/-   0.03436136     [0.00300]
  drIn02             =  -1.97435099    # +/-   0.11784219     [0]
  ssIn02             =   0.06931305    # +/-   0.05352755     [0.00300]

: k-range              = 3 - 14
: dk                   = 1
: k-window             = hanning
: k-weight             = 1,2,3
: R-range              = 1 - 3.9
: dR                   = 0.0
: R-window             = hanning
: fitting space        = r
: background function  = no
: phase correction     =
: R-factor by k-weight = 1 -> 0.00250,  2 -> 0.00735,  3 -> 0.02175
```

name	N	S02	sigma^2	e0	delr	Reff	R
O1.1	6.000	0.000	0.00000	-0.184	0.00000	2.28290	2.28290
Zn1.2	3.000	0.000	0.00000	-0.184	0.00000	2.68470	2.68470
O1.1	6.000	0.925	0.00000	-0.184	0.00000	2.16060	2.16060
In2.1	3.000	0.925	0.00000	-0.184	0.00000	3.34450	3.34450
In2.2	6.000	0.925	0.02086	-0.184	0.00000	3.82560	3.82560
Zn1.1	3.000	0.000	0.00000	-0.184	0.00000	1.99580	1.99580

In_{Zn} and In_2O_3-like

```
guess parameters:
  alpha              =  -0.01865032    # +/-   0.00369275     [0]
  dele               =   2.34389775    # +/-   0.51937340     [0]
  amp                =   0.69548658    # +/-   0.05773459     [1.00000]
  ss0In              =   0.00619344    # +/-   0.00223311     [0.00300]
  ssZn2              =   0.00450656    # +/-   0.00199980     [0.00300]
  drZn2              =   0.17103559    # +/-   0.01152215     [0]
  doping             =   0.19411612    # +/-   0.07640048     [1]
  drO1               =  -0.26829511    # +/-   0.04245699     [0]
  ssZn               =   0.01082469    # +/-   0.00451393     [0.00300]
  drZn               =   0.31413154    # +/-   0.02608621     [0]
  alpha1             =  -0.03572821    # +/-   0.00298959     [0]
  ssIn               =   0.01631869    # +/-   0.00140493     [0.00300]
  ssO1               =   0.00360873    # +/-   0.00393918     [0.00300]

: k-range              = 3 - 14
: dk                   = 1
: k-window             = hanning
: k-weight             = 1,2,3
: R-range              = 1 - 3.9
: dR                   = 0.0
: R-window             = hanning
: fitting space        = r
: background function  = no
: phase correction     =
```

```
: R-factor by k-weight = 1 -> 0.00106,  2 -> 0.00179,  3 -> 0.00541

  name                    N       S02     sigma^2   e0      delr     Reff     R
================================================================================
 O1.1                  6.000   0.695   0.00619   2.344 -0.04030  2.16060  2.12030
 In2.1                 6.000   0.695   0.01632   2.344 -0.11949  3.34450  3.22501
 Zn1.1                 3.000   0.135   0.01083   2.344  0.31413  1.99580  2.30993
 O1.1                  6.000   0.135   0.00361   2.344 -0.26830  2.28290  2.01461
 Zn1.2                 3.000   0.135   0.00451   2.344  0.17104  2.68470  2.85574
```

G.2.4 Models for 12.5IZO

In_{Zn} and In_{int}

```
  amp               =   1.31549652    # +/-   0.72922560     [1.00000]
  dele              =  -5.13690766    # +/-   3.54262260     [0]
  drO1              =  -0.08116265    # +/-   0.11794418     [0]
  ssO1              =   0.02581380    # +/-   0.01447930     [0.00300]
  drO2              =  -0.07941381    # +/-   0.05025381     [0]
  ssO2              =   0.00878514    # +/-   0.00598761     [0.00300]
  drZn              =   0.25289896    # +/-   0.05421925     [0]
  ssZn              =   0.02483674    # +/-   0.00616759     [0.00300]
  drZn2             =   0.21318299    # +/-   0.07795663     [0]
  doping            =   0.81707417    # +/-   0.74975397     [1.00000]
  ssZn2             =   0.02656730    # +/-   0.02380292     [0.00300]
  drO3              =  -0.20227216    # +/-   0.02487878     [0]
  ssO3              =   0.00810946    # +/-   0.00539316     [0.00300]

: k-range             = 3.000 - 13.5
: dk                  = 1
: k-window            = hanning
: k-weight            = 1,2,3
: R-range             = 1 - 3.9
: dR                  = 0.0
: R-window            = hanning
: fitting space       = r
: background function = no
: phase correction    =
: R-factor by k-weight = 1 -> 0.00951,  2 -> 0.02867,  3 -> 0.10863

  name                    N       S02     sigma^2   e0      delr     Reff     R
================================================================================
 O1.1                  4.000   1.315   0.02581  -5.137 -0.08116  1.97730  1.89614
 Zn1.1                 6.000   1.315   0.02484  -5.137  0.25290  3.20820  3.46110
 Zn1.2                 6.000   1.315   0.02484  -5.137  0.25290  3.24880  3.50170
 O1.4                  9.000   1.315   0.00878  -5.137 -0.07941  3.80490  3.72549
 O1.3                  1.000   1.315   0.00878  -5.137 -0.07941  3.22210  3.14269
[ZnO]  Zn1.1_int       3.000   1.075   0.02657  -5.137  0.21318  1.99580  2.20898
[ZnO]  O1.1_int        6.000   1.075   0.00811  -5.137 -0.20227  2.28290  2.08063
```

In_2O_3-like

```
guess parameters:
  amp                =   0.89236404    # +/-   0.07901441     [0.89447]
  dele               =   2.28192286    # +/-   0.95038440     [2.19726]
  drIn0              =  -0.03767668    # +/-   0.00867901     [-0.03837]
  ssIn0              =   0.00819636    # +/-   0.00141538     [0.00824]
  drIn2              =   0.00879628    # +/-   0.03954828     [0.02021]
  ssIn2              =   0.01356735    # +/-   0.00366695     [0.01703]
  drIn1              =  -0.06031047    # +/-   0.01503616     [-0.06132]
  ssIn1              =   0.01426519    # +/-   0.00188680     [0.01482]
  drIn02             =   0.20332405    # +/-   0.04454068     [0.22227]
  ssIn02             =   0.00296937    # +/-   0.00384681     [.00754]

: k-range              = 3.000 - 13.5
: dk                   = 1
: k-window             = hanning
: k-weight             = 1,2,3
: R-range              = 1 - 3.9
: dR                   = 0.0
: R-window             = hanning
: fitting space        = r
: background function  = no
: phase correction     =
: R-factor by k-weight = 1 -> 0.00672,  2 -> 0.02137,  3 -> 0.07417

  name         N       S02     sigma^2   e0     delr     Reff     R
=================================================================
 O1.1       6.000   0.892   0.00820   2.282 -0.03768  2.16060  2.12292
 In2.1      6.000   0.892   0.01427   2.282 -0.06031  3.34450  3.28419
 In2.2      6.000   0.892   0.01357   2.282  0.00880  3.82560  3.83440
 O1.2       6.000   0.892   0.00297   2.282  0.20332  3.97540  4.17872
```

In_2O_3-like w/ Zn

```
guess parameters:
  alpha              =  -0.02030143    # +/-   0.00310128     [-0.01398]
  dele               =   1.57954922    # +/-   0.74964767     [2.37394]
  amp                =   0.87142771    # +/-   0.05477848     [1.00000]
  ssOIn              =   0.00803817    # +/-   0.00099341     [0.00300]
  doping             =   0.21066607    # +/-   0.27810275     [1.00000]
  ssIn2              =   0.00339546    # +/-   0.01212107     [0.00300]
  ssIn3              =   0.01248868    # +/-   0.00724317     [0.00300]
  alpha1             =  -0.01851941    # +/-   0.00499013     [-0.02072]
  alpha2             =   0.01106772    # +/-   0.01628790     [0.03121]
  ssIn               =   0.00539480    # +/-   0.00326320     [0.00300]
  alpha3             =  -0.00659093    # +/-   0.01002704     [0]
  ssIn1              =   0.03121517    # +/-   0.01225142     [0.00300]
  alpha4             =  -0.05346297    # +/-   0.03097866     [0]

: k-range              = 3 - 13.5
: dk                   = 1
: k-window             = hanning
: k-weight             = 1,2,3
```

```
: R-range              = 1 - 3.9
: dR                   = 0.0
: R-window             = hanning
: fitting space        = r
: background function  = no
: phase correction     =
: R-factor by k-weight = 1 -> 0.00215,  2 -> 0.00695,  3 -> 0.02209
```

name	N	S02	sigma^2	e0	delr	Reff	R
O1.1	6.000	0.871	0.00804	1.580	-0.04386	2.16060	2.11674
In2.1	3.000	0.871	0.00539	1.580	-0.06194	3.34450	3.28256
In2.2	6.000	0.871	0.03122	1.580	0.04234	3.82560	3.86794
[In2O3_su] Zn2.1	6.000	0.184	0.00340	1.580	-0.02204	3.34450	3.32246
[In2O3_su] Zn2.2	6.000	0.184	0.01249	1.580	-0.20453	3.82560	3.62107

Appendix H

Publications Resulting From This Work

As of the time of writing, the following is a list of the peer-reviewed publications that have arisen as a result of the work described in this thesis:

1. Vai, A. T.; Kuznetsov, V. L.; Jain, H.; Slocombe, D.; Rashidi, N.; Pepper, M.; Edwards, P. P.; **The Transition to the Metallic State in Polycrystalline n-type Doped ZnO Thin Films** *Z. Anorg. Allg. Chem.* **2014**, *640*, 1054–1062.
2. Vai, A. T.; Kuznetsov, V. L.; Dilworth, J. R.; Edwards, P. P.; **UV-induced Improvement in ZnO Thin Film Conductivity: a New *in situ* Approach** *J. Mater. Chem. C* **2014**, *2*, 9643–9652.
3. Rashidi, N.†; Vai, A. T.†; Kuznetsov, V. L.; Dilworth, J. R.; Edwards, P. P.; **Origins of Conductivity Improvement in Fluoride-Enhanced Silicon Doping of ZnO Films** *Chem. Commun.* **2015**, *51*, 9280–9283.
4. Vai, A. T.; Rashidi, N.; Fang, Y.; Kuznetsov, V. L.; Edwards, P. P.; **Contrasting the Grain Boundary-Affected Performance of Zinc and Indium Oxide Transparent Conductors** *J. Phys.: Condens. Matter* **2015**. (*In Press, Accepted Manuscript*)
5. Kuznetsov, V. L.; Vai, A. T.; Al-Mamouri, M.; Abell, J. S.; Pepper, M.; Edwards, P. P.; **Electronic Transport in Highly Conducting Si-Doped ZnO Thin Films Prepared by Pulsed Laser Deposition** *Appl. Phys. Lett* **2015**, *107*, 232103.

† These authors contributed equally to this work.

Additionally, manuscripts are currently in preparation on the following topics:

- Disposition of indium dopant in IZO thin films
- Thermal decomposition of precursors under spray pyrolysis conditions